

1

2

3

4

5

Simultaneous Measurement of Oscillation Parameters in Beam and Atmospheric Neutrino Data from Tokai-to-Kamioka and Super-Kamiokande Experiments

6

Daniel Robert Clement Barrow

7

8

Magdalen College,
Oxford University

9

Version 1.2

10

A Dissertation Submitted to Oxford University
11 for the Degree of Doctor of Philosophy

13 **Simultaneous Measurement of**

14 **Oscillation Parameters in Beam and**

15 **Atmospheric Neutrino Data from**

16 **Tokai-to-Kamioka and**

17 **Super-Kamiokande Experiments**

18 *Abstract*

19 Lorem ipsum dolor sit amet, consectetur adipiscing elit, sed do eiusmod tempor incididunt ut labore et dolore magna aliqua. Nulla aliquet porttitor lacus luctus accumsan tortor posuere. Pulvinar neque laoreet suspendisse interdum. Sem viverra aliquet eget sit. Nunc sed velit dignissim sodales ut eu sem integer vitae. At erat pellentesque adipiscing commodo elit at imperdiet dui accumsan. Fames ac turpis egestas integer eget aliquet nibh. Scelerisque eu ultrices vitae auctor eu augue. Purus non enim praesent elementum facilisis leo vel. Sollicitudin nibh sit amet commodo. Vitae auctor eu augue ut. Vel quam elementum pulvinar etiam. A condimentum vitae sapien pellentesque habitant morbi tristique senectus. Viverra accumsan in nisl nisi scelerisque eu ultrices. Sed viverra ipsum nunc aliquet bibendum enim.

32 Declaration

33 This dissertation is the result of my own work, except where ex-
34 plicit reference is made to the work of others, and has not been sub-
35 mitted for another qualification to this or any other university. This
36 dissertation does not exceed the word limit for the respective Degree
37 Committee.

38 Daniel Robert Clement Barrow

39 ©The copyright of this thesis rests with the author and is made available under a Creative
40 Commons Attribution Non-Commercial No Derivatives licence. Researchers are free to copy,
41 distribute or transmit the thesis on the condition that they attribute it, that they do not use
42 it for commercial purposes and that they do not alter, transform or build upon it. For any
43 reuse or redistribution, researchers must make clear to others the licence terms of this work.

44

Acknowledgements

45 at pretium nibh ipsum. Eget nunc scelerisque viverra mauris in aliquam. Arcu vitae
46 elementum curabitur vitae nunc sed velit dignissim. Sed arcu non odio euismod lacinia
47 at quis risus sed. Vitae tempus quam pellentesque nec nam aliquam sem et tortor.
48 Viverra aliquet eget sit amet tellus cras adipiscing. Purus sit amet luctus venenatis
49 lectus magna. In aliquam sem fringilla ut morbi tincidunt augue. Fermentum dui
50 faucibus in ornare. Aliquam malesuada bibendum arcu vitae elementum curabitur
51 vitae nunc sed.

52 Ultricies leo integer malesuada nunc vel risus commodo. Tellus cras adipiscing
53 enim eu turpis egestas pretium. Dictumst quisque sagittis purus sit amet volutpat
54 consequat mauris nunc. Vitae congue mauris rhoncus aenean vel elit scelerisque
55 mauris pellentesque. Vel facilisis volutpat est velit egestas dui id ornare. Suscipit
56 adipiscing bibendum est ultricies. At in tellus integer feugiat scelerisque varius
57 morbi enim. Cras semper auctor neque vitae tempus. Commodo sed egestas egestas
58 fringilla phasellus faucibus. Cras pulvinar mattis nunc sed blandit. Pretium viverra
59 suspendisse potenti nullam ac tortor vitae. Purus sit amet volutpat consequat. Orci
60 sagittis eu volutpat odio facilisis mauris. Sit amet massa vitae tortor condimentum
61 lacinia quis. Commodo sed egestas egestas fringilla phasellus. Sed libero enim sed
62 faucibus turpis. Vitae tempus quam pellentesque nec.

63 Blandit massa enim nec dui. Viverra tellus in hac habitasse platea dictumst vestibulu-
64 lum. Bibendum enim facilisis gravida neque convallis. Sagittis nisl rhoncus mattis
65 rhoncus urna neque. Nisl rhoncus mattis rhoncus urna neque. Ac tortor vitae purus
66 faucibus ornare. Aenean sed adipiscing diam donec adipiscing tristique risus. Sapien
67 nec sagittis aliquam malesuada bibendum. Et leo duis ut diam quam nulla. Tellus
68 rutrum tellus pellentesque eu tincidunt tortor aliquam nulla facilisi.

69 **Contents**

70	1. Introduction	1
71	2. Neutrino Oscillation Physics	2
72	2.1. Discovery of Neutrinos	2
73	2.2. Theory of Neutrino Oscillation	4
74	2.2.1. Three Flavour Oscillations	4
75	2.2.2. The MSW Effect	8
76	2.3. Neutrino Oscillation Measurements	9
77	2.3.1. Solar Neutrinos	11
78	2.3.2. Atmospheric Neutrinos	13
79	2.3.3. Accelerator Neutrinos	16
80	2.3.4. Reactor Neutrinos	18
81	2.4. Summary	20
82	3. T2K and SK Experiment Overview	23
83	3.1. The Super-Kamiokande Experiment	23
84	3.1.1. The SK Detector	24
85	3.1.2. Calibration	28
86	3.1.3. Data Acquisition and Triggering	31
87	3.1.4. Cherenkov Radiation	33
88	3.2. The Tokai to Kamioka Experiment	35
89	3.2.1. The Neutrino Beam	38
90	3.2.2. The Near Detector at 280m	41
91	3.2.2.1. Fine Grained Detectors	44
92	3.2.2.2. Time Projection Chambers	45

93	3.2.2.3. π^0 Detector	47
94	3.2.2.4. Electromagnetic Calorimeter	47
95	3.2.2.5. Side Muon Range Detector	49
96	3.2.3. The Interactive Neutrino GRID	49
97	4. Bayesian Statistics and Markov Chain Monte Carlo Techniques	51
98	4.1. Bayesian Statistics	52
99	4.2. Monte Carlo Simulation	53
100	4.2.1. Markov Chain Monte Carlo	54
101	4.2.2. Metropolis-Hastings Algorithm	57
102	4.2.3. MCMC Optimisation	59
103	4.3. Understanding the MCMC Results	62
104	4.3.1. Marginalisation	63
105	4.3.2. Parameter Estimation and Credible Intervals	64
106	4.3.3. Bayesian Model Comparisons	66
107	4.3.4. Comparison of MCMC Output to Expectation	67
108	5. Simulation, Reconstruction, and Event Reduction	69
109	5.1. Simulation	69
110	5.2. Event Reconstruction at SK	74
111	5.2.1. Validation of Reconstruction in SK-V	82
112	5.3. Event Reduction at SK	86
113	6. Sample Selections and Systematics	92
114	6.1. Atmospheric Samples	94
115	6.2. Near Detector Beam Samples	101
116	6.3. Far Detector Beam Samples	103
117	6.4. Systematic Uncertainties	109
118	6.4.1. Beam Flux	109

119	6.4.2. Atmospheric Flux	111
120	6.4.3. Neutrino Interaction	113
121	6.4.4. Near Detector	119
122	6.4.5. Far Detector	121
123	6.4.5.1. Beam Samples	121
124	6.4.5.2. Atmospheric Samples	124
125	6.4.5.3. Correlated Detector Model	125
126	7. Oscillation Probability Calculation	133
127	7.1. Overview	134
128	7.2. Treatment of Fast Oscillations	142
129	7.3. Calculation Engine	149
130	7.4. Matter Density Profile	154
131	7.5. Production Height Averaging	159
132	8. Oscillation Analysis	163
133	8.1. Likelihood Calculation	163
134	8.1.1. Likelihood Scans	166
135	8.2. Monte Carlo Prediction	169
136	A. Atmospheric Sample Spectra	173
137	A.1. Binning	173
138	A.2. Fully Contained Sub-GeV Samples	173
139	A.3. Fully Contained Multi-GeV Samples	177
140	A.4. Fully Contained Multi-Ring Samples	178
141	A.5. Partially Contained Samples	179
142	A.6. Upward-Going Muon Samples	180
143	Bibliography	181

¹⁴⁵ **Chapter 1**

¹⁴⁶ **Introduction**

¹⁴⁷ **Chapter 2**

¹⁴⁸ **Neutrino Oscillation Physics**

¹⁴⁹ When first proposed, neutrinos were expected to be massless fermions that only in-
¹⁵⁰ teract through weak and gravitational forces. This meant they were very difficult to
¹⁵¹ detect as they can pass through significant amounts of matter without interacting. De-
¹⁵² spite this, experimental neutrino physics has developed with many different detection
¹⁵³ techniques and neutrino sources being used today. In direct tension with standard
¹⁵⁴ model physics, neutrinos have been determined to oscillate between different lepton
¹⁵⁵ flavours, requiring them to have mass.

¹⁵⁶ The observation techniques which lead to the discovery of the neutrino are doc-
¹⁵⁷ umented in section 2.1. The theory underpinning neutrino oscillation is described
¹⁵⁸ in section 2.2 and includes the approximations which can be made to simplify the
¹⁵⁹ understanding of neutrino oscillation in the two-flavour approximation. Past, current,
¹⁶⁰ and future neutrino experiments are detailed in section 2.3, including the reactor,
¹⁶¹ atmospheric, and long-baseline accelerator neutrino sources that have been used to
¹⁶² successfully constrain oscillation parameters. Finally, the current state of oscillation
¹⁶³ parameter measurements are summarised in section 2.4.

¹⁶⁴ **2.1. Discovery of Neutrinos**

¹⁶⁵ At the start of the 20th century, the electrons emitted from the β -decay of the nucleus
¹⁶⁶ were found to have a continuous energy spectrum [1,2]. This observation seemingly
¹⁶⁷ broke the energy conservation invoked within that period's nuclear models. Postulated

168 in 1930 by Pauli as the solution to this problem, the neutrino (originally termed
169 “neutron”) was theorized to be an electrically neutral spin-1/2 fermion with a mass of
170 the same order of magnitude as the electron [3]. This neutrino was to be emitted with
171 the electron in β -decay to alleviate the apparent breaking of energy conservation. As a
172 predecessor of today’s weak interaction model, Fermi’s theory of β -decay developed
173 the understanding by coupling the four constituent particles; electron, proton, neutron,
174 and neutrino, into a consistent model [4].

175 Whilst Pauli was not convinced of the ability to detect neutrinos, the first observa-
176 tions of the particle were made in the mid-1950s when neutrinos from a reactor were
177 observed via the inverse β -decay (IBD) process, $\bar{\nu}_e + p \rightarrow n + e^+$ [5, 6]. The detector
178 consisted of two parts: a neutrino interaction medium and a liquid scintillator. The
179 interaction medium was built from two water tanks. These were loaded with cadmium
180 chloride to allow increased efficiency of neutron capture. The positron emitted from
181 IBD annihilates, $e^+ + e^- \rightarrow 2\gamma$, generating a prompt signal and the neutron is captured
182 on the cadmium via $n + {}^{108}Cd \rightarrow {}^{109*}Cd \rightarrow {}^{109}Cd + \gamma$, producing a delayed signal. An
183 increase in the coincidence rate was observed when the reactor was operating which
184 was interpreted as interactions from neutrinos generated in the reactor.

185 After the discovery of the ν_e , the natural question of how many flavours of neutrino
186 exist was asked. In 1962, a measurement of the ν_μ was conducted at the Brookhaven
187 National Laboratory [7]. A proton beam was directed at a beryllium target, generating
188 a π -dominated beam which then decayed via $\pi^\pm \rightarrow \mu^\pm + (\nu_\mu, \bar{\nu}_\mu)$, and the subsequent
189 interactions of the ν_μ were observed. As the subsequent interaction of the neutrino
190 generates muons rather than electrons, it was determined the ν_μ was fundamentally
191 different from ν_e . The final observation to be made was that of the ν_τ from the DONUT
192 experiment [8]. Three neutrinos seem the obvious solution as it mirrors the known
193 number of charged lepton (as they form weak isospin doublets) but there could be

¹⁹⁴ evidence of more. Several neutrino experiments have found anomalous results [9, 10]
¹⁹⁵ which could be attributed to sterile neutrinos. However, cosmological observations
¹⁹⁶ indicate the number of neutrino species $N_{eff} = 2.99 \pm 0.17$ [11], as measured from
¹⁹⁷ the cosmic microwave background power spectrum, and LEP measured the number
¹⁹⁸ of active neutrino flavours to be $N_\nu 2.9840 \pm 0.0082$ [12] from measurements of the
¹⁹⁹ Z -decay width.

²⁰⁰ 2.2. Theory of Neutrino Oscillation

²⁰¹ As direct evidence of beyond Standard Model physics, a neutrino generated with
²⁰² lepton flavour α can change into a different lepton flavour β after propagating some
²⁰³ distance. This phenomenon is called neutrino oscillation and requires that neutrinos
²⁰⁴ must have a non-zero mass (as seen in subsection 2.2.1). This observation is direct
²⁰⁵ evidence of beyond standard model physics. This behaviour has been characterised
²⁰⁶ by the Pontecorvo-Maki-Nakagawa-Sakata (PMNS) [13–15] mixing matrix which
²⁰⁷ describes how the flavour and mass of neutrinos are associated. This is analogous to
²⁰⁸ the Cabibbo-Kobayashi-Maskawa (CKM) [16] matrix measured in quark physics.

²⁰⁹ 2.2.1. Three Flavour Oscillations

²¹⁰ The PMNS parameterisation defines three flavour eigenstates, ν_e , ν_μ and ν_τ (indexed
²¹¹ ν_α), which are eigenstates of the weak interaction and three mass eigenstates, ν_1 , ν_2 and
²¹² ν_3 (indexed ν_i). Each mass eigenstate is the superposition of all three flavour states,

$$|\nu_i\rangle = \sum_\alpha U_{\alpha i} |\nu_\alpha\rangle. \quad (2.1)$$

²¹³ Where U is the PMNS matrix which is unitary and connects the mass and flavour
²¹⁴ eigenstates.

²¹⁵ The weak interaction couples to flavour eigenstates so neutrinos interact with
²¹⁶ leptons of the same flavour. The propagation of a neutrino flavour eigenstate, in a
²¹⁷ vacuum, can be re-written as a plane-wave solution to the time-dependent Schrödinger
²¹⁸ equation,

$$|\nu_\alpha(t)\rangle = \sum_i U_{\alpha i}^* |\nu_i\rangle e^{-i\phi_i}. \quad (2.2)$$

²¹⁹ The probability of observing a neutrino of flavour eigenstate β from one which
²²⁰ originated as flavour α can be calculated as,

$$P(\nu_\alpha \rightarrow \nu_\beta) = |\langle \nu_\beta | \nu_\alpha(t) \rangle|^2 = \sum_{i,j} U_{\alpha i}^* U_{\beta i} U_{\alpha j} U_{\beta j}^* e^{-i(\phi_j - \phi_i)} \quad (2.3)$$

²²¹ The ϕ_i term can be expressed in terms of the energy, E_i , and magnitude of the
²²² three momenta, p_i , of the neutrino, $\phi_i = E_i t - p_i x$ (t and x being time and position
²²³ coordinates). Therefore,

$$\phi_j - \phi_i = E_j t - E_i t - p_j x + p_i x. \quad (2.4)$$

²²⁴ For a relativistic particle, $E_i \gg m_i$,

$$p_i = \sqrt{E_i^2 - m_i^2} \approx E_i - \frac{m_i^2}{2E_i}. \quad (2.5)$$

²²⁵ Making the approximations that neutrinos are relativistic, the mass eigenstates
²²⁶ were created with the same energy and that $x = L$, where L is the distance traveled by
²²⁷ the neutrino, Equation 2.4 then becomes

$$\phi_j - \phi_i = \frac{\Delta m_{ij}^2 L}{2E}, \quad (2.6)$$

²²⁸ where $\Delta m_{ij}^2 = m_j^2 - m_i^2$. This, combined with further use of unitarity relations
²²⁹ results in Equation 2.3 becoming

$$P(\nu_\alpha \rightarrow \nu_\beta) = \delta_{\alpha\beta} - 4 \sum_{i>j} \Re \left(U_{\alpha i}^* U_{\beta i} U_{\alpha j} U_{\beta j}^* \right) \sin^2 \left(\frac{\Delta m_{ij}^2 L}{4E} \right) + (-) 2 \sum_{i>j} \Im \left(U_{\alpha i}^* U_{\beta i} U_{\alpha j} U_{\beta j}^* \right) \sin \left(\frac{\Delta m_{ij}^2 L}{2E} \right). \quad (2.7)$$

²³⁰ Where $\delta_{\alpha\beta}$ is the Kronecker delta function and the negative sign on the last term is
²³¹ included for the oscillation probability of antineutrinos.

²³² Typically, the PMNS matrix is parameterised into three mixing angles, a charge
²³³ parity (CP) violating phase δ_{CP} , and two Majorana phases $\alpha_{1,2}$,

$$U = \underbrace{\begin{pmatrix} 1 & 0 & 0 \\ 0 & c_{23} & s_{23} \\ 0 & -s_{23} & c_{23} \end{pmatrix}}_{\text{Atmospheric, Accelerator}} \underbrace{\begin{pmatrix} c_{13} & 0 & s_{13}e^{-i\delta_{CP}} \\ 0 & 1 & 0 \\ -s_{13}e^{-i\delta_{CP}} & 0 & c_{13} \end{pmatrix}}_{\text{Reactor, Accelerator}} \underbrace{\begin{pmatrix} c_{12} & s_{12} & 0 \\ -s_{12} & c_{12} & 0 \\ 0 & 0 & 1 \end{pmatrix}}_{\text{Reactor, Solar}} \underbrace{\begin{pmatrix} e^{i\alpha_1/2} & 0 & 0 \\ 0 & e^{i\alpha_2/2} & 0 \\ 0 & 0 & 1 \end{pmatrix}}_{\text{Majorana}}. \quad (2.8)$$

²³⁴ Where $s_{ij} = \sin(\theta_{ij})$ and $c_{ij} = \cos(\theta_{ij})$. The oscillation parameters are often
²³⁵ grouped; (1,2) as “solar”, (2,3) as “atmospheric” and (1,3) as “reactor”. Many
²³⁶ neutrino experiments aim to measure the PMNS parameters from a wide array of
²³⁷ origins, as is the purpose of this thesis.

²³⁸ The Majorana phase, $\alpha_{1,2}$, included within the fourth matrix in Equation 2.8 is only
²³⁹ included for completeness. For an oscillation analysis experiment, any terms contain-
²⁴⁰ ing this phase disappear due to taking the expectation value of the PMNS matrix.
²⁴¹ Measurements of these phases are typically performed by experiments searching for
²⁴² neutrino-less double β -decay [17].

²⁴³ A two flavour approximation can be obtained when one assumes the third mass
²⁴⁴ eigenstate is degenerate with another. As discussed in section 2.3, it is found that
²⁴⁵ $\Delta m_{21}^2 \ll |\Delta m_{31}^2|$. This results in the two flavour approximation being reasonable for
²⁴⁶ understanding the features of the oscillation. In this two flavour case, the mixing
²⁴⁷ matrix becomes,

$$U_{2 \text{ Flav.}} = \begin{pmatrix} \cos(\theta) & \sin(\theta) \\ -\sin(\theta) & \cos(\theta) \end{pmatrix}. \quad (2.9)$$

²⁴⁸ This culminates in the oscillation probability,

$$\begin{aligned} P(\nu_\alpha \rightarrow \nu_\alpha) &= 1 - \sin^2(2\theta) \sin^2\left(\frac{\Delta m^2 L}{4E}\right), \\ P(\nu_\alpha \rightarrow \nu_\beta) &= \sin^2(2\theta) \sin^2\left(\frac{\Delta m^2 L}{4E}\right). \end{aligned} \quad (2.10)$$

²⁴⁹ Where $\alpha \neq \beta$. For a fixed neutrino energy, the oscillation probability is a sinusoidal
²⁵⁰ function depending upon the distance over which the neutrino propagates. The
²⁵¹ frequency and amplitude of oscillation are dependent upon $\Delta m^2/4E$ and $\sin^2 2\theta$,
²⁵² respectively. The oscillation probabilities presented thus far assume $c = 1$, where
²⁵³ c is the speed of light in vacuum. In more familiar units, the maximum oscillation
²⁵⁴ probability for a fixed value of θ is given at $L[km]/E[GeV] \sim 1.27/\Delta m^2$. It is this
²⁵⁵ calculation that determines the best L/E value for a given experiment to be designed
²⁵⁶ around for measurements of a specific value of Δm^2 .

²⁵⁷ 2.2.2. The MSW Effect

²⁵⁸ The theory of neutrino oscillation in a vacuum has been described in subsection 2.2.1.
²⁵⁹ However, the beam neutrinos and atmospheric neutrinos originating from below the
²⁶⁰ horizon propagate through matter in the Earth. The coherent scattering of neutrinos
²⁶¹ from a material target modifies the Hamiltonian of the system. This results in a change
²⁶² in the oscillation probability. Notably, charged current scattering ($\nu_e + e^- \rightarrow \nu_e + e^-$,
²⁶³ propagated by a W boson) only affects electron neutrinos whereas the neutral current
²⁶⁴ scattering ($\nu_l + l^- \rightarrow \nu_l + l^-$, propagated by a Z^0 boson) interacts through all neutrino
²⁶⁵ flavours equally. In the two-flavour approximation, the effective mixing parameter
²⁶⁶ becomes

$$\sin^2(2\theta) \rightarrow \sin^2(2\theta_m) = \frac{\sin^2(2\theta)}{(A/\Delta m^2 - \cos(2\theta))^2 + \sin^2(2\theta)}, \quad (2.11)$$

267 where $A = 2\sqrt{2}G_F N_e E$, N_e is the electron density of the medium and G_F is Fermi's
268 constant. It is clear to see that there exists a value of $A = \Delta m^2 \cos(2\theta)$ for $\Delta m^2 > 0$
269 which results in a divergent mixing parameter. This resonance is termed the Mikheyev-
270 Smirnov-Wolfenstein (MSW) effect (or more colloquially, the matter resonance) which
271 regenerates the electron neutrino component of the neutrino flux [18–20]. The density
272 at which the resonance occurs is given by

$$N_e = \frac{\Delta m^2 \cos(2\theta)}{2\sqrt{2}G_F E}. \quad (2.12)$$

273 At densities lower than this critical value, the oscillation probability will be much
274 closer to that of vacuum oscillation. For antineutrinos, $N_e \rightarrow -N_e$ [21]. The resonance
275 occurring from the MSW effect depends on the sign of Δm^2 . Therefore, any neutrino
276 oscillation experiment which observes neutrinos and antineutrinos which have propa-
277 gated through matter can have some sensitivity to the ordering of the neutrino mass
278 eigenstates.

279 2.3. Neutrino Oscillation Measurements

280 As evidence of beyond standard model physics, the 2015 Nobel Prize in Physics was
281 awarded to the Super-Kamiokande (SK) [22] and Sudbury Neutrino Observatory
282 (SNO) [23] collaborations for the first definitive observation of solar and atmospheric

283 neutrino oscillation [24]. Since then, the field has seen a wide array of oscillation
284 measurements from a variety of neutrino sources. As seen in subsection 2.2.1, the
285 neutrino oscillation probability is dependent on the ratio of the propagation baseline, L ,
286 to the neutrino energy, E . It is this ratio that determines the type of neutrino oscillation
287 a particular experiment is sensitive to.

288 As illustrated in Figure 2.1, there are many neutrino sources that span a wide
289 range of energies. The least energetic neutrinos are from diffuse supernovae and
290 terrestrial neutrinos at $O(1)$ MeV whereas the most energetic neutrinos originate from
291 atmospheric and galactic neutrinos of $> O(1)$ TeV.

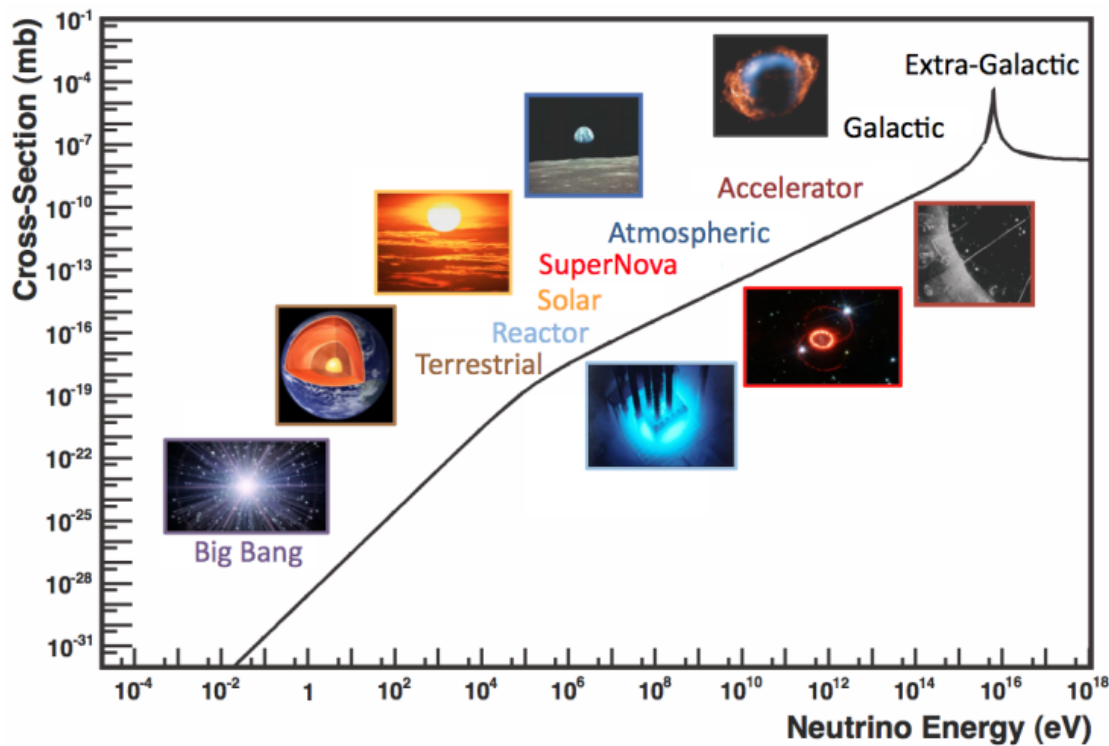


Figure 2.1.: The cross-section of neutrinos from various natural and man-made sources as a function of neutrino energy. Taken from [25]

²⁹² 2.3.1. Solar Neutrinos

²⁹³ Solar neutrinos are emitted from fusion reaction chains at the center of the Sun. The
²⁹⁴ solar neutrino flux, given as a function of neutrino energy for different fusion and
²⁹⁵ decay chains, is illustrated in Figure 2.2. Whilst proton-proton fusion generates the
²⁹⁶ largest flux of neutrinos, the neutrinos are of low energy and are difficult to reconstruct
²⁹⁷ due to the IBD interaction threshold of 1.8MeV. Consequently, most experiments focus
²⁹⁸ on the neutrinos from the decay of 8B (via $^8B \rightarrow ^8Be^* + e^+ + \nu_e$), which are higher
²⁹⁹ energy.

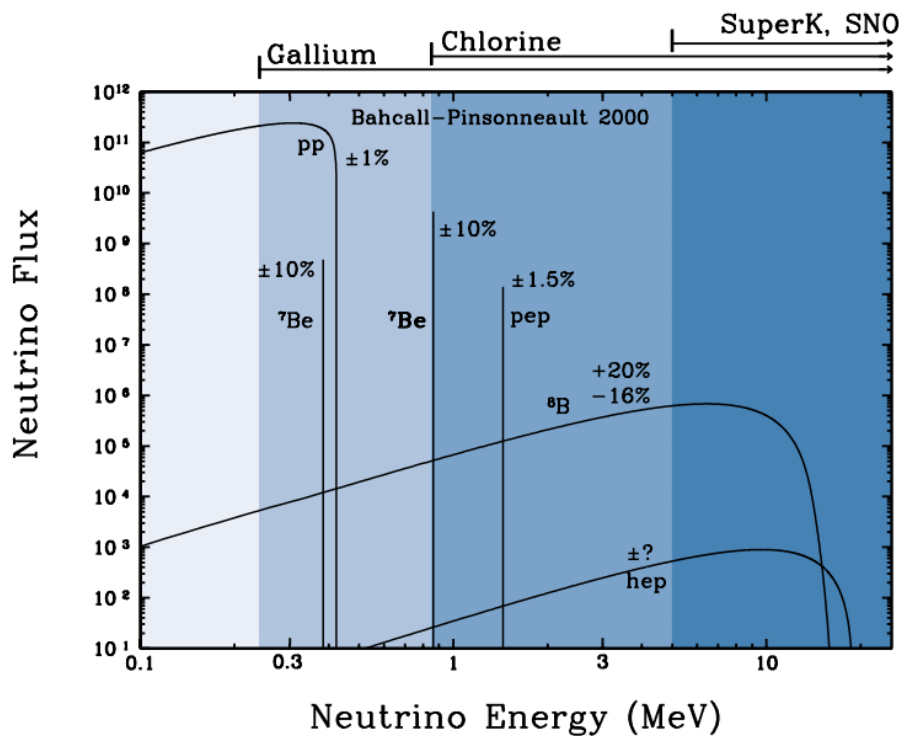
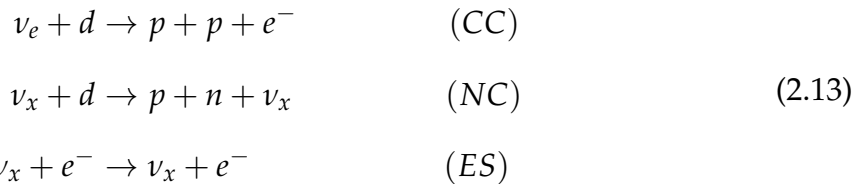


Figure 2.2.: The solar neutrino flux as a function of neutrino energy for various fusion reactions and decay chains as predicted by the Standard Solar Model. Taken from [26].

³⁰⁰ The first measurements of solar neutrinos observed a significant reduction in the
³⁰¹ event rate compared to predictions from the Standard Solar Model [27, 28]. The
³⁰² proposed solution to this “solar neutrino problem” was $\nu_e \leftrightarrow \nu_\mu$ oscillations in a

³⁰³ precursory version of the PMNS model [29]. The Kamiokande [30], Gallex [31] and
³⁰⁴ Sage [32] experiments confirmed the ~ 0.5 factor deficit of solar neutrinos.

³⁰⁵ The conclusive solution to this problem was determined by the SNO collaboration
³⁰⁶ [33]. Using a deuterium water target to observe 8B neutrinos, the event rate of charged
³⁰⁷ current (CC), neutral current (NC), and elastic scattering (ES) interactions (Given in
³⁰⁸ Equation 2.13) was simultaneously measured. CC events can only occur for electron
³⁰⁹ neutrinos, whereas the NC channel is agnostic to neutrino flavour, and the ES reaction
³¹⁰ has a slight excess sensitivity to electron neutrino interactions. This meant that there
³¹¹ were direct measurements of the ν_e and ν_x neutrino flux. It was concluded that the
³¹² CC and ES interaction rates were consistent with the deficit previously observed.
³¹³ Most importantly, the NC reaction rate was only consistent with the others under the
³¹⁴ hypothesis of flavour transformation.



³¹⁵ Many experiments have since measured the neutrino flux of different interaction
³¹⁶ chains within the sun [34–36]. The most recent measurement was that of CNO neutrinos
³¹⁷ which were recently observed with 5σ significance by the Borexino collaboration.
³¹⁸ Future neutrino experiments aim to further these spectroscopic measurements of
³¹⁹ different fusion chains within the Sun [37–39]. Solar neutrinos act as an irreducible
³²⁰ background for dark matter experiments like DARWIN but oscillation parameter
³²¹ measurements can be made [40].

³²² 2.3.2. Atmospheric Neutrinos

- ³²³ The interactions of primary cosmic ray protons in Earth's upper atmosphere generate
³²⁴ showers of energetic hadrons. These are mostly pions and kaons which when they
³²⁵ decay produce a natural source of neutrinos spanning energies of MeV to TeV [41].
³²⁶ The main decay is via

$$\begin{aligned} \pi^\pm &\rightarrow \mu^\pm + (\nu_\mu, \bar{\nu}_\mu) \\ \mu^\pm &\rightarrow e^\pm + (\nu_e, \bar{\nu}_e) + (\nu_\mu, \bar{\nu}_\mu) \end{aligned} \tag{2.14}$$

³²⁷ such that for a single pion decay, three neutrinos are typically produced. The
³²⁸ atmospheric neutrino flux energy spectra as predicted by the Bartol [42], Honda
³²⁹ [43–45], and FLUKA [46] models are illustrated in Figure 2.3. The flux distribution
³³⁰ peaks at an energy of $O(10)\text{GeV}$. The uncertainties associated with these models
³³¹ are dominated by the hadronic production of kaon and pions as well as the primary
³³² cosmic flux.

³³³ Unlike long-baseline experiments which have a fixed baseline, the distance at-
³³⁴ mospheric neutrinos propagate is dependent upon the zenith angle at which they
³³⁵ interact. This is illustrated in Figure 2.4. Neutrinos that are generated directly above
³³⁶ the detector ($\cos(\theta) = 1.0$) have a baseline equivalent to the height of the atmosphere
³³⁷ whereas neutrinos that interact directly below the detector ($\cos(\theta) = -1.0$) have to
³³⁸ travel a length equal to the diameter of the Earth. This means atmospheric neutrinos
³³⁹ have a baseline that varies from $O(20)\text{km}$ to $O(6 \times 10^3)\text{km}$. Any neutrino generated
³⁴⁰ at or below the horizon will be subject to matter effects as they propagate through the
³⁴¹ Earth.

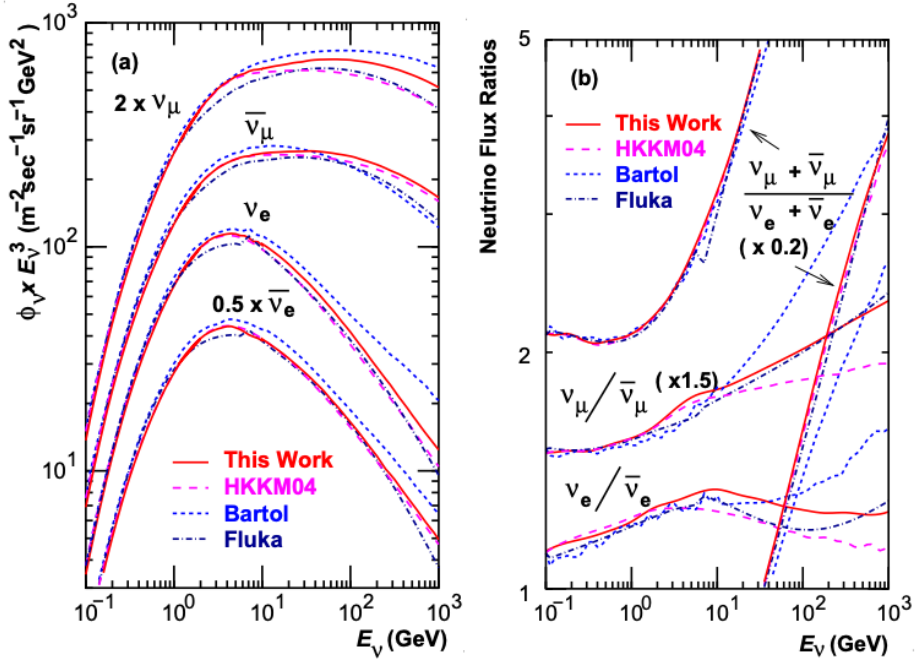


Figure 2.3.: Left panel: The atmospheric neutrino flux for different neutrino flavours as a function of neutrino energy as predicted by the 2007 Honda model (“This work”) [43], the 2004 Honda model (“HKKM04”) [44], the Bartol model [42] and the FLUKA model [46]. Right panel: The ratio of the muon to electron neutrino flux as predicted by all the quoted models. Both figures taken from [43].

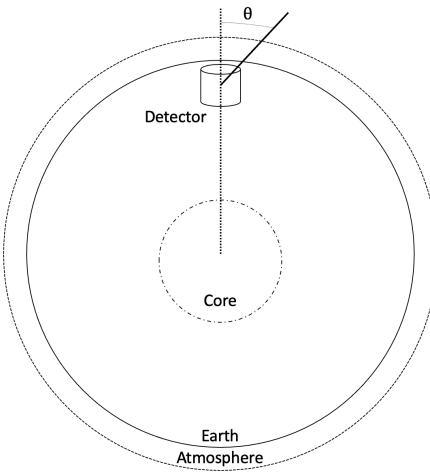


Figure 2.4.: A diagram illustrating the definition of zenith angle as used in the Super Kamiokande experiment [47].

Figure 2.5 highlights the neutrino flux as a function of the zenith angle for different

slices of neutrino energy. For medium to high-energy neutrinos (and to a lesser degree

for low-energy neutrinos), the flux is approximately symmetric around $\cos(\theta) = 0$.

To the accuracy of this approximation, the systematic uncertainties associated with atmospheric flux for comparing upward-going and down-going neutrino cancels. This allows the down-going events, which are mostly insensitive to oscillation probabilities, to act as an unoscillated prediction (similar to a near detector in an accelerator neutrino experiment).

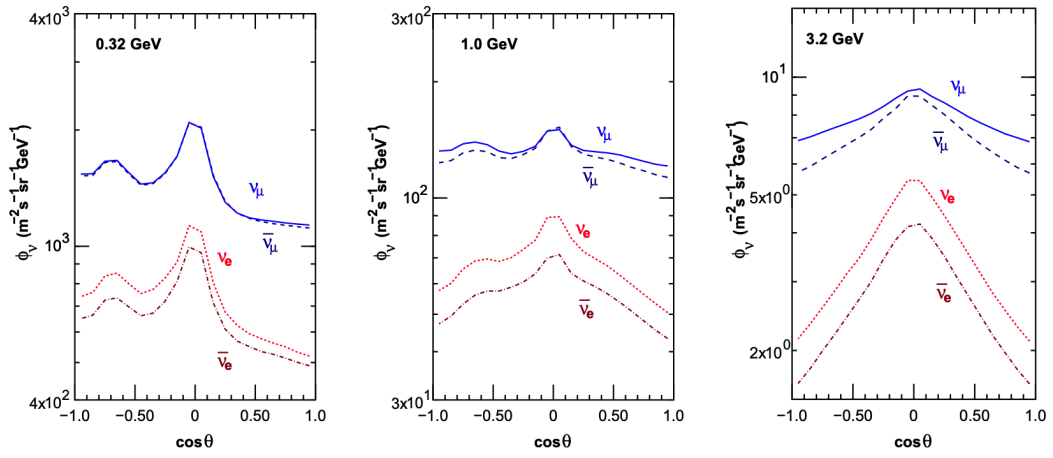


Figure 2.5.: Prediction of ν_e , $\bar{\nu}_e$, ν_μ , $\bar{\nu}_\mu$ fluxes as a function of zenith angle as calculated by the HKKM model [45]. The left, middle and right panels represent three values of neutrino energy, 0.32GeV, 1.0GeV and 3.2GeV respectively. Predictions for other models including Bartol [42], Honda [43] and FLUKA [46] are given in [47].

Precursory hints of atmospheric neutrinos were observed in the mid-1960s searching for $\nu_\mu + X \xrightarrow{(-)} X^* + \mu^\pm$ [48], although it was called an anomaly at the time of measurement. This was succeeded with the IMB-3 [49] and Kamiokande [50] experiments which measured the ratio of muon neutrinos compared to electron neutrinos $R(\nu_\mu/\nu_e)$. Both experiments were found to have a consistent deficit of muon neutrinos, with $R(\nu_\mu/\nu_e) = 0.67 \pm 0.17$ and $R(\nu_\mu/\nu_e) = 0.60^{+0.07}_{-0.06} \pm 0.05$. Super-Kamiokande (SK) [47] extended this analysis by fitting oscillation parameters in $P(\nu_\mu \rightarrow \nu_\tau)$ which found best fit parameters $\sin^2(2\theta) > 0.92$ and $1.5 \times 10^{-3} < \Delta m^2 < 3.4 \times 10^{-3} \text{ eV}^2$.

Since then, atmospheric neutrino experiments have been making precision measurements of the $\sin^2(\theta_{23})$ and Δm^2_{32} oscillation parameters. Atmospheric neutrino oscillation is dominated by $P(\nu_\mu \rightarrow \nu_\tau)$, where SK observed a 4.6σ discovery of ν_τ

³⁶¹ appearance [51]. Figure 2.6 illustrates the current estimates on the atmospheric mixing
³⁶² parameters from a wide range of atmospheric and accelerator neutrino observatories.

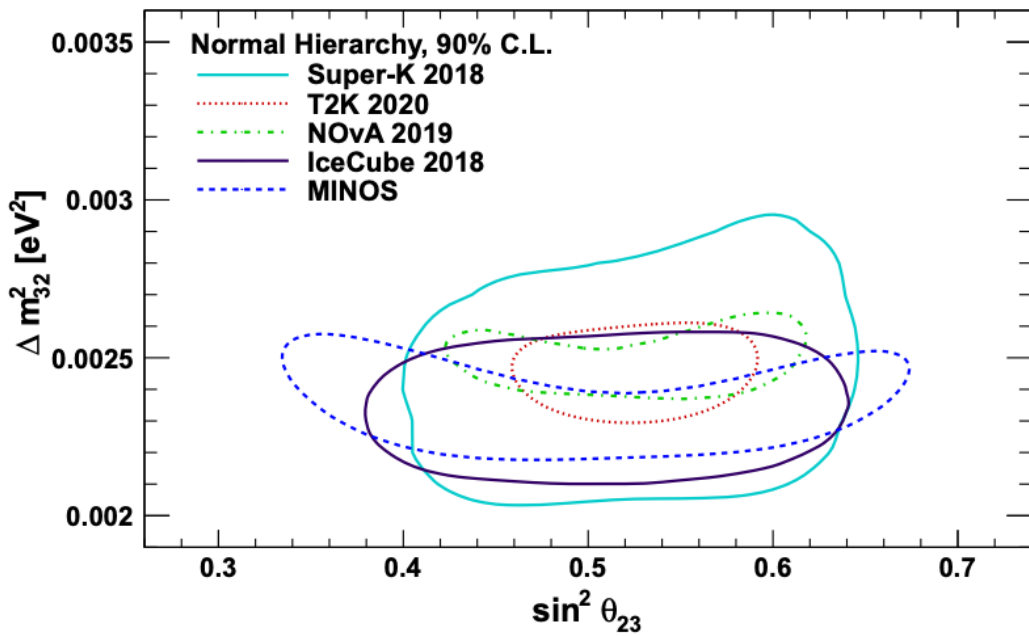


Figure 2.6.: Constraints on the atmospheric oscillation parameters, $\sin^2(\theta_{23})$ and Δm_{23}^2 , from atmospheric and long baseline experiments: SK [52], T2K [53], NOvA [54], IceCube [55] and MINOS [56]. Figure taken from [57].

³⁶³ 2.3.3. Accelerator Neutrinos

³⁶⁴ The concept of using a man-made “neutrino beam” was first realised in 1962 [58].
³⁶⁵ Since then, many experiments have followed which all use the same fundamental
³⁶⁶ concepts. Typically, a proton beam is aimed at a target producing charged mesons that
³⁶⁷ decay to neutrinos. The mesons can be sign-selected by the use of magnetic focusing
³⁶⁸ horns to generate a neutrino or antineutrino beam. Pions are the primary meson that
³⁶⁹ decay and depending on the orientation of the magnetic field, a muon (anti-)neutrino
³⁷⁰ beam is generated via $\pi^+ \rightarrow \mu^+ + \nu_\mu$ or $\pi^- \rightarrow \mu^- + \bar{\nu}_\mu$. The decay of muons and
³⁷¹ kaons does result in an irreducible intrinsic electron neutrino background. In T2K,
³⁷² this background contamination is $O(< 1\%)$ [59]. There is also an approximately $\sim 5\%$

³⁷³ “wrong-sign” neutrino background of $\bar{\nu}_\mu$ generated via the same decays. As the beam is
³⁷⁴ generated by proton interactions (rather than anti-proton interactions), the wrong-sign
³⁷⁵ component in the antineutrino beam is larger when operating in neutrino mode.

³⁷⁶ Tuning the proton energy in the beam and using beam focusing techniques allows
³⁷⁷ the neutrino energy to be set to a value that maximises the disappearance oscillation
³⁷⁸ probability in the L/E term in Equation 2.10. This means that accelerator experiments
³⁷⁹ are typically more sensitive to the mixing parameters as compared to a natural neutrino
³⁸⁰ source. However, the disadvantage compared to atmospheric neutrino experiments is
³⁸¹ that the baseline has to be shorter due to the lower flux. Consequently, there is typically
³⁸² less sensitivity to matter effects and the ordering of the neutrino mass eigenstates.

³⁸³ A neutrino experiment measures

$$R(\vec{x}) = \Phi(E_\nu) \times \sigma(E_\nu) \times \epsilon(\vec{x}) \times P(\nu_\alpha \rightarrow \nu_\beta), \quad (2.15)$$

³⁸⁴ where $R(\vec{x})$ is the event rate of neutrinos at position \vec{x} , $\Phi(E_\nu)$ is the flux of neutrinos
³⁸⁵ with energy E_ν , $\sigma(E_\nu)$ is the cross-section of the neutrino interaction and $\epsilon(\vec{x})$ is the
³⁸⁶ efficiency and resolution of the detector. In order to leverage the most out of an
³⁸⁷ accelerator neutrino experiment, the flux and cross-section systematics need to be
³⁸⁸ constrained. This is typically done via the use of a “near detector”, situated at a baseline
³⁸⁹ of $O(1)$ km. This detector observes the unoscillated neutrino flux and constrains the
³⁹⁰ parameters used within the flux and cross-section model.

³⁹¹ The first accelerator experiments to precisely measure oscillation parameters were
³⁹² MINOS [60] and K2K [61]. These experiments confirmed the ν_μ disappearance seen in
³⁹³ atmospheric neutrino experiments by finding consistent parameter values for $\sin^2(\theta_{23})$
³⁹⁴ and Δm_{23}^2 . The current generation of accelerator neutrino experiments, T2K and NO ν A

³⁹⁵ extended this field by observing $\bar{\nu}_\mu \rightarrow \bar{\nu}_e$ and lead the sensitivity to atmospheric mix-
³⁹⁶ ing parameters as seen in Figure 2.6 [62]. The two experiments differ in their peak
³⁹⁷ neutrino energy, baseline, and detection technique. The NO ν A experiment is situated
³⁹⁸ at a baseline of 810km from the NuMI beamline which delivers 2GeV neutrinos. The
³⁹⁹ T2K neutrino beam is peaked around 0.6GeV and propagates 295km. The NO ν A
⁴⁰⁰ experiment also uses functionally identical detectors (near and far) which allow the
⁴⁰¹ approximate cancellation of detector systematics whereas T2K uses a plastic scintil-
⁴⁰² lator technique at the near detector and a water Cherenkov far detector. The future
⁴⁰³ generation experiments DUNE [63] and Hyper-Kamiokande [64] will succeed these
⁴⁰⁴ experiments as the high-precision era of neutrino oscillation parameter measurements
⁴⁰⁵ develops.

⁴⁰⁶ Several anomalous results have been observed in the LSND [9] and MiniBooNE [10]
⁴⁰⁷ detectors which were designed with purposefully short baselines. Parts of the neu-
⁴⁰⁸ trino community attributed these results to oscillations induced by a fourth “sterile”
⁴⁰⁹ neutrino [65] but several searches in other experiments, MicroBooNE [66] and KAR-
⁴¹⁰ MEN [67], found no hints of additional neutrino species. The solution to the anomalous
⁴¹¹ results is still being determined.

⁴¹² 2.3.4. Reactor Neutrinos

⁴¹³ As illustrated in the first discovery of neutrinos (section 2.1), nuclear reactors are a very
⁴¹⁴ useful man-made source of electron antineutrinos. For reactors that use low-enriched
⁴¹⁵ uranium ^{235}U as fuel, the antineutrino flux is dominated by the β -decay fission of ^{235}U ,
⁴¹⁶ ^{238}U , ^{239}Pu and ^{241}Pu [68] as illustrated in Figure 2.7.

⁴¹⁷ Due to their low energy, reactor electron antineutrinos predominantly interact
⁴¹⁸ via the inverse β -decay (IBD) interaction. The typical signature contains two signals

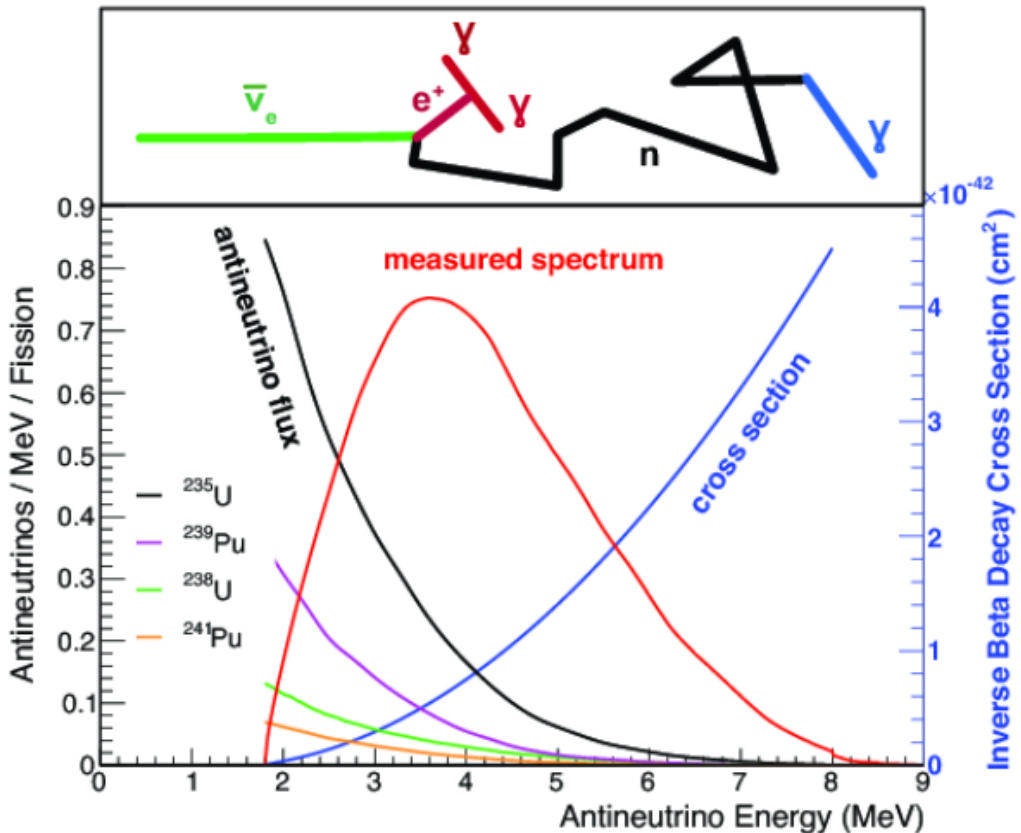


Figure 2.7.: Reactor electron antineutrino fluxes for ^{235}U (Black), ^{238}U (Green), ^{239}Pu (Purple), and ^{241}Pu (Orange) isotopes. The inverse β -decay cross-section (Blue) and corresponding measurable neutrino spectrum (Red) are also given. Top panel: Schematic of Inverse β -decay interaction including the eventual capture of the emitted neutron. This capture emits a γ -ray which provides a second signal of the event. Taken from [69].

delayed by $O(200)\mu\text{s}$; firstly the prompt photons from positron annihilation, and secondly the photons emitted ($E_{tot}^\gamma = 2.2\text{MeV}$) from de-excitation after neutron capture on hydrogen. Searching for both signals improves the detector's ability to distinguish between background and signal events [70]. Recently, SK included gadolinium dopants into the ultra-pure water to increase the energy released from the photon cascade to $\sim 8\text{MeV}$ and reduce the time of the delayed signal to $\sim 28\mu\text{s}$.

There are many short baseline experiments ($L \sim O(1)\text{km}$) that have measured the $\sin^2(\theta_{13})$ and Δm_{23}^2 oscillation parameters. Daya Bay [71], RENO [72] and Double Chooz [73] have all provided precise measurements, with the first discovery of a

428 non-zero θ_{13} made by Daya Bay and RENO (and complemented by T2K [73]). The
429 constraints on $\sin^2(\theta_{13})$ by the reactor experiments lead the field and are often used as
430 external inputs to accelerator neutrino experiments to improve their sensitivity to δ_{CP}
431 and mass hierarchy determination. JUNO-TAO [74], a small collaboration within the
432 larger JUNO experiment, is a next-generation reactor experiment that aims to precisely
433 measure the isotopic antineutrino yields from the different fission chains. Alongside
434 this, it aims to explain the ‘5MeV excess’ [75–77] by conducting a search for sterile
435 neutrinos with a mass scale of around 1eV.

436 Kamland [78] is the only experiment to have observed reactor neutrinos using a
437 long baseline (flux weighted averaged baseline of $L \sim 180\text{km}$) which allows it to have
438 sensitivity to Δm_{12}^2 . Combined with the SK solar neutrino experiment, the combined
439 analysis puts the most stringent constraint on Δm_{12}^2 [79].

440 2.4. Summary

441 Since observing the first evidence of neutrino oscillations in the late 1990’s, numerous
442 measurements of the mixing parameters have been made. Many experiments use
443 neutrinos as a tool for discovery of new physics (diffuse supernova background,
444 neutrinoless double beta decay and others) so the PMNS parameters are summarised
445 in the Particle Data Group (PDG) review tables. The analysis presented in this thesis
446 focuses on the 2020 T2K oscillation analysis presented in [80] where the 2018 PDG
447 constraints [81] were used. These constraints are outlined in Table 2.1.

448 The $\sin^2(\theta_{13})$ measurement stems from the electron antineutrino disappearance,
449 $P(\bar{\nu}_e \rightarrow \bar{\nu}_e)$, and is take as the average best-fit from the combination of Daya Bay,
450 Reno and Double Chooz. It is often used as a prior uncertainty within other neu-
451 trino oscillation experiments, typically termed the reactor constraint. The $\sin^2(\theta_{12})$

Parameter	2018 Constraint
$\sin^2(\theta_{12})$	0.307 ± 0.013
Δm_{21}^2	$(7.53 \pm 0.18) \times 10^{-5} \text{ eV}^2$
$\sin^2(\theta_{13})$	$(2.12 \pm 0.08) \times 10^{-2}$
$\sin^2(\theta_{23})$ (I.H., Q1)	$0.421^{+0.033}_{-0.025}$
$\sin^2(\theta_{23})$ (I.H., Q2)	$0.592^{+0.023}_{-0.030}$
$\sin^2(\theta_{23})$ (N.H., Q1)	$0.417^{+0.025}_{-0.028}$
$\sin^2(\theta_{23})$ (N.H., Q2)	$0.597^{+0.024}_{-0.030}$
Δm_{32}^2 (I.H.)	$(-2.56 \pm 0.04) \times 10^{-3} \text{ eV}^2$
Δm_{32}^2 (N.H.)	$(2.51 \pm 0.05) \times 10^{-3} \text{ eV}^2$

Table 2.1.: The 2018 Particle Data Group constraints of the oscillation parameters taken from [81]. The value of Δm_{23}^2 is given for both normal hierarchy (N.H.) and inverted hierarchy (I.H.) and $\sin^2(\theta_{23})$ is broken down by whether its value is below (Q1) or above (Q2) 0.5.

parameter is predominantly measured through electron neutrino disappearance, $P(\nu_e \rightarrow \nu_{\mu,\tau})$, in solar neutrino experiments. The long-baseline reactor neutrino experiment Kamland also has sensitivity to this parameter and is used in a joint fit to solar data from SNO and SK, using the reactor constraint. Measurements of $\sin^2(\theta_{23})$ are made by long-baseline and atmospheric neutrino experiments. The PDG value is a joint fit of T2K, NOvA, MINOS and IceCube DeepCore experiments. The latest T2K-only measurement, provided at Neutrino2020 and is the basis of this thesis, is given as $\sin^2(\theta_{23}) = 0.546^{+0.024}_{-0.046}$ [80]. The PDG constraint on Δm_{12}^2 is provided by the KamLAND experiment using solar and geoneutrino data. This measurement utilised a $\sin^2(\theta_{13})$ constraint from accelerator (T2K, MINOS) and reactor neutrino (Daya Bay, RENO, Double Chooz) experiments. Accelerator measurements make some of the most stringent constraints on Δm_{23}^2 although atmospheric experiments have more sensitivity to the mass hierarchy determination. The PDG performs a joint fit of accelerator and atmospheric data, in both normal and inverted hierarchy separately. The latest T2K-only result is $\Delta m_{32}^2 = 2.49^{+0.058}_{-0.082} \times 10^{-3} \text{ eV}^2$ favouring normal hierarchy [80]. The value of δ_{CP} is largely undetermined. CP-conserving values of 0 and π were

⁴⁶⁸ rejected with $\sim 2\sigma$ intervals, as published in Nature, although more recent analysis
⁴⁶⁹ have reduced the rejection intervals to 90%. Since the 2018 PDG publication, there has
⁴⁷⁰ been a new measurement of $\sin^2(\theta_{13}) = (2.20 \pm 0.07) \times 10^{-2}$ [82], alongside updated
⁴⁷¹ Δm_{23}^2 and $\sin^2(\theta_{23})$ measurements.

⁴⁷² Throughout this thesis, several sample spectra predictions and contours are pre-
⁴⁷³ sented which require oscillation parameters to be assumed. Table 2.2 defines two sets
⁴⁷⁴ of oscillation parameters, with “Asimov A” set being close to the preferred values
⁴⁷⁵ from a previous T2K-only fit [83] and “Asimov B” being CP-conserving and further
⁴⁷⁶ from maximal θ_{23} mixing.

Parameter	Asimov A	Asimov B
Δm_{12}^2	$7.53 \times 10^{-5} \text{ eV}^2$	
Δm_{32}^2	$2.509 \times 10^{-3} \text{ eV}^2$	
$\sin^2(\theta_{12})$	0.304	
$\sin^2(\theta_{13})$	0.0219	
$\sin^2(\theta_{23})$	0.528	0.45
δ_{CP}	-1.601	0.0

Table 2.2.: Reference values of the neutrino oscillation parameters for two different oscillation parameter sets.

⁴⁷⁷ **Chapter 3**

⁴⁷⁸ **T2K and SK Experiment Overview**

⁴⁷⁹ As the successor of the Kamiokande experiment, the Super-Kamiokande (SK) collabora-
⁴⁸⁰ ration has been leading atmospheric neutrino oscillation analyses for over two decades.
⁴⁸¹ The detector has provided some of the strongest constraints on proton decay and the
⁴⁸² first precise measurements of the Δm_{23}^2 and $\sin^2(\theta_{23})$ neutrino oscillation parameters.
⁴⁸³ The ability of the detector to low-energy neutrino events has been significantly im-
⁴⁸⁴ proved with the recent gadolinium doping of the ultra-pure water target. The history,
⁴⁸⁵ detection technique, and operation of the SK detector is described in section 3.1.

⁴⁸⁶ The Tokai-to-Kamioka (T2K) experiment was one of the first long-baseline ex-
⁴⁸⁷ periments to use both neutrino and antineutrino beams to precisely measure the
⁴⁸⁸ charge parity violation within the neutrino sector. With the SK detector observing
⁴⁸⁹ the oscillated neutrino flux, the T2K experiment observed the first hints of a non-zero
⁴⁹⁰ $\sin^2(\theta_{13})$ measurement and continues to lead the field with the constraints it provides
⁴⁹¹ on $\sin^2(\theta_{13})$, $\sin^2(\theta_{23})$, Δm_{23}^2 and δ_{CP} . The techniques which T2K uses in gener-
⁴⁹² ating its neutrino beam as well as the near-detector used to constrain the flux and
⁴⁹³ cross-section parameters used in this analysis are documented in section 3.2.

⁴⁹⁴ **3.1. The Super-Kamiokande Experiment**

⁴⁹⁵ The SK experiment began taking data in 1996 [84] and has had many modifications
⁴⁹⁶ throughout its lifespan. There have been seven defined periods of data taking as
⁴⁹⁷ noted in Table 3.1. Data taking began in SK-I which ran for five years. Between the

498 SK-I and SK-II periods, a significant proportion of the PMTs were damaged during
 499 maintenance. Those that survived were equally distributed throughout the detector
 500 in the SK-II era, which resulted in a reduced photo-coverage. From SK-III onwards,
 501 repairs to the detector meant the full suite of PMTs was operational. Before the
 502 start of SK-IV, the data acquisition and electronic systems were upgraded. Between
 503 SK-IV and SK-V, a significant effort was placed into tank open maintenance and
 504 repair/replacement of defective PMTs, a task for which the author of this thesis was
 505 required. Consequently, the detector conditions were significantly different between
 506 the two operational periods. SK-VI saw the start of the 0.01% gadolinium doped water.
 507 SK-VII, which started during the writing of this thesis, has increased the gadolinium
 508 concentration to 0.03% for continued operation [85].

Period	Start Date	End Date	Live-time (days)
I	April 1996	July 2001	1489.19
II	October 2002	October 2005	798.59
III	July 2006	September 2008	518.08
IV	September 2008	May 2018	3244.4
V	January 2019	July 2020	461.02
VI	July 2020	May 2022	583.3
VII	May 2022	Ongoing	N/A

Table 3.1.: The various SK periods and respective live-time. The SK-VI live-time is calculated until 1st April 2022. SK-VII started during the writing of this thesis.

509 3.1.1. The SK Detector

510 The basic structure of the Super-Kamiokande (SK) detector is a cylindrical tank with a
 511 diameter 39.3m and height 41.1m filled with ultrapure water [86]. A diagram of the
 512 significant components of the SK detector is given in Figure 3.1. The SK detector is
 513 situated in the Kamioka mine in Gifu, Japan. The mine is underground with roughly
 514 1km rock overburden (2.7km water equivalent overburden) [87]. At this depth, the

515 rate of cosmic ray muons is significantly decreased to a value of $\sim 2\text{Hz}$. The top of
 516 the tank is covered with stainless steel which is designed as a working platform for
 517 maintenance, calibration, and location for high voltage and data acquisition electronics.

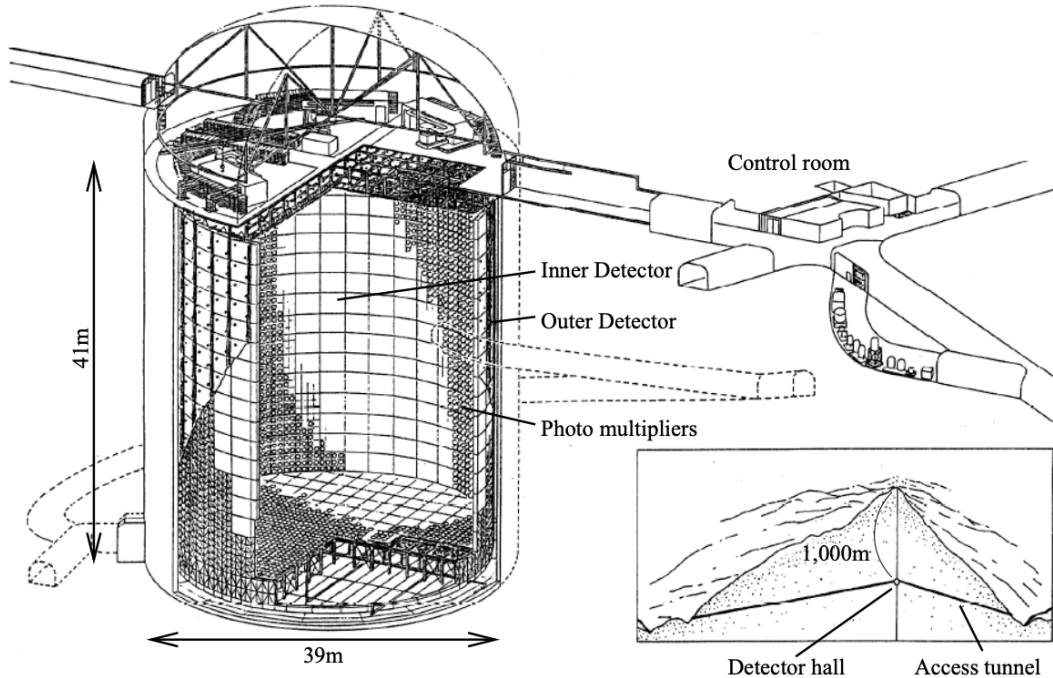


Figure 3.1.: A schematic diagram of the Super-Kamiokande Detector. Taken from [88].

518 A smaller cylindrical structure (36.2m diameter, 33.8m height) is situated inside the
 519 tank, with an approximate 2m gap between this structure and the outer tank wall. The
 520 purpose of this structure is to support the photomultiplier tubes (PMTs). The volume
 521 inside and outside the support structure is referred to as the inner detector (ID) and
 522 outer detector (OD), respectively. In the SK-IV era, the ID and OD are instrumented
 523 by 11,129 50cm and 1,885 20cm PMTs respectively [86]. The ID contains a 32kton
 524 mass of water. Many analyses performed at SK use a “fiducial volume” defined by the
 525 volume of water inside the ID excluding some distance to the ID wall. This reduces the
 526 volume of the detector which is sensitive to neutrino events but reduces radioactive
 527 backgrounds and allows for better reconstruction performance. The nominal fiducial

528 volume is defined as the area contained inside 2m from the ID wall for a total of
529 22.5kton water [89].

530 The two regions of the detector (ID and OD) are optically separated with opaque
531 black plastic. The purpose of this is to determine whether a track entered or exited
532 the ID. This allows cosmic ray muons and partially contained events to be tagged and
533 separated from neutrino events entirely contained within the ID. This black plastic is
534 also used to cover the area between the ID PMTs to reduce photon reflection from the
535 ID walls. Opposite to this, the OD is lined with a reflective material to allow photons to
536 reflect around inside the OD until collected by one of the PMTs. Furthermore, each OD
537 PMT is backed with $50 \times 50\text{cm}$ plates of wavelength shifting acrylic which increases
538 the efficiency of light collection [87].

539 In the SK-IV data-taking period, the photocathode coverage of the detector, or the
540 fraction of the ID wall instrumented with PMTs, is $\sim 40\%$ [87]. The PMTs have a
541 quantum efficiency (the ratio of detected electrons to incident photons) of $\sim 21\%$ for
542 photons with wavelengths of $360\text{nm} < \lambda < 390\text{nm}$. The proportion of photoelectrons
543 that produce a signal in the dynode of a PMT, termed the collection efficiency, is
544 $> 70\%$ [87]. The PMTs used within SK are most sensitive to photons with wavelength
545 $300\text{nm} \leq \lambda \leq 600\text{nm}$ [87]. One disadvantage of using PMTs as the detection media
546 is that the Earth's geomagnetic field can modify its response. Therefore, a set of
547 compensation coils is built around the inner surface of the detector to mitigate this
548 effect [90].

549 As mentioned, the SK detector is filled with ultrapure water, which in a perfect
550 world would contain no impurities. However, bacteria and organic compounds can
551 significantly degrade the water quality. This decreases the attenuation length, which
552 reduces the total number of photons that hit a PMT. To combat this, a sophisticated
553 water treatment system has been developed [87, 91]. UV lights, mechanical filters,

554 and membrane degasifiers are used to reduce the bacteria, suspended particulates,
555 and radioactive materials from the water. The flow of water within the tank is also
556 critical as it can remove stagnant bacterial growth or build-up of dust on the surfaces
557 within the tank. Gravity drifts impurities in the water towards the bottom of the
558 tank which, if left uncontrolled, can create asymmetric water conditions between
559 the top and bottom of the tank. Typically, the water entering the tank is cooled
560 below the ambient temperature of the tank to control convection and inhibit bacteria
561 growth. Furthermore, the rate of dark noise hits within PMTs is sensitive to the PMT
562 temperature [92] so controlling the temperature gradients within the tank is beneficial
563 for stable measurements.

564 SK-VI is the first phase of the SK experiment to use gadolinium dopants within
565 the ultrapure water [85]. As such, the SK water system had to be replaced to avoid
566 removing the gadolinium concentrate from the ultrapure water [93]. For an inverse
567 β -decay (IBD) interaction in a water target, the emitted neutron is thermally captured
568 on hydrogen. This process releases 2.2MeV γ rays which are difficult to detect as
569 the resulting Compton scattered electrons are very close to the Cherenkov threshold,
570 limiting the number of photons produced. Thermal capture of neutrons on gadolin-
571 ium generates γ rays with higher energy (8MeV [70]) meaning they are more easily
572 detected. SK-VI has 0.01% Gd loading (0.02% gadolinium sulphate by mass) which
573 causes \approx 50% of neutrons emitted by IBD to be captured on gadolinium [94, 95].
574 Whilst predominantly useful for low energy analyses, Gd loading allows better $\nu/\bar{\nu}$
575 separation for atmospheric neutrino event selections [96]. Efforts are currently in place
576 to increase the gadolinium concentrate to 0.03% for \approx 75% neutron capture efficiency
577 on gadolinium [97]. The final stage of loading targets 0.1% concentrate.

578 3.1.2. Calibration

579 The calibration of the SK detector is documented in [86] and summarised below. The
580 analysis presented within this thesis is dependent upon ‘high energy events’ (Charged
581 particles with $O(> 100)\text{MeV}$ momenta). These are events that are expected to generate
582 a larger number of photons such that each PMT will be hit with multiple photons.
583 The reconstruction of these events depends upon the charge deposited within each
584 PMT and the timing response of each individual PMT. Therefore, the most relevant
585 calibration techniques to this thesis are outlined.

586 Before installation, 420 PMTs were calibrated to have identical charge responses
587 and then distributed throughout the tank in a cross-shape pattern (As illustrated by
588 Figure 3.2). These are used as a standardised measure for the rest of the PMTs installed
589 at similar geometric positions within SK to be calibrated against. To perform this
590 calibration, a xenon lamp is located at the center of the SK tank which flashes uniform
591 light at 1Hz. This allows for geometrical effects, water quality variation, and timing
592 effects to be measured in-situ throughout normal data-taking periods.

593 When specifically performing calibration of the detector (in out-of-data taking
594 mode), the water in the tank was circulated to avoid top/bottom asymmetric water
595 quality. Any non-uniformity within the tank significantly affects the PMT hit proba-
596 bility through scattering or absorption. This becomes a dominant effect for the very
597 low-intensity light sources discussed later which are designed such that only one
598 photon is incident upon a given PMT.

599 The “gain” of a PMT is defined as the ratio of the total charge of the signal produced
600 compared to the charge of photoelectrons emitted by the photocathodes within the
601 PMT. To calibrate the signal of each PMT, the “relative” and “absolute” gain values are

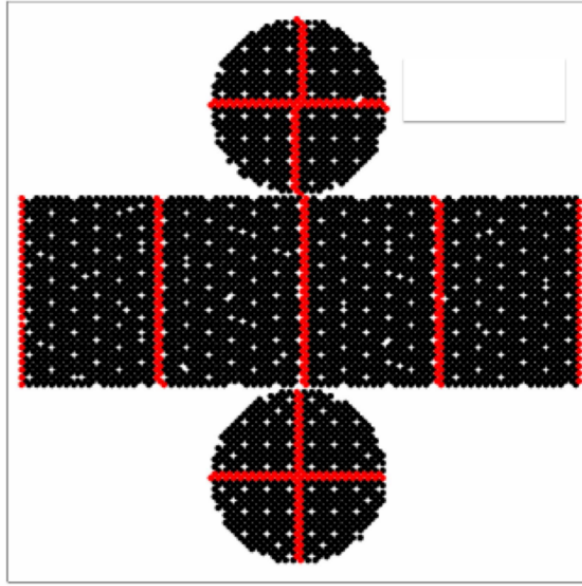


Figure 3.2.: The location of “standard PMTs” (red) inside the SK detector. Taken from [86].

602 measured. The relative gain is the variation of gain among each of the PMTs whereas
 603 the absolute gain is the average gain of all PMTs.

604 The relative gain is calibrated as follows. A laser is used to generate two measure-
 605 ments: a high-intensity flash that illuminates every PMT with a sufficient number of
 606 photons, and a low-intensity flash in which only a small number of PMTs collect light.
 607 The first measurement creates an average charge, $Q_{obs}(i)$ on PMT i , whereas the second
 608 measurement ensures that each hit PMT only generates a single photoelectron. For the
 609 low-intensity measurement, the number of times each PMT records a charge larger
 610 than 1/4 photoelectrons, $N_{obs}(i)$, is counted. The values measured can be expressed as

$$\begin{aligned} Q_{obs}(i) &\propto I_H \times f(i) \times \epsilon(i) \times G(i), \\ N_{obs}(i) &\propto I_L \times f(i) \times \epsilon(i), \end{aligned} \tag{3.1}$$

611 Where I_H and I_L is the intensity of the high and low flashes, $f(i)$ is the acceptance
 612 efficiency of the i^{th} PMT, $\epsilon(i)$ is the product of the quantum and collection efficiency

613 of the i^{th} PMT and $G(i)$ is the gain of the i^{th} PMT. The relative gain for each PMT can
614 determined by taking the ratio of these quantities.

615 The absolute gain calibration is performed by observing fixed energy γ -rays of
616 $E_{\gamma} \sim 9\text{MeV}$ emitted isotropically from neutron capture on a NiCf source situated at
617 the center of the detector. This generates a photon yield of about 0.004 photoelec-
618 trons/PMT/event, meaning that $> 99\%$ of PMT signals are generated from single
619 photoelectrons. A charge distribution is generated by performing this calibration over
620 all PMTs, and the average value of this distribution is taken to be the absolute gain
621 value.

622 As mentioned in subsection 3.1.1, the average quantum and collection efficiency
623 for the SK detector is $\sim 21\%$ and $> 70\%$ respectively. However, these values do differ
624 between each PMT and need to be calibrated accordingly. Consequently, the NiCf
625 source is also used to calibrate the “quantum \times collection” efficiency (denoted “QE”)
626 value of each PMT. The NiCf low-intensity source is used as the PMT hit probability
627 is proportional to the QE ($N_{\text{obs}}(i) \propto \epsilon(i)$ in Equation 3.1). A Monte Carlo prediction
628 which includes photon absorption, scattering, and reflection is made to estimate the
629 number of photons incident on each PMT and the ratio of the number of predicted
630 to observed hits is calculated. The difference is attributed to the QE efficiency of that
631 PMT. This technique is extended to calculate the relative QE efficiency by normalizing
632 the average of all PMTs which removes the dependence on the light intensity.

633 Due to differing cable lengths and readout electronics, the timing response between
634 a photon hitting the PMT and the signal being captured by the data acquisition can be
635 different between each PMT. Due to threshold triggers (Described in subsection 3.1.3),
636 the time at which a pulse reaches a threshold is dependent upon the size of the pulse.
637 This is known as the ‘time-walk’ effect and also needs to be accounted for in each PMT.
638 To calibrate the timing response, a pulse of light with width 0.2ns is emitted into the

639 detector through a diffuser. Two-dimensional distributions of time and pulse height
640 (or charge) are made for each PMT and are used to calibrate the timing response. This
641 is performed in-situ during data taking with the light source pulsing at 0.03Hz.

642 The top/bottom water quality asymmetry is measured using the NiCf calibration
643 data and cross-referencing these results to the “standard PMTs”. The water attenuation
644 length is continuously measured by the rate of vertically-downgoing cosmic-ray
645 muons which enter via the top of the tank.

646 Dark noise is the phenomenon where a PMT registers a pulse that is consistent
647 with a single photoelectron emitted from photon detection despite the PMT being in
648 complete darkness. This is predominately caused by two processes. Firstly there is
649 intrinsic dark noise which is where photoelectrons gain enough thermal energy to be
650 emitted from the photocathode, and secondly, the radioactive decay of contaminants
651 inside the structure of the PMT. Typical dark noise rate for PMTs used within SK are
652 $O(3)$ kHz [87]. This is lower than the expected number of photons generated for a ‘high
653 energy event’ (As described in subsection 3.1.4) but instability in this value can cause
654 biases in reconstruction. Dark noise is related to the gain of a PMT and is calibrated
655 using hits inside a time window recorded before an event trigger [98].

656 3.1.3. Data Acquisition and Triggering

657 The analysis presented in this thesis only uses the SK-IV period of the SK experiment
658 so this subsection focuses on the relevant points of the data acquisition and triggering
659 systems to that SK period. The earlier data acquisition and triggering systems are
660 documented in [99, 100].

661 Before the SK-IV period started, the existing front-end electronics were replaced
662 with “QTC-Based Electrons with Ethernet, QBEE” systems [101]. When the QBEE

observes a signal above a 1/4 photoelectron threshold, the charge-to-time (QTC) converter generates a rectangular pulse. The start of the rectangular pulse indicates the time at which the analog photoelectron signal was received and the width of the pulse indicates the total charge integrated throughout the signal. This is then digitized by time-to-digital converters and sent to the “front-end” PCs. The digitized signal from every QBEE is then chronologically ordered and sent to the “merger” PCs. It is the merger PCs that apply the software trigger. Any triggered events are passed to the “organizer” PC. This sorts the data stream of multiple merger PCs into chronologically ordered events which are then saved to disk. The schematic of data flow from PMTs to disk is illustrated in Figure 3.3.

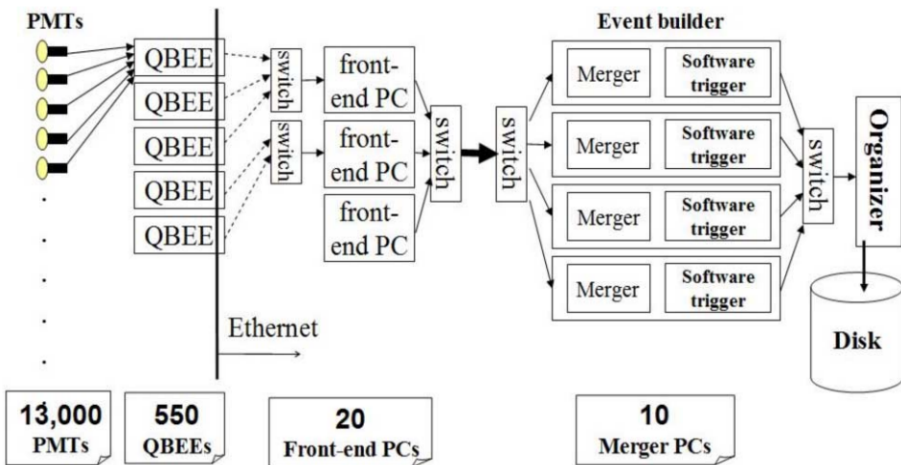


Figure 3.3.: Schematic view of the data flow through the data acquisition and online system. Taken from [102].

The software trigger (described in [103]) operates by determining the number of PMT hits within a 200ns sliding window, N_{200} . This window coincides with the maximum time that a Cherenkov photon would take to traverse the length of the SK tank [100]. For lower energy events that generate fewer photons, this technique is useful for eliminating background processes like dark noise and radioactive decay which would be expected to separate in time. When the value of N_{200} exceeds some threshold, a software trigger is issued. There are several trigger thresholds used within

the SK-IV period which are detailed in Table 3.2. If one of these thresholds is met, the PMT hits within an extended time window are also read out and saved to disk. In the special case of an event that exceeds the SHE trigger but does not exceed the OD trigger, the AFT trigger looks for delayed coincidences of 2.2MeV gamma rays emitted from neutron capture in a $535\mu\text{s}$ window after the SHE trigger. A similar but more complex “Wideband Intelligent Trigger (WIT)” has been deployed and is described in [104].

Trigger	Acronym	Condition	Extended time window (μs)
Super Low Energy	SLE	>34/31 hits	1.3
Low Energy	LE	>47 hits	40
High Energy	HE	>50 hits	40
Super High Energy	SHE	>70/58 hits	40
Outer Detector	OD	>22 hits in OD	N/A

Table 3.2.: The trigger thresholds and extended time windows saved around an event which were utilised throughout the SK-IV period. The exact thresholds can change and the values listed here represent the thresholds at the start and end of the SK-IV period.

3.1.4. Cherenkov Radiation

Cherenkov light is emitted from any highly energetic charged particle traveling with relativistic velocity, β , greater than the local speed of light in a medium [105]. Cherenkov light is formed at the surface of a cone with characteristic pitch angle,

$$\cos(\theta) = \frac{1}{\beta n}. \quad (3.2)$$

where n is the refractive index of the medium. Consequently, the Cherenkov momentum threshold, P_{thres} , is dependent upon the mass, m , of the charged particle moving through the medium,

$$P_{thres} = \frac{m}{\sqrt{n^2 - 1}} \quad (3.3)$$

For water, where $n = 1.33$, the Cherenkov threshold momentum and energy for various particles are given in Table 3.3. In contrast, γ -rays are detected indirectly via the combination of photons generated by Compton scattering and pair production. The threshold for detection in the SK detector is typically higher than the threshold for photon production. This is due to the fact that the attenuation of photons in the water means that typically $\sim 75\%$ of Cherenkov photons reach the ID PMTs. Then the collection and quantum efficiencies described in subsection 3.1.1 result in the number of detected photons being lower than the number of photons which reach the PMTs.

Particle	Threshold Momentum (MeV)	Threshold Energy (MeV)
Electron	0.5828	0.7751
Muon	120.5	160.3
Pion	159.2	211.7
Proton	1070.0	1423.1

Table 3.3.: The threshold momentum and energy for a particle to generate Cherenkov light in ultrapure water, as calculated in Equation 3.2 in ultrapure water which has refractive index $n = 1.33$.

The Frank-Tamm equation [106] describes the relationship between the number of Cherenkov photons generated per unit length, dN/dx , the wavelength of the photons generated, λ , and the relativistic velocity of the charged particle,

$$\frac{d^2N}{dxd\lambda} = 2\pi\alpha \left(1 - \frac{1}{n^2\beta^2}\right) \frac{1}{\lambda^2}. \quad (3.4)$$

where α is the fine structure constant. For a 100MeV momentum electron, approximately 330 photons will be produced per centimeter in the $300\text{nm} \leq \lambda \leq 700\text{nm}$ region which the ID PMTs are most sensitive to [87].

3.2. The Tokai to Kamioka Experiment

The Tokai to Kamioka (T2K) experiment is a long-baseline neutrino oscillation experiment located in Japan. Proposed in the early 2000s [107, 108] to replace K2K [109], T2K was designed to observe electron neutrino appearance whilst precisely measuring the oscillation parameters associated with muon neutrino disappearance [110]. The experiment consists of a neutrino beam generated at the Japan Proton Accelerator Research Complex (J-PARC), a suite of near detectors situated 280m from the beam target, and the Super Kamiokande far detector positioned at a 295km baseline. The cross-section view of the T2K experiment is drawn in Figure 3.4.

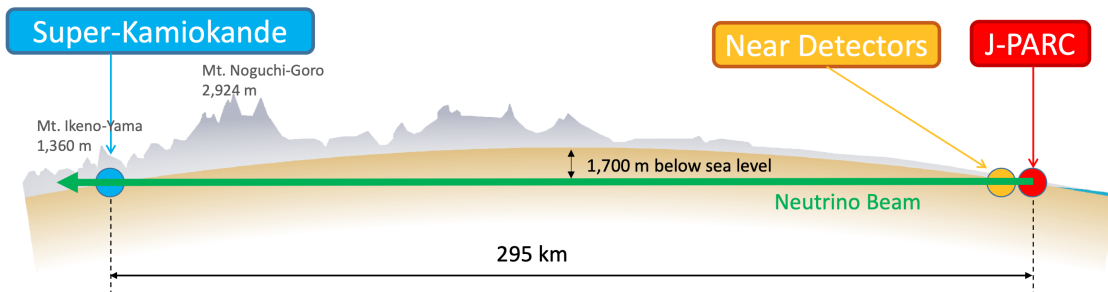


Figure 3.4.: The cross-section view of the Tokai to Kamioka experiment illustrating the beam generation facility at J-PARC, the near detector situated at a baseline of 280m and the Super Kamiokande far detector situated 295km from the beam target.

717 The T2K collaboration makes world-leading measurements of the $\sin^2(\theta_{23})$, Δm_{23}^2 ,

718 and δ_{CP} oscillation parameters. Improvements in the precision and accuracy of param-

719 eter estimates are still being made by including new data samples and developing the

720 models which describe the neutrino interactions and detector responses [111]. Electron

721 neutrino appearance was first observed at T2K in 2014 [112] with 7.3σ significance.

722 The near detectors provide constraints on the beam flux and cross-section model

723 parameters used within the oscillation analysis by observing the unoscillated neutrino

724 beam. There are a host of detectors situated in the near detector hall (As illustrated

725 in Figure 3.5): ND280 (subsection 3.2.2), INGRID (subsection 3.2.3), NINJA [113],

726 WAGASCI [114], and Baby-MIND [115]. The latter three are not currently used within

727 the oscillation analysis presented within this thesis.

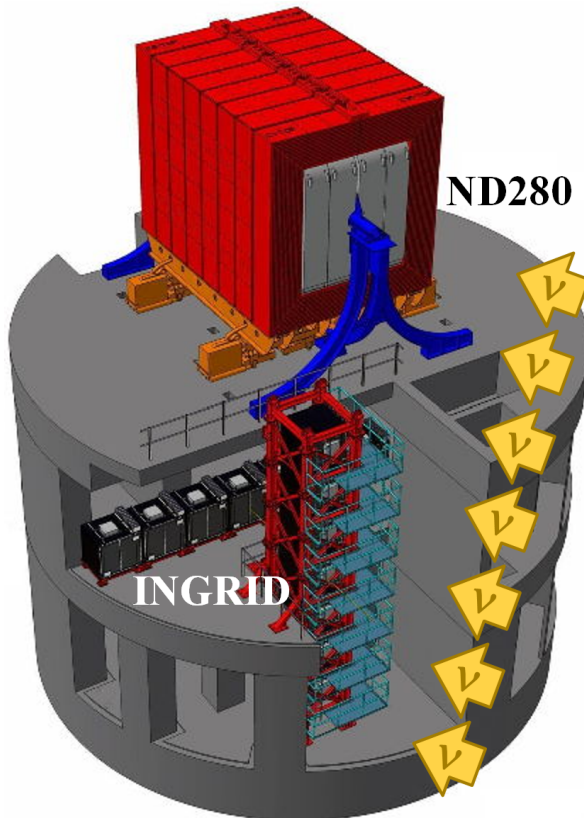


Figure 3.5.: The near detector suite for the T2K experiment showing the ND280 and INGRID detectors. The distance between the detectors and the beam target is 280m.

Whilst this thesis presents the ND280 in terms of its purpose for the oscillation analysis, the detector can also make many cross-section measurements at neutrino energies of $O(1)\text{GeV}$ for the different targets within the detector [116, 117]. These measurements are of equal importance as they can lead the way in determining the model parameters used in the interaction models for the future high-precision era of neutrino physics.

Review the rest of this subsection

There are two independent fitters, MaCh3 and BANFF, which perform the near detector fit. MaCh3 is the basis of this analysis and uses a bayesian Markov Chain Monte Carlo fitting technique, whereas BANFF uses a frequentist gradient descent technique. The output of each fitter is converted into a covariance matrix to describe the error and correlations between all the flux and cross-section parameters. This is then propagated to the far-detector oscillation analysis group for use in the P-Theta and VALOR fitting framework. As MaCh3 can handle both near and far detector samples, it does not use this covariance matrix and instead opts for a simultaneous fit of the two detector measurements. This is an analysis choice which removes the assumption of Gaussian posterior distributions required when building the post-fit covariance matrix.

DB: MaCh3 vs PTheta and Valor

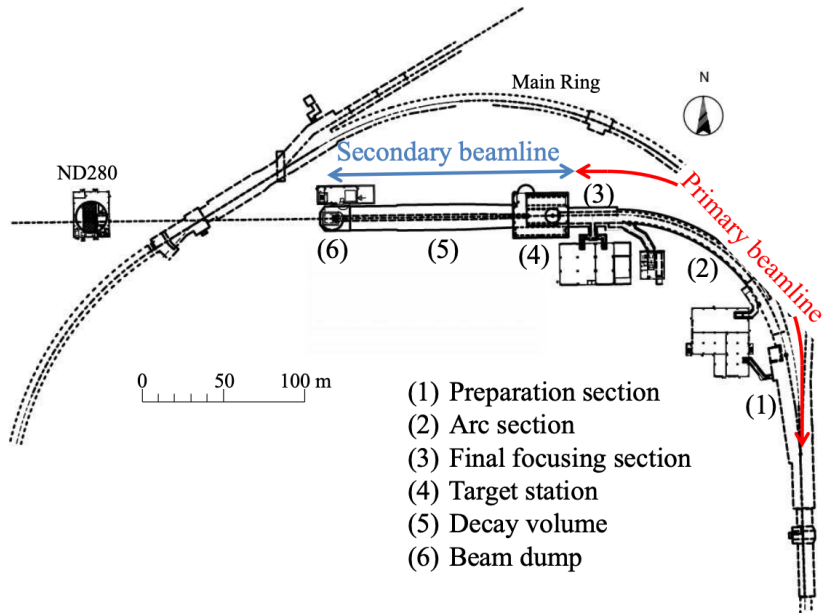
There are three particular tunes of the T2K flux and low energy cross section model typically considered. Firstly, the “generated” tune which is the set of dial values with which the Monte Carlo was generated. Secondly, the set of dial values which are taken from external data measurements and used as inputs. These are the “pre-fit” dial values. The reason these two sets of dial values are different is that the external data measurements are continually updated but it is very computationally intensive to regenerate a Monte Carlo prediction after each update. The final tune is the “post-fit”,

⁷⁵³ “post-ND fit” or “post-BANFF” dial values. These are the values taken from the fit to
⁷⁵⁴ the beam near detector data.

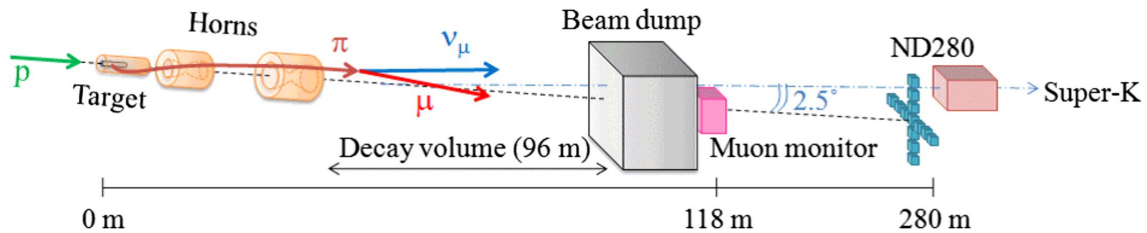
⁷⁵⁵ 3.2.1. The Neutrino Beam

⁷⁵⁶ The neutrino beam used within the T2K experiment is described in [59, 118] and
⁷⁵⁷ summarised below. The accelerating facility at J-PARC is composed of two sections; the
⁷⁵⁸ primary and secondary beamlines. Figure 3.6 illustrates a schematic of the beamline,
⁷⁵⁹ focusing mostly on the components of the secondary beamline. The primary beamline
⁷⁶⁰ has three accelerators that progressively accelerate protons; a linear accelerator, a rapid-
⁷⁶¹ cycling synchrotron, and the main-ring (MR) synchrotron. Once fully accelerated by
⁷⁶² the MR, the protons have a kinetic energy of 30GeV. Eight bunches of these protons,
⁷⁶³ separated by 500ns, are extracted per “spill” from the MR and directed towards a
⁷⁶⁴ graphite target (a rod of length 91.4cm and diameter 2.6cm). Spills are extracted at
⁷⁶⁵ 0.5Hz with $\sim 3 \times 10^{14}$ protons contained per spill.

⁷⁶⁶ The secondary beamline consists of three main components: the target station, the
⁷⁶⁷ decay volume, and the beam dump. The target station is comprised of the target, beam
⁷⁶⁸ monitors, and three magnetic focusing horns. The proton beam interacts with the
⁷⁶⁹ graphite target to form a secondary beam of mostly pions and kaons. The secondary
⁷⁷⁰ beam travels through a 96m long decay volume, generating neutrinos through the
⁷⁷¹ following decays [59],



(a) Primary and secondary beamline



(b) Secondary beamline

Figure 3.6.: Top panel: Bird's eye view of the most relevant part of primary and secondary beamline used within the T2K experiment. The primary beamline is the main-ring proton synchrotron, kicker magnet, and graphite target. The secondary beamline consists of the three focusing horns, decay volume, and beam dump. Figure taken from [118]. Bottom panel: The side-view of the secondary beamline including the focusing horns, beam dump and neutrino detectors. Figure taken from [119].

$$\pi^+ \rightarrow \mu^+ + \nu_\mu$$

$$\pi^- \rightarrow \mu^- + \bar{\nu}_\mu$$

$$K^+ \rightarrow \mu^+ + \nu_\mu$$

$$K^- \rightarrow \mu^- + \bar{\nu}_\mu$$

$$\rightarrow \pi^0 + e^+ + \nu_e$$

$$\rightarrow \pi^0 + e^- + \bar{\nu}_e$$

$$\rightarrow \pi^0 + \mu^+ + \nu_\mu$$

$$\rightarrow \pi^0 + \mu^- + \bar{\nu}_\mu$$

$$K_L^0 \rightarrow \pi^- + e^+ + \nu_e$$

$$K_L^0 \rightarrow \pi^+ + e^- + \bar{\nu}_e$$

$$\rightarrow \pi^- + \mu^+ + \nu_\mu$$

$$\rightarrow \pi^+ + \mu^- + \bar{\nu}_\mu$$

$$\mu^+ \rightarrow e^+ + \bar{\nu}_\mu + \nu_e$$

$$\mu^- \rightarrow e^- + \nu_\mu + \bar{\nu}_e$$

The electrically charged component of the secondary beam is focused towards the far detector by the three magnetic horns. These horns direct charged particles of a particular polarity towards SK whilst defocusing the oppositely charged particles. This allows a mostly neutrino or mostly antineutrino beam to be used within the experiment, denoted as “forward horn current (FHC)” or “reverse horn current (RHC)” respectively.

Figure 3.7 illustrates the different contributions to the FHC and RHC neutrino flux.

The low energy flux is dominated by the decay of pions whereas kaon decay becomes the dominant source of neutrinos for $E_\nu > 3\text{GeV}$. The “wrong-sign” component, which is the $\bar{\nu}_\mu$ background in a ν_μ beam, and the intrinsic irreducible ν_e background, are predominantly due to muon decay for $E_\nu < 2\text{GeV}$. As the antineutrino production cross-section is smaller than the neutrino cross-section, the wrong-sign component is more dominant in the RHC beam as compared to that in the FHC beam.

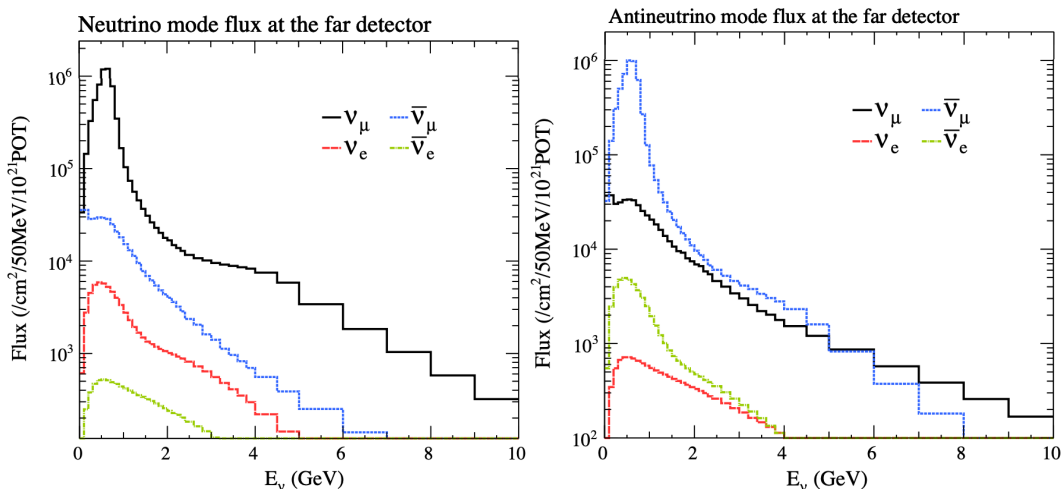


Figure 3.7.: The Monte Carlo prediction of the energy spectrum for each flavour of neutrino (ν_e , $\bar{\nu}_e$, ν_μ and $\bar{\nu}_\mu$) in the neutrino dominated beam FHC mode (Left) and antineutrino dominated beam RHC mode (Right) expected at SK. Taken from [120].

The beam dump, situated at the end of the decay volume, stops all charged particles other than highly energetic muons ($p_\mu > 5\text{GeV}$). The MuMon detector monitors the

⁷⁸⁸ penetrating muons to determine the beam direction and intensity which is used to
⁷⁸⁹ constrain some of the beam flux systematics within the analysis [119, 121].

⁷⁹⁰ The T2K experiment uses an off-axis beam to narrow the neutrino energy distribution.
⁷⁹¹ This was the first implementation of this technique in a long-baseline neutrino
⁷⁹² oscillation experiment after its original proposal [122]. Pion decay, $\pi \rightarrow \mu + \nu_\mu$, is a
⁷⁹³ two-body decay. Consequently, the neutrino energy, E_ν , can be determined based on
⁷⁹⁴ the pion energy, E_π , and the angle at which the neutrino is emitted, θ ,

$$E_\nu = \frac{m_\pi^2 - m_\mu^2}{2(E_\pi - p_\pi \cos(\theta))}, \quad (3.5)$$

⁷⁹⁵ where m_π and m_μ are the mass of the pion and muon respectively. For a fixed
⁷⁹⁶ energy pion, the neutrino energy distribution is dependent upon the angle at which the
⁷⁹⁷ neutrinos are observed from the initial pion beam direction. For the 295km baseline at
⁷⁹⁸ T2K, $E_\nu = 0.6\text{GeV}$ maximises the electron neutrino appearance probability, $P(\nu_\mu \rightarrow \nu_e)$,
⁷⁹⁹ whilst minimising the muon disappearance probability, $P(\nu_\mu \rightarrow \nu_\mu)$. Figure 3.8
⁸⁰⁰ illustrates the neutrino energy distribution for a range of off-axis angles, as well as the
⁸⁰¹ oscillation probabilities most relevant to T2K.

⁸⁰² 3.2.2. The Near Detector at 280m

⁸⁰³ Whilst all the near detectors are situated in the same “pit” located at 280m from the
⁸⁰⁴ beamline, the “ND280” detector is the off-axis detector which is situated at the same
⁸⁰⁵ off-axis angle as the Super-Kamiokande far detector. It has two primary functions;
⁸⁰⁶ firstly it measures the neutrino flux and secondly it counts the event rates of different
⁸⁰⁷ types of neutrino interactions. Both of these constrain the flux and cross-section

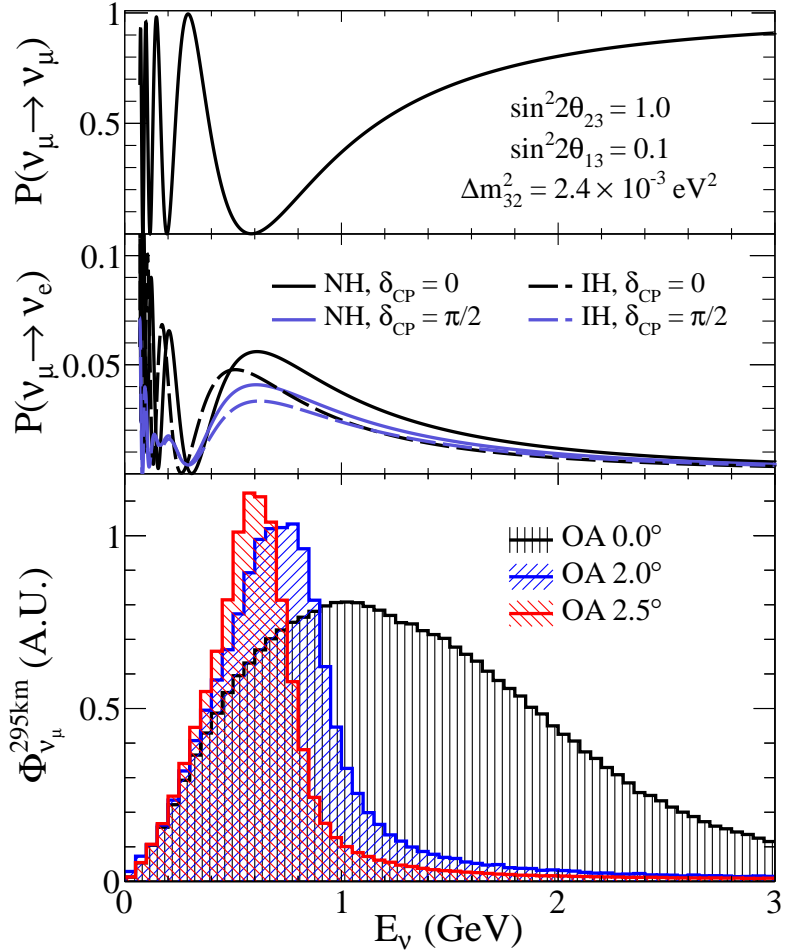


Figure 3.8.: Top panel: T2K muon neutrino disappearance probability as a function of neutrino energy. Middle panel: T2K electron neutrino appearance probability as a function of neutrino energy. Bottom panel: The neutrino flux distribution for three different off-axis angles (Arbitrary units) as a function of neutrino energy.

808 systematics invoked within the model for a more accurate prediction of the expected
 809 event rate at the far detector.

810 As illustrated in Figure 3.9, the ND280 detector consists of several sub-detectors.
 811 The most important part of the detector for this analysis is the tracker region. This is
 812 comprised of two time projection chambers (TPCs) sandwiched between three fine
 813 grain detectors (FGDs). The FGDs contain both hydrocarbon plastics and water tar-
 814 gets for neutrino interactions and provide track reconstruction near the interaction
 815 vertex. The emitted charged particles can then propagate into the TPCs which pro-
 816 vide particle identification and momentum reconstruction. The FGDs and TPCs are

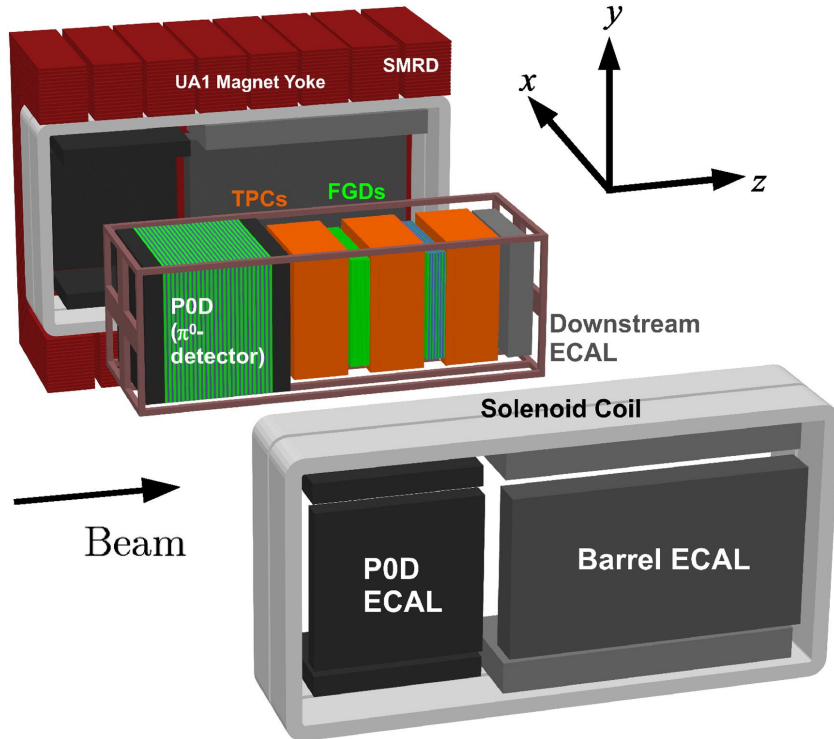


Figure 3.9.: The components of the ND280 detector. The neutrino beam travels from left to right. Taken from [118].

817 further described in subsubsection 3.2.2.1 and subsubsection 3.2.2.2 respectively. The
 818 electromagnetic calorimeter (ECAL) encapsulates the tracker region alongside the π^0
 819 detector (P0D). The ECAL measures the deposited energy from photons emitted from
 820 interactions within the FGD. The P0D constrains the cross-section of neutral current
 821 interactions which generate neutral pions, which is one of the largest backgrounds in
 822 the electron neutrino appearance oscillation channel. The P0D and ECAL detectors
 823 are detailed in subsubsection 3.2.2.3 and subsubsection 3.2.2.4 respectively. The entire
 824 detector is located within a large yoke magnet which produces a 0.2T magnetic field.
 825 This design of the magnet also includes a scintillating detector called the side muon
 826 range detector (SMRD) which is used to track high-angle muons as well as acting as a
 827 cosmic veto. The SMRD is described in subsubsection 3.2.2.5.

3.2.2.1. Fine Grained Detectors

The T2K tracker region is comprised of two fine grained detectors (FGD) and three Time Projection Chambers (TPC). A detailed description of the FGD design, construction, and assembly is found in [123] and summarised below. The FGDs are the primary target for neutrino interactions with a mass of 1.1 tonnes per FGD. Alongside this, the FGDs are designed to be able to track short-range particles which do not exit the FGD. Typically, short-range particles are low momentum and are observed as tracks that deposit a large amount of energy per unit length. This means the FGD needs good granularity to resolve these particles. The FGDs have the best timing resolution ($\sim 3\text{ns}$) of any of the sub-detectors of the ND280 detector. As such, the FGDs are used for time of flight measurements to distinguish forward going positively charged particles from backward going negatively charged particles. Finally, any tracks which pass through multiple sub-detectors are required to be track matched to the FGD.

Both FGDs are made from square scintillator planes of side length 186cm and width 2.02cm. Each plane consists of two layers of 192 scintillator bars in an X or Y orientation. A wavelength shifting fiber is threaded through the center of each bar and is read out by a multi-pixel photon counter (MPPC). FGD1 is the most upstream of the two FGDs and contains 15 planes of carbon plastic scintillator which is a common target in external neutrino scattering data. As the far detector is a pure water target, 7 of the 15 scintillator planes in FGD2 have been replaced with a hybrid water-scintillator target. Due to the complexity of the nucleus, nuclear effects can not be extrapolated between different nuclei. Therefore having the ability to take data on one target which is the same as external data and another target which is the same as the far detector target is beneficial for reliable model parameter estimates.

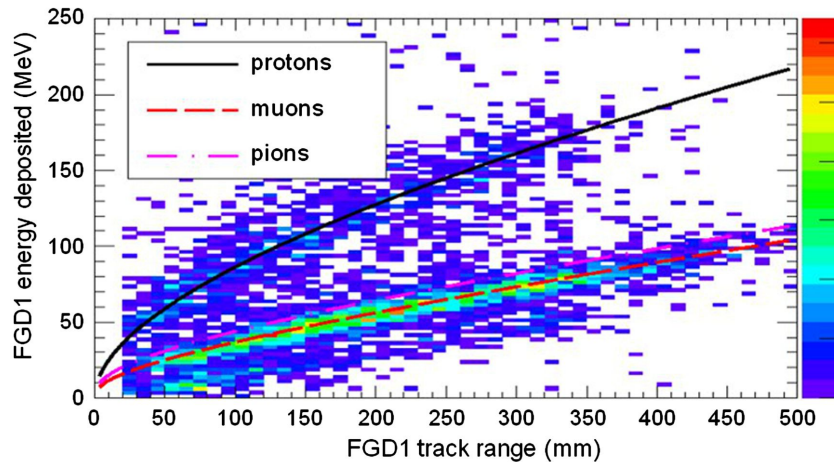


Figure 3.10.: Comparison of data to Monte Carlo prediction of integrated deposited energy as a function of track length for particles that stopped in FGD1. Taken from [123].

852 The integrated deposited energy is used for particle identification. The FGD
 853 can distinguish protons from other charged particles by comparing the integrated
 854 deposited energy from data to Monte Carlo prediction as seen in Figure 3.10.

855 **3.2.2.2. Time Projection Chambers**

856 The majority of particle identification and momentum measurements within ND280
 857 are provided by three Time Projection Chambers (TPCs) [124]. The TPCs are located
 858 on either side of the FGDs. They are located inside of the magnetic field meaning the
 859 momentum of a charged particle can be determined from the bending of the track.

860 Each TPC module consists of two gas-tight boxes, as shown in Figure 3.11, which
 861 are made of non-magnetic material. The outer box is filled with CO₂ which acts as
 862 an electrical insulator between the inner box and the ground. The inner box forms
 863 the field cage which produces a uniform electric drift field of $\sim 275\text{V}/\text{cm}$ and is filled
 864 with an argon gas mixture. Charged particles moving through this gas mixture ionize
 865 the gas and the ionised charge is drifted towards micromegas detectors which measure
 866 the ionization charge. The time and position information in the readout allows a
 867 three-dimensional image of the neutrino interaction.

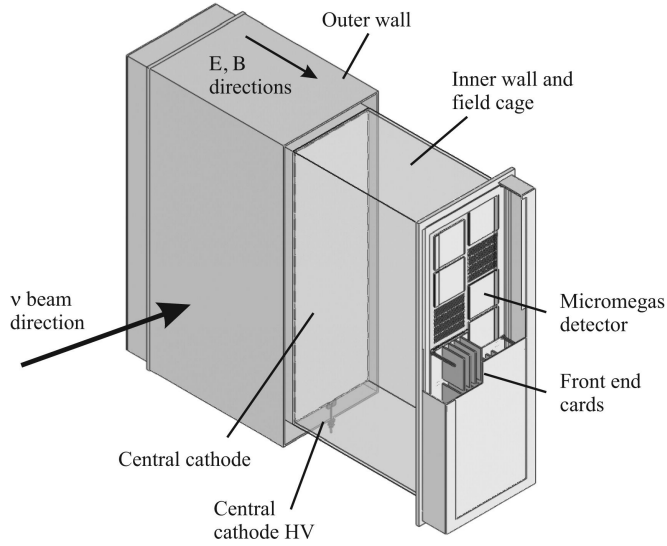


Figure 3.11.: Schematic design of a Time Projection Chamber detector. Taken from [124].

The particle identification of tracks that pass through the TPCs is performed using

dE/dx measurements. Figure 3.12 illustrates the data to Monte Carlo distributions of the energy lost by a charged particle passing through the TPC as a function of the reconstructed particle momentum. The resolution is $7.8 \pm 0.2\%$ meaning that electrons and muons can be distinguished. This allows reliable measurements of the intrinsic ν_e component of the beam.

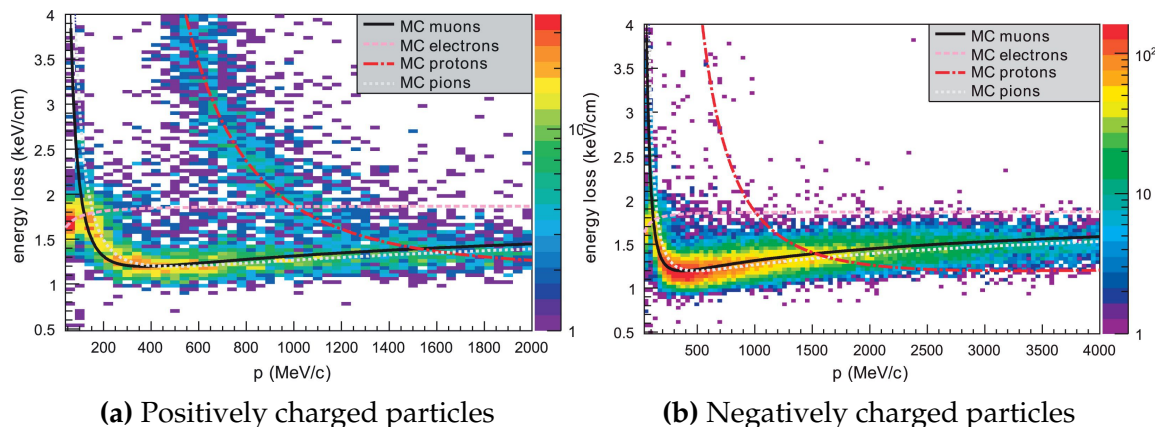


Figure 3.12.: The distribution of energy loss as a function of reconstructed momentum for charged particles passing through the TPC, comparing data to Monte Carlo prediction. Taken from [124].

874 3.2.2.3. π^0 Detector

875 If one of the γ -rays from a $\pi^0 \rightarrow 2\gamma$ decay is missed at the far detector, the recon-
876 struction will determine that event to be a charge current ν_e -like event. This is one of
877 the main backgrounds hindering the electron neutrino appearance searches. The π^0
878 detector (P0D) measures the cross-section of the neutral current induced neutral pion
879 production on a water target to constrain this background.

880 The P0D is a cube of approximately 2.5m length consisting of layers of scintillating
881 bars, brass and lead sheets, and water bags as illustrated in Figure 3.13. Two electro-
882 magnetic calorimeters are positioned at the most upstream and most downstream
883 position in the sub-detector and the water target is situated in between them. The
884 scintillator layers are built from two triangular bars orientated in opposite directions
885 to form a rectangular layer. Each triangular scintillator bar is threaded with optical
886 fiber which is read out by MPPCs. The high-Z brass and lead regions produce electron
887 showers from the photons emitted in π^0 decay.

888 The sub-detector can generate measurements of NC1 π^0 cross-sections on a water
889 target by measuring the event rate both with and without the water target, with the
890 cross-section on a water target being determined as the difference. The total active
891 mass is 16.1 tonnes when filled with water and 13.3 tonnes when empty.

892 3.2.2.4. Electromagnetic Calorimeter

893 The electromagnetic calorimeter [126] (ECal) encapsulates the P0D and tracking sub-
894 detectors. Its primary purpose is to aid π^0 reconstruction from any interaction in
895 the tracker. To do this, it measures the energy and direction of photon showers from
896 $\pi^0 \rightarrow 2\gamma$ decay. It can also distinguish pion and muon tracks depending on the shape
897 of the photon shower deposited.

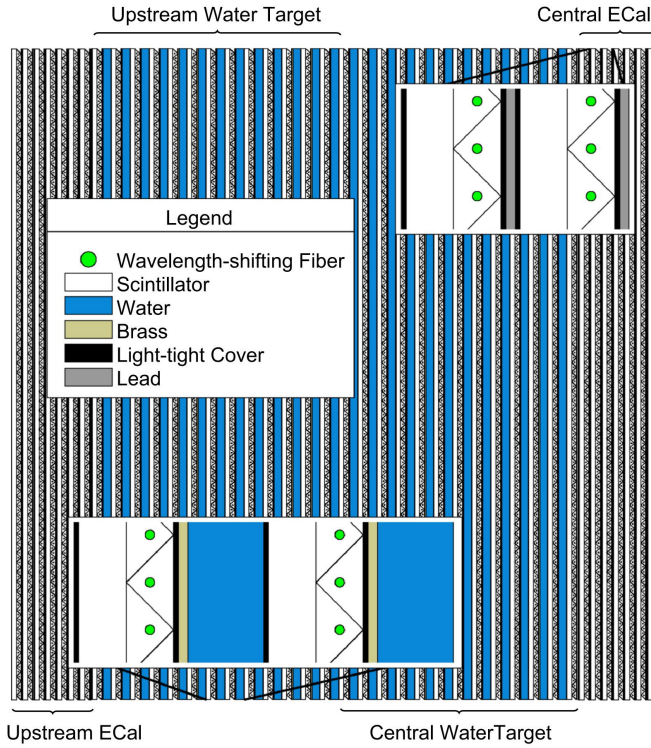


Figure 3.13.: A schematic of the P0D side-view. Taken from [125].

898 The ECal is comprised of three sections; the P0D ECal which surrounds the P0D,
 899 the barrel ECal which encompasses the tracking region, and the downstream ECal
 900 which is situated downstream of the tracker region. The barrel and downstream
 901 ECals are tracking calorimeters that focus on electromagnetic showers from high-angle
 902 particles emitted from the tracking sub-detectors. Particularly in the TPC, high-angle
 903 tracks (those which travel perpendicularly to the beam-axis) can travel along a single
 904 scintillator bar resulting in very few hits. The width of the barrel and downstream
 905 ECal corresponds to ~ 11 electron radiation lengths to ensure a significant amount of
 906 the π^0 energy is contained. As the P0D has its own calorimetry which reconstructs
 907 showers, the P0D ECal determines the energy which escapes the P0D.

908 Each ECal is constructed of multiple layers of scintillating bars sandwiched between
 909 lead sheets. The scintillating bars are threaded with optical fiber and read out by
 910 MPPCs. Each sequential layer of the scintillator is orientated perpendicular to the
 911 previous which allows a three dimensional event reconstruction. The target mass

912 of the P0D ECal, barrel ECal, and downstream ECal are 1.50, 4.80 and 6.62 tonnes
913 respectively.

914 **3.2.2.5. Side Muon Range Detector**

915 As illustrated in Figure 3.9, the ECal, FGDs, P0D, and TPCs are enclosed within the
916 UA1 magnet. Originally designed for the NOMAD [127] experiment and reconditioned
917 for use in the T2K experiment [128], the UA1 magnet provides a uniform horizontal
918 magnetic field of 0.2T with an uncertainty of 2×10^{-4} T.

919 Built into the UA1 magnet, the side muon range detector (SMRD) [129] monitors
920 high-energy muons which leave the tracking region and permeate through the ECal.
921 It additionally acts as a cosmic muon veto and trigger.

922 **3.2.3. The Interactive Neutrino GRID**

923 The Interactive Neutrino GRID (INGRID) detector is situated within the same “pit” as
924 the other near detectors. It is aligned with the beam in the “on-axis” position and mea-
925 sures the beam direction, spread, and intensity. The detector was originally designed
926 with 16 identical modules [118] (two modules have since been decommissioned) and a
927 “proton” module. The design of the detector is cross-shaped with length and height
928 10m × 10m as illustrated in Figure 3.14.

929 Each module is composed of iron sheets interlaced with eleven tracking scintillator
930 planes for a total target mass of 7.1 tonnes per module. The scintillator design is an X-Y
931 pattern of 24 bars in both orientations, where each bar contains wave-length shifting
932 fibers which are connected to multi-pixel photon counters (MPPCs). Each module is
933 encapsulated inside veto planes to aid the rejection of charged particles entering the
934 module.

935 The proton module is different from the other modules in that it consists of entirely
 936 scintillator planes with no iron target. The scintillator bars are also smaller than those
 937 used in the other modules to increase the granularity of the detector and improve
 938 tracking capabilities. The module sits in the center of the beamline and is designed to
 939 give precise measurements of quasi-elastic charged current interactions to evaluate
 940 the performance of the Monte Carlo simulation of the beamline.

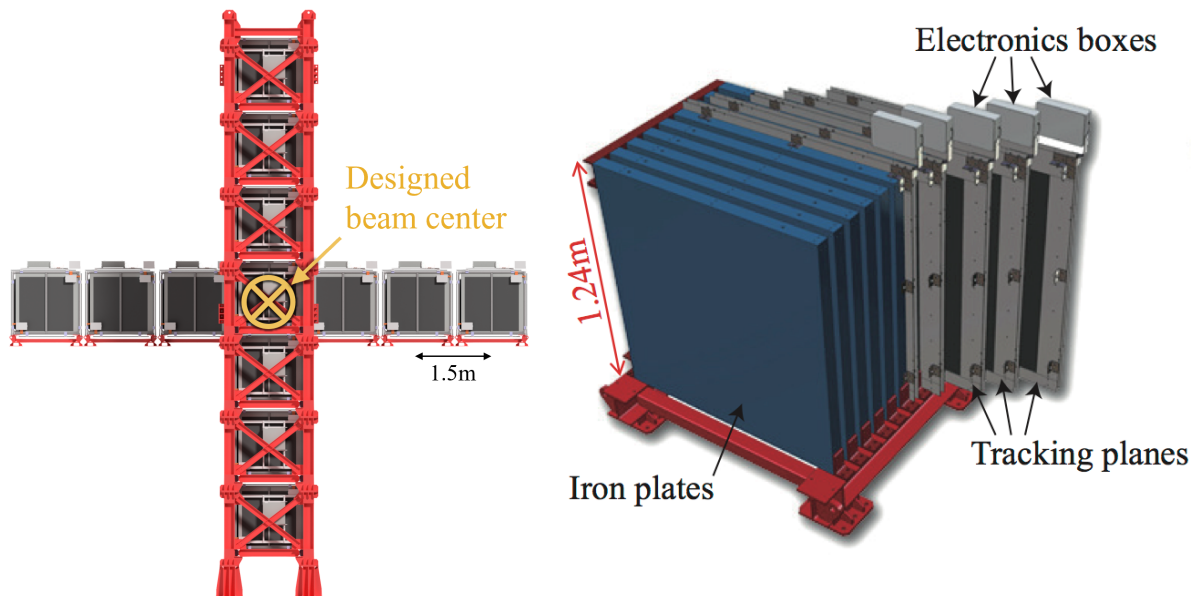


Figure 3.14.: Left panel: The Interactive Neutrino GRID on-axis Detector. 14 modules are arranged in a cross-shape configuration, with the center modules being directly aligned with the on-axis beam. Right panel: The layout of a single module of the INGRID detector. Both figures are recreated from [118].

941 The INGRID detector can measure the beam direction to an uncertainty of 0.4mrad
 942 and the beam center within a resolution of 10cm [118]. The beam direction in both the
 943 vertical and horizontal directions is discussed in [130] and it is found to be in good
 944 agreement with the MUMON monitor described in subsection 3.2.1.

945 **Chapter 4**

946 **Bayesian Statistics and Markov Chain
Monte Carlo Techniques**

948 This thesis presents a Bayesian oscillation analysis. To extract the oscillation parameters,
949 a Markov Chain Monte Carlo (MCMC) method is used. This chapter explains
950 the theory of how parameter estimates can be determined using this technique and
951 condenses the material found in the literature [131–134].

952 The oscillation parameter determination presented within this thesis is built upon
953 a simultaneous fit to neutrino beam data in the near detector, beam data at SK and
954 atmospheric data at SK. In total, there are four oscillation parameters of interest
955 ($\sin^2(\theta_{23})$, $\sin^2(\theta_{13})$, Δm_{23}^2 , and δ_{CP}), two oscillation parameters to which this study
956 will not be sensitive ($\sin^2(\theta_{12})$, Δm_{12}^2) and many nuisance parameters that control the
957 systematic uncertainty models invoked within this study.

958 The MCMC technique generates a multi-dimensional probability distribution across
959 all of the model parameters used in the fit. To determine the parameter estimate of a
960 single parameter, this multi-dimensional object is integrated over all other parameters.
961 This process is called Marginalisation and is further described in subsection 4.3.1.
962 Monte Carlo techniques approximate the probability distribution of each parameter
963 within the limit of generating infinite samples. As ever, generating a large number of
964 samples is time and resource-dependent. Therefore, an MCMC technique is utilised
965 within this analysis to reduce the required number of steps to sufficiently sample the
966 parameter space. This technique is described in further detail in subsection 4.2.1.

⁹⁶⁷ 4.1. Bayesian Statistics

⁹⁶⁸ Bayesian inference treats observable data, D , and model parameters, $\vec{\theta}$, on equal
⁹⁶⁹ footing such that a probability model of both data and parameters is required. This is
⁹⁷⁰ the joint probability distribution $P(D, \vec{\theta})$ and can be described by the prior distribution
⁹⁷¹ for model parameters $P(\vec{\theta})$ and the likelihood of the data given the model parameters
⁹⁷² $P(D|\vec{\theta})$,

$$P(D, \vec{\theta}) = P(D|\vec{\theta})P(\vec{\theta}). \quad (4.1)$$

⁹⁷³ The prior distribution, $P(\vec{\theta})$, describes all previous knowledge about the parameters
⁹⁷⁴ within the model. For example, if the risk of developing health problems is known
⁹⁷⁵ to increase with age, the prior distribution would describe the increase. For the
⁹⁷⁶ purpose of this analysis, the prior distribution is typically the best-fit values taken
⁹⁷⁷ from external data measurements with a Gaussian uncertainty. The prior distribution
⁹⁷⁸ can also contain correlations between model parameters. In an analysis using Monte
⁹⁷⁹ Carlo techniques, the likelihood of measuring some data assuming some set of model
⁹⁸⁰ parameters is calculated by comparing the Monte Carlo prediction generated at that
⁹⁸¹ particular set of model parameters to the data.

⁹⁸² It is parameter estimation that is important for this analysis and as such, we apply
⁹⁸³ Bayes' theorem [135] to calculate the probability for each parameter to have a certain
⁹⁸⁴ value given the observed data, $P(\vec{\theta}|D)$, which is known as the posterior distribution
⁹⁸⁵ (often termed the posterior). This can be expressed as

$$P(\vec{\theta}|D) = \frac{P(D|\vec{\theta})P(\vec{\theta})}{\int P(D|\vec{\theta})P(\vec{\theta})d\vec{\theta}}. \quad (4.2)$$

986 The denominator in Equation 4.2 is the integral of the joint probability distribution
 987 over all values of all parameters used within the fit. For brevity, we say that the
 988 posterior distribution is

$$P(\vec{\theta}|D) \propto P(D|\vec{\theta})P(\vec{\theta}). \quad (4.3)$$

989 In subsection 4.3.1, we see that for the cases used within this analysis, it is reason-
 990 able to know the posterior to some normalisation constant.

991 **4.2. Monte Carlo Simulation**

992 Monte Carlo techniques are used to numerically solve a complex problem that does
 993 not necessarily have an analytical solution. These techniques rely on building a large
 994 ensemble of samples from an unknown distribution and then using the ensemble to
 995 approximate the properties of the distribution.

996 An example that uses Monte Carlo techniques is to calculate the area underneath
 997 a curve. For example, take the problem of calculating the area under a straight line
 998 with gradient $M = 0.4$ and intercept $C = 1.0$. Analytically, one can calculate the area
 999 under the line is equal to 30 units for $0 \leq x \leq 10$. Using Monte Carlo techniques,
 1000 one can calculate the area under this line by throwing many random values for the x
 1001 and y components of each sample and then calculating whether that point falls below

the line. The area can then be calculated by the ratio of points below the line to the total number of samples thrown multiplied by the total area in which samples were scattered. The study is shown in Figure 4.1 highlights this technique and finds the area under the curve to be 29.9 compared to an analytical solution of 30.0. The deviation of the numerical to analytical solution can be attributed to the number of samples used in the study. The accuracy of the approximation in which the properties of the Monte Carlo samples replicate those of the desired distribution is dependent on the number of samples used. Replicating this study with a differing number of Monte Carlo samples used in each study (As shown in Figure 4.2) highlights how the Monte Carlo techniques are only accurate within the limit of a high number of samples.

Whilst the above example has an analytical solution, these techniques are just as applicable to complex solutions. Clearly, any numerical solution is only as useful as its efficiency. As discussed, the accuracy of the Monte Carlo technique is dependent upon the number of samples generated to approximate the properties of the distribution. Furthermore, if the positions at which the samples are evaluated are not ‘cleverly’ picked, the efficiency of the Monte Carlo technique significantly drops. Given the example in Figure 4.1, if the region in which the samples are scattered significantly extends passed the region of interest, many calculations will be calculated but do not add to the ability of the Monte Carlo technique to achieve the correct result. For instance, any sample evaluated at a $y \geq 5$ could be removed without affecting the final result. This does bring in an aspect of the ‘chicken and egg’ problem in that to achieve efficient sampling, one needs to know the distribution beforehand.

4.2.1. Markov Chain Monte Carlo

This analysis utilises a multi-dimensional probability distribution, with some dimensions being significantly more constrained than others. This could be from prior

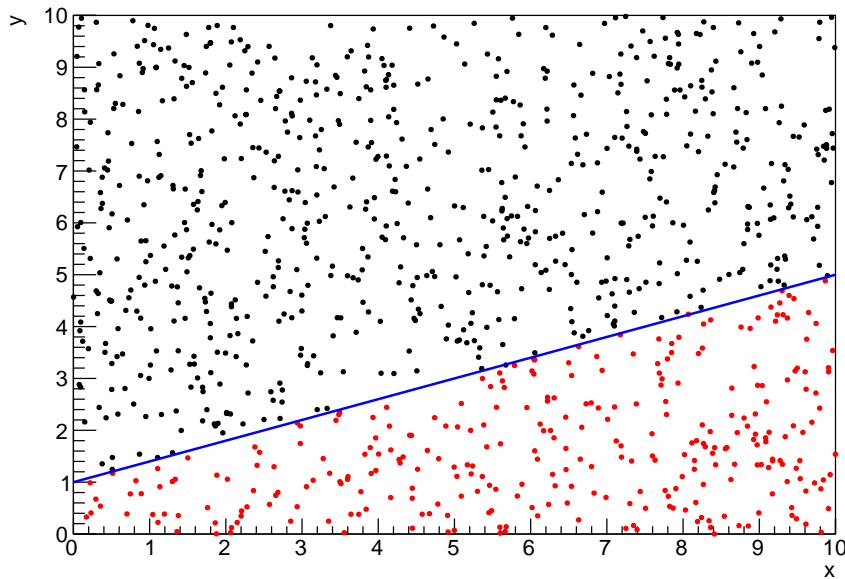


Figure 4.1.: Example of using Monte Carlo techniques to find the area under the blue line. The gradient and intercept of the line are 0.4 and 1.0 respectively. The area found to be under the curve using one thousand samples is 29.9 units.

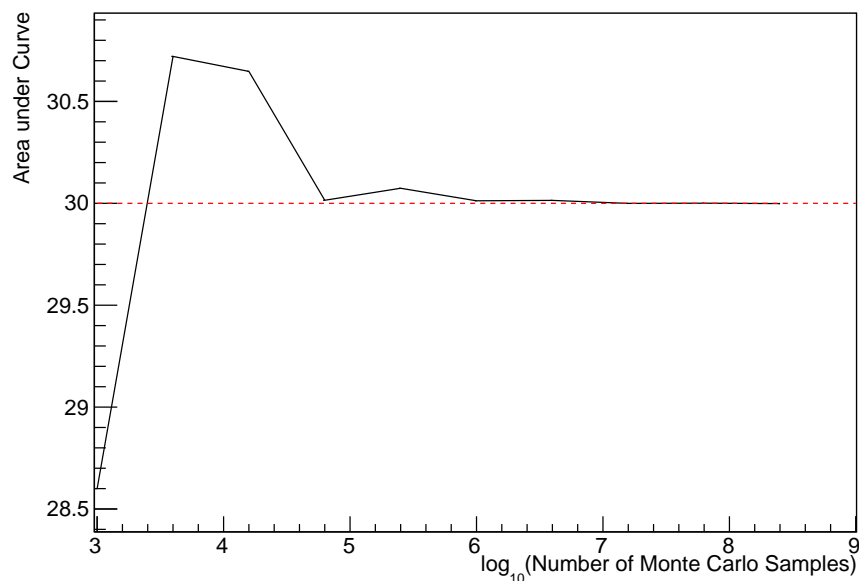


Figure 4.2.: The area under a line of gradient 0.4 and intercept 1.0 for the range $0 \leq x \leq 10$ as calculated using Monte Carlo techniques as a function of the number of samples used in each repetition. The analytical solution to the area is 30 units as given by the red line.

knowledge of parameter distributions from external data or un-physical regions in which parameters can not exist. Consequently, the Monte Carlo techniques used need to be as efficient as possible. For this analysis, the Markov Chain Monte Carlo (MCMC) technique is chosen. An MCMC technique is a Monte Carlo technique that uses a Markov chain to select which points at which to sample the parameter distribution. This technique performs a semi-random stochastic walk through the allowable parameter space. This builds a posterior distribution which has the property that the density of sampled points is proportional to the probability density of that parameter. This does mean that the samples produced by this technique are not statistically independent but they will cover the space of the distribution.

A Markov chain functions by selecting the position of step \vec{x}_{i+1} based on the position of \vec{x}_i . The space in which the Markov chain selects samples is dependent upon the total number of parameters utilised within the fit, where a discrete point in this space is described by the N-dimensional space \vec{x} . In a perfectly operating Markov chain, the position of the next step depends solely on the previous step and not on the further history of the chain (\vec{x}_0, \vec{x}_1 , etc.). However, in solving the multi-dimensionality of the fit used within this analysis, each step becomes correlated with several of the steps preceding itself. This behaviour is further explained in subsection 4.2.3. Providing the MCMC chain is well optimised, it will begin to converge towards a unique stationary distribution. The period between the chain's initial starting point and the convergence to the unique stationary distribution is colloquially known as the burn-in period. This is discussed further in subsection 4.2.3. Once the chain reaches the stationary distribution, all points sampled after that point will look like samples from that distribution.

1051 Further details of the theories underpinning MCMC techniques are discussed
1052 in [132] but can be summarised by the requirement that the chain satisfies the three
1053 ‘regularity conditions’:

- 1054 • Irreducibility: From every position in the parameter space \vec{x} , there must exist a
1055 non-zero probability for every other position in the parameter space to be reached.
- 1056 • Recurrence: Once the chain arrives at the stationary distribution, every step fol-
1057 lowing from that position must be samples from the same stationary distribution.
- 1058 • Aperiodicity: The chain must not repeat the same sequence of steps at any point
1059 throughout the sampling period.

1060 The output of the chain after burn-in (ie. the sampled points after the chain
1061 has reached the stationary distribution) can be used to approximate the posterior
1062 distribution and model parameters $\vec{\theta}$. To achieve the requirement that the unique
1063 stationary distribution found by the chain be the posterior distribution, one can use
1064 the Metropolis-Hastings algorithm. This guides the stochastic process depending on
1065 the likelihood of the current proposed step compared to that of the previous step.
1066 Implementation and other details of this technique are discussed in subsection 4.2.2.

1067 4.2.2. Metropolis-Hastings Algorithm

1068 As a requirement for MCMCs, the Markov chain implemented in this technique must
1069 have a unique stationary distribution that is equivalent to the posterior distribution.
1070 To ensure this requirement and that the regularity conditions are met, this analysis
1071 utilises the Metropolis-Hastings (MH) algorithm [136,137]. For the i^{th} step in the chain,
1072 the MH algorithm determines the position in the parameter space to which the chain
1073 moves to based on the current step, \vec{x}_i , and the proposed step, \vec{y}_{i+1} . The proposed step
1074 is randomly selected from some proposal function $f(\vec{x}_{i+1}|\vec{x}_i)$, which depends solely

on the current step (ie. not the further history of the chain). The next step in the chain \vec{x}_{i+1} can be either the current step or the proposed step determined by whether the proposed step is accepted or rejected. To decide if the proposed step is selected, the acceptance probability, $\alpha(\vec{x}_i, \vec{y}_i)$, is calculated as

$$\alpha(\vec{x}_i, \vec{y}_{i+1}) = \min \left(1, \frac{P(\vec{y}_{i+1}|D)f(\vec{x}_i|\vec{y}_{i+1})}{P(\vec{x}_i|D)f(\vec{y}_{i+1}|\vec{x}_i)} \right). \quad (4.4)$$

Where $P(\vec{y}_{i+1}|D)$ is the posterior distribution as introduced in section 4.1. To simplify this calculation, the proposal function is required to be symmetric such that $f(\vec{x}_i|\vec{y}_{i+1}) = f(\vec{y}_{i+1}|\vec{x}_i)$. In practice, a multi-variate Gaussian distribution is used to throw parameter proposals from. This reduces Equation 4.4 to

$$\alpha(\vec{x}_i, \vec{y}_{i+1}) = \min \left(1, \frac{P(\vec{y}_{i+1}|D)}{P(\vec{x}_i|D)} \right). \quad (4.5)$$

After calculating this quantity, a random number, β , is generated uniformly between 0 and 1. If $\beta \leq \alpha(\vec{x}_i, \vec{y}_{i+1})$, the proposed step is accepted. Otherwise, the chain sets the next step equal to the current step and this procedure is repeated. This can be interpreted as if the posterior probability of the proposed step is greater than that of the current step, ($P(\vec{y}_{i+1}|D) \geq P(\vec{x}_i|D)$), the proposed step will always be accepted. If the opposite is true, ($P(\vec{y}_{i+1}|D) \leq P(\vec{x}_i|D)$), the proposed step will be accepted with probability $P(\vec{x}_i|D)/P(\vec{y}_{i+1}|D)$. This ensures that the Markov chain does not get trapped in any local minima in the potentially non-Gaussian posterior distribution. The outcome of this technique is that the density of steps taken in a discrete region is directly proportional to the probability density in that region.

¹⁰⁹³ 4.2.3. MCMC Optimisation

¹⁰⁹⁴ As discussed in subsection 4.2.2, the proposal function invoked within the MH algo-
¹⁰⁹⁵ rithm can take any form and the chain will still converge to the stationary distribution.
¹⁰⁹⁶ At each set of proposed parameter values, a prediction of the same spectra has to be
¹⁰⁹⁷ generated which requires significant computational resources. Therefore, the number
¹⁰⁹⁸ of steps taken before the unique stationary distribution is found should be minimised
¹⁰⁹⁹ as only steps after convergence add information to the oscillation analysis. Further-
¹¹⁰⁰ more, the chain should entirely cover the allowable parameter space to ensure that all
¹¹⁰¹ values have been considered. Tuning the distance that the proposal function jumps
¹¹⁰² between steps on a parameter-by-parameter basis can both minimise the length of the
¹¹⁰³ burn-in period and ensure that the correlation between step \vec{x}_i and \vec{x}_j is sufficiently
¹¹⁰⁴ small.

¹¹⁰⁵ The effect of changing the width of the proposal function is highlighted in Figure 4.3.
¹¹⁰⁶ Three scenarios, each with the same underlying stationary distribution (A Gaussian of
¹¹⁰⁷ width 1.0 and mean 0.), are presented. The only difference between the three scenarios
¹¹⁰⁸ is the width of the proposal function, colloquially known as the ‘step size σ ’. Each
¹¹⁰⁹ scenario starts at an initial parameter value of 10.0 which would be considered an
¹¹¹⁰ extreme variation. For the case where $\sigma = 0.1$, it is clear to see that the chain takes
¹¹¹¹ a long time to reach the expected region of the parameter. This indicates that this
¹¹¹² chain would have a large burn-in period and does not converge to the stationary
¹¹¹³ distribution until step ~ 500 . Furthermore, whilst the chain does move towards the
¹¹¹⁴ expected region, each step is significantly correlated with the previous. Considering
¹¹¹⁵ the case where $\sigma = 5.0$, the chain approaches the expected parameter region almost
¹¹¹⁶ instantly meaning that the burn-in period is not significant. However, there are clearly
¹¹¹⁷ large regions of steps where the chain does not move. This is likely due to the chain
¹¹¹⁸ proposing steps in the tails of the distribution which have a low probability of being

accepted. Consequently, this chain would take a significant number of steps to fully span the allowable parameter region. For the final scenario, where $\sigma = 0.5$, you can see a relatively small burn-in period of approximately 100 steps. Once the chain reaches the stationary distribution, it moves throughout the expected region of parameter values many times, sufficiently sampling the full parameter region. This example is a single parameter varying across a continuous distribution and does not fully reflect the difficulties in the many-hundred multi-variate parameter distribution used within this analysis. However, it does give a conceptual idea of the importance of selecting the proposal function and associated step size.

As discussed, step size tuning directly correlates to the average step acceptance rate. If the step size is too small, many steps will be accepted but the chain moves slowly. If the opposite is true, many steps will be rejected as the chain proposes steps in the tails of the distribution. Discussion in [138] suggests that the ‘ideal’ acceptance rate of a high dimension MCMC chain should be approximately $\sim 25\%$. An “ideal” step size [138] of

$$\sigma = \frac{2.4}{N_p}, \quad (4.6)$$

where N_p is the number of parameters included in the MCMC fit. However, the complex correlations between systematics mean that some parameters have to be hand tuned and many efforts have been taken to select a set of parameter-by-parameter step sizes to approximately reach the ideal acceptance rate.

Figure 4.3 highlights the likelihood as calculated by the fit in [DB: Link to AsimovA Sensitivity Section](#) as a function of the number of steps in each chain. In practice, many independent MCMC chains are run simultaneously to parallelise the task of

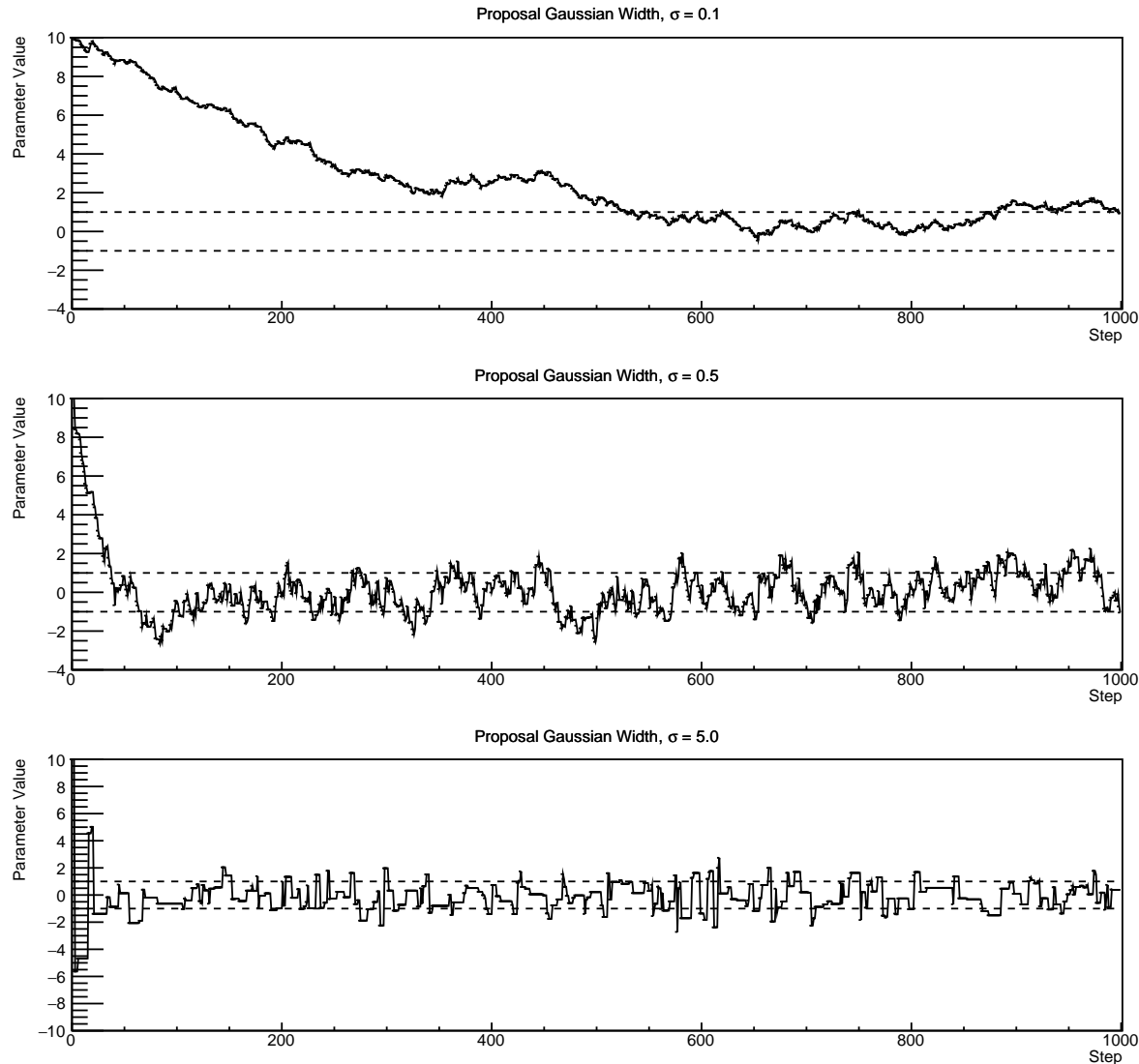


Figure 4.3.: Three MCMC chains, each with a stationary distribution equal to a Gaussian centered at 0 and width 1 (As indicated by the black dotted lines). All of the chains use a Gaussian proposal function but have different widths (or ‘step size σ ’). The top panel has $\sigma = 0.1$, middle panel has $\sigma = 0.5$ and the bottom panel has $\sigma = 5.0$.

₁₁₄₁ performing the fit. This figure overlays the distribution found in each chain. As seen,
₁₁₄₂ the likelihood decreases from its initial value and converges towards a stationary
₁₁₄₃ distribution after $\sim 1 \times 10^5$ steps.

₁₁₄₄ Multiple configurations of this analysis have been performed throughout this thesis
₁₁₄₅ where different samples or systematics have been used. For all of these configurations,
₁₁₄₆ it was found that a burnin period of 1×10^5 was sufficient in all cases.

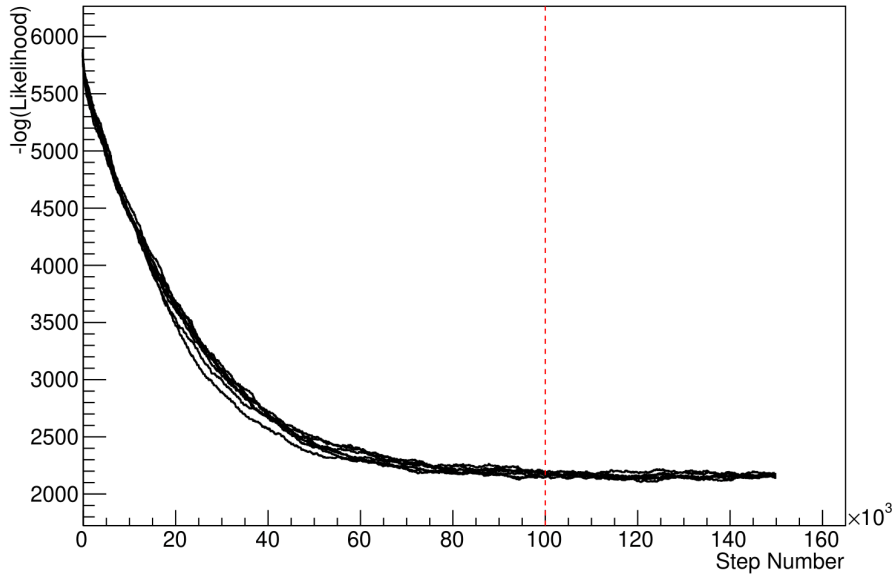


Figure 4.4.: The log-likelihood from the fit detailed in DB: Link to AsimovA Sensitivity Section as a function of the number of steps accumulated in each fit. Many independent MCMC chains were run in parallel and overlaid on this plot. The red line indicates the 1×10^5 step burn-in period after which the log-likelihood becomes stable.

¹¹⁴⁷ 4.3. Understanding the MCMC Results

¹¹⁴⁸ The previous sections have described how to generate the posterior probability distri-
¹¹⁴⁹ bution using Bayesian MCMC techniques. However, this analysis focuses on oscillation
¹¹⁵⁰ parameter determination. The posterior distribution output from the chain is a high
¹¹⁵¹ dimension object, with as many dimensions as there are parameters included in the os-
¹¹⁵² cillation analysis. However, this multi-dimensional object is difficult to conceptualize
¹¹⁵³ so parameter estimations are often presented in one or two-dimensional projections
¹¹⁵⁴ of this probability distribution. To do this, we invoke the marginalisation technique
¹¹⁵⁵ highlighted in subsection 4.3.1.

¹¹⁵⁶ 4.3.1. Marginalisation

¹¹⁵⁷ The output of the MCMC chain is a highly dimensional probability distribution
¹¹⁵⁸ which is very difficult to interpret. From the standpoint of an oscillation analysis
¹¹⁵⁹ experiment, the one or two-dimensional ‘projections’ of the oscillation parameters of
¹¹⁶⁰ interest are most relevant. Despite this, the best fit values and uncertainties on the
¹¹⁶¹ oscillation parameters of interest should correctly encapsulate the correlations to the
¹¹⁶² other systematic uncertainties (colloquially called ‘nuisance’ parameters). For this joint
¹¹⁶³ beam and atmospheric analysis, the oscillation parameters of interest are $\sin^2(\theta_{23})$,
¹¹⁶⁴ $\sin^2(\theta_{13})$, Δm_{23}^2 , and δ_{CP} . All other parameters (Including the oscillation parameter
¹¹⁶⁵ this fit is insensitive to) are deemed nuisance parameters. To generate these projections,
¹¹⁶⁶ we rely upon integrating the posterior distribution over all nuisance parameters. This
¹¹⁶⁷ is called marginalisation. A simple example of this technique is to imagine the scenario
¹¹⁶⁸ where two coins are flipped. To determine the probability that the first coin returned
¹¹⁶⁹ a ‘head’, the exact result of the second coin flip is disregarded and simply integrated
¹¹⁷⁰ over. For the parameters of interest, $\vec{\theta}_i$, we can calculate the marginalised posterior by
¹¹⁷¹ integrating over the nuisance parameters, $\vec{\theta}_n$. In this case, Equation 4.2 becomes

$$P(\vec{\theta}_i|D) = \frac{\int P(D|\vec{\theta}_i, \vec{\theta}_n)P(\vec{\theta}_i, \vec{\theta}_n)d\vec{\theta}_n}{\int P(D|\vec{\theta})P(\vec{\theta})d\vec{\theta}} \quad (4.7)$$

¹¹⁷² Where $P(\vec{\theta}_i, \vec{\theta}_n)$ encodes the prior knowledge about the uncertainty and correlations
¹¹⁷³ between the parameters of interest and the nuisance parameters. In practice, this
¹¹⁷⁴ is simply taking the one or two-dimensional projection of the multi-dimensional
¹¹⁷⁵ probability distribution.

Whilst in principle an easy solution to a complex problem, correlations between the interesting and nuisance parameters can bias the marginalised results. A similar effect is found when the parameters being marginalised over have non-Gaussian probability distributions. For example, Figure 4.5 highlights the marginalisation bias in the probability distribution found for a parameter when requiring a correlated parameter to have a positive parameter value. Due to the complex nature of this oscillation parameter fit presented in this thesis, there are correlations occurring between the oscillation parameters of interest and the other nuisance parameters included in the fit.

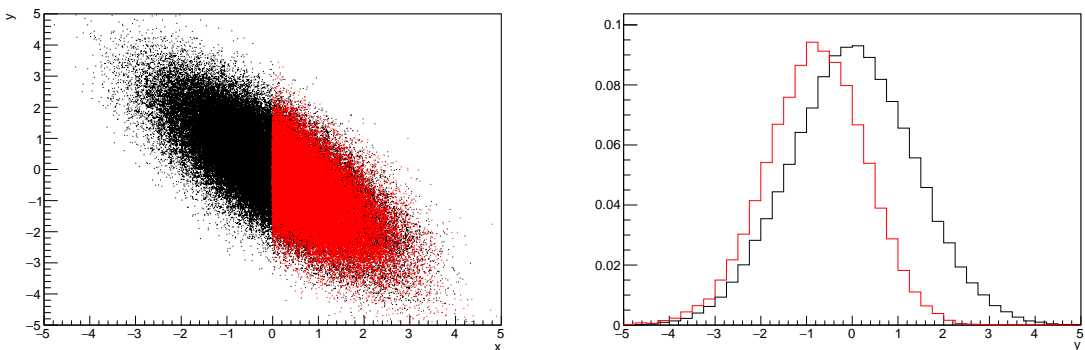


Figure 4.5.: Left: The two dimensional probability distribution for two correlated parameters x and y . The red distribution shows the two dimensional probability distribution when $0 \leq x \leq 5$. Right: The marginalised probability distribution for the y parameter found when requiring the x to be bound between $-5 \leq x \leq 5$ and $0 \leq x \leq 5$ for the black and red distribution, respectively.

4.3.2. Parameter Estimation and Credible Intervals

The purpose of this analysis is to determine the best fit values for the oscillation parameters that the beam and atmospheric samples are sensitive to: $\sin^2(\theta_{23})$, $\sin^2(\theta_{13})$, Δm_{23}^2 , and δ_{CP} . Typically, the results presented take the form of one or two-dimension marginalised probability distributions for the appearance ($\sin^2(\theta_{13})$ and δ_{CP}) and disappearance ($\sin^2(\theta_{23})$ and Δm_{23}^2) parameters. The posterior probability density

₁₁₉₁ taken from the output MCMC chain is binned in these parameters. The parameter
₁₁₉₂ best-fit point is then taken to be the value that has the highest posterior probability.
₁₁₉₃ This is performed in both one and two-dimensional projections.

₁₁₉₄ However, the single best-fit point in a given parameter is not of much use on its
₁₁₉₅ own. We would also like to determine the uncertainty, or credible interval, on that
₁₁₉₆ best-fit point. The definition of the 1σ credible interval is that we have 68% belief that
₁₁₉₇ the parameter is within those bounds. For a more generalised definition, the credible
₁₁₉₈ interval is the region, R , of the posterior distribution that contains a specific fraction of
₁₁₉₉ the total probability, such that

$$\int_R P(\theta|D)d\theta = \alpha \quad (4.8)$$

₁₂₀₀ Where θ is the parameter on which we calculate the credible interval. This technique
₁₂₀₁ then calculates the $\alpha \times 100\%$ credible interval.

₁₂₀₂ In practice, this analysis uses the highest posterior density (HPD) credible intervals
₁₂₀₃ which are calculated through the following method. First, the probability distribution
₁₂₀₄ is area-normalised such that it has an integrated area equal to 1.0. The bins of proba-
₁₂₀₅ bility are then summed from the highest to lowest until the sum exceeds the 1σ level
₁₂₀₆ (0.68 in this example). This process is repeated for a range of credible intervals, notably
₁₂₀₇ the 1σ , 2σ and 3σ along with other levels where the critical values for each level can
₁₂₀₈ be found in [139]. This process can be repeated for the two-dimensional probability
₁₂₀₉ distributions by creating two-dimensional contours of credible intervals rather than a
₁₂₁₀ one-dimensional result.

1211 4.3.3. Bayesian Model Comparisons

1212 Due to the matter resonance, this analysis has some sensitivity to the mass hierarchy
 1213 of neutrino states (whether Δm_{23}^2 is positive or negative) and the octant of $\sin^2(\theta_{23})$
 1214 . The Bayesian approach utilised within this analysis gives an intuitive method of
 1215 model comparison by determining which hypothesis is most favourable. Taking the
 1216 ratio of Equation 4.3 for the two hypotheses of normal hierarchy, NH , and inverted
 1217 hierarchy, IH , gives

$$\frac{P(\vec{\theta}_{NH}|D)}{P(\vec{\theta}_{IH}|D)} = \frac{P(D|\vec{\theta}_{NH})}{P(D|\vec{\theta}_{IH})} \times \frac{P(\vec{\theta}_{NH})}{P(\vec{\theta}_{IH})}. \quad (4.9)$$

1218 The middle term defines the Bayes factor which is a data-driven interpretation of
 1219 how strong the data prefers one hierarchy to the other. For this analysis, equal priors
 1220 on both mass hierarchy hypotheses are chosen ($P(\vec{\theta}_{NH}) = P(\vec{\theta}_{IH}) = 0.5$). In practice,
 1221 the MCMC chain proposes a value of $|\Delta m_{23}^2|$ and then applies a 50% probability
 1222 that the value is sign flipped. Consequently, the Bayes factor can be calculated from
 1223 the ratio of the probability density in either hypothesis. This equates to counting the
 1224 number of steps taken in the normal and inverted hierarchies and taking the ratio. The
 1225 same approach can be taken to compare the upper octant (UO) compared to the lower
 1226 octant (LO) hypothesis of $\sin^2(\theta_{23})$.

1227 Whilst the value of the Bayes factor should always be shown, the Jeffreys scale [140]
 1228 (highlighted in Table 4.1) gives an indication of the strength of preference for one model
 1229 compared to the other. Other interpretations of the strength of preference of a model
 1230 exist, e.g. the Kass and Raferty Scale [141].

$\log_{10}(B_{AB})$	B_{AB}	Strength of Preference
< 0.0	< 1	No preference for hypothesis A (Supports hypothesis B)
0.0 – 0.5	1.0 – 3.16	Preference for hypothesis A is weak
0.5 – 1.0	3.16 – 10.0	Preference for hypothesis A is substantial
1.0 – 1.5	10.0 – 31.6	Preference for hypothesis A is strong
1.5 – 2.0	31.6 – 100.0	Preference for hypothesis A is very strong
> 2.0	> 100.0	Decisive preference for hypothesis A

Table 4.1.: Jeffreys scale for strength of preference for two models A and B as a function of the calculated Bayes factor ($B_{AB} = B(A/B)$) between the two models [140]. The original scale is given in terms of $\log_{10}(B(A/B))$ but converted to linear scale for easy comparison throughout this thesis.

1231 4.3.4. Comparison of MCMC Output to Expectation

1232 To ensure the fit is performing well, a best-fit spectrum is produced using the pos-
1233 terior probability distribution and compared with the data, allowing easy by-eye
1234 comparisons to be made. A simple method of doing this is to perform a comparison
1235 in the fitting parameters (For instance, the reconstructed neutrino energy and lepton
1236 direction for T2K far detector beam samples) of the spectra generated by the MCMC
1237 chain to ‘data’. This ‘data’ could be true data or some variation of Monte Carlo predic-
1238 tion. This allows easy comparison of the MCMC probability distribution to the data.
1239 To perform this, N steps from the post burn-in MCMC chain are randomly selected
1240 (Where for all plots of this style in this thesis, $N = 3000$). From these, the Monte Carlo
1241 prediction at each step is generated by reweighting the model parameters to the values
1242 specified at that step. Due to the probability density being directly correlated with
1243 the density of steps in a certain region, parameter values close to the best fit value are
1244 most likely to be selected.

1245 In practice, for each bin of the fitting parameters has a probability distribution
1246 of event rates, with one entry per sampled MCMC step. This distribution is binned
1247 where the bin with the highest probability is selected as the mean and an error on

1248 the width of this probability distribution is calculated using the approach highlighted
1249 in subsection 4.3.2. Consequently, the best fit distribution in the fit parameter is not
1250 necessarily that which would be attained by reweighting the Monte Carlo prediction
1251 to the most probable parameter values.

1252 A similar study can be performed to illustrate the freedom of the model parameter
1253 space prior to the fit. This can be done by throwing parameter values from the prior
1254 uncertainty of each parameter. This becomes troublesome for parameters with no
1255 prior uncertainty as the range is technically infinite. Where applicable solutions to
1256 remove these have been addressed.

1257 **Chapter 5**

1258 **Simulation, Reconstruction, and Event
Reduction**

1260 As a crucial part of the oscillation analysis, an accurate prediction of the expected
1261 neutrino spectrum at the far detector is required. This includes modeling the flux
1262 generation, neutrino interactions, and detector effects. All of the simulation packages
1263 required to do this are briefly described in section 5.1. The reconstruction of neutrino
1264 events inside the far detector, including the `fitQun` algorithm, is documented in
1265 section 5.2. This also includes data quality checks of the SK-V data which the author
1266 performed for the T2K oscillation analysis presented at Neutrino 2020 [80]. Finally,
1267 section 5.3 describes the steps taken in the SK detector to trigger on events of interest
1268 whilst removing the comparatively large rate of cosmic ray muon events.

1269 **5.1. Simulation**

1270 In order to generate a Monte Carlo prediction of the expected event rate at the far
1271 detector, all the processes in the beam and atmospheric flux, neutrino interaction, and
1272 detector need to be modeled. Each of these parts is individually modeled and each of
1273 them is detailed below.

1274 The beamline simulation consists of three distinct parts: the initial hadron inter-
1275 action modeled by FLUKA [142], the target station geometry and particle tracking

1276 performed by JNUBEAM, [143, 144] and any hadronic re-interactions simulated by
 1277 GCALOR [145]. The primary hadronic interactions are $O(10)\text{GeV}$, where FLUKA
 1278 matches external cross-section data better than GCALOR [146]. However, FLUKA
 1279 is not very adaptable so a small simulation is built to model the interactions in the
 1280 target and the output is then passed to JNUBEAM and GCALOR for propagation.
 1281 The hadronic interactions are tuned to data from the NA61/SHINE [147–149] and
 1282 HARP [150] experiments. The tuning is done by reweighting the FLUKA and GCALOR
 1283 predictions to match the external data multiplicity and cross-section measurements,
 1284 based on final state particle kinematics [146]. The culmination of this simulation
 1285 package generates the predicted flux for neutrino and antineutrino beam modes which
 1286 are illustrated in Figure 3.7.

1287 The atmospheric neutrino flux is simulated by the HKKM model [43, 45]. The
 1288 primary cosmic ray flux is tuned to AMS [151] and BESS [152] data assuming the US-
 1289 standard atmosphere '76 [153] density profile and includes geomagnetic field effects.
 1290 The primary cosmic rays interact to generate pions and muons. The interaction of these
 1291 secondary particles to generate neutrinos is handled by DPMJET-III [154] for energies
 1292 above 32GeV and JAM [45, 155] for energies below that value **DB: Question for Giles:**
 1293 **Why different generators for above/below 32GeV?** These hadronic interactions are
 1294 tuned to BESS and L3 data [156, 157] using the same methodology as the tuning of the
 1295 beamline simulation. The energy and cosine zenith predictions of $\nu_e, \bar{\nu}_e, \nu_\mu, \bar{\nu}_\mu$ flux are
 1296 given in Figure 2.3 and Figure 2.5, respectively. The flux is approximately symmetrical
 1297 and peaked around the horizon ($\cos(\theta_Z) = 0.0$). This is because horizontally-going
 1298 pions and kaons can travel further than their vertically-going counterparts resulting in
 1299 a larger probability of decaying to neutrinos. The symmetry is broken in lower-energy
 1300 neutrinos due to geomagnetic effects, which modify the track of the primary cosmic
 1301 rays. Updates to the HKKM model are currently ongoing [158].

Once a flux prediction has been made for all three detectors, NEUT 5.4.0 [159, 160] models the interactions of the neutrinos in the detectors. For the purposes of this analysis, quasi-elastic (QE), meson exchange (MEC), single meson production (PROD), coherent pion production (COH), and deep inelastic scattering (DIS) interactions are simulated. These interaction categories can be further broken down by whether they were propagated via a W^\pm boson in Charged Current (CC) interactions or via a Z^0 boson in Neutral Current (NC) interactions. CC interactions have a charged lepton in the final state, which can be flavour-tagged in reconstruction to determine the flavour of the neutrino. In contrast, NC interactions have a neutrino in the final state so no flavour information can be determined from the observables left in the detector after an interaction. This is the reason why neutrinos which interact through NC modes are assumed to not oscillate within this analysis. Both CC and NC interactions are modeled for all the above interaction categories, other than MEC interactions which are only modeled for CC events.

As illustrated in Figure 5.1, CCQE interactions dominate the cross-section of neutrino interactions around $E_\nu \sim 0.5\text{GeV}$. The NEUT implementation adopts the Llewellyn Smith [161] model for neutrino-nucleus interactions, where the nuclear ground state of any bound nucleons (neutrino-oxygen interactions) is approximated by a spectral-function [162] model that simulates the effects of Fermi momentum and Pauli blocking. The cross-section of QE interactions is controlled by vector and axial-vector form factors parameterised by the BBBA05 [163] model and a dipole form factor with $M_A^{QE} = 1.21\text{GeV}$ fit to external data [164], respectively. NEUT implements the Valencia [165] model to simulate MEC events, where two nucleons and two holes in the nuclear target are produced (Often called 2p2h interactions).

For neutrinos of energy $O(1)\text{GeV}$, PROD interactions become dominant. These predominantly produce charged and neutral pions although γ , kaon, and η production

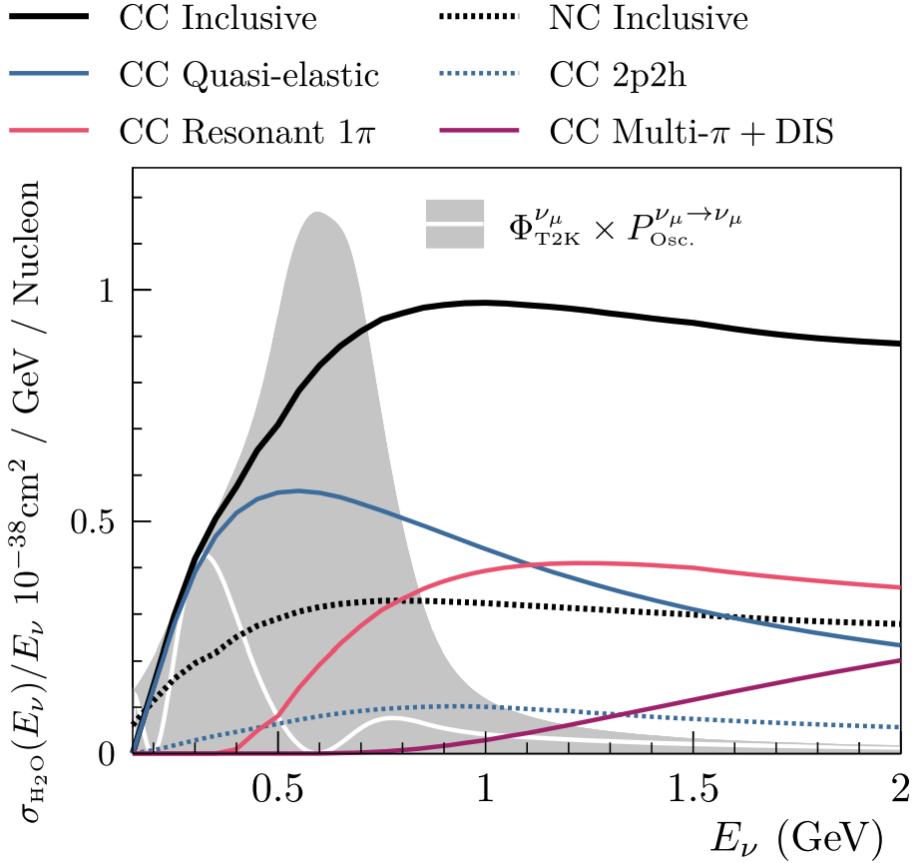


Figure 5.1.: The NEUT prediction of the ν_μ -H₂O cross-section overlaid on the T2K ν_μ flux. The charged current (black, solid) and neutral current (black, dashed) inclusive, charged current quasi-elastic (blue, solid), charged current 2p2h (blue, dashed), charged current single pion production (pink), and charged current multi- π and DIS (Purple) cross-sections are illustrated. Figure taken from [159].

is also considered. To simulate these interactions, the Berger-Sehgal [166] model is implemented within NEUT. It simulates the excitation of a nucleon from a neutrino interaction, production of an intermediate baryon, and the subsequent decay to a single meson or γ . Pions can also be produced through COH interactions, which occur when the incoming neutrino interacts with the entire oxygen nucleus leaving a single pion outside of the nucleus. NEUT utilises the Berger-Sehgal [167] model to simulate these COH interactions.

DIS and multi- π producing interactions become the most dominant for energies $> O(5)\text{GeV}$. PYTHIA [168] is used to simulate any interaction with invariant mass

₁₃₃₇ $W > 2\text{GeV}/c^2$, which produces at least one meson. For any interaction which produces
₁₃₃₈ at least two mesons but has $W < 2\text{GeV}/c^2$, the Bronner model is used [169]. Both
₁₃₃₉ of these models use parton distribution functions based on the Bodek-Yang model
₁₃₄₀ [170–172].

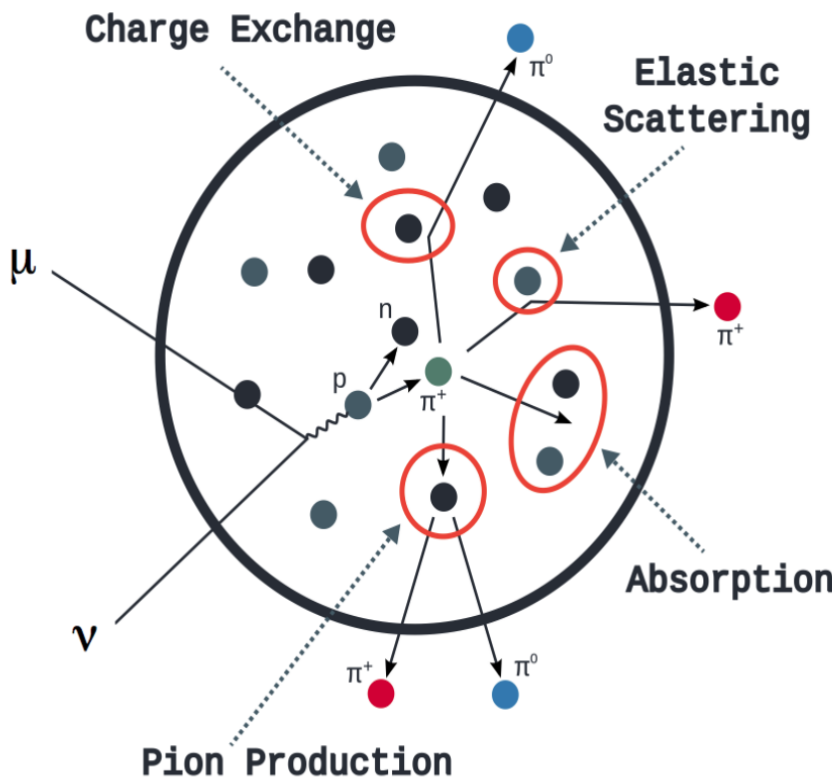


Figure 5.2.: Illustration of the various processes which a pion can undergo before exiting the nucleus. Taken from [173].

₁₃₄₁ Any pion which is produced within the nucleus can re-interact through final state
₁₃₄₂ interactions before it exits, as illustrated by the scattering, absorption, production, and
₁₃₄₃ exchange interactions in Figure 5.2. These re-interactions alter the observable particles
₁₃₄₄ within the detector. For instance, if the charged pion from a CC PROD interaction is
₁₃₄₅ absorbed, the observables would mimic a CC QE interaction. To simulate these effects,
₁₃₄₆ NEUT uses a semi-classical intranuclear cascade model [159]. This cascade functions by
₁₃₄₇ stepping the pion through the nucleus in fixed-length steps equivalent to $dx = R_N/100$,

1348 where R_N is the radius of the nucleus. At each step, the simulation allows the pion
1349 to interact through scattering, charged exchange, absorption, or production with an
1350 interaction-dependent probability calculated from a fit to external data [174]. This
1351 cascade continues until the pion is absorbed or exits the nucleus.

1352 Once the final state particle kinematics have been determined by NEUT, they are
1353 passed into the detector simulation. The near detectors, ND280 and INGRID, are
1354 simulated using a GEANT4 package [118,175] to simulate the detector geometry, particle
1355 tracking, and energy deposition. The response of the detectors is simulated using
1356 the elecSim package [118]. The far detector simulation is based upon the original
1357 Kamiokande experiment software which uses the GEANT3-based SKDETSIM [118,176]
1358 package. This simulates the interactions of particles in the water as well as Cherenkov
1359 light production. The water quality and PMT calibration measurements detailed in
1360 subsection 3.1.2 are also used within this simulation to make accurate predictions of
1361 the detector response.

1362 5.2. Event Reconstruction at SK

1363 Any event which generates optical photons that occurs in SK will be observed by the
1364 PMT array, where each PMT records the time and accumulated charge. This recorded
1365 information is shown in event displays similar to those illustrated in Figure 5.3. To
1366 be useful for physics analyses, this series of PMT hit information needs to be recon-
1367 structed to determine the particle's identity and kinematics (or track parameters):
1368 four-vertex, direction, and momenta. The reconstruction uses the fact that the charge
1369 and timing distribution of photons generated by a particular particle in an event is
1370 dependent upon its initial kinematics. Electron and muon rings are distinguished by
1371 their "fuzziness". Muons are heavier and less affected by scattering or showering

1372 meaning they typically produce “crisp” rings. Electrons are more likely to interact
1373 via electromagnetic showering or scattering which results in larger variations of their
1374 direction from the initial direction. Consequently, electrons typically produce “fuzzier”
1375 rings compared to muons.

1376 For the purposes of this analysis, the `fitQun` reconstruction algorithm is utilised.
1377 Its core function is to compare a prediction of the accumulated charged and timing
1378 distribution from each PMT, generated for a particular particle identity and track
1379 parameters, to that observed in the neutrino event. It determines the preferred values
1380 by minimising a likelihood function which includes information from PMTs which
1381 were hit and those that were not hit. `fitQun` performs a simultaneous fit of particle
1382 kinematics and identity, improving both the accuracy of the fit parameters and the
1383 rejection of neutral current π^0 events [177, 178]. The `fitQun` algorithm is based on
1384 the key concepts of the MiniBooNE reconstruction algorithm [179] and is described
1385 in [180] which is summarised below. The `fitQun` algorithm improves upon the APFit
1386 reconstruction algorithm which has been used for many previous SK analyses. APFit
1387 fits the vertex from timing information and then fits the momentum and direction
1388 of the particle from PMT hits within a 43 deg Cherenkov cone (which assumes an
1389 ultra-relativistic particle). It then fits the particle identity once the track parameters
1390 have been fit.

1391 The `fitQun` reconstruction algorithm proceeds by:

- 1392 • **Vertex pre-fitting:** An estimate of the vertex is made using a goodness-of-fit
1393 metric
- 1394 • **Peak finding:** The initial time of the event is determined by clustering events by
1395 time residuals

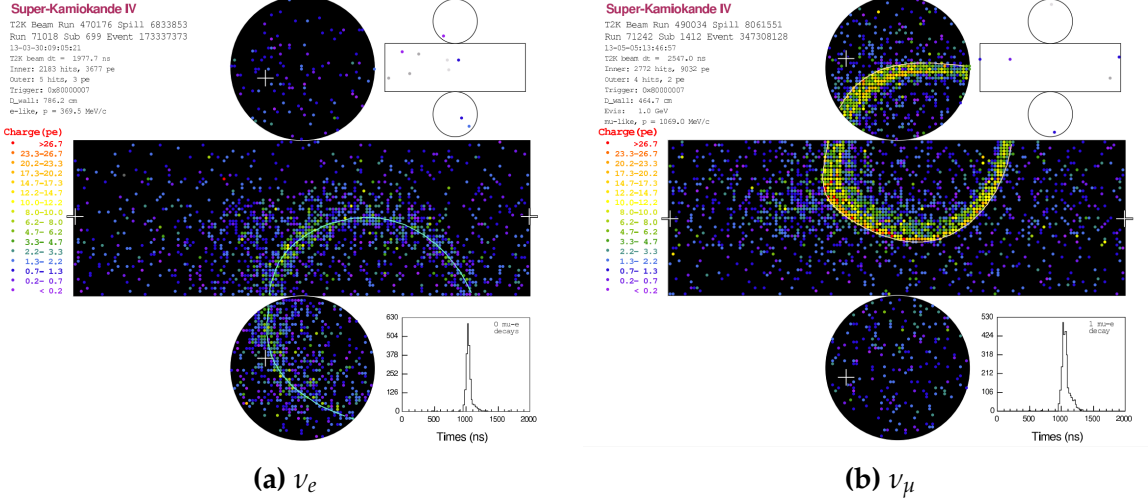


Figure 5.3.: Event displays from Super Kamiokande illustrating the “crisp” ring from a muon and the typically “fuzzy” electron ring. Each pixel represents a PMT and the color scheme denotes the accumulated charge deposited on that PMT. Figures taken from [181].

- **Single-ring fits:** Given the pre-fit vertex and estimated time of interaction, a maximum likelihood technique searches for a single particle generating light
- **Multi-ring fits:** Seeded from the single-ring fits, hypotheses with multiple light-producing particles are considered using the same maximum likelihood technique

An event in SK can consist of a primary and decay particles. For example, a charged current muon neutrino interaction can generate two particles that have the potential of generating Cherenkov photons: the primary muon, and the secondary decay-electron from the muon. To ensure the particles are reconstructed separately, each event is divided into time clusters which are called “subevents”. Subevents after the primary subevent are considered to be decay electrons. To find all the subevents in an event, a vertex goodness metric is calculated for some vertex position \vec{x} and time t ,

$$G(\vec{x}, t) = \sum_i^{\text{hit PMTs}} \exp \left(-\frac{1}{2} \left(\frac{T_{\text{Res}}^i(\vec{x}, t)}{\sigma} \right)^2 \right) \quad (5.1)$$

1407 where

$$T_{Res}^i(\vec{x}, t) = t^i - t - |R_{PMT}^i - \vec{x}| / c_n \quad (5.2)$$

1408 is the residual hit time. It is the difference in time between the PMT hit time, t^i ,
1409 of the i^{th} PMT and the expected time of the PMT hit if the photon was emitted at
1410 the start of the vertex. R_{PMT}^i is the position of the i^{th} PMT, c_n is the speed of light in
1411 water and $\sigma = 4\text{ns}$ which is comparable to the time resolution of the PMT. When the
1412 proposed fit values of time and vertex are close to the true values, $T_{Res}^i(\vec{x}, t)$ tends to
1413 zero resulting in subevents appearing as spikes in the goodness metric. The proposed
1414 fit vertex and time are grid-scanned, and the values which maximise the goodness
1415 metric are selected as the “pre-fit vertex”. Whilst this predicts a vertex for use in
1416 the clustering algorithm, the final vertex is fit using the higher-precision maximum
1417 likelihood method described below.

1418 Once the pre-fit vertex has been determined, the goodness metric is scanned as
1419 a function of t to determine the number of subevents. A peak-finding algorithm is
1420 then used on the goodness metric, requiring the goodness metric to exceed some
1421 threshold and drop below a reduced threshold before any subsequent additional
1422 peaks are considered. The thresholds are set such that the rate of false peak finding
1423 is minimised while still attaining good data to Monte Carlo agreement. To improve
1424 performance, the pre-fit vertex for each delayed subevent is re-calculated after PMT
1425 hits from the previous subevent are masked. This improves the decay-electron tagging
1426 performance. Once all subevents have been determined, the time window around
1427 each subevent is then defined by the earliest and latest time which satisfies $-180 <$

¹⁴²⁸ $T_{Res}^i < 800\text{ns}$. The subevents and associated time windows are then used as seeds for
¹⁴²⁹ further reconstruction.

¹⁴³⁰ For a given subevent, the `fitQun` algorithm constructs a likelihood based on the
¹⁴³¹ accumulated charge q_i and time information t_i from the i^{th} PMT,

$$L(\Gamma, \vec{\theta}) = \prod_j^{\text{unhit}} P_j(\text{unhit}|\Gamma, \vec{\theta}) \prod_i^{\text{hit}} \{1 - P_i(\text{unhit}|\Gamma, \vec{\theta})\} f_q(q_i|\Gamma, \vec{\theta}) f_t(t_i|\Gamma, \vec{\theta}), \quad (5.3)$$

¹⁴³² where $\vec{\theta}$ defines the track parameters; vertex position, direction vector and mo-
¹⁴³³ ments, and Γ represents the particle hypothesis. $P_i(\text{unhit}|\Gamma, \vec{\theta})$ is the probability of the
¹⁴³⁴ i^{th} tube to not register a hit given the track parameters and particle hypothesis. The
¹⁴³⁵ charge likelihood, $f_q(q_i|\Gamma, \vec{\theta})$, and time likelihood, $f_t(t_i|\Gamma, \vec{\theta})$, represents the probability
¹⁴³⁶ density function of observing charge q_i and time t_i on the i^{th} PMT given the specified
¹⁴³⁷ track parameters and particle hypothesis.

¹⁴³⁸ The predicted charge is calculated based on contributions from both the direct
¹⁴³⁹ light and the scattered light. The direct light contribution is determined based on the
¹⁴⁴⁰ integration of the Cherenkov photon profile along the track. PMT angular acceptance,
¹⁴⁴¹ water quality, and calibration measurements discussed in subsection 3.1.2 are included
¹⁴⁴² to accurately predict the charge probability density at each PMT. The scattered light
¹⁴⁴³ is calculated in a similar way, although it includes a scattering function that depends
¹⁴⁴⁴ on the vertex of the particle and the position of the PMT. The charge likelihood is
¹⁴⁴⁵ calculated by comparing the prediction to the observed charge in the PMT.

¹⁴⁴⁶ The time likelihood is approximated to depend on the vertex \vec{x} , direction \vec{d} , and
¹⁴⁴⁷ time t of the track as well as the particle hypothesis. The expected time for PMT hits is

₁₄₄₈ calculated by assuming unscattered photons being emitted from the midpoint of the
₁₄₄₉ track, S_{mid} ,

$$t_{exp}^i = t + S_{mid}/c + |R_{PMT}^i - \vec{x} - S_{mid}\vec{d}|/c_n, \quad (5.4)$$

₁₄₅₀ where c is the speed of light in a vacuum. The time likelihood is then expressed in
₁₄₅₁ terms of the residual difference between the PMT hit time and the expected hit time,
₁₄₅₂ $t_{Res}^i = t^i - t_{exp}^i$. The particle hypothesis and momentum also affect the Cherenkov
₁₄₅₃ photon distribution. These parameters modify the shape of the time likelihood density
₁₄₅₄ since in reality not all photons are emitted at the midpoint of the track. As with the
₁₄₅₅ charge likelihood, the contributions from both the direct and scattered light to the time
₁₄₅₆ likelihood density are calculated separately, which are both calculated from particle
₁₄₅₇ gun studies.

₁₄₅₈ The track parameters and particle identity which maximise $L(\Gamma, \vec{\theta})$ are defined as
₁₄₅₉ the best-fit parameters. In practice MINUIT [182] is used to minimise the value of
₁₄₆₀ $-\ln L(\Gamma, \vec{\theta})$. The `fitQun` algorithm considers an electron-like, muon-like, and charged
₁₄₆₁ pion-like hypothesis for events with a single final state particle, denoted “single-ring
₁₄₆₂ events”. The particle’s identity is determined by taking the ratio of the likelihood
₁₄₆₃ of each of the hypotheses. For instance, electrons and muons are distinguished by
₁₄₆₄ considering the value of $\ln(L(e, \vec{\theta}_e)/L(\mu, \vec{\theta}_\mu))$ in comparison to the reconstructed
₁₄₆₅ momentum of the electron hypothesis, as illustrated by Figure 5.4. The coefficients of
₁₄₆₆ the discriminator between electron-like and muon-like events are determined from
₁₄₆₇ Monte Carlo studies [180]. Similar distributions exist for distinguishing electron-like
₁₄₆₈ events from π^0 -like events, and muon-like events from pion-like events. The cuts are
₁₄₆₉ defined as,

$$\text{Electron/Muon} : \ln(L_e/L_\mu) > 0.2 \times p_e^{rec} [\text{MeV}],$$

$$\text{Electron}/\pi^0 : \ln(L_e/L_{\pi^0}) < 175 - 0.875 \times m_{\gamma\gamma} [\text{MeV}], \quad (5.5)$$

$$\text{Muon/Pion} : \ln(L_\mu/L_{\pi^\pm}) < 0.15 \times p_\mu^{rec} [\text{MeV}],$$

as taken from [183], where p_e^{rec} and p_μ^{rec} are the reconstructed momentum of the single-ring electron and muon fits, respectively. $m_{\gamma\gamma}$ represents the reconstructed invariant mass of the two photons emitted from π^0 decay. Typically, the distance between a particular entry in these two-dimensional distributions and the cut-line is termed the PID parameter and is illustrated in Figure 5.5.

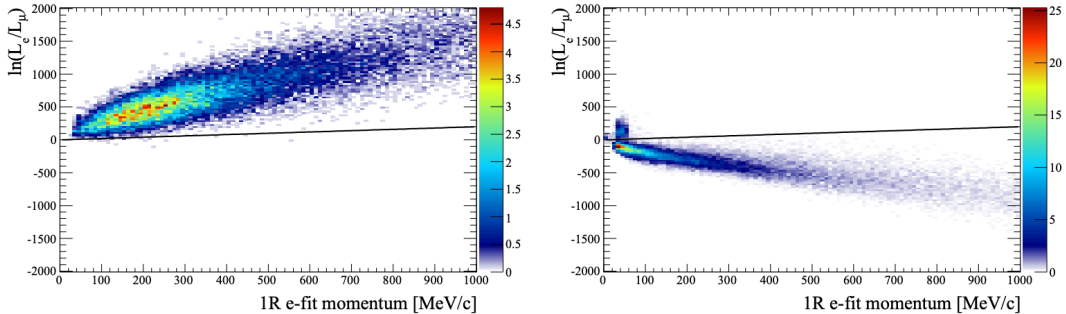


Figure 5.4.: The difference of the electron-like and muon-like log-likelihood compared to the reconstructed single-ring fit momentum for atmospheric ν_e (left) and ν_μ (right) samples. The black line represents the cut used to discriminate electron-like and muon-like events, which coefficients obtained from Monte Carlo studies. Figures taken from [180].

The `fitQun` algorithm also considers a π^0 hypothesis. To do this, it performs a fit looking for two standard electron-hypothesis tracks which point to the same four-vertex. This assumes the electron tracks are generated from photon-conversion so the electron tracks actually appear offset from the proposed π^0 vertex. For these fits, the conversion length, direction, and momentum of each photon are also considered as track parameters which are then fit in the same methodology as the standard single-ring hypotheses.

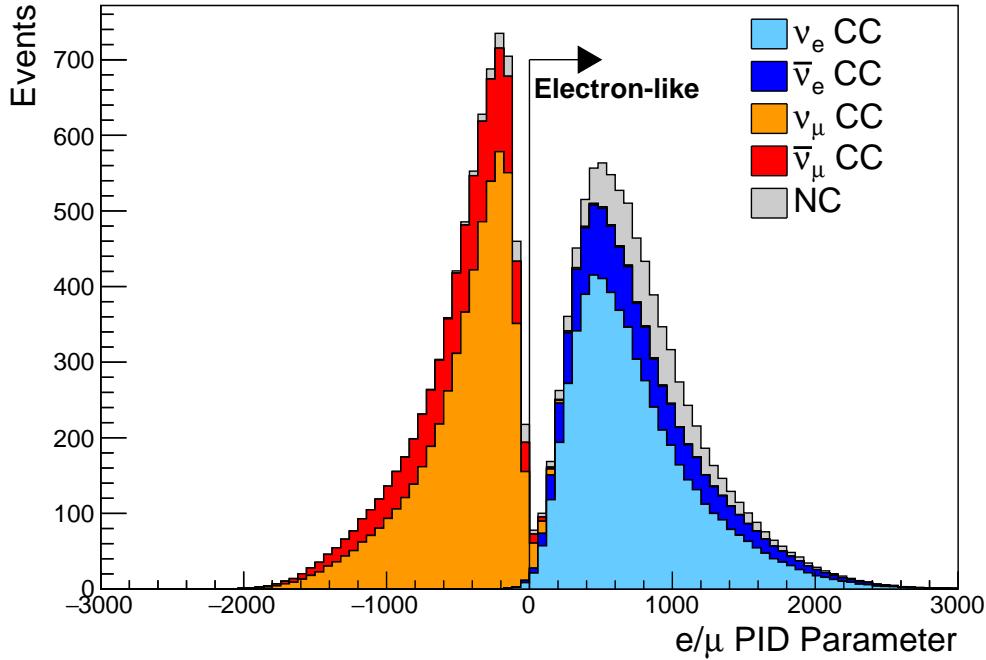


Figure 5.5.: The electron/muon PID separation parameter for all sub-GeV single-ring events in SK-IV. The charged current (CC) component is broken down in four flavours of neutrino (ν_μ , $\bar{\nu}_\mu$, ν_e and $\bar{\nu}_e$). Events with positive values of the parameter are determined to be electron-like.

Whilst lower energy events are predominantly single-ring events, higher energy neutrino events can generate final states with multiple particles which generate Cherenkov photons. These “multi-ring” hypotheses are also considered in the `fitQun` algorithm. When calculating the charge likelihood density, the predicted charge associated with each ring is calculated separately and then summed to calculate the total accumulated charge on each PMT. Similarly, the time likelihood for the multi-ring hypothesis is calculated assuming each ring is independent. Each track is time-ordered based on the time of flight from the center of the track to the PMT and the direct light from any ring incident on the PMT is assumed to arrive before any scattered light. To reduce computational resource usage, the multi-ring fits only consider electron-like and charged pion-like rings as the pion fit can be used as a proxy for a muon fit due to their similar mass.

1494 Multi-ring fits proceed by proposing another ring to the previous fit and then
1495 fitting the parameters in the method described above. Typically, multi-ring fits have
1496 the largest likelihood because of the additional degrees of freedom introduced. A
1497 likelihood value is calculated for the n -ring and $(n + 1)$ -ring hypotheses, where the
1498 additional ring is only included if the likelihood value is above 9.35, based on Monte
1499 Carlo studies in [184].

1500 **5.2.1. Validation of Reconstruction in SK-V**

1501 As an example of how the reconstruction depends on the detector conditions, the
1502 author of this thesis assessed the quality of event reconstruction for SK-V data. The
1503 detector systematics used in the T2K-only oscillation analysis are determined using
1504 data-to-Monte Carlo comparisons of the SK-IV data [185]. Due to tank-open mainte-
1505 nance occurring between SK-IV and SK-V, the dark rate of each PMT was observed to
1506 increase in SK-V due to light exposure for a significant time during the repairs. This
1507 increase can be seen in Figure 5.6. Run-10 of the T2K experiment was conducted in
1508 the SK-V period, so the consistency of SK-IV and SK-V data needs to be studied to
1509 determine whether the SK-IV-defined systematics can be applied to the run-10 data.
1510 This comparison study was performed using the stopping muon data set for both the
1511 SK-IV and SK-V periods. This data sample is used due to the high rate of interactions
1512 ($O(200)$ events per hour) as well as having similar energies to muons from CCQE
1513 ν_μ interactions from beam interactions. The rate of cosmic muons does depend on
1514 the solar activity cycle [186] but has been neglected in this comparison study. This
1515 is because the shape of the distributions is most important for the purposes of being
1516 compared to the detector systematics. The SK-IV and SK-V data samples consist of
1517 2398.42 and 626.719 hours of data which equates to 686k and 192k events respectively.

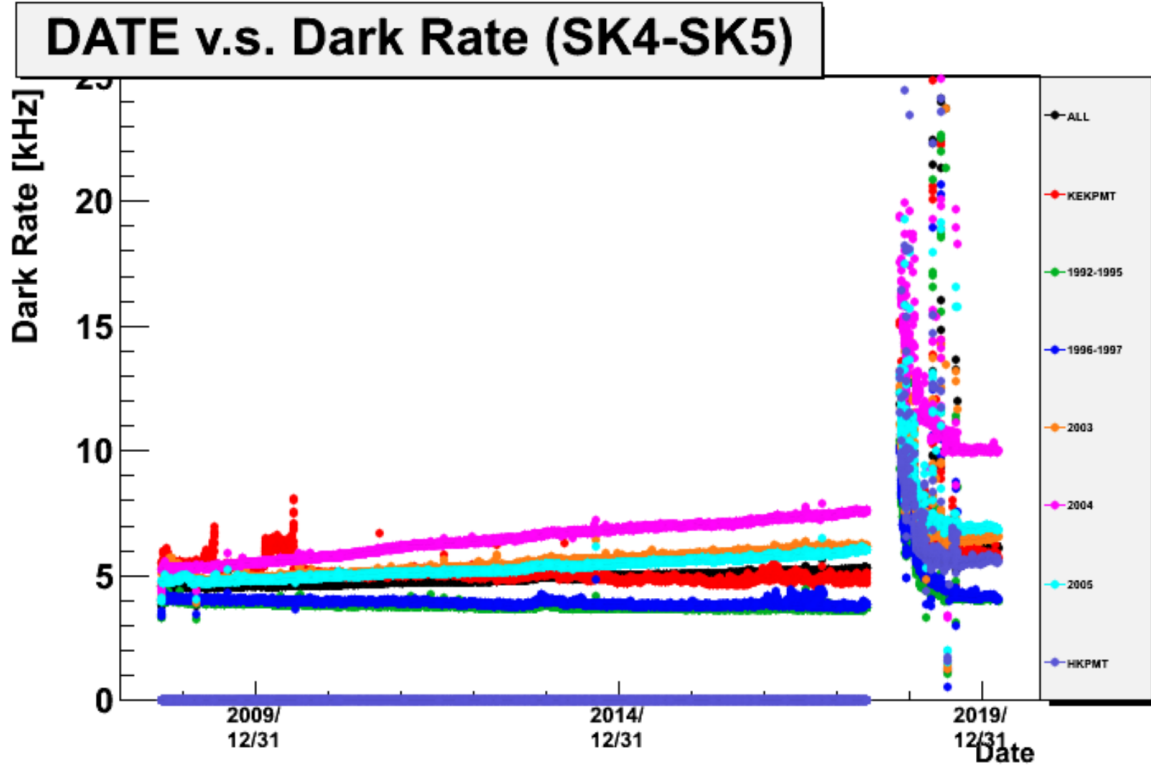


Figure 5.6.: The variation of the measured dark rate as a function of date, broken down by PMT type. The SK-IV and SK-V periods span September 2008 to May 2018 and January 2019 to July 2020, respectively. The break in measurement in 2018 corresponds to the period of tank repair and refurbishment. Figure adapted from [185].

1518 The predicted charge calculated in the `fitQun` algorithm includes a contribution
 1519 from the photoelectron emission due to dark noise. Therefore, the increase in the
 1520 SK-V dark rate needs to be accounted for. In practice, the average dark rate in each
 1521 SK period is calculated and used as an input in the reconstruction. This is calculated
 1522 by averaging the dark rate per run for each period separately, using the calibration
 1523 measurements detailed in subsection 3.1.2. The average dark rate from SK-IV and
 1524 SK-V were found to be 4.57kHz and 6.30kHz, respectively. The charges associated with
 1525 the muon and decay electron subevents are illustrated in Figure 5.7. The photoelectron
 1526 emission from dark noise is more significant for events that have lower energy. This is
 1527 because this contribution becomes more comparable to the number of photoelectrons
 1528 emitted from incident photons in lower-energy events. This behaviour is observed

in the data, where the charge deposited by the muon subevent is mostly unaffected by the increase in dark rate, whilst the charge associated with the decay-electron is clearly affected.

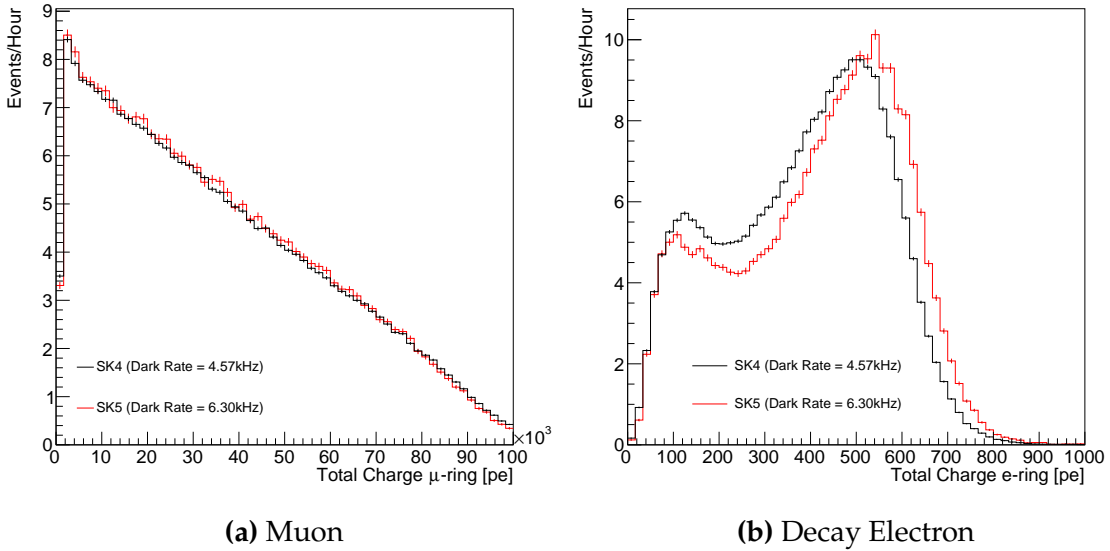


Figure 5.7.: Comparison of the measured raw charge deposited per event from the stopping muon data samples between SK-IV (Blue) and SK-V (Red), split by the primary muon subevent and the associated decay electron subevent.

The energy scale systematic is estimated from data-to-Monte Carlo differences in the stopping muon sample in [187] and found to be 2.1%. To determine the consistency of SK-IV and SK-V with respect to the energy scale systematic, the muon momentum distribution is compared between the two SK periods. As the total number of Cherenkov photons is integrated across the track length, the reconstructed momentum divided by track length (or range) is compared between SK-IV and SK-V as illustrated in Figure 5.8.

The consistency between these distributions has been computed in two ways. Firstly, a Gaussian is fit to the peak of each distribution separately, whose mean is found to be $(2.272 \pm 0.003)\text{MeV/cm}$ and $(2.267 \pm 0.006)\text{MeV/cm}$ for SK-IV and SK-V respectively. The ratio of these is equal to 1.002 ± 0.003 . The means of the

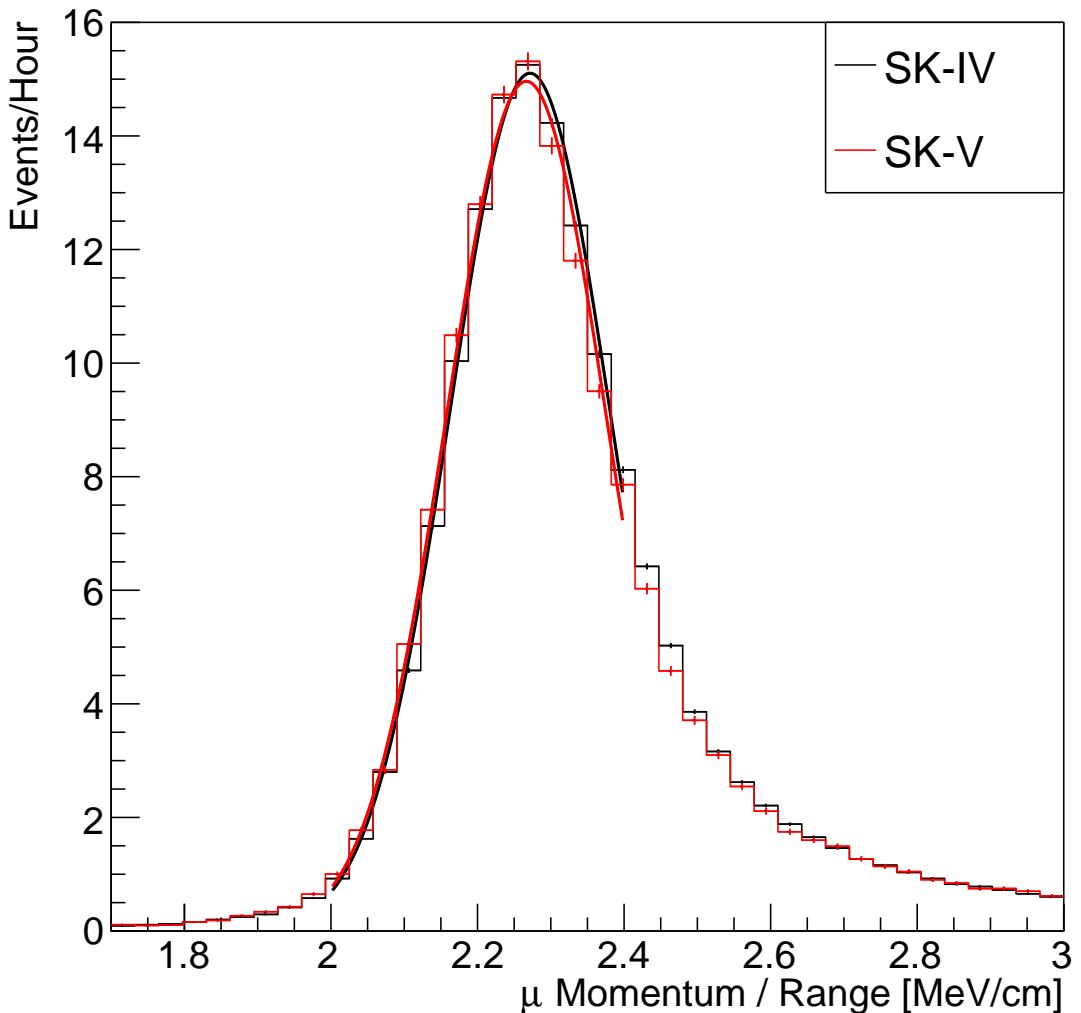


Figure 5.8.: The distribution of the reconstructed momentum from the muon ring divided by the distance between the reconstructed muon and decay electron vertices as found in the stopping muon data sets of SK-IV (Black) and SK-IV (Red). Only events with one tagged decay electron are considered. A Gaussian fit is considered in the range [2.0, 2.4] MeV/cm and illustrated as the solid curve.

1543 Gaussian fits are consistent with the expected stopping power of a minimum ionising
 1544 muon for a target material (water) with $Z/A \sim 0.5$ [188]. The second consistency
 1545 check is performed by introducing a nuisance parameter, α , which modifies the SK-
 1546 V distribution. The value of α which minimises the χ^2 value between the SK-IV
 1547 and SK-V is determined by scanning across a range of values. This is repeated by
 1548 applying the nuisance parameter as both a multiplicative factor and an additive

1549 shift. The χ^2 distributions for different values of α is illustrated in Figure 5.9. The
1550 values which minimise the χ^2 are found to be 0.0052 and 1.0024 for the additive and
1551 multiplicative implementations, respectively. No evidence of shifts larger than the
1552 2.1% uncertainty on the energy scale systematic has been found in the reconstructed
1553 momentum distribution of SK-IV and SK-V.

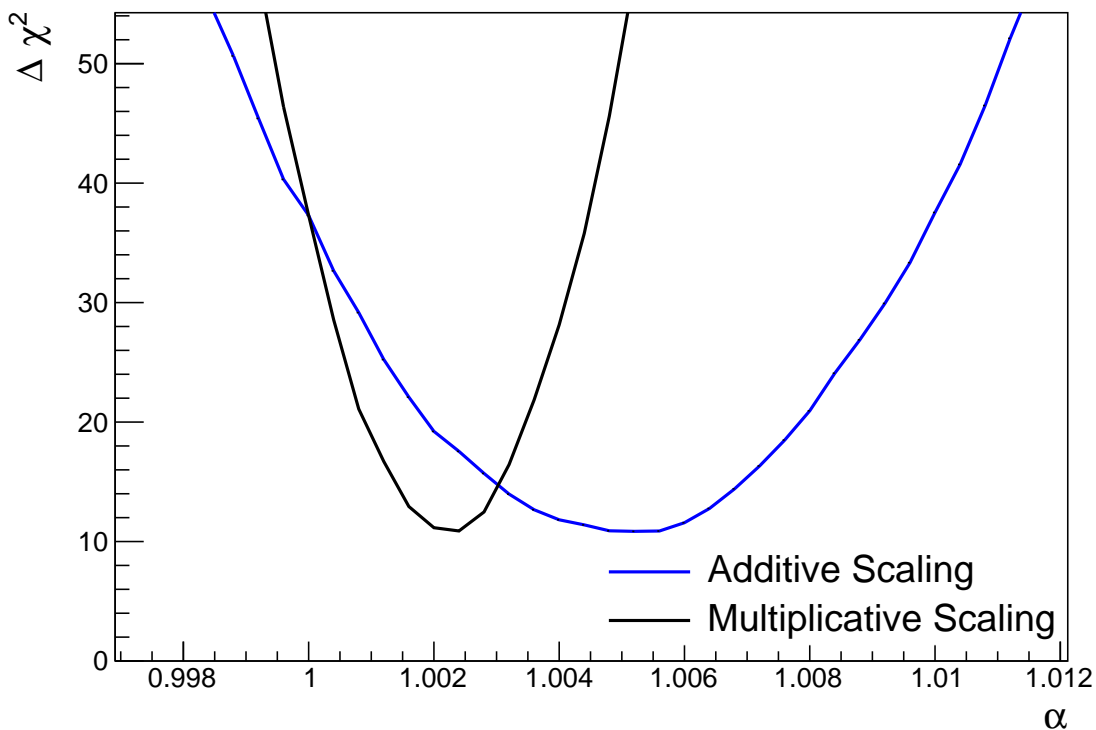


Figure 5.9.: The χ^2 difference between the SK-IV and SK-V reconstructed muon momentum divided by range when the SK-V is modified by the scaling parameter α . Both additive (Blue) and multiplicative (Black) scaling factors have been considered. In practice, the additive scaling factor actually uses the value of $(\alpha - 1.0)$ but is illustrated like this so the results can be shown on the same axis range.

1554 5.3. Event Reduction at SK

1555 Atmospheric neutrino events observed in the SK detector are categorised into three
1556 different types of samples: fully contained (FC), partially contained (PC) and up-going

muon (Up- μ), using PMT hit signatures in the inner and outer detector (ID and OD, respectively). To identify FC neutrino events, it is required that the neutrino interacts inside the fiducial volume of the ID and that no significant OD activity is observed. For this analysis, an event is defined to be in the fiducial volume provided the event vertex is at least 0.5m away from the ID walls. PC events have the same ID requirements but can have a larger signal present inside the OD. Typically, only high energy muons from ν_μ interactions can penetrate the ID wall. The Up- μ sample contains events where muons are created from neutrino interactions in the OD water or rock below the tank. They then propagate upwards through the detector. Downward-going muons generated from neutrino interactions above the tank are neglected because of the difficulty in separating their signature from the cosmic muon shower background. The sample categories are visually depicted in Figure 5.10.

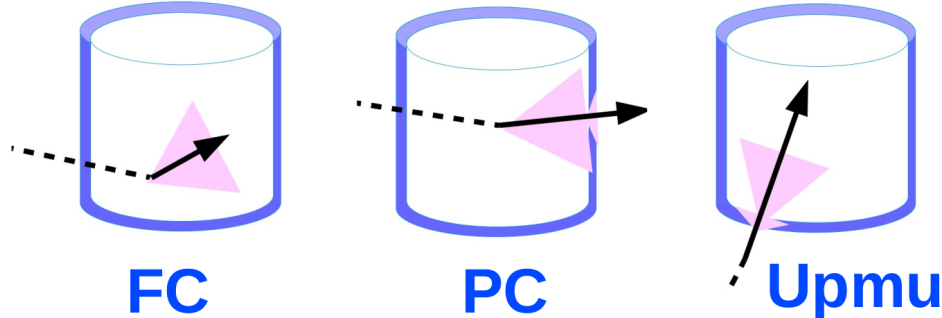


Figure 5.10.: A depiction of the topology patterns for fully-contained (FC), partially-contained (PC) and up-going muon (Up- μ) samples included in this analysis.

Based on the event characteristics, as defined by the `fitQun` event reconstruction software, the FC events are categorised by

- **Visible Energy:** equal to the sum of the reconstructed kinetic energy of particles above the Cerenkov threshold for all rings present in the event. The purpose is to separate events into sub-GeV and multi-GeV categories.
- **Number of observed Cerenkov rings.** The purpose is to separate single-ring and multi-ring events, where single-ring events predominantly consist of quasi-elastic

1576 interactions and multi-ring events are typically resonant pion production or deep
1577 inelastic scattering events.

- 1578 • **Particle identification parameter of the most energetic ring:** A value deter-
1579 mined from the maximum likelihood value based on `fitQun`'s electron, muon, or
1580 pion hypothesis. The purpose is to separate electron-like and muon-like events.
1581 • **Number of decay electrons:** The purpose is to separate quasi-elastic events
1582 (which have one decay electron emitted from the muon decay) and resonant pion
1583 production events (which have two decay electrons emitted from the muon and
1584 pion).

1585 The PC and Up- μ categories are broken down into “through-going” and “stopping”
1586 samples depending on whether the muon leaves the detector. This is because the PC
1587 stopping events deposit the entire energy of the interaction into the detector, resulting
1588 in better reconstruction. The energy of events that exit the detector has to be estimated,
1589 with typically worse resolution, which introduces much larger systematic uncertainties.
1590 Through-going Up- μ samples are further broken down by whether any hadronic
1591 showering was observed in the event which typically indicates DIS interactions. The
1592 expected neutrino energy for the different categories is given in Figure 5.11. FC sub-
1593 GeV and multi-GeV events peak around 0.7GeV and 3GeV respectively, with slightly
1594 different peak energies for ν_e and $n\nu_\mu$ oscillation channels. PC and Up- μ are almost
1595 entirely comprised of ν_μ events and peak around 7GeV and 100GeV, respectively.

1596 In normal data-taking operations, the SK detector observes many background
1597 events alongside the beam and atmospheric neutrino signal events of physics interest
1598 for this thesis. Cosmic ray muons and flasher events, which are the spontaneous
1599 discharge of a given PMT, contribute the largest amount of background events in the
1600 energy range relevant to this thesis. Lower energy analyses like DSNB searches are
1601 also subject to radioactive backgrounds [189]. Therefore the data recorded is reduced

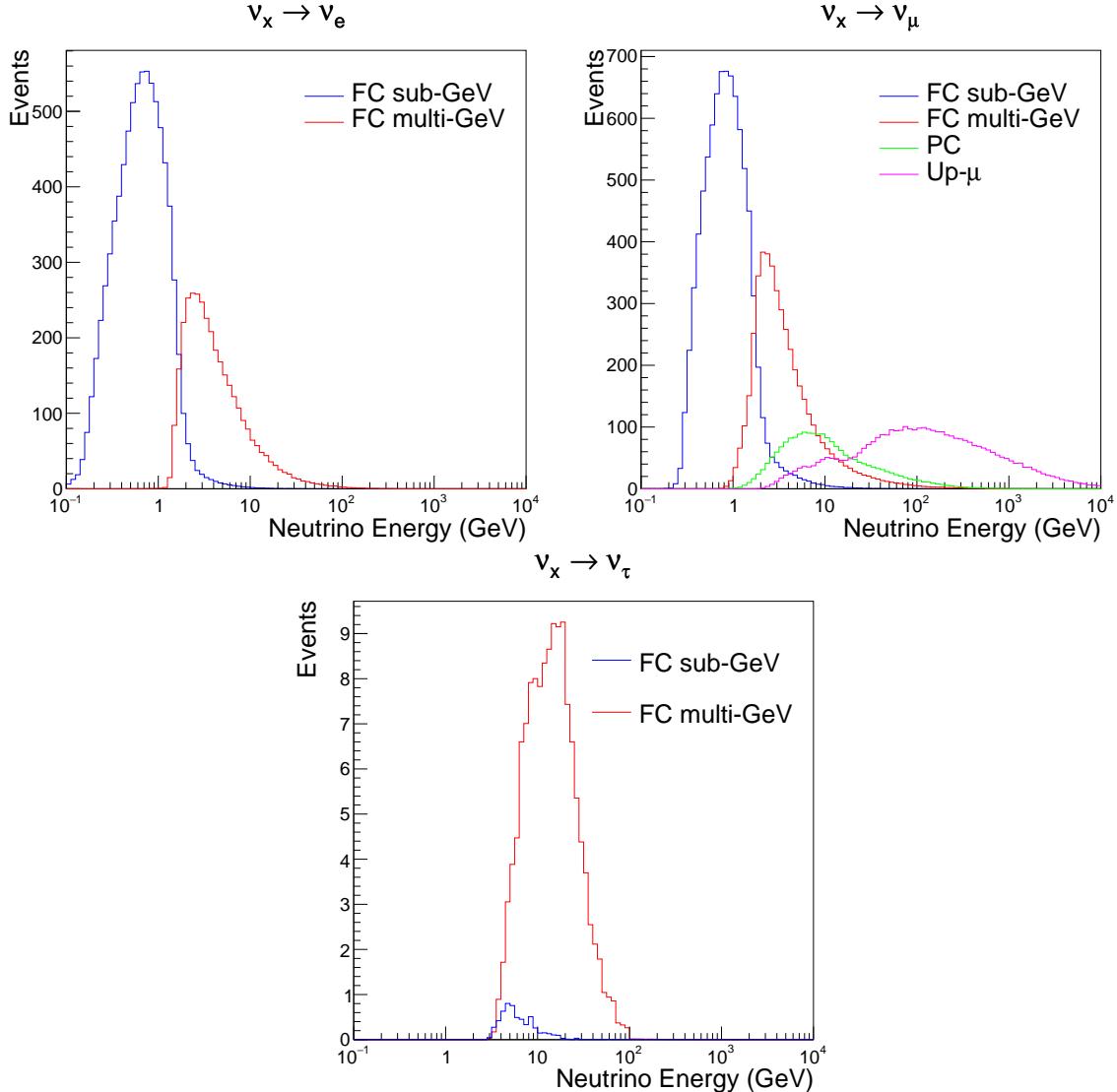


Figure 5.11.: The predicted neutrino flux of the fully contained (FC) sub-GeV and multi-GeV, partially contained (PC), and upward-going muon (Up- μ) events. The prediction is broken down by the $\nu_x \rightarrow \nu_e$ prediction (top left), $\nu_x \rightarrow \nu_\mu$ prediction (top right) and $\nu_x \rightarrow \nu_\tau$ prediction (bottom). Asimov A oscillation parameters are assumed (given in Table 2.2).

with the aim of removing these background events. The reduction process is detailed in [47, 89] and briefly summarised below.

The first two steps in the FC reconstruction remove the majority of cosmic ray muons by requiring a significant amount of ID activity compared to that measured in the OD. Events that pass this cut are typically very high momentum muons or events that leave very little activity in the OD. Consequently, a third reduction step is then

applied to select cosmic-ray muons that pass the initial reduction step. A purpose-built
 cosmic muon fitter is used to determine the entrance (or exit) position of the muon and
 a cut is applied to OD activity contained within 8m of this position. Flasher events are
 removed in the fourth reduction step which is based on the close proximity of PMT
 hits surrounding the PMT producing the flash. Events that pass all these reduction
 steps are reconstructed with the APFit algorithm. The fifth step of the reduction uses
 information from the more precise fitter to repeat the previous two steps with tighter
 cuts. Muons below the Cherenkov threshold can not generate optical photons in the
 ID but the associated decay electron can due to its lower mass. These are the types of
 events targeted in the fifth reduction step. The final cuts require the event vertex to be
 within the fiducial volume (0.5m from the wall although the nominal distance is 2.0m),
 visible energy $E_{vis} > 30\text{MeV}$ and fewer than 16 hits within the higher energy OD
 cluster. The culmination of the fully contained reduction results in 8.09 events/day in
 the nominal fiducial volume [190]. The uncertainty in the reconstruction is calculated
 by comparing Monte Carlo prediction to data. The largest discrepancy is found to be
 1.3% in the fourth reduction step.

The PC and Up- μ events are processed through their own reduction processes
 detailed in [47]. Both of these samples are reconstructed with the APFit algorithm
 rather than fitQun. This is because the efficiency of reconstructing events that leave
 the detector has not been sufficiently studied for reliable systematic uncertainties wth
 fitQun. The PC and Up- μ samples acquire events at approximately 0.66 and 1.44
 events/day.

Events due to beam neutrinos undergo the same reduction steps as FC events and
 are then subject to further cuts [191]. The GPS system which links the timing between
 the beam facility and SK needs to be operating correctly and there should be no activity

₁₆₃₃ within the detector in the previous $100\mu\text{s}$ before the trigger. The events then need to
₁₆₃₄ triggered between $-2\mu\text{s}$ and $10\mu\text{s}$ of the expected spill timing.

₁₆₃₅ The beam neutrino samples are not split by visible energy since their energy range
₁₆₃₆ is smaller than the atmospheric neutrino events. Following the T2K analysis in [80],
₁₆₃₇ only single-ring beam neutrino events are considered. Similar to atmospheric event
₁₆₃₈ selection, the number of decay electrons is used as a proxy for distinguishing CCQE
₁₆₃₉ and CCRES events. The expected neutrino energy, broken down by number of decay
₁₆₄₀ electrons, is given in Figure 5.12.

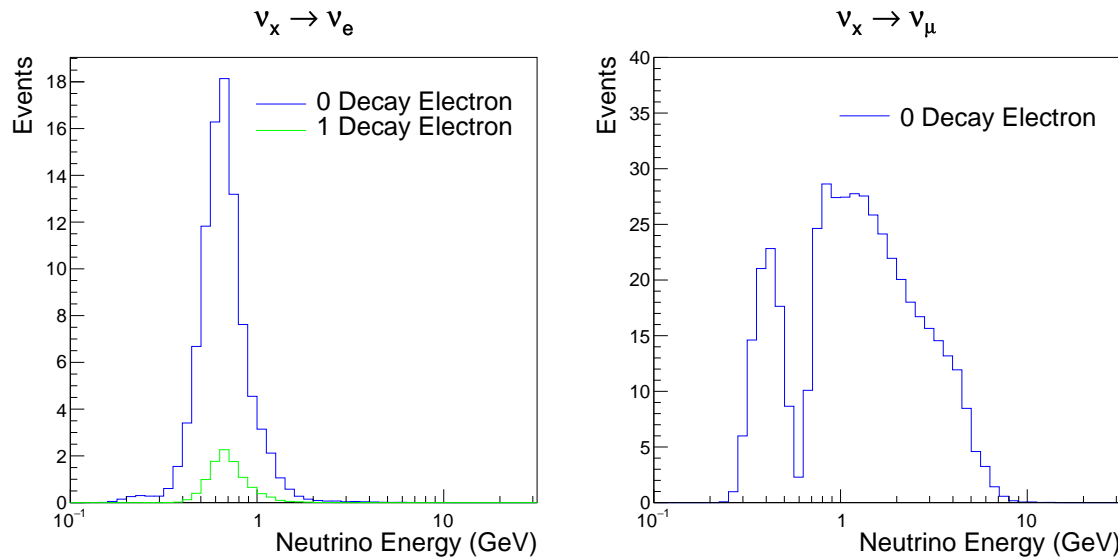


Figure 5.12.: The predicted flux of beam neutrinos, as a function of neutrino energy. The predictions are broken down by the number of decay electrons associated with the particular events. Asimov A oscillation parameters are assumed (given in Table 2.2).

₁₆₄₁ **Chapter 6**

₁₆₄₂ **Sample Selections and Systematics**

₁₆₄₃ The oscillation analysis presented within this thesis is built upon a simultaneous
₁₆₄₄ fit to atmospheric data at SK, neutrino beam data in the near detector, and beam
₁₆₄₅ data measured at SK. The definitions of these samples are documented in section 6.1,
₁₆₄₆ section 6.2, and section 6.3, respectively. The data collected and used within this
₁₆₄₇ analysis is detailed in Table 6.1. The near and far detector data corresponds to T2K
₁₆₄₈ runs 2-9 and runs 1-10, respectively. The accumulated POT and beam power for runs
₁₆₄₉ 1 – 10 are illustrated in Figure 6.1.

Data Type	Total
Near Detector FHC	1.15×10^{21} POT
Near Detector RHC	8.34×10^{20} POT
Far Detector FHC	1.97×10^{21} POT
Far Detector RHC	1.63×10^{21} POT
Atmospheric SK-IV	3244.4 days

Table 6.1.: The amount of data collected in each detector used within this analysis. The data collected at the near and far detector, for both neutrino beam (FHC) and antineutrino beam (RHC), is measured as the number of protons on target (POT).

₁₆₅₀ The difference in POT recorded at the near and far detector is due to the difference
₁₆₅₁ in downtime. The SK detector is very stable with almost 100% of data recorded during
₁₆₅₂ beam operation. Due to various technical and operational issues, the downtime of
₁₆₅₃ the near detector is significantly higher due to its more complex design and operating
₁₆₅₄ requirements.

1655 The systematic parameters invoked within the flux, detector, and interaction models
 1656 used within this analysis are documented in section 6.4. The standard configuration of
 1657 the joint beam and atmospheric data fit utilises far detector systematics provided in
 1658 the official inputs from the two experiments. Additionally, a correlated detector model
 1659 which fits the parameters used in sample selections to data has been developed and
 1660 documented in subsection 6.4.5.

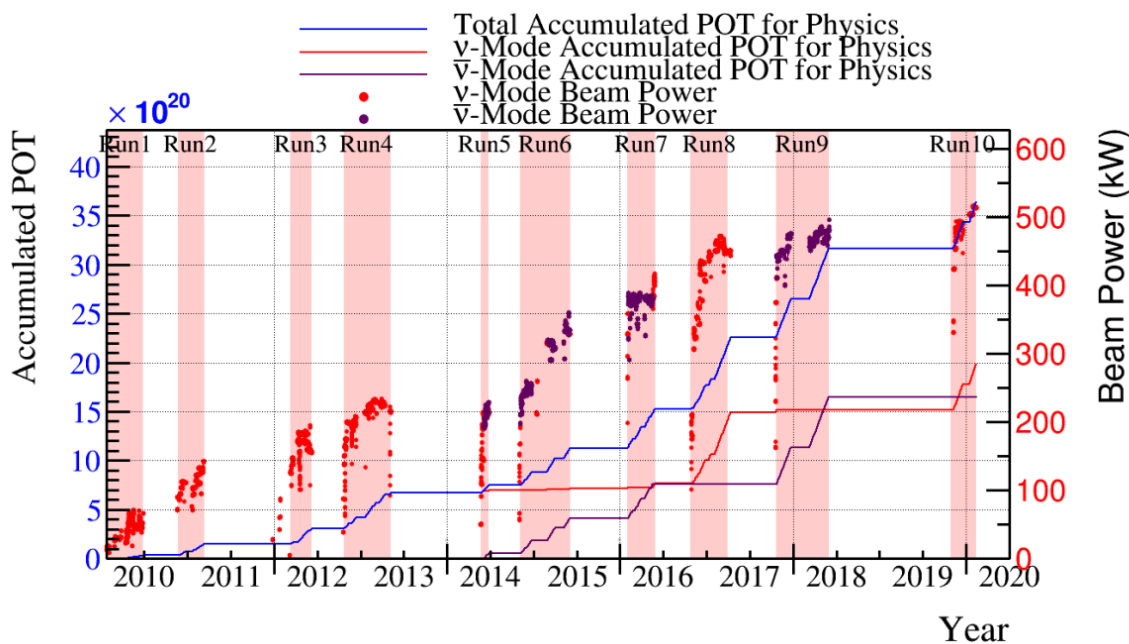


Figure 6.1.: The accumulated beam data, measured as the number of protons on target (POT). The total data (blue) is given which comprises of the neutrino beam (red) and antineutrino (purple) components. The beam power for neutrino and antineutrino beams is given as the markers using the same colour scheme. The timescale runs from Run 1 which started in January 2010 until Run 10 which ended in February 2020. The ratio of accumulated data in neutrino and antineutrino beam is 54.7% : 45.3%.

1661 6.1. Atmospheric Samples

1662 The atmospheric event selection follows the official SK-IV analysis presented in [89]
1663 and is documented below. The Monte Carlo prediction used within this analysis
1664 corresponds to 500 years worth of neutrino events, which is scaled down to match the
1665 SK-IV livetime of 3244.4 days.

1666 The fully contained (FC), partially contained (PC), and upward going muon events
1667 ($\text{up-}\mu$) which pass the reduction cuts discussed in section 5.3 are further broken down
1668 into different samples based on reconstruction information. This section details the
1669 samples used within this oscillation analysis, alongside the chosen binning,~~used~~
1670 [within the fit.](#)

1671 FC events are first separated by the visible energy deposited within the detector.
1672 This is calculated as the sum of the reconstructed kinetic energy above the Cherenkov
1673 threshold for all rings present in the event. Events are separated by whether they were
1674 above or below $E_{\text{vis}} = 1.33\text{GeV}$. This separates “subGeV” and “multiGeV” events.
1675 Typically, lower energy events consist of charged current quasi-elastic (CCQE) inter-
1676 actions which are better understood and simpler to reconstruct resulting in smaller
1677 systematic uncertainties. Events are further separated by the number of rings as-
1678 sociated with the event due to similar reasoning. As the oscillation probability is
1679 dependent upon the flavour of neutrino, electron and muon events are separated
1680 using a similar likelihood method to that discussed in section 5.2. To reduce computa-
1681 tional resources required for the reconstruction, only electron and pion hypotheses are
1682 considered so this separation cut depends on the ratio of the electron to pion likeli-
1683 hoods, $\log(L_e/L_\pi)$. Finally, the number of decay electrons is used to classify events.
1684 Charged current resonant pion production (CCRES) interactions generate a final-state
1685 pion. This can decay, mostly likely through a muon, into a decay electron. Therefore

₁₆₈₆ any electron-like event with one decay electron or muon-like event with two decay
₁₆₈₇ electrons was most likely produced by a CCRES interaction. Consequently, the number
₁₆₈₈ of decay electrons can be used to distinguish CCQE and CCRES interaction modes.
₁₆₈₉ Ultimately, FC subGeV events are separated into the samples listed in Table 6.2.

Sample Name	Description
SubGeV- <i>e</i> like-0dcy	Single ring <i>e</i> -like events with zero decay electrons
SubGeV- <i>e</i> like-1dcy	Single ring <i>e</i> -like events with one or more decay electrons
SubGeV- <i>μ</i> like-0dcy	Single ring <i>μ</i> -like events with zero decay electrons
SubGeV- <i>μ</i> like-1dcy	Single ring <i>μ</i> -like events with one decay electrons
SubGeV- <i>μ</i> like-2dcy	Single ring <i>μ</i> -like events with two or more decay electrons
SubGeV- <i>π</i> 0like	Two <i>e</i> -like ring events with zero decay electrons and reconstructed π^0 mass $85 \leq m_{\pi^0} < 215$ MeV

Table 6.2.: The fully contained subGeV samples, defined as events with visible energy $E_{vis} < 1.33$ GeV, used within this oscillation analysis.

₁₆₉₀ In addition to the cuts discussed above, multiGeV samples also have additional
₁₆₉₁ cuts to separate samples which target neutrino and antineutrino **separation events**.
₁₆₉₂ As discussed in section 7.1, the matter resonance only occurs for neutrinos in normal
₁₆₉₃ hierarchy and antineutrinos in an inverted mass hierarchy. Therefore, having flavour-
₁₆₉₄ enriched samples aids in the determination of the mass hierarchy. For a CCRES
₁₆₉₅ interaction,

$$\begin{aligned}
 \bar{\nu}_e + N &\rightarrow e^+ + N' + \pi^-, \\
 \nu_e + N &\rightarrow e^- + N' + \pi^+ \\
 &\quad \downarrow \mu^+ + \nu_\mu \\
 &\quad \downarrow e^+ + \nu_e + \bar{\nu}_\mu.
 \end{aligned} \tag{6.1}$$

1696 The π^- emitted from a $\bar{\nu}_e$ interaction is more likely to be absorbed within the
 1697 oxygen nucleus ~~compared to than~~ the π^+ from ν_e interactions [192]. These pions
 1698 then decay, mostly through muons, to electrons. Therefore the number of tagged
 1699 decay electrons associated with an event gives an indication of whether the interaction
 1700 was due to a neutrino or antineutrino: zero for $\bar{\nu}_e$ events, and one for ν_e events. The
 1701 ability to separate neutrino from antineutrino events is illustrated in Table 6.4, where
 1702 the MultiGeV-*elike-nue* has 78% purity of CC neutrino interactions with only 7%
 1703 antineutrino background ~~in that sample and the rest of the sample comprising of~~
 1704 ~~neutral current backgrounds, the rest consisting of NC backgrounds.~~

1705 ~~This relatively simple The number of decay electrons~~ discriminator works rea-
 1706 sonably well for single-ring events. However, this is not the case for multi-ring events.
 1707 A multiGeV multiring ~~electron-like separation~~ (MME) likelihood cut ~~which specifi-~~
 1708 ~~cally targets multiGeV multiRing electron-like events~~ was introduced in [193, 194].
 1709 This is a two-stage likelihood selection cut. Four observables are used in the first
 1710 likelihood cut to distinguish $CC\nu_e$ and $CC\bar{\nu}_e$ events from background:

- 1711 • The number of decay electrons
- 1712 • The maximum distance between the vertex of the neutrino and the decay electrons
- 1713 • The energy deposited by the highest energy ring
- 1714 • The particle identification of that highest energy ring

1715 ~~Below Paragraph Re-written~~

1716 Background events consist of $CC\nu_\mu$ and NC interactions. Typically, the majority of
 1717 the energy in these background events is carried by the hadronic system. Additionally,
 1718 muons tend to travel further than the pions from $CC\nu_e$ before decaying. Thus, the
 1719 parameters used within the likelihood cut target these typical background interaction
 1720 kinematics.

Sample Name	Description
MultiGeV-elike-nue	Single ring e -like events with zero decay electrons
MultiGeV-elike-nuebar	Single ring e -like events with one or more decay electrons
MultiGeV-mulike	Single ring μ -like events
MultiRing-elike-nue	Two or more ring events with leading energy e -like ring and passed both MME and $\nu/\bar{\nu}$ separation cuts
MultiRing-elike-nuebar	Two or more ring events with leading energy e -like ring and passed MME and failed $\nu/\bar{\nu}$ separation cuts
MultiRing-mulike	Two or more ring events with leading energy μ -like ring and only requires $E_{vis} > 0.6\text{GeV}$ DB: Why is this not 1.33GeV? N
MultiRing-Other1	Two or more ring events with leading energy e -like ring and failed the MME likelihood cut

Table 6.3.: The fully contained multiGeV samples used within this oscillation analysis. Both the sample name and description are given.

1721 Neutrino and antineutrino events are then separated by a second likelihood method
 1722 ($\nu/\bar{\nu}$ separation) detailed in [52]. This uses the number of decay electrons, the number
 1723 of reconstructed rings, and the event's transverse momentum. The last two parameters
 1724 are used because higher-energy samples tend to have more pions produced above
 1725 the Cherenkov threshold which results in more rings compared to an antineutrino
 1726 interaction. Furthermore, the angular distribution also tends to be more forward
 1727 peaked in antineutrino interactions as compared to neutrino interactions [89]. These
 1728 FC multiGeV sample definitions are detailed in Table 6.3.

1729 **Below Paragraph Re-worded**

1730 The PC and up- μ **events samples** are split by the amount of energy deposited
 1731 within the outer detector, into “stopping” and “through-going” samples. If an event
 1732 leaves the detector, the energy it takes with it has to be estimated which increases
 1733 the systematic uncertainty compared to events entirely contained within the inner
 1734 detector. This estimation is particularly poor at high energies, thus the up- μ through-

¹⁷³⁵ going events are not binned in reconstructed momentum. The through-going up- μ
¹⁷³⁶ are further separated by the presence of any electromagnetic showering in the event,
¹⁷³⁷ as the assumption of non-showering muon does not give reliable reconstruction for
¹⁷³⁸ these types of events [47]. In total, 13 FC, 2 PC, and 3 up- μ atmospheric samples are
¹⁷³⁹ included within this analysis.

Sample	CC ν_e	CC $\bar{\nu}_e$	CC($\nu_\mu + \bar{\nu}_\mu$)	CC($\nu_\tau + \bar{\nu}_\tau$)	NC
SubGeV- <i>elike-0dcy</i>	72.17	23.3	0.724	0.033	3.77
SubGeV- <i>elike-1dcy</i>	86.81	1.773	7.002	0.062	4.351
SubGeV- <i>mulike-0dcy</i>	1.003	0.380	90.07	0.036	8.511
SubGeV- <i>mulike-1dcy</i>	0.023	0.	98.46	0.029	1.484
SubGeV- <i>mulike-2dcy</i>	0.012	0.	99.25	0.030	0.711
SubGeV- <i>pi0like</i>	6.923	2.368	0.928	0.011	89.77
MultiGeV- <i>elike-nue</i>	78.18	7.041	3.439	1.886	9.451
MultiGeV- <i>elike-nuebar</i>	56.68	37.81	0.174	0.614	4.718
MultiGeV- <i>mulike</i>	0.024	0.005	99.67	0.245	0.058
MultiRing- <i>elike-nue</i>	59.32	12.39	4.906	3.385	20
MultiRing- <i>elike-nuebar</i>	52.39	31.03	1.854	1.585	13.14
MultiRing- <i>mulike</i>	0.673	0.080	97.33	0.342	1.578
MultiRingOther-1	27.98	2.366	34.93	4.946	29.78
PCStop	8.216	3.118	84.45	0.	4.214
PCThrus	0.564	0.207	98.65	0.	0.576
UpStop-mu	0.829	0.370	98.51	0.	0.289
UpThruNonShower-mu	0.206	0.073	99.62	0.	0.103
UpThruShower-mu	0.128	0.054	99.69	0.	0.132

Table 6.4.: The purity of each atmospheric sample used within this analysis, broken down by charged current (CC) and neutral current (NC) interactions and which neutrino flavour interacted within the detector. Asimov A oscillation parameter sets are assumed (given in Table 2.2). Electron neutrino and antineutrino events are separated to illustrate the ability of the separation likelihood cuts used within the multiGeV and multiring sample selections.

¹⁷⁴⁰ The atmospheric samples are binned in direct observables: reconstructed lepton
¹⁷⁴¹ momentum and direction, as given by Table A.1. The distribution of the reconstructed
¹⁷⁴² lepton momentum (for samples that only have one bin in reconstructed zenith angle)

₁₇₄₃ and reconstructed direction for each atmospheric sample used within this analysis is
₁₇₄₄ illustrated in Figure 6.2. The by-mode breakdown of each of the atmospheric samples
₁₇₄₅ is given in Appendix A.

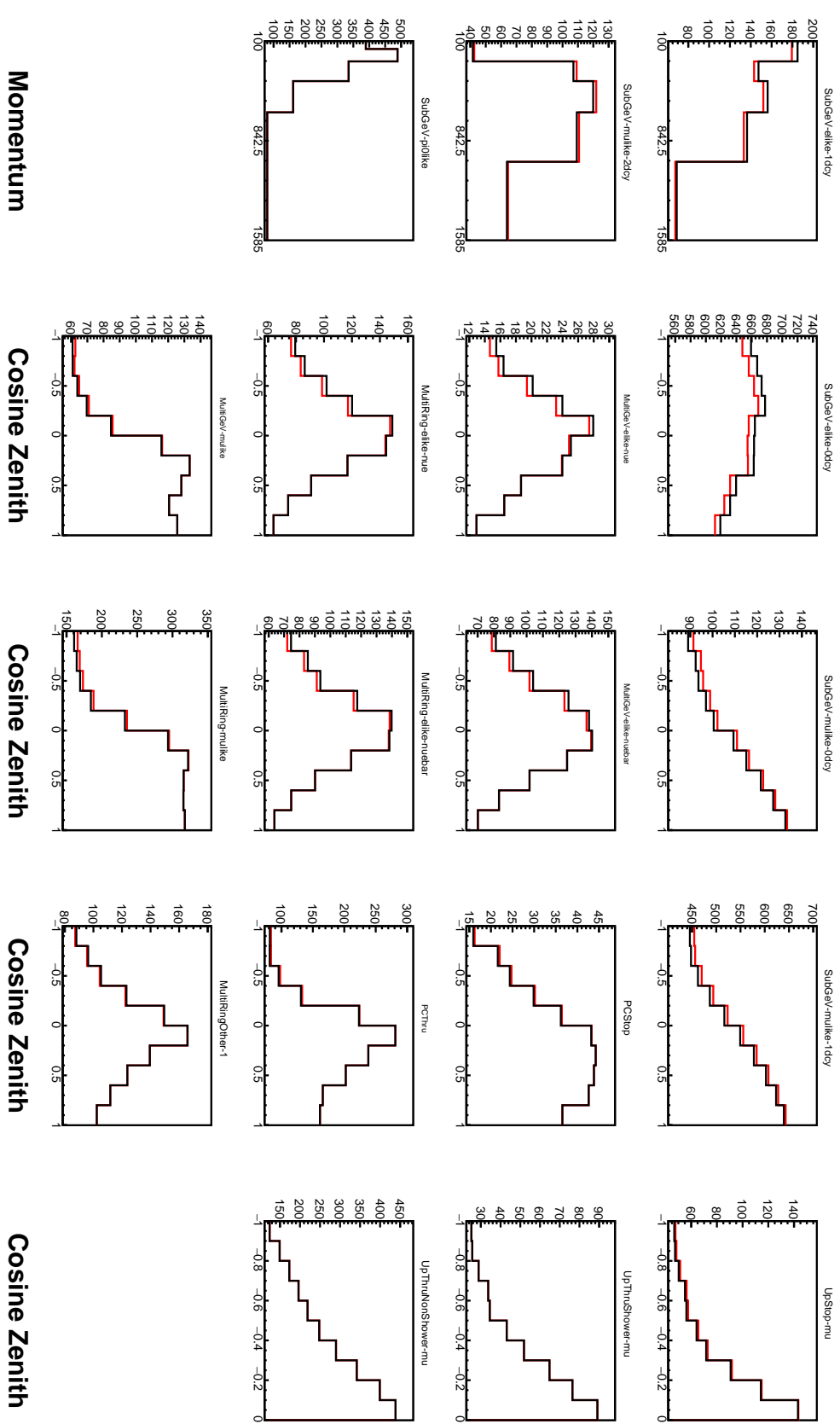


Figure 6.2: Comparison of the SK-IV atmospheric samples between predictions made with the CP-violating Asimov A (Black) and CP-conserving Asimov B (Red) oscillation parameter sets (given in Table 2.2). The subGeV samples CCRES and π^0 -like samples are given in their reconstructed lepton momentum. All other samples are presented in their reconstructed zenith angle projection.

¹⁷⁴⁶ 6.2. Near Detector Beam Samples

¹⁷⁴⁷ The near detector sample selections are documented in detail within [195] and sum-
¹⁷⁴⁸ marised below. Samples are selected based upon the which Fine Grained Detector
¹⁷⁴⁹ (FGD) that the vertex is reconstructed in as well as the operating mode of the beam:
¹⁷⁵⁰ FHC or RHC. ~~For additional constraints on model parameters, wrong-sign neutrino~~
¹⁷⁵¹ ~~samples are also considered when the beam is operating in RHC mode. Wrong-~~
¹⁷⁵² ~~sign neutrino samples are considered in the RHC mode in order to add additional~~
¹⁷⁵³ ~~constraints on model parameters.~~ Samples from the wrong-sign component of the
¹⁷⁵⁴ FHC beam mode are not included as they are statistically insignificant compared to
¹⁷⁵⁵ those samples already listed.

¹⁷⁵⁶ For additional constraints on model parameters, wrong-sign neutrino samples are
¹⁷⁵⁷ also considered when the beam is operating in RHC mode.

¹⁷⁵⁸ The reconstruction algorithm uses a clustering algorithm to group hits within the
¹⁷⁵⁹ TPC. It then adds information from the upstream FGD to form a track which passes
¹⁷⁶⁰ through both sub-detectors. In FHC(RHC), the highest momentum negative(positive)
¹⁷⁶¹ curvature track is defined as the muon candidate. Before being assigned a sample,
¹⁷⁶² these candidate muon events must ~~undergo pass~~ CC-inclusive cuts, as defined in [196]:

- ¹⁷⁶³ • Event Timing: The DAQ must be operational and the event must occur within
¹⁷⁶⁴ the expected beam time window consistent with the beam spill
- ¹⁷⁶⁵ • TPC Requirement: The muon-candidate track path must intercept one or more
¹⁷⁶⁶ TPCs
- ¹⁷⁶⁷ • Fiducial volume: The event must originate from within the fiducial volume .
¹⁷⁶⁸ ~~The fiducial volumes are defined as a region within each sub-detector defined~~
¹⁷⁶⁹ ~~in [197].~~

1770 • Upstream Background: Remove events that have muon tracks that originate
 1771 upstream of the FGDs by requiring no high-momentum tracks within 150mm
 1772 upstream of the candidate vertex. Additionally, events that occur within the
 1773 downstream FGD are vetoed if a secondary track starts within the upstream FGD

1774 • Broken track removal: All candidates where the muon candidate is broken in two
 1775 are removed

1776 • Muon PID: Measurements of dE/dx in a TPC are used to distinguish muon-like
 1777 events **from electron-like or proton-like**, using a likelihood cut

1778 In addition to these cuts, RHC neutrino events also have to undergo the following

1779 cuts to aid in the separation of neutrino and antineutrino [198]:

1780 • TPC Requirement: The track path must intercept TPC2

1781 • Positive Track: The highest momentum track must have positive reconstructed
 1782 charge

1783 • TPC1 Veto: Remove any events originating upstream of TPC1

1784 Once all CC-inclusive events have been determined, they are further **separated**

1785 ~~into sub-samples that target the constraints on interaction modes most relevant at~~
 1786 ~~the far-detector. They are~~ split by pion multiplicity: CC0 π , CC1 π , and CCOther.

1787 These target specific interaction modes CCQE, CCRES, and other CC background
 1788 interactions, respectively. Pions in the TPCs and FGDs are selected by requiring a
 1789 second track to be observed, which is separate from the muon track and is in the same
 1790 beam spill window and sub-detector. If the pion originated within a FGD, it must also
 1791 pass through the sequential downstream TPC (TPC2 for FGD1, TPC3 for FGD2).

1792 CC0 π , CC1 π , and CCOther samples are defined with the following cuts:

1793 DB: Understand pion cuts at ND

1794 • ν_μ **CC0 π Selection:** No electrons in TPC and no charged pions or decay electrons
1795 within the TPC or FGD

1796 • ν_μ **CC1 π Selection:** Exactly one charged pion in either the TPC or FGD, where
1797 the number of charged pions in the FGD is equal to the number of decay electrons

1798 • ν_μ **CCOther Selection:** All events which are not classified into the above two
1799 selections.

1800 Counting the three selections for each FGD in FHC and RHC running, including
1801 the wrong-sign background in RHC, 18 near detector samples are used within this
1802 analysis. These samples are binned in reconstructed lepton momentum (illustrated in
1803 Figure 6.3) and direction with respect to the beam. The binning is chosen such that
1804 each event has at least 20 Monte Carlo events in each bin [197]. This is to ensure that
1805 the bins are coarse enough to ensure the reduction of statistical errors, whilst also
1806 being fine enough to sample the high-resolution peak regions. The exact binning is
1807 detailed in [197].

1808 6.3. Far Detector Beam Samples

1809 The beam neutrino events which occur at the SK detector, which pass the reduction
1810 cuts detailed in section 5.3, are separated **depending based** on whether the beam was
1811 operating in FHC or RHC mode. The events are then separated into three samples:
1812 electron-like (1Re), muon-like (1R μ), and CC1 π^+ -like (1Re1de) which are observed as
1813 electron-like events with an associated decay electron [185]. As discussed in section 6.1,
1814 positively charged pions emitted from neutrino interactions are more likely to produce
1815 decay electrons than negatively charged pions. Consequently, the CC1 π^+ -like sample
1816 is only selected when the beam is operating in FHC mode. Therefore, five beam
1817 samples measured at SK are used in this analysis.

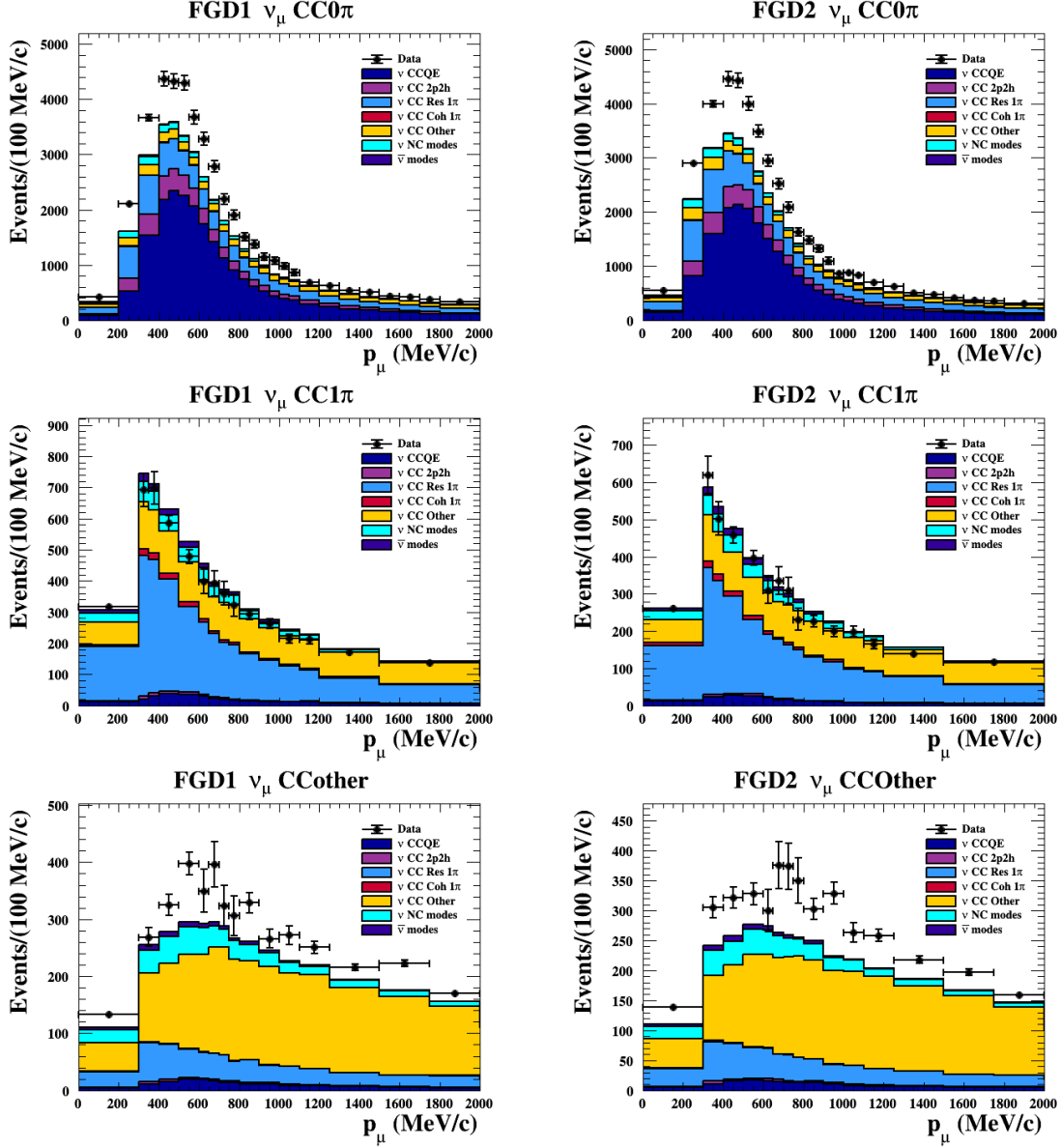


Figure 6.3.: The nominal Monte Carlo predictions compared to data for the FGD1 and FGD2 samples in neutrino beam mode, broken down into the $\text{CC}\nu_\mu 0\pi$, $\text{CC}\nu_\mu 1\pi$ and $\text{CC}\nu_\mu$ Other categories. Figures taken from [195].

1818 The fiducial volume definition for beam samples is slightly different from that
 1819 used **within for** the atmospheric samples. It uses both the distance to the closest wall
 1820 (`dWall`) and the distance to the wall along the trajectory of the particle (`toWall`). This
 1821 allows events that originate close to the wall but are facing into the tank to be included
 1822 within the analysis, which would have otherwise been removed. These additional
 1823 events are beneficial for a statistics-limited experiment. The exact cut values for both

1824 dWall and toWall are different for each of the three types of sample and are optimised
1825 based on T2K sensitivity to δ_{CP} [183, 199]. They are:

1826 **1Re event selection** For an event to be classified as a 1Re-like, the event must **follow**
1827 **satisfy**:

- 1828 • Fully-contained and **within have** $d_{Wall} > 80\text{cm}$ and $t_{Wall} > 170\text{cm}$
- 1829 • Total of one ring which is reconstructed as electron-like with reconstructed mo-
- 1830 mentum $P_e > 100\text{MeV}$
- 1831 • Zero decay electrons are associated with the event
- 1832 • Passes π^0 rejection cut discussed in section 5.2

1833 **The zero decay electron cut removes non-CCQE interactions and The zero-de-**
1834 **cay electron cut specifically targets CCQE interactions. Whereas,** the π^0 rejection
1835 cut is designed to remove neutral current π^0 background events which can be easily
1836 reconstructed as 1Re-like events.

1837 The zero decay electron cut removes non-CCQE interactions and the π^0 rejection
1838 cut is designed to remove neutral current π^0 background events which can be easily
1839 reconstructed as 1Re-like events.

1840 **CC1 π^+ event selection** This event selection is very similar to that of the 1Re sample.
1841 The only **difference is differences are** that the dWall and toWall criteria are changed
1842 to $> 50\text{cm}$ and $> 270\text{cm}$, respectively. **Furthermore, , and** exactly one decay electron
1843 is required from the π^+ decay.

1844 **1R μ event selection** A 1R μ -like event is determined by the following cuts:

- 1845 • Fully-contained and **within have** $d_{Wall} > 50\text{cm}$ and $t_{Wall} > 250\text{cm}$
- 1846 • Total of one ring which is reconstructed as muon-like with reconstructed momentum $P_\mu > 200\text{MeV}$
- 1847 • Fewer than two decay electrons are associated with the event
- 1848 • Passes π^+ rejection cut discussed in section 5.2

1850 All of these samples are binned in reconstructed neutrino energy. This is possible
 1851 under a particular interaction mode assumption, as the direction from the source is
 1852 known extremely well. **This value is calculated** For the 1Re-like and 1R μ -like samples
 1853 **assuming CCQE interactions,**

$$E_\nu^{rec} = \frac{(M_N - V_{nuc})E_l - m_l^2/2 + M_N V_{nuc} - V_{nuc}^2/2 + (M_P^2 + M_N^2)/2}{M_N - V_{nuc} - E_l + P_l \cos(\theta_{beam})} \quad (6.2)$$

1854 Where M_N , M_P and m_l are the masses of the neutron, proton and outgoing lepton,
 1855 respectively. $V_{nuc} = 27\text{MeV}$ is the binding energy of the oxygen **nuclei nucleus** [185],
 1856 θ_{beam} is the angle between the beam and the direction of the outgoing lepton, and E_l
 1857 and P_l are the energy and momentum of that outgoing lepton.

1858 The reconstructed neutrino energy of the CC1 π^+ -like events **is modified to include**
 1859 **also accounts for** the delta resonance produced within the interaction,

$$E_\nu^{rec} = \frac{2M_N E_l + M_{\Delta^{++}}^2 - M_N^2 - m_l^2}{2(M_N - E_l + P_l \cos(\theta_{beam}))} \quad (6.3)$$

1860 Where $M_{\Delta^{++}}$ is the mass of the delta baryon. Binding energy effects are not
 1861 considered as a two-body process with the delta baryon is assumed. This follows

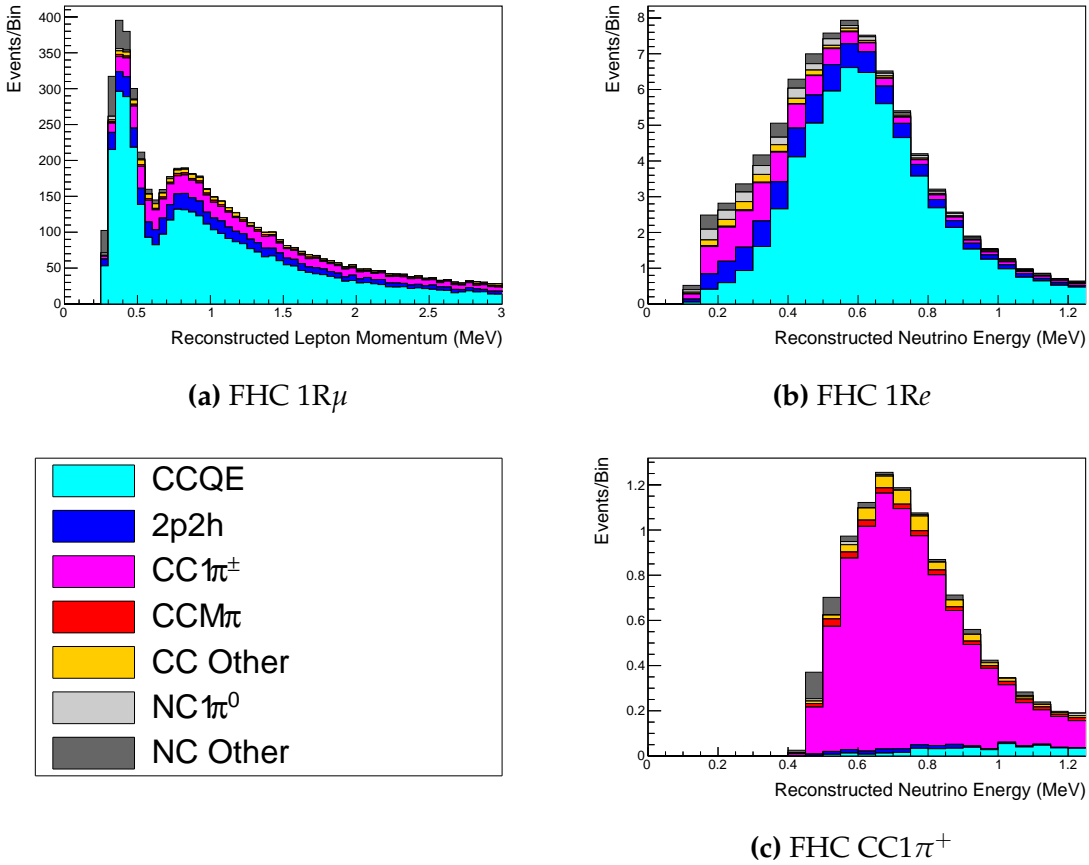


Figure 6.4.: The reconstructed neutrino energy, as defined by Equation 6.2 and Equation 6.3, for the 1R μ -like, 1Re-like and CC1 π^+ -like samples. Asimov A oscillation parameter sets are assumed (given in Table 2.2). These samples are the FHC mode samples. For ease of viewing, the 1R μ sample only shows the $0. \leq E_\nu^{rec} < 3.0\text{GeV}$ but the binning extends to 30.0GeV.

1862 the T2K oscillation analysis presented in [80], although recent developments of the
 1863 interaction model in the latest T2K oscillation analysis do include effects from binding
 1864 energy in this calculation [200].

1865 The reconstructed neutrino energy for the FHC samples is illustrated in Figure 6.4.
 1866 As expected, the 1R μ -like and 1Re-like samples are heavily dominated by CCQE in-
 1867 teractions, with smaller contributions from 2p2h meson exchange and resonant pion
 1868 production interactions. The CC1 π^+ -like sample predominantly consists of charged
 1869 current resonant pion production interactions. The 1Re-like and CC1 π^+ -like samples
 1870 are also binned by the angle between the neutrino beam and the reconstructed lepton

momentum. This is to aid in charged current and neutral current separation, as indicated in Figure 6.5. This is because the neutral current backgrounds are predominantly due to π^0 -decays, where the opening angle of the two gammas alongside the different final state kinematics produces a slightly broader angular distribution compared to the **final state particles electron** originating from charged current ν_e interactions.

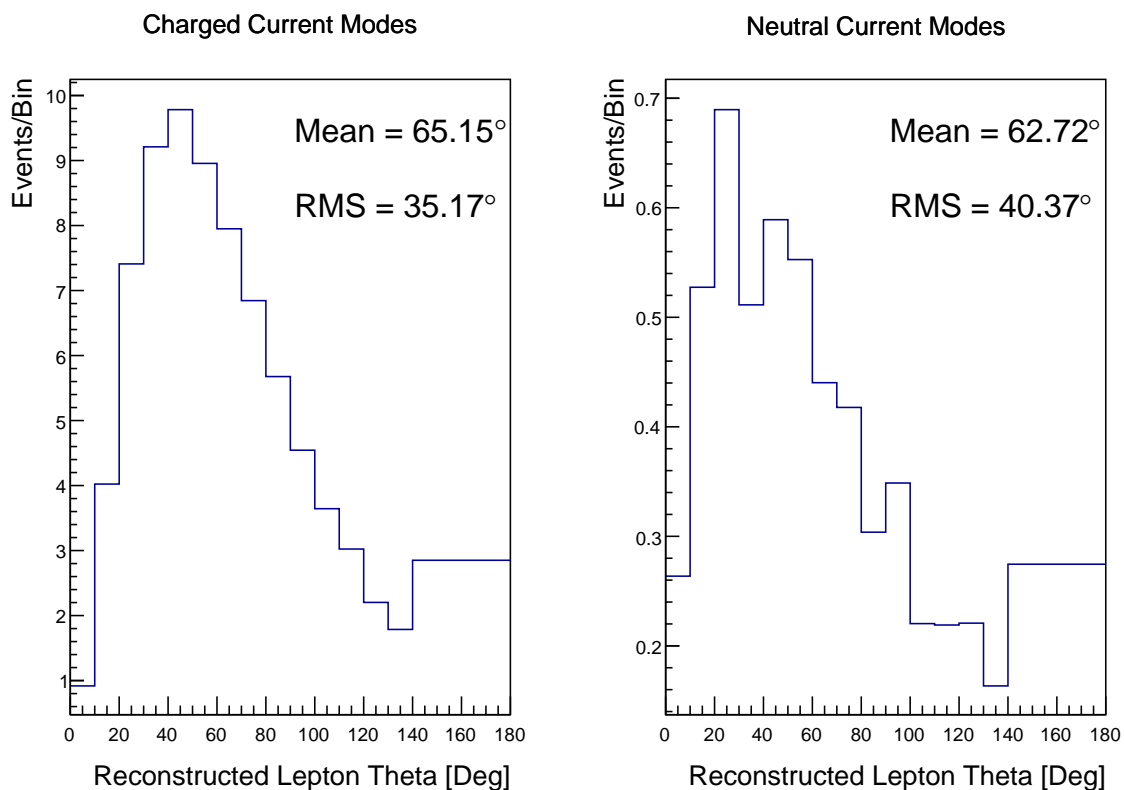


Figure 6.5.: The distribution of the angle between the neutrino beam direction and the reconstructed final state lepton, for the FHC 1Re-like sample. The distribution is broken down by neutrino interaction mode into charged current (left) and neutral current (right) components. Asimov A oscillation parameter sets are assumed (given in Table 2.2). The RMS of the charged and neutral current plots are 35.17° and 40.37° , respectively.

1876 6.4. Systematic Uncertainties

1877 The systematic model parameters for this analysis are split into groups, or blocks,
1878 depending on their purpose. They consist of flux uncertainties, neutrino-matter in-
1879 teraction systematics, and detector efficiencies. There are also uncertainties on the
1880 oscillation parameters which this analysis **will not be is not** sensitive to, **namely** Δm_{12}^2
1881 and $\sin^2(\theta_{12})$. These **osscillation parameters** uncertainties are taken from the 2018
1882 PDG measurements [81]. As described in chapter 4, each model parameter used within
1883 this analysis requires a prior uncertainty. This is provided via separate covariance ma-
1884 trices for each block. The covariance matrices can include prior correlations between
1885 parameters within a single block, but the separate treatment means prior **uncertainties**
1886 **correlations** can not be included for parameters in different groups. Some parame-
1887 ters in these models have no reasonably motivated uncertainties and are assigned
1888 flat priors which do not modify the likelihood penalty. **In practice, these flat prior**
1889 **parameters are actually assigned a Gaussian with a very large width to ensure the**
1890 **covariance matrix is positive definite. They are then checked at run time to deter-**
1891 **mine if they contribute to the likelihood.** The flux, neutrino interaction, and detector
1892 modeling simulations have already been discussed in section 5.1 and section 5.2. The
1893 uncertainties invoked within each of these models are described below.

1894 6.4.1. Beam Flux

1895 The neutrino beam flux systematics **is are** based upon the uncertainty in the modeling
1896 of the components of the beam **simulation**. This includes the **hadron production**
1897 **model and their re-interactions model of hadron productions and reinteractions**,
1898 the shape, intensity, and alignment of the beam with respect to the target, and the
1899 uniformity of the magnetic field produced by the horn, alongside other effects. The

uncertainty, as a function of neutrino energy, is illustrated in Figure 6.6 which includes a depiction of the total uncertainty as well as the contribution from individual components. The uncertainty around the peak of the energy distribution ($E_\nu \sim 0.6\text{GeV}$) is dominated by **the measurements of uncertainties in** the beam profile and alignment. Outside of this region, **the** uncertainties **within** on hadron production dominate the **uncertainty error**.

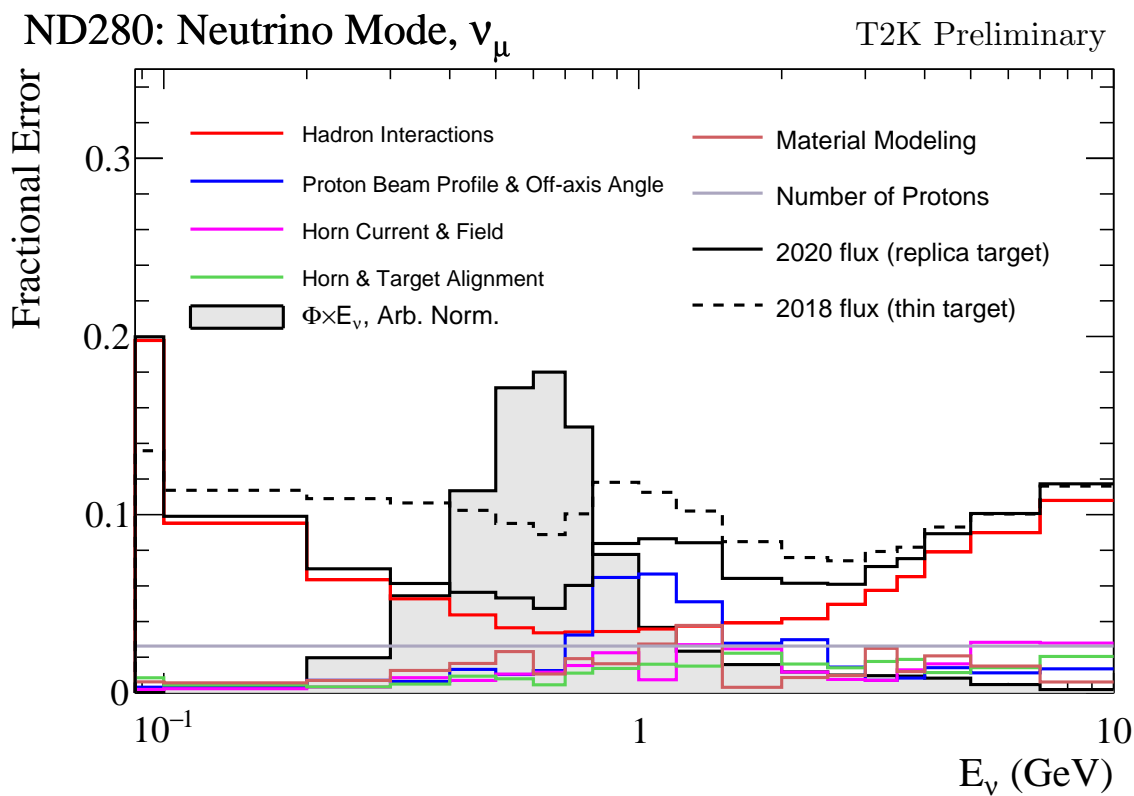


Figure 6.6.: The total uncertainty evaluated on the near detector ν_μ flux prediction constrained by the replica-target data, illustrated as a function of neutrino energy. The solid(dashed) line indicates the uncertainty used within this analysis(the T2K 2018 analysis [201]). The solid histogram indicates the neutrino flux as a function of energy. Figure taken from [202].

The beam flux uncertainties are described by one hundred parameters. They are split between the ND280 and SK detectors and binned by neutrino flavour: ν_μ , $\bar{\nu}_\mu$, ν_e and $\bar{\nu}_e$. The response is then broken down as a function of neutrino energy. The bin density in the neutrino energy is the same for the ν_μ in FHC and $\bar{\nu}_\mu$ in RHC beams,

¹⁹¹⁰ and narrows for neutrino energies close to the oscillation maximum of $E_\nu = 0.6\text{GeV}$.
¹⁹¹¹ This binning is specified in Table 6.5. All of these systematic uncertainties are applied
¹⁹¹² as normalisation parameters with Gaussian priors centered at 1.0 and error specified
¹⁹¹³ from a covariance matrix provided by the T2K beam group [202].

Neutrino Flavour	Sign	Neutrino Energy Bin Edges (GeV)
μ	Right	0., 0.4, 0.5, 0.6, 0.7, 1., 1.5, 2.5, 3.5, 5., 7., 30.
μ	Wrong	0., 0.7, 1., 1.5, 2.5, 30.
e	Right	0., 0.5, 0.7, 0.8, 1.5, 2.5, 4., 30.
e	Wrong	0., 2.5, 30.

Table 6.5.: The neutrino energy binning for the different neutrino flavours. “Right” sign indicates neutrinos in the FHC beam and antineutrinos in the RHC beam. “Wrong” sign indicates antineutrinos in the FHC beam and neutrinos in the RHC beam. The binning of the detector response is identical for the FHC and RHC modes as well as at ND280 and SK.

¹⁹¹⁴ 6.4.2. Atmospheric Flux

¹⁹¹⁵ The atmospheric neutrino flux is modeled by the HKKM model [43]. 16 systematic
¹⁹¹⁶ uncertainties are applied to control the normalisation of each neutrino flavour, energy,
¹⁹¹⁷ and direction. They are summarised below:

¹⁹¹⁸ • **Absolute Normalisation:** The overall normalisation of each neutrino flavour is
¹⁹¹⁹ controlled by two independent systematic uncertainties, for $E_\nu < 1\text{GeV}$ and $E_\nu >$
¹⁹²⁰ 1GeV , respectively. This is driven mostly by hadronic interaction uncertainties for
¹⁹²¹ the production of pions and kaons [43]. The strength of the response is dependent
¹⁹²² upon the neutrino energy. [The uncertainty is parameterized following Figure 11 in \[43\]](#).

¹⁹²⁴ • **Relative Normalisation:** Uncertainties on the ratio of $(\nu_\mu + \bar{\nu}_\mu) / (\nu_e + \bar{\nu}_e)$ are
¹⁹²⁵ controlled by the difference between the HKKM model [43], FLUKA [46] and

1926 Bartol models [42]. Three independent parameters are applied in the energy
1927 ranges: $E_\nu < 1\text{GeV}$, $1\text{GeV} < E_\nu < 10\text{GeV}$, and $E_\nu > 10\text{GeV}$.

- 1928 • **$\nu/\bar{\nu}$ Normalisation:** The uncertainties in the π^+/π^- (and kaon equivalent) production uncertainties in the flux of $\nu/\bar{\nu}$. The response is applied using the same methodology as the relative normalisation parameters.
- 1931 • **Up/Down and Vertical/Horizontal Ratio:** Similar to the above two systematics, the difference between the HKKM, FLUKA, and Bartol model predictions, as a function of $\cos(\theta_Z)$, is used to control the normalisation of events as a function of zenith angle.
- 1935 • **K/π Ratio:** Higher energy neutrinos ($E_\nu > 10\text{GeV}$) ~~become dependent upon kaon decay as the dominant source of neutrinos mostly originate in kaon decay~~. Measurements of the ratio of K/π [203] are used to control the systematic uncertainty of the expected ratio of pion and kaon production.
- 1939 • **Solar Activity:** As the 11-year solar cycle can affect the Earth's magnetic field, the flux of primary cosmic rays varies across the same period. The uncertainty is calculated by taking a ± 1 year variation, equating to a 10% uncertainty for the SK-IV period.
- 1943 • **Atmospheric Density:** The height of the interaction of the primary cosmic rays is dependent upon the atmospheric density. The HKKM assumes the US standard 1976 [153] profile. This systematic controls the uncertainty in that model.

1946 **~~Added the following paragraph and associated plot~~**

1947 The total uncertainty is dominated by the absolute and relative normalisation parameters. The effect of which is illustrated in Figure 6.7. Generally, the uncertainty 1948 is large at low energy, reducing to $O(10\%)$ around the peak of the flux distribution 1949 and then increasing once the neutrino energy exceeds 10GeV.

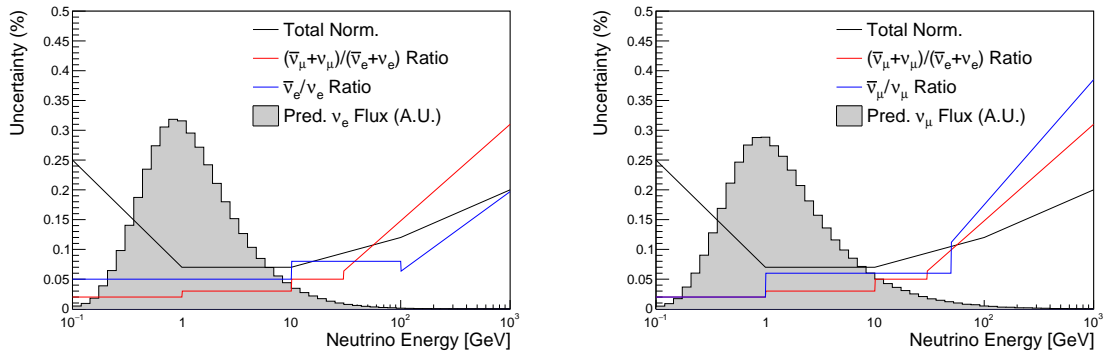


Figure 6.7.: The uncertainty evaluated on the atmospheric ν_e (left) and ν_μ (right) flux predictions. The absolute normalisation and flavour ratio uncertainties are given. The solid histogram indicates the neutrino flux as a function of energy.

1951 Updates to the HKKM and Bartol models are underway [158] to use a similar
 1952 tuning technique to that used in the beam flux predictions. After those updates, it may
 1953 be possible to include correlations in the hadron production uncertainty systematics
 1954 for beam and atmospheric flux predictions.

1955 6.4.3. Neutrino Interaction

1956 **The neutrino interactions which occur within all Neutrino interactions in the detec-**
 1957 **tors are modeled by NEUT. The two independent oscillation analyses, T2K-only [204]**
 1958 **and the SK-only [52], have developed separate interaction models. To leverage the**
 1959 **most maximise** sensitivity out of this simultaneous beam and atmospheric analysis,
 1960 a correlated interaction model has been defined in [205]. Where applicable, corre-
 1961 lations allow the systematic uncertainties applied to the atmospheric samples to be
 1962 constrained by **measurements of the near detector in the beam experiment near**
 1963 **detector neutrino beam measurements.** This can lead to stronger sensitivity to oscil-
 1964 lation parameters as compared to an uncorrelated model.

1965 The low-energy T2K systematic model has a more sophisticated treatment of CCQE,
 1966 2p2h, and CCRES uncertainties, **where which is due to the purpose-made cross-sec-**

1967 ~~tion measurements made by the near detector. Furthermore,~~ extensive comparisons
1968 of this model have been performed to external data [204]. However, the model
1969 is not designed for high-energy atmospheric events, like those illustrated in Fig-
1970 ure 5.11. Therefore the high energy systematic model from the SK-only analysis is
1971 implemented for the relevant multiGeV, PC, and up- μ samples. **The T2K CCQE model**
1972 **is more sophisticated so it has been implemented for all samples within this anal-**
1973 **ysis, where separate low-energy and high-energy dials have been implemented.**
1974 **The low-energy dials are constrained by the near detector measurements and are**
1975 **uncorrelated to their high-energy counterparts. The author of this thesis was re-**
1976 **sponsible for implementing and validating the combined cross section model as**
1977 **documented in [205, 206].**

1978 The high energy systematic model includes parameters developed from com-
1979 parisons of Nieves and Rein-Seghal models which affect resonant pion producing
1980 interactions, comparisons of the GRV98 and CKMT models which control DIS interac-
1981 tions, and hadron multiplicity measurements which modulate the normalisation of
1982 multi-pion producing events. The uncertainty on the ν_τ cross-section is particularly
1983 large and is controlled by a 25% normalisation uncertainty. These uncertainties are
1984 applied via normalisation or shape parameters. The former linearly scales the weight
1985 of all affected Monte-Carlo events, whereas the latter can increase or decrease a partic-
1986 ular event's weight depending on its neutrino energy and mode of interaction. The
1987 response of the shape parameters is defined by third-order polynomial splines which
1988 return a weight for a particular neutrino energy. To reduce computational resources
1989 for the far detector fit, the response is binned by neutrino energy and sample binning:
1990 lepton momentum and cosine zenith binning for atmospheric splined responses and
1991 reconstructed neutrino energy and direction binning for beam samples. In total, 17
1992 normalisation and 15 shape parameters are included in the high-energy model within
1993 this analysis.

1994 Figure 6.8 indicates the predicted neutrino energy distribution for both beam and
1995 subGeV atmospheric samples. There is clearly significant overlap in neutrino energy
1996 between the subGeV atmospheric and beam samples, allowing similar kinematics in
1997 the final state particles. Figure 6.9 illustrates the fractional contribution of the different
1998 interaction modes per sample.

1999 Comparing beam and atmospheric samples which target CCQE interactions (S.G.
2000 e-like 0de, S.G. μ -like [0,1]de, [FHC,RHC] 1R μ -like and [FHC,RHC] 1R e-like
2001 samples), there is a very similar contribution of CCQE, CC 2p2h, and CC1 π^\pm in-
2002 teractions. The samples which target CC1 π^\pm interactions, (S.G. e-like 0de, S.G.
2003 μ -like 2de and FHC 1R+1d.e e-like) also consist of very similar mode interactions.

2004 As a consequence of the similarity in energy and mode contributions, correlating
2005 the systematic model between the beam and subGeV atmospheric samples ensures
2006 that this analysis attains the largest sensitivity to oscillation parameters while still
2007 ensuring neutrino interaction systematics are correctly accounted for. Due to its more
2008 sophisticated CCQE and 2p2h model, the T2K systematic model was chosen as the
2009 basis of the correlated model.

2010 The T2K systematic model [204] is applied in a similar methodology to the SK model
2011 parameters. It consists of 19 shape parameters and 24 normalisation parameters. Four
2012 additional parameters, which model the uncertainty in the binding energy, are applied
2013 in a way to shift the momentum of the lepton emitted from a nucleus. This controls
2014 the uncertainty specified on the 27MeV binding energy assumed within Equation 6.2.
2015 The majority of these parameters are assigned a Gaussian prior uncertainty. Those
2016 that have no reasonably motivated uncertainty, or those which have not been fit to
2017 external data, are assigned a flat prior which does not affect the penalty term.

2018 DB: Move to earlier section

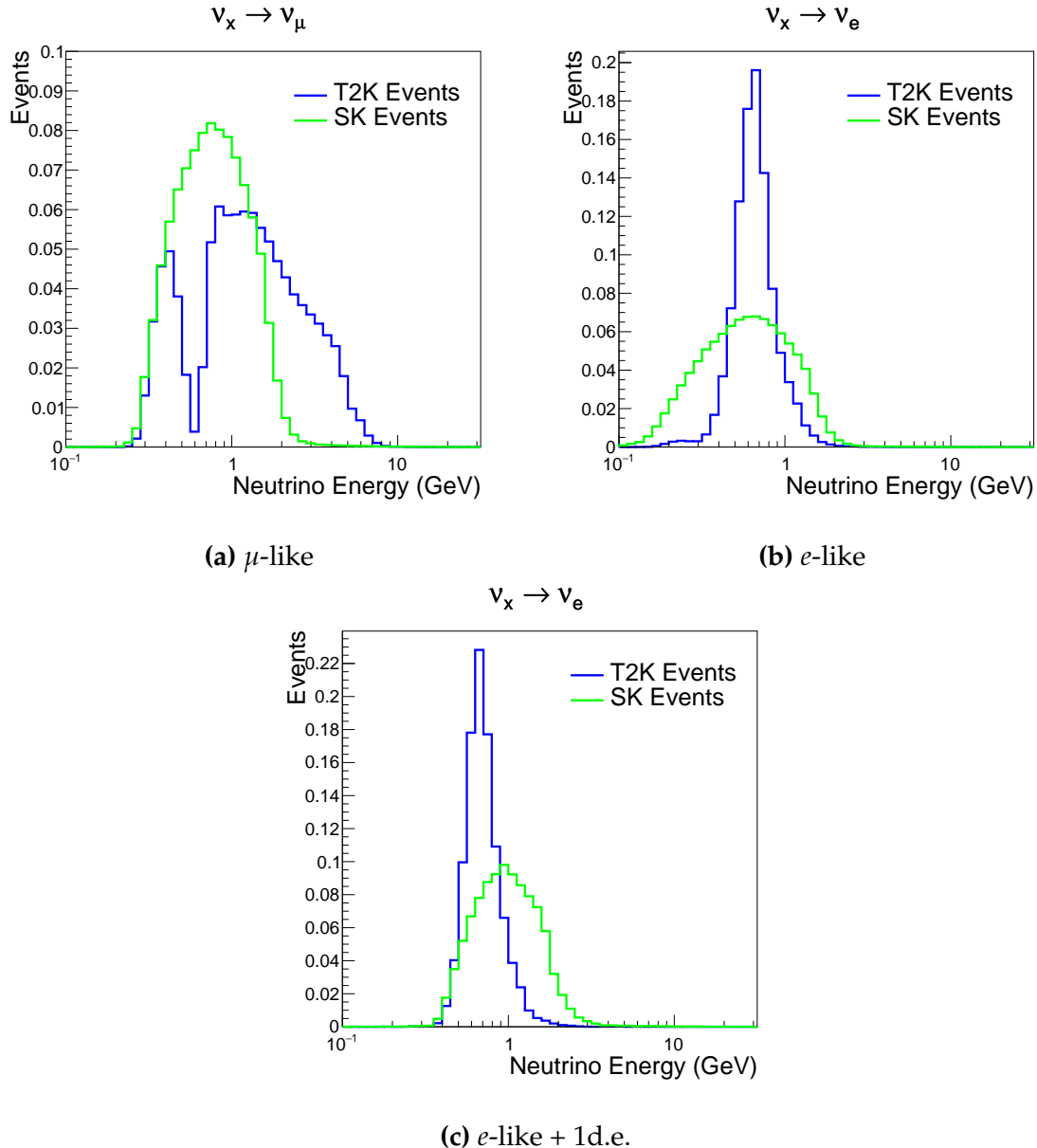


Figure 6.8.: The predicted neutrino energy distribution for subGeV atmospheric and beam samples. FHC and RHC beam samples are summed together Asimov A oscillation parameters are assumed (given in Table 2.2). Beam and atmospheric samples with similar cuts are compared against one another.

2019 There are three particular tunes of the T2K flux and low energy cross section model
 2020 typically considered. Firstly, the “generated” tune which is the set of dial values with
 2021 which the Monte Carlo was generated. Secondly, the set of dial values which are taken
 2022 from external data measurements and used as inputs. These are the “pre-fit” dial
 2023 values. The reason these two sets of dial values are different is that the external data

	CC QE	CC 2p2h	CC $1\pi^\pm$	CC $M\pi$	CC Other	NC π^0	NC $1\pi^\pm$	NC $M\pi$	NC Coh.	NC Other
FHC 1R+1d.e. e-like	0.04	0.02	0.83	0.03	0.04	0.01	0.01	0.01	0.00	0.01
RHC 1R e-like	0.62	0.12	0.11	0.01	0.02	0.06	0.01	0.01	0.01	0.04
FHC 1R e-like	0.68	0.12	0.10	0.00	0.02	0.04	0.01	0.00	0.00	0.02
RHC 1R μ -like	0.62	0.13	0.17	0.02	0.03	0.00	0.02	0.00	0.00	0.00
FHC 1R μ -like	0.62	0.12	0.16	0.02	0.03	0.00	0.03	0.00	0.00	0.00
S.G. π^0 -like	0.05	0.01	0.02	0.00	0.01	0.68	0.06	0.07	0.06	0.04
S.G. μ -like 2de	0.04	0.01	0.80	0.10	0.04	0.00	0.00	0.00	0.00	0.00
S.G. μ -like 1de	0.72	0.11	0.12	0.01	0.02	0.00	0.01	0.00	0.00	0.00
S.G. μ -like 0de	0.68	0.11	0.10	0.01	0.02	0.01	0.05	0.01	0.00	0.02
S.G. e-like 1de	0.05	0.01	0.75	0.10	0.05	0.00	0.01	0.02	0.00	0.01
S.G. e-like 0de	0.73	0.11	0.10	0.01	0.02	0.02	0.00	0.00	0.00	0.00

Figure 6.9.: The interaction mode contribution of each sample given as a fraction of the total event rate in that sample. Asimov A oscillation parameters are assumed (given in Table 2.2). The Charged Current (CC) modes are broken into quasi-elastic (QE), 2p2h, resonant charged pion production ($1\pi^\pm$), multi-pion production ($M\pi$), and other interaction categories. Neutral Current (NC) interaction modes are given in interaction mode categories: π^0 production, resonant charged pion production, multi-pion production, and others.

2024 measurements are continually updated but it is very computationally intensive to
 2025 regenerate a Monte Carlo prediction after each update. The final tune is the “post-fit”,
 2026 “post-ND fit” or “post-BANFF” dial values. These are the values taken from a fit to the
 2027 beam near detector data. This fit is performed by two independent fitting frameworks,
 2028 MaCh3 and BANFF, which ensures reliable measurements. The output of each fitter is
 2029 converted into a covariance matrix to describe the error and correlations between
 2030 all the flux and cross-section parameters. This is then propagated to the far-detector
 2031 oscillation analysis group for use in the P-Theta fitting framework. As MaCh3 can
 2032 perform a near detector fit, it is included within the simultaneous fit of the far-detector
 2033 beam and atmospheric oscillation analysis. This is because this technique does not

2034 require any assumption of Gaussian posterior distributions which is required in the
 2035 covariance matrix methodology.

2036 On top of the combination of the SK and T2K interaction models, several other
 2037 parameters have been specifically developed for the joint oscillation analysis. The
 2038 majority of the atmospheric samples' δ_{CP} sensitivity comes from the normalisation
 2039 of subGeV electron-like events. These are modeled using a spectral function **model**
 2040 to approximate the nuclear ground state. However, the near detector is not able to
 2041 constrain the model. **Therefore, so** an additional systematic is introduced which **mod-**
 2042 **els applies** an alternative Continuous Random Phase Approximation (CRPA) nuclear
 2043 ground state. **The reasoning is documented in ???.** **As the near detector can not suffi-**
 2044 **ciently constrain the model, this** This dial approximates the event weights if a CRPA
 2045 model had been assumed rather than a spectral function. This dial only **effects applies**
 2046 **to** ν_e and $\bar{\nu}_e$ **as the near detector does not constraint** ν_e cross-section measurements.
 2047 **and It** is applied as a shape parameter.

2048 Further additions to the model have been introduced due to the inclusion of the
 2049 subGeV π^0 atmospheric sample. This particularly targets charged current and neutral
 2050 current π^0 producing interactions to help constrain the systematic uncertainties. **There**
 2051 **is no analogous sample in the T2K beam-only analysis so no significant effort has**
 2052 **been placed into building a sufficient uncertainty model.** Therefore, an uncertainty
 2053 that affects neutral current resonant π^0 production is incorporated into this analysis.
 2054 Comparisons of NEUT's NC resonant pion production predictions have been made to
 2055 MiniBooNE [207] data and a consistent 16% to 21% underprediction is observed [205].
 2056 Consequently, a conservative 30% normalisation parameter is invoked.

2057 Down-going events are mostly insensitive to oscillation parameters and can act
 2058 similar to the near detector within an accelerator experiment (Details will be discussed
 2059 in chapter 7). This region of phase space can act as a sideband and allows the cross-

2060 section model and near detector constraint to be studied. The distribution of events
2061 in this region is calculated using the technique outlined in subsection 4.3.4. **The**
2062 **results are illustrated in Figure 6.10**. For CCQE-targeting samples, the application
2063 of the near detector constraint is well within the statistical fluctuation of the down-
2064 going data such that no significant tension is observed between the data and the
2065 Monte Carlo prediction after the near detector constraint is applied. This is not the
2066 case for samples with target CCRES interactions. The electron-like data is consistent
2067 with the constrained prediction at high reconstructed momenta but diverges at lower
2068 momentum, whereas the muon-like sample is under-predicted throughout the range
2069 of momenta. To combat this disagreement, an additional cross-section systematic dial,
2070 specifically designed to inflate the low pion momentum systematics was developed
2071 in [205]. This is a shape parameter implemented through a splined response.

2072 6.4.4. Near Detector

2073 The systematics applied due to uncertainties arising from the response of the near
2074 detector is documented in [133]. The response is described by 574 normalisation param-
2075 eters binned in the selected sample as well as momentum and angle, P_μ and $\cos(\theta_\mu)$,
2076 of the final-state muon. These are applied via a covariance matrix with each parameter
2077 being assigned a Gaussian prior from that covariance matrix. These normalisation
2078 parameters are built from underlying systematics, e.g. pion secondary interaction
2079 systematics, which are randomly thrown and the variation in each $P_\mu \times \cos(\theta_\mu)$ bin is
2080 determined. Two thousand throws are evaluated and a covariance matrix response is
2081 created. This allows significant correlations between FGD1 and FGD2 samples, as well
2082 as adjacent $P_\mu \times \cos(\theta_\mu)$ bins. Statistical uncertainties are accounted for by including
2083 fluctuations of each event's weight from a Poisson distribution.

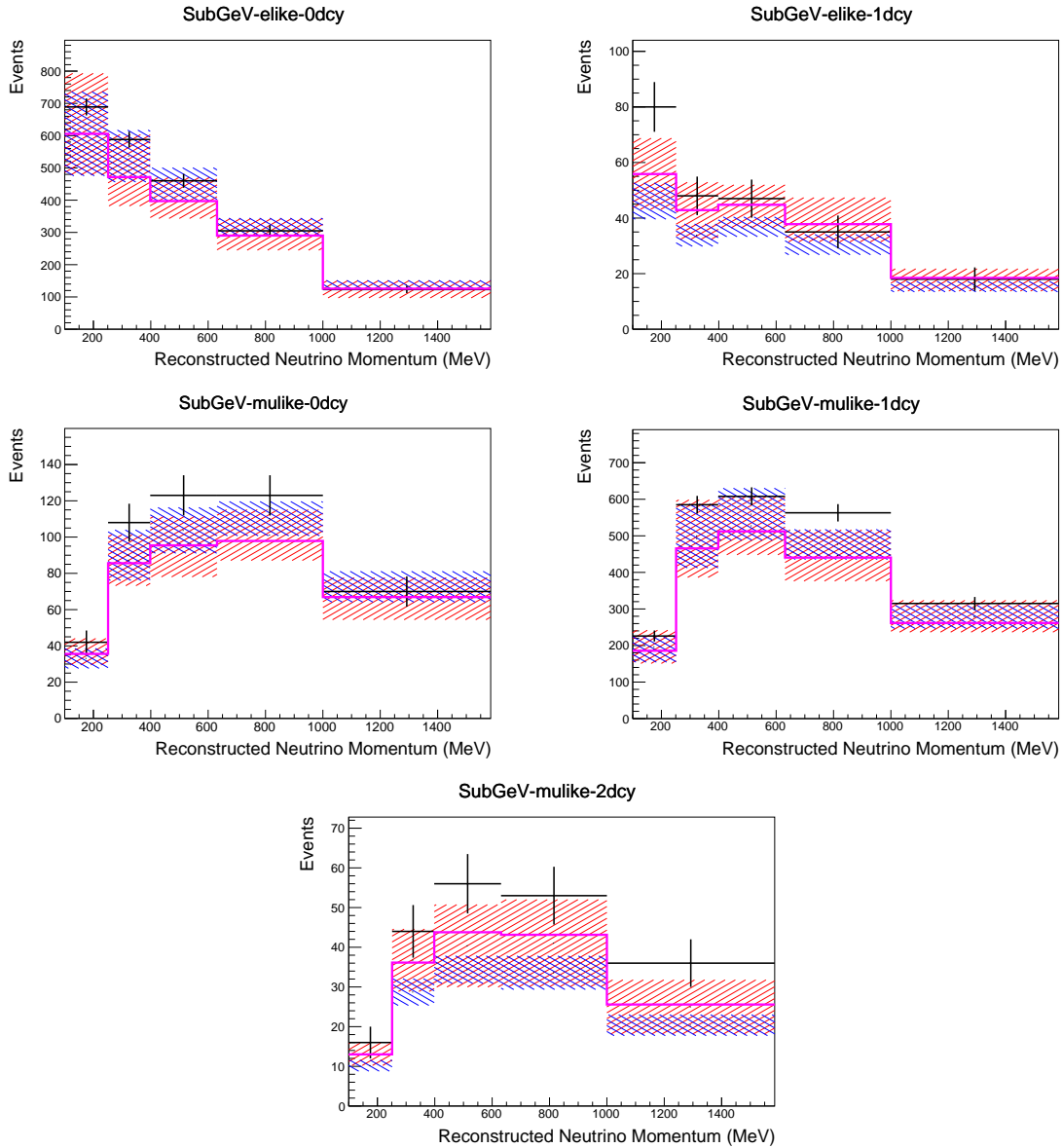


Figure 6.10.: Down-going atmospheric subGeV single-ring samples comparing the mean and error of the pre-fit and post-fit Monte Carlo predictions in red and blue, respectively. The magenta histogram illustrates the Monte Carlo prediction using the generated dial values. The black points illustrate the down-going data with statistical errors given. The mean and errors of the Monte Carlo predictions are calculated by the techniques documented in subsection 4.3.4. The pre-fit spectrum is calculated by throwing the cross-section and atmospheric flux dial values from the pre-fit covariance matrix. The post-fit spectrum is calculated by sampling the cross-section dial values from an ND fit MCMC chain, whilst still throwing the atmospheric flux dials from the pre-fit covariance.

Similar to the cross-section systematics, MaCh3 and BANFF are used to constrain
the uncertainty of these systematics through independent validations. Each fitter

2086 generates a post-fit covariance matrix which is compared and passed to the far-detector
2087 oscillation analysis working group. As the analysis presented within this thesis uses
2088 the MaCh3 framework, a joint oscillation analysis fit of all three sets of samples and
2089 their respective systematics is performed.

2090 **6.4.5. Far Detector**

2091 Two configurations of the far detector systematic model implementation have been
2092 considered. Firstly, the far detector systematic uncertainties for beam and atmospheric
2093 samples are taken from their respective analysis inputs, denoted “official inputs” anal-
2094 ysis. Consequently, no correlations are assumed between the beam and atmospheric
2095 samples. The generation of the beam- and atmospheric-specific inputs are documented
2096 in subsubsection 6.4.5.1 and subsubsection 6.4.5.2. Secondly, a correlated detector
2097 model has been developed. Here, the distribution of parameters used for applying
2098 event cuts (e.g. electron-muon PID separation) is modified within the fit. It follows
2099 a similar methodology to the beam far detector systematics implementation but per-
2100 forms a joint fit of the beam and atmospheric data. This alternative implementation is
2101 detailed in subsubsection 6.4.5.3.

2102 **6.4.5.1. Beam Samples**

2103 There are 45 systematics which describe the response of the far detector to beam
2104 events [185], split into 44 normalisation parameters and one energy scale systematic.
2105 The energy scale systematic is applied as a multiplicative scaling of the reconstructed
2106 neutrino energy. It is described by a Gaussian, centered at one with equal to the
2107 difference in Monte Carlo to data comparisons performed in [187]. The normalisation
2108 parameters are assigned a Gaussian error centralised at one with width taken from a

2109 covariance matrix. A detailed breakdown of the generation of the covariance matrix
2110 is found in [199]. To build the covariance matrix, a fit is performed on atmospheric
2111 data which has been selected using beam sample selection cuts. These cuts use the
2112 variables, L_j^i , where the index i is detailed in Table 6.6. Each L_j^i is a smear, α , and shift,
2113 β parameter such that,

$$L_j^i \rightarrow \bar{L}_j^i = \alpha_j^i L + \beta_j^i \quad (6.4)$$

2114 Where L_j^i (\bar{L}_j^i) correspond to nominal(varied) PID cut parameters given in Table 6.6.
2115 The shift and smear parameters are binned by final-state topology, j , where the binning
2116 is given in Table 6.7. The final-state topology binning is because the detector will
2117 respond differently to events that have one or multiple rings. For example, the detector
2118 will be able to distinguish single-ring events better than two overlapping ring events,
2119 resulting in smaller systematic uncertainty for one-ring events compared to two-ring
2120 events. This approach is used to allow the cut parameter distributions to be modified
2121 within the fit, allowing for better data to Monte Carlo agreement. Only the shape
2122 of each of the cut variables is used within this fit, such that physics effects are not
2123 considered.

Cut Variable	Parameter Name
0	<code>fitQun e/mu PID</code>
1	<code>fitQun e/pi^0 PID</code>
2	<code>fitQun mu/pi PID</code>
3	<code>fitQun Ring-Counting Parameter</code>

Table 6.6.: List of cut variables that are included within the shift/smear fit documented in [199].

2124 Beyond the uncertainty on the PID cut criteria, the mis-modeling of π^0 events
2125 is also considered. If one of the two rings from a π^0 event is missed, this will be

Category	Description
$1e$	Only one electron above Cherenkov threshold in the final state
1μ	Only one muon above Cherenkov threshold in the final state
$1e+other$	One electron and one or more other charged particles above Cherenkov threshold in the final state
$1\mu+other$	One muon and one or more other charged particles above Cherenkov threshold in the final state
$1\pi^0$	Only one π^0 in the final state
$1\pi^\pm$ or $1p$	Only one hadron (typically charged pion or proton) in the final state
Other	Any other final state

Table 6.7.: Reconstructed event topology categories on which the SK detector systematics [199] are based.

reconstructed as a $CC\nu_e$ -like event. This is one of the largest systematics hindering the electron neutrino appearance analyses. Consequently, additional systematics has been introduced to constrain the mis-modeling of π^0 events in SK, binned by reconstructed neutrino energy. To evaluate this systematic uncertainty, a set of “hybrid- π^0 ” samples is constructed. These events are built by overlaying one electron-like ring from the SK atmospheric neutrino samples or decay electron ring from a stopping cosmic ray muon with one simulated photon ring. Both rings are chosen so that momenta and opening angle follow the decay kinematics of NC π^0 events from the T2K-MC. Hybrid- π^0 Monte Carlo samples with both rings from the SK Monte Carlo are produced to compare with the hybrid- π^0 data samples and the difference in the fraction of events that pass the ν_e selection criteria is used to assign the systematic errors. In order to investigate any data to Monte Carlo differences that may originate from either the higher energy ring or lower energy ring, two samples are built; a sample in which the electron constitutes the higher energy ring from the π^0 decay called the primary sample and another one in which it constitutes the lower energy ring called the secondary sample. The standard T2K ν_e fitQun event selection criteria are used to select events.

2143 Final contributions to the covariance matrix are determined by supplementary
 2144 uncertainties attained by comparing stopping muon data to Monte Carlo prediction,
 2145 as first introduced in section 5.2. The efficiency of tagging decay electrons is estimated
 2146 by the stopping muon data to Monte Carlo differences by comparing the number
 2147 of one decay electron events to the number of events with one or fewer decay elec-
 2148 trons. Similarly, the rate at which fake decay electrons are reconstructed by `fitQun`
 2149 is estimated by comparing the number of two decay electron events to the number
 2150 of events with one or two reconstructed decay electrons. The two sources of sys-
 2151 tematics are added in quadrature weighted by the number of events with one true
 2152 decay electron yielding a 0.2% systematic uncertainty. A fiducial volume systematic of
 2153 $\pm 2.5\text{cm}$ which corresponds to a 0.5% shift in the normalisation of events. Additional
 2154 normalisation uncertainties based on neutrino flavour and interaction mode are also
 2155 defined in [185, 208, 209].

2156 Two additional sources of uncertainty are included: secondary and photo-nuclear
 2157 interactions. These are estimated by varying the underlying parameters are building a
 2158 distribution of sample event rates. These contributions are then added in quadrature
 2159 to the above covariance matrix.

2160 6.4.5.2. Atmospheric Samples

2161 The systematic parameters which control the detector systematics for atmospheric
 2162 samples, documented in [89], are split into two sub-groups. Those which are related
 2163 to particle identification and ring counting systematics and those which are related to
 2164 calibration, separation, and reduction uncertainties.

2165 The particle identification systematics consist of five parameters. The ring sepa-
 2166 ration systematic enforces an anti-correlated response between the single-ring and
 2167 multi-ring samples. This is implemented as a fractional increase/decrease in the

2168 overall normalisation of each sample, depending on the distance to the nearest wall
2169 from an event’s vertex. The coefficients of the normalisation are estimated prior to the
2170 fit and depend on the particular atmospheric sample. The single-ring and multi-ring
2171 PID systematics encode the detector’s ability to separate electron-like and muon-like
2172 events and are implemented in a similar way to the ring separation systematic.

2173 The multi-ring electron-like separation likelihood, discussed in section 6.1, encodes
2174 the ability of the detector to separate neutrino from anti-neutrino events. As an impor-
2175 tant systematic in the mass hierarchy determination, systematic uncertainties control
2176 the relative normalisations of the ν_e and $\bar{\nu}_e$ enriched samples. Two normalisation
2177 parameters are implemented which vary the event rate of each multi-ring sample,
2178 whilst ensuring the total event rate is conserved.

2179 There are 22 systematics related to calibration measurements, including effects
2180 from backgrounds, reduction, and showering effects. They are documented in [89] and
2181 briefly summarised in Table 6.8. They are applied via normalisation parameters, with
2182 the separation systematics requiring the conservation of event rate across all samples.

2183 **6.4.5.3. Correlated Detector Model**

2184 A complete uncertainty model of the SK detector would be able to determine the
2185 systematic shift on the sample spectra for a variation of the underlying parameters,
2186 e.g. PMT angular acceptance. However, this is computationally intensive, requiring
2187 Monte Carlo predictions to be made for each plausible variation. Consequently, an
2188 effective parameter model has been utilised for a correlated detector model following
2189 from the T2K-only model implementation documented in subsubsection 6.4.5.1. The
2190 implementation performs a simultaneous fit of detector and oscillation parameters,
2191 for the detector parameters given in Table 6.6.

Table 6.8.: Sources of systematic errors specified within the grouped into the “calibration” systematics model.

Index	Description
0	Partially contained reduction
1	Fully contained reduction
2	Separation of fully contained and partially contained events
3	Separation of stopping and through-going partially contained events in top of detector
4	Separation of stopping and through-going partially contained events in barrel of detector
5	Separation of stopping and through-going partially contained events in bottom of detector
6	Background due to cosmic rays
7	Background due to flasher events
8	Vertex systematic moving events into and out of fiducial volume
9	Upward going muon event reduction
10	Separation of stopping and through-going in upward going muon events
11	Energy systematic in upward going muon events
12	Reconstruction of the path length of upward going muon events
13	Separation of showering and non-showering upward going muon events
14	Background of stopping upward going muon events
15	Background of non-showering through-going upward going muon events
16	Background of showering through-going upward going muon events
17	Efficiency of tagging two rings from π^0 decay
18	Efficiency of decay electron tagging
19	Background from downgoing cosmic muons
20	Asymmetry of energy deposition in tank
21	Energy scale deposition

2192 The correlated detector model utilises the same smear and shift parameters docu-
2193 mented in subsubsection 6.4.5.1, split by final state topology. Beyond this, the shift
2194 and smear parameters are split by visible energy deposited within the detector, with
2195 binning specified in Table 6.9. This is because atmospheric events are categorised by
2196 subGeV and multiGeV events based on visible energy, so this splitting is required

2197 when correlating the systematic model for beam and atmospheric events. Alongside
2198 the technical requirement, higher energy events will be better reconstructed due to
2199 fractionally less noise within the detector. This implementation correlates the detector
2200 systematics between the far-detector beam and subGeV atmospheric samples due
2201 to their similar energies and interaction types. As a result of the inclusion of visible
2202 energy binning, Equation 6.4 becomes

$$L_{jk}^i \rightarrow \bar{L}_{jk}^i = \alpha_{jk}^i L + \beta_{jk}^i, \quad (6.5)$$

2203 where k is the visible energy bin. As there are no equivalent beam samples, the
2204 multiGeV, multiring, PC, and Up- μ samples will be subject to the ATMPD particle
2205 identification systematics implementation as described in subsubsection 6.4.5.2 rather
2206 than using this correlated detector model. The calibration systematics also described
2207 in the aforementioned chapter still apply to all atmospheric samples.

Index	Range (MeV)
0	$30 \geq x > 300$
1	$300 \geq x > 700$
2	$700 \geq x > 1330$
3	$1330 \geq x$

Table 6.9.: Visible energy binning for which the correlated SK detector systematics are based

2208 The implementation of this systematic model takes the events reconstructed values
2209 of the cut parameters, modifies them by the particular shift and smear parameter for
2210 that event, and then re-applies event selection. This invokes event migration, which is
2211 a new feature incorporated into the MaCh3 framework which is only achievable due
2212 to the event-by-event reweighting scheme.

Particular care has to be taken when varying the ring counting parameter. This is because the number of rings is a finite value (one-ring, two-rings, etc.) which can not be continuously varied through this shift and smear technique. Consequently a ring counting parameter, RC_i , is calculated for the i^{th} event, following the definition in [184]. The likelihood from all considered one-ring (L_{1R}) and two-ring (L_{2R}) fits are compared to determine the preferred hypothesis. The difference is computed as $\Delta_{LLH} = \log(L_{1R}) - \log(L_{2R})$. The ring counting parameter is then defined as,

$$RC_i = \text{sgn}(\Delta_{LLH}) \times \sqrt{|\Delta_{LLH}|}, \quad (6.6)$$

where $\text{sgn}(x) = x/|x|$. This ring counting parameter corresponds to an intermediate likelihood value used within the `fitQun` algorithm to decide the number of rings associated with a particular event. However, fake-ring merging algorithms are applied after this likelihood value is used. Consequently, this ring counting parameter does not always exactly correspond to the number of reconstructed rings. This can be seen in Figure 6.11.

As the `fitQun` algorithm does not provide a likelihood value after the fake-ring algorithms have been applied, the ring counting parameter distribution is correlated to the final number of reconstructed rings through “maps”. These are two-dimensional distributions of the ring counting parameter and the final number of reconstructed rings. An example is illustrated in Figure 6.12. In principle, the `fitQun` reconstruction algorithm should be re-run after the variation in the ring counting parameter. However, this is not computationally viable. Therefore the “maps” are used as a reweighting template.

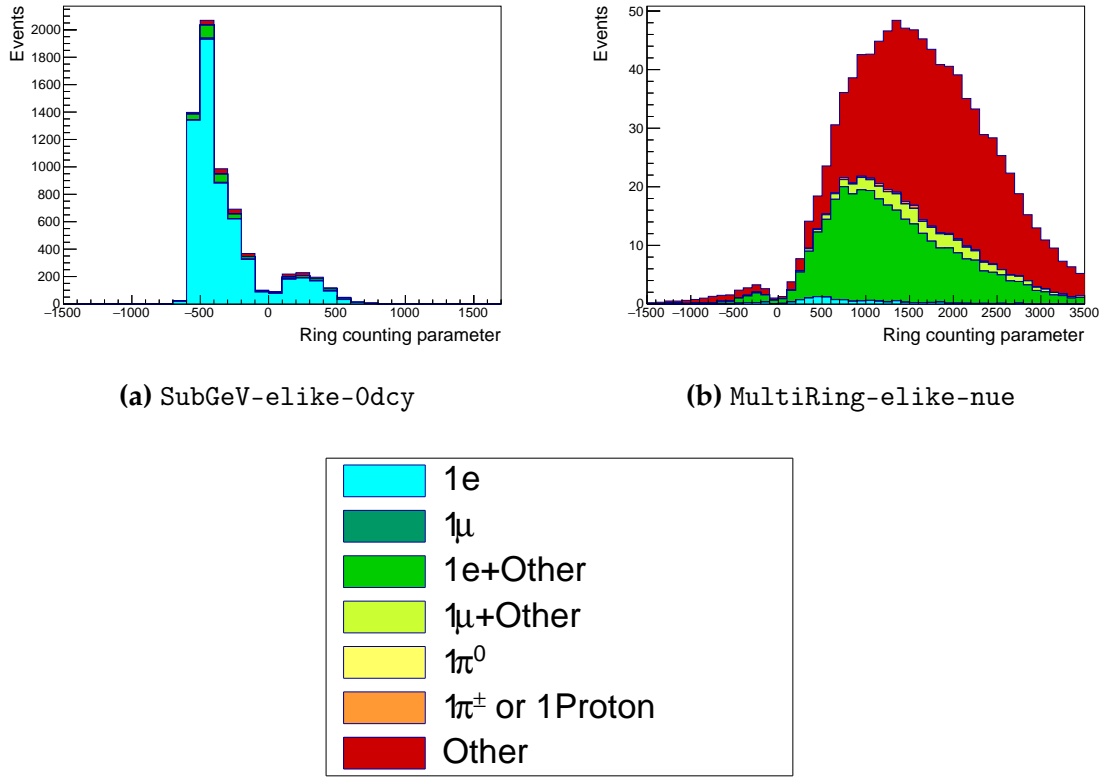


Figure 6.11.: The ring counting parameter as defined in Equation 6.6 for the SubGeV-else-0dcy and MultiRing-else-nue samples.

The maps are split by final state topology and true neutrino flavour and all fiTQun-reconstructed Monte Carlo events are used to fill them. The maps are row-normalised to represent the probability of X number of rings for a given RC_i value. Prior to the fit, an event's nominal weight is calculated as $W^i(N_{Rings}^i, L_{jk}^i)$, where N_{Rings}^i is the reconstructed number of rings for the i^{th} event and $W^i(x, y)$ is the bin content in map associated with the i^{th} event, where x number of rings and y is ring counting parameter. Then during the fit, the value of $R = W^i(N_{Rings}^i, \bar{L}_{jk}^i) / W^i(N_{Rings}^i, L_{jk}^i)$ is calculated as the event weight for the i^{th} event. This is the only cut variable that uses a reweighting scheme rather than event migration.

The π^0 systematics introduced in subsection 6.4.4 are applied via a covariance matrix. This is not possible in the alternative model as no covariance matrix is used. Thus, the implementation of the π^0 systematics has been modified. The inputs from

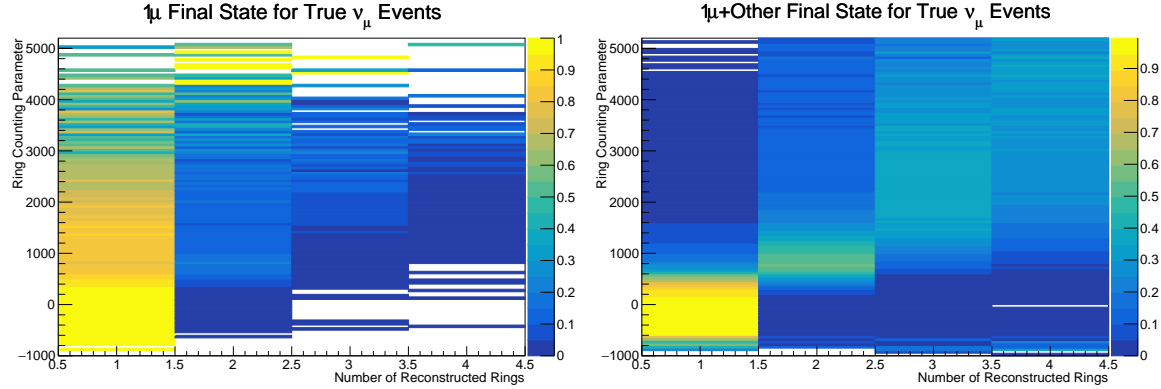


Figure 6.12.: The ring counting parameter, defined in Equation 6.6, as a function of the number of reconstructed rings as found by the `fitQun` reconstruction algorithm. Left: true ν_μ events with only one muon above the Cherenkov threshold in the final state. Right: true ν_μ events with one muon and at least one other charged particle above the Cherenkov threshold in the final state.

the hybrid π^0 sample is included via the use of “ χ^2 maps”, which are two-dimensional histograms in α_{jk}^i and β_{jk}^i parameters over some range. Illustrative examples of the χ^2 maps are given in Figure 6.13. Due to their nature, the shift and smear parameters are typically very correlated. A map is produced for each cut parameter given in Table 6.6 and for each visible energy bin given in Table 6.9.

The maps are filled through the χ^2 comparison of the hybrid π^0 Monte Carlo and data in the particle identification parameters documented in Table 6.6. The Monte Carlo distribution is modified by the α_{jk}^i and β_{jk}^i scaling, whilst cross-section and flux nuisance parameters are thrown from their prior uncertainties. The χ^2 between the scaled Monte Carlo and data is calculated and the relevant point in the χ^2 map is filled.

The implementation within this alternative detector model is to add the bin contents of the maps, for the relevant values of the α_{jk}^i and β_{jk}^i parameters, to the likelihood penalty. Only $1\pi^0$ final state topology shift and smear parameters use this prior uncertainty.

Similarly, the implementation of the supplementary systematics documented in subsubsection 6.4.5.1 needs to be modified. A new framework [210] was built in

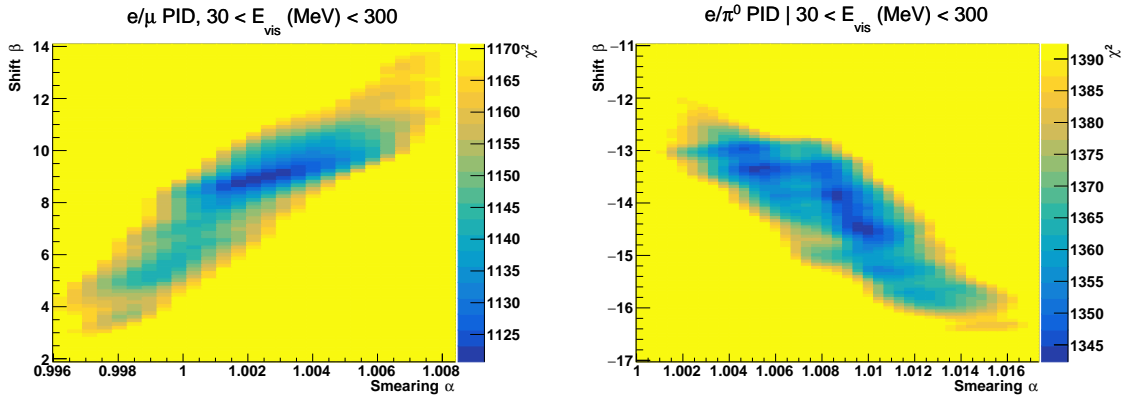


Figure 6.13.: The χ^2 between the hybrid- π^0 Monte Carlo and data samples, as a function of smear (α) and shift (β) parameters, for events which have $1\pi^0$ final state topology. Left: Electron-muon separation PID parameter for events with $30 \geq E_{vis}(\text{MeV}) < 300$. Right: Electron- π^0 separation PID parameter for events with $30 \geq E_{vis}(\text{MeV}) < 300$.

tandem with the T2K-SK working group [185] so the additional parameters can be incorporated into the MaCh3 framework. These are applied as normalisation parameters, depending on the particular interaction mode, number of tagged decay electrons, and whether the primary particle generated Cherenkov light. They are assigned Gaussian uncertainties with widths described by a covariance matrix. Furthermore, the secondary interaction and photo-nuclear effects need to be accounted for in this detector model using a different implementation than that in subsubsection 6.4.5.1. This was done by including a shape parameter for each of the secondary interactions and the photo-nuclear systematic parameters.

There are a total of 224 α_{jk}^i and β_{jk}^i parameters, of which 32 have prior constraints from the hybrid π^0 samples.

One final complexity of this correlated detector model is that the two sets of samples, beam and subGeV atmospheric, use slightly different parameters to distinguish electron and muon-like events. The T2K samples use the value of $\log(L_e/L_\mu)$ whereas the atmospheric samples use the value of $\log(L_e/L_\pi)$, where L_X is the likelihood for hypothesis X. This is because the T2K fits use single-ring `fitQun` fitting techniques, whereas multi-ring fits are applied to the atmospheric samples where only the electron

²²⁷⁹ and pion hypothesis are considered. The correlation between the two likelihood ratios
²²⁸⁰ is illustrated in Figure 6.14. As discussed in section 5.2, the pion hypothesis is a very
²²⁸¹ good approximation of the muon hypothesis due to their similar mass. Consequently,
²²⁸² using the same shift and smear parameters correlated between the beam and subGeV
²²⁸³ atmospheric samples is deemed a good approximation.

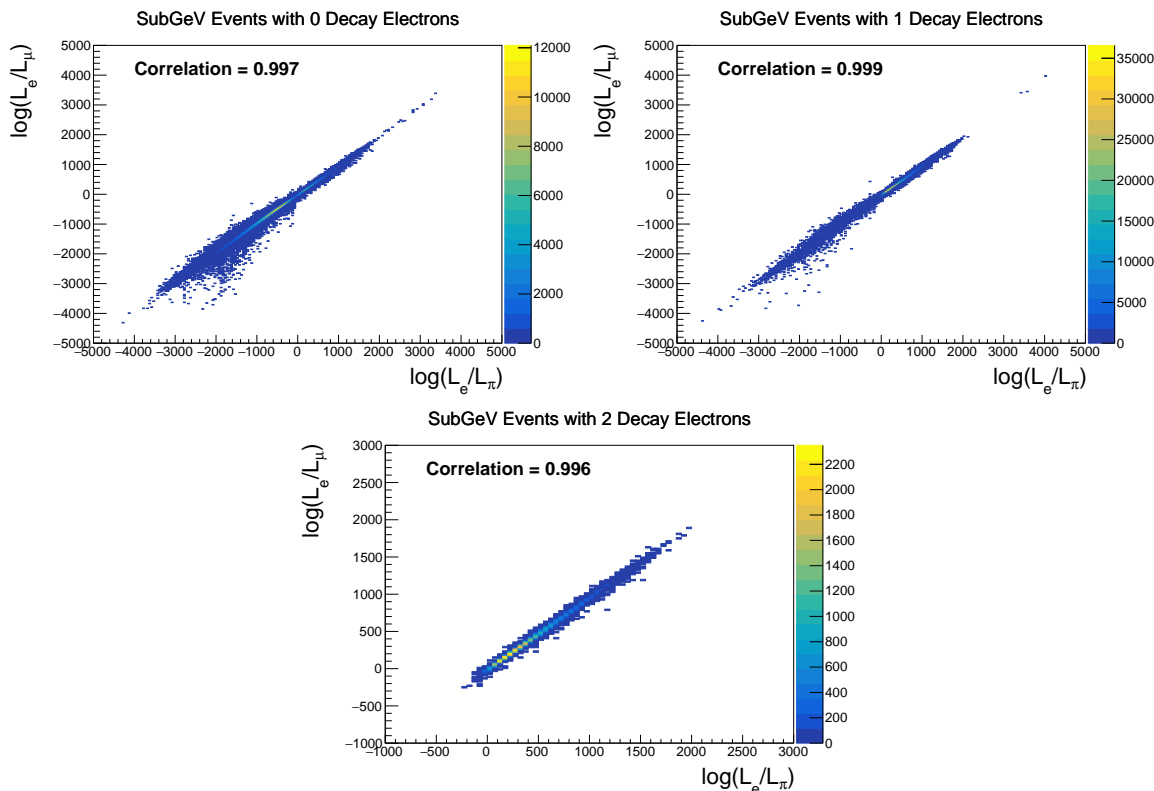


Figure 6.14.: The distribution of $\log(L_e/L_\mu)$ compared to $\log(L_e/L_\pi)$ for subGeV events with zero (top left), one (top right) or two (bottom) decay electrons. The correlation in the distribution is calculated as 0.997, 0.999 and 0.996, respectively.

2284

Chapter 7

2285

Oscillation Probability Calculation

2286 It is important to understand how and where the sensitivity to the oscillation parame-
2287 ters comes from for both atmospheric and beam samples. An overview of how these
2288 samples observe changes in δ_{CP} , Δm_{23}^2 , and $\sin^2(\theta_{23})$ **affect these samples** is given
2289 in section 7.1. **If This section** also explains the additional complexities involved when
2290 performing an atmospheric neutrino analysis as compared to a beam-only analysis.

2291 Without additional techniques, atmospheric sub-GeV upward-going neutrinos
2292 ($E_\nu < 1.33\text{GeV}, \cos(\theta_Z) < 0.$) can artificially inflate the sensitivity to δ_{CP} due to the
2293 quickly varying oscillation probability in this region. Therefore, a “sub-sampling”
2294 approach has been developed to reduce these biases ensuring accurate and reliable
2295 sensitivity measurements. This technique ensures that small-scale unresolvable fea-
2296 tures of the oscillation probability have been averaged over whilst the large-scale
2297 features in the oscillation probability are unaffected. The documentation and valida-
2298 tion of this technique are found in section 7.2. The oscillation probability calculation is
2299 computationally intensive due to the large number of matrix multiplications needed.
2300 Consequently, the CUDAProb3 implementation choice made within the fitting frame-
2301 work, as detailed in section 7.3, ensures that the analysis can be done in a timely
2302 manner.

2303 Whilst the beam neutrinos are assumed to propagate through a constant density
2304 slab of material, the density variations through the Earth result in more complex
2305 oscillation patterns **for atmospheric neutrinos**. Furthermore, the uncertainty in the
2306 electron density can modify the oscillation probability for the denser core layers of the

2307 Earth. The model of the Earth used within this analysis is detailed in section 7.4. This
2308 includes information about the official SK-only methodology as well as improvements
2309 that **can be have been** made to remove some of the approximations **made used** in that
2310 analysis. Another complexity of atmospheric neutrinos oscillation studies is that the
2311 height of production in the atmosphere is not known on an event-by-event basis. An
2312 analytical averaging technique that approximates the uncertainty of the oscillation
2313 probability has been followed, with the author of this thesis being responsible for
2314 the implementation and validation. This implementation of an external technique is
2315 illustrated in section 7.5.

2316 7.1. Overview

2317 DB: Should this be moved into an earlier chapter? The selections chapter references
2318 the matter resonance which has not yet been explained at that point

2319 The analysis presented within this thesis focuses on the determination of oscillation
2320 parameters from atmospheric and beam neutrinos. Whilst subject to the same oscil-
2321 lation formalism, the way in which the two samples have sensitivity to the different
2322 oscillation parameters differs **quite** significantly.

2323 Atmospheric neutrinos have a varying baseline, or “path length”, L , such that
2324 the distance each neutrino travels before interacting is dependent upon the zenith
2325 angle, θ_Z . As primary cosmic rays can interact anywhere between the Earth’s surface
2326 and $\sim 50\text{km}$ above that, the height, h , in the atmosphere at which the neutrino was
2327 generated also affects the path length,

$$L = \sqrt{(R_E + h)^2 - R_E^2 (1 - \cos^2(\theta_Z))} - R_E \cos(\theta_Z). \quad (7.1)$$

2328 Where $R_E = 6,371\text{km}$ is the Earth's radius. Consequently, the oscillation probability
 2329 is dependent upon two parameters, $\cos(\theta_Z)$ and E_ν .

2330 The oscillation probability used within this analysis is based on [21]. The neutrino
 2331 wavefunction in the vacuum Hamiltonian evolves in each layer of constant matter
 2332 density via

$$i \frac{d\psi_j(t)}{dt} = \frac{m_j^2}{2E_\nu} \psi_j(t) - \sum_k \sqrt{2} G_F N_e U_{ej} U_{ke}^\dagger \psi_k(t), \quad (7.2)$$

2333 where m_j^2 is the square of the j^{th} vacuum eigenstate mass, E_ν is the neutrino
 2334 energy, G_F is Fermi's constant, N_e is the electron number density and U is the PMNS
 2335 matrix. The transformation $N_e \rightarrow -N_e$ and $\delta_{CP} \rightarrow -\delta_{CP}$ is applied for antineutrino
 2336 propagation. Thus, a model of the Earth's density is required for **atmospheric** neutrino
 2337 propagation. Following the official SK-only methodology [211], this analysis uses
 2338 the Preliminary Reference Earth Model (PREM) [212]. **This model which** provides
 2339 piecewise cubic polynomials as a function of the Earth's radius. **which results in the**
 2340 **This** density profile **is** illustrated in Figure 7.1. As **discussed**, the propagator requires
 2341 layers of constant density. **The , the** SK methodology approximates the PREM model
 2342 by using four layers of constant density [211]. **The details of these layers are**, detailed
 2343 in Table 7.1.

2344 The atmospheric neutrino oscillation probabilities can be presented as two di-
 2345 mensional "oscillograms" as illustrated in Figure 7.2. The distinct discontinuities,

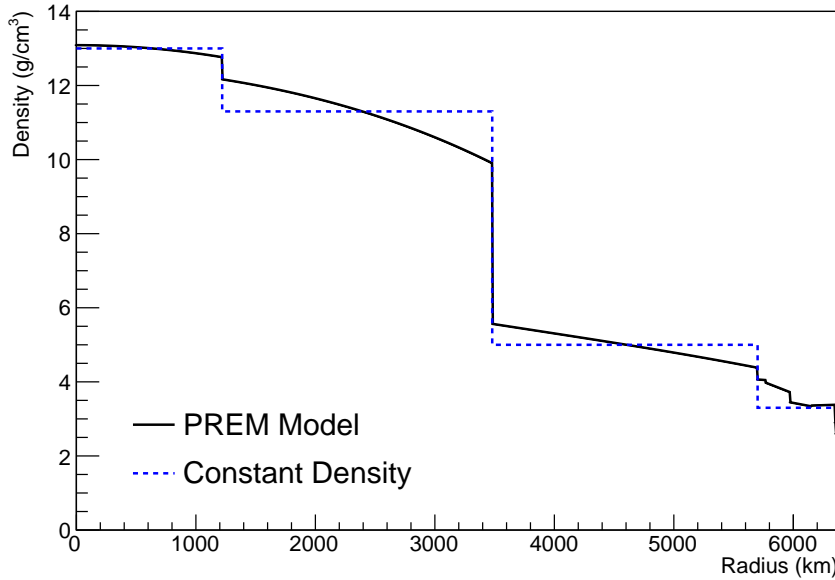


Figure 7.1.: The density of the Earth given as a function of the radius, as given by the PREM model (Black), and the constant density four-layer approximation (Blue), as used in the official SK-only analysis.

Layer	Outer Radius [km]	Density [g/cm ³]	Chemical composition (Z/A)
Inner Core	1220	13	0.468 ± 0.029
Outer Core	3480	11.3	0.468 ± 0.029
Lower Mantle	5701	5.0	0.496
Transition Zone	6371	3.3	0.496

Table 7.1.: Description of the four layers of the Earth invoked within the constant density approximation of the PREM model [212].

²³⁴⁶ as a function of $\cos(\theta_Z)$, are due to the **discrete change in density invoked within**
²³⁴⁷ **discontinuous density** in the PREM model.

²³⁴⁸ Atmospheric neutrinos have sensitivity to δ_{CP} through **a normalisation term**
²³⁴⁹ **the overall event rate**. Figure 7.3 illustrates the difference in oscillation probability
²³⁵⁰ between CP-conserving ($\delta_{CP} = 0$) and a CP-violating ($\delta_{CP} = -1.601$) value taken
²³⁵¹ from Asimov A oscillation parameter set (Table 2.2). The result is a complicated
²³⁵² oscillation pattern in the appearance probability for sub-GeV upgoing neutrinos. The
²³⁵³ detector does not have sufficient resolution to resolve these individual patterns so the

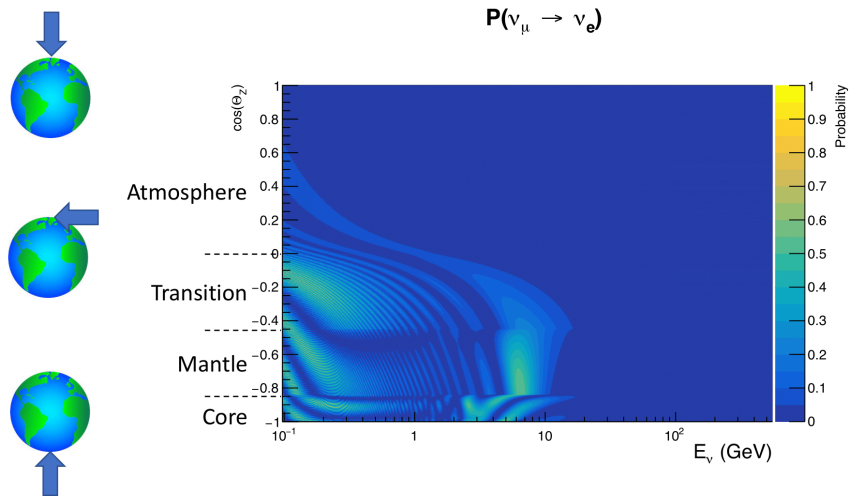


Figure 7.2.: An “oscillogram” that depicts the $P(\nu_\mu \rightarrow \nu_e)$ oscillation probability as a function of neutrino energy and cosine of the zenith angle. The zenith angle is defined such that $\cos(\theta_Z) = 1.0$ represents neutrinos that travel from directly above the detector. The four-layer constant density PREM model approximation is used and Asimov A oscillation parameters are assumed (Table 2.2).

2354 sensitivity to δ_{CP} for atmospheric neutrinos comes via the overall normalisation of
 2355 these events.

2356 **Below paragraph has been reworded**

2357 The presence of matter means that the effect δ_{CP} has on the oscillation probabil-
 2358 ity is not equal between neutrinos and antineutrinos. Furthermore, the interaction
 2359 cross-section for neutrinos is larger than antineutrinos so the two effects have to be
 2360 disentangled. These effects are further convoluted by detector efficiencies as SK cannot
 2361 distinguish neutrinos and antineutrinos well. Furthermore, the sample selections dis-
 2362 cussed in section 6.1 have difference efficiencies for neutrino-antineutrino selections.
 2363 All of these effects lead to a difference in the number of neutrinos detected compared
 2364 to antineutrinos. This changes how the δ_{CP} normalisation term is observed, resulting
 2365 in a very complex sensitivity to δ_{CP} .

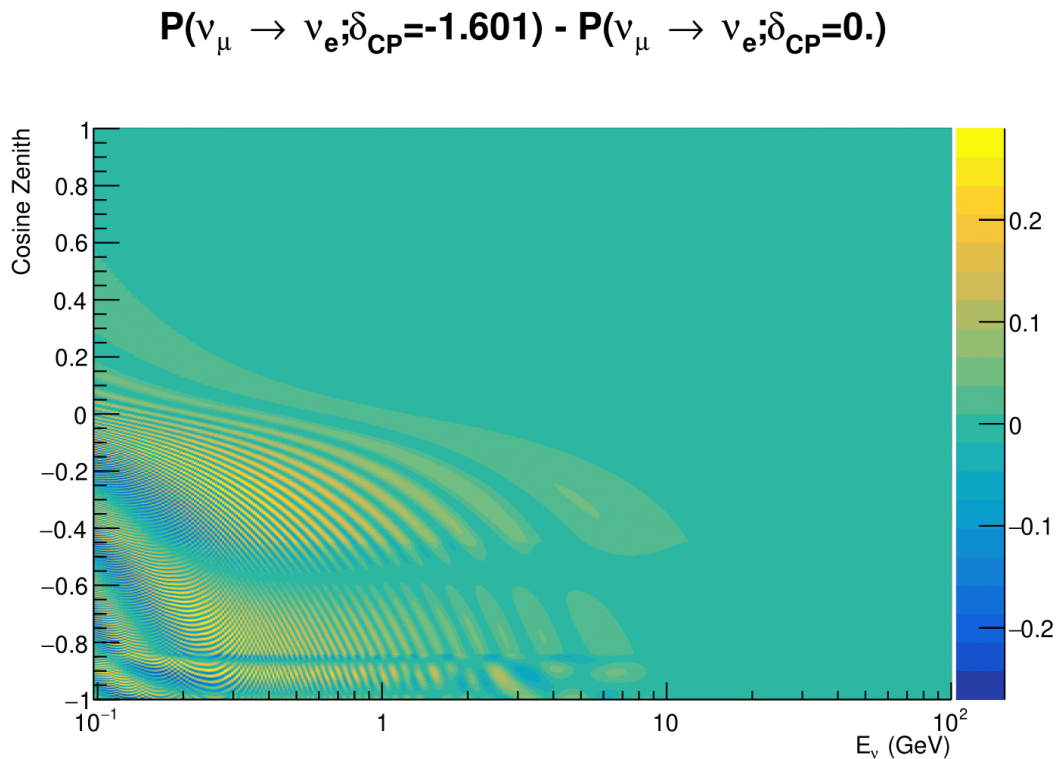


Figure 7.3.: The effect of δ_{CP} for atmospheric neutrinos given in terms of the neutrino energy and zenith angle. This oscillogram compares the $P(\nu_\mu \rightarrow \nu_e)$ oscillation probability for a CP conserving ($\delta_{CP} = 0.0$) and a CP violating ($\delta_{CP} = -1.601$) value taken from the Asimov A parameter set. The other oscillation parameters assume the Asimov A oscillation parameter set given in Table 2.2.

2366 Atmospheric neutrinos are subject to matter effects as they travel through the
 2367 dense matter in the Earth. The vacuum and matter oscillation probabilities for $P(\nu_e \rightarrow$
 2368 $\nu_e)$ and $P(\bar{\nu}_e \rightarrow \bar{\nu}_e)$ are presented in Figure 7.4, where the PREM model has been
 2369 assumed. The oscillation probability for both neutrinos and antineutrinos is affected
 2370 in the presence of matter. However, the resonance effects around $O(5)\text{GeV}$ only occur
 2371 for neutrinos in normal mass hierarchy and antineutrinos in inverse mass hierarchy.
 2372 The exact position and amplitude of the resonance depend on $\sin^2(\theta_{23})$ meaning that
 2373 , further increasing the atmospheric neutrinos' have sensitivity to the parameter.

2374 As the T2K beam flux is centered at the first oscillation maximum ($E_\nu = 0.6\text{GeV}$),
 2375 the sensitivity to δ_{CP} is predominantly observed as a change in the event-rate of e-like

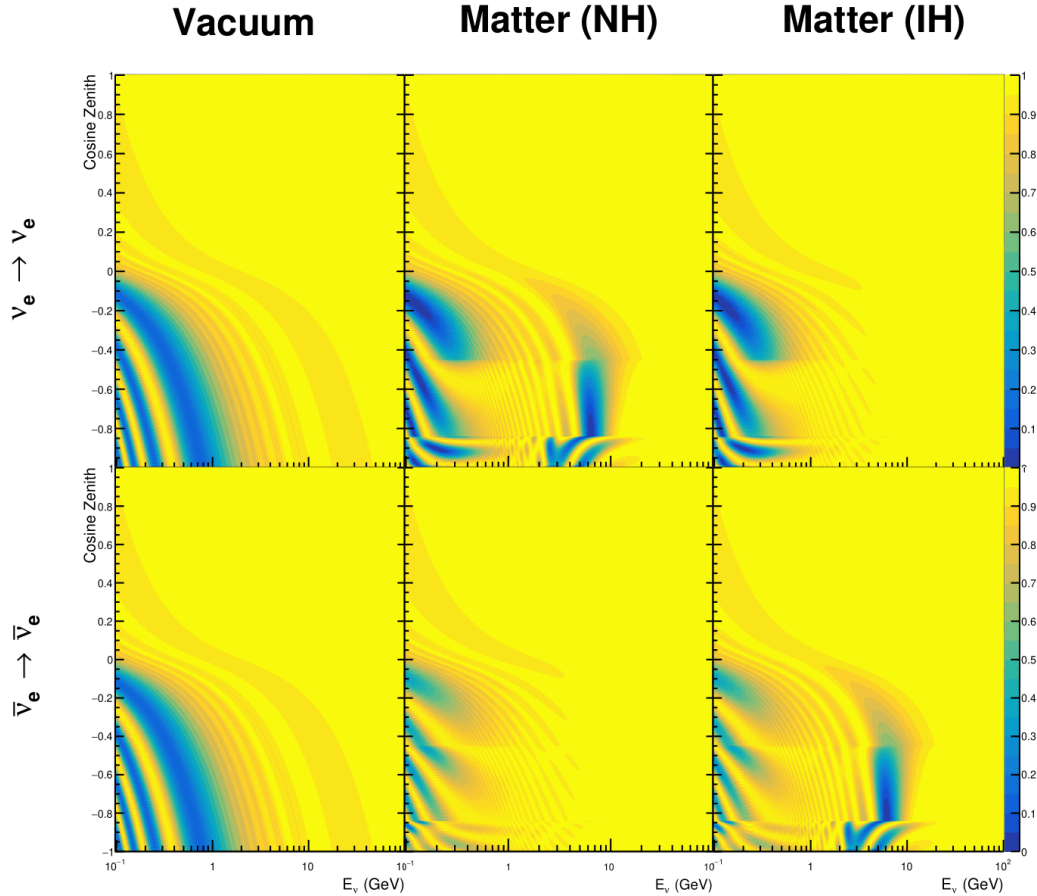


Figure 7.4.: An illustration of the matter-induced effects on the oscillation probability, given as a function of neutrino energy and zenith angle. The top row of panels gives the $P(\nu_e \rightarrow \nu_e)$ oscillation probability and the bottom row illustrates the $P(\bar{\nu}_e \rightarrow \bar{\nu}_e)$ oscillation probability. The left column highlights the oscillation probability in a vacuum, whereas the middle and right column represents the oscillation probabilities when the four-layer fixed density PREM model is assumed. All oscillation probabilities assume the “Asimov A” set given in Table 2.2, but importantly, the right column sets an inverted mass hierarchy. The “matter resonance” effects at $E_\nu \sim 5\text{GeV}$ can be seen in the $P(\nu_e \rightarrow \nu_e)$ for normal mass hierarchy and $P(\bar{\nu}_e \rightarrow \bar{\nu}_e)$ for inverted hierarchy.

samples in $\nu/\bar{\nu}$ modes. Figure 7.5 illustrates the $P(\nu_\mu \rightarrow \nu_e)$ oscillation probability for a range of δ_{CP} values. A circular modulation of the first oscillation peak (in both magnitude and position) is observed when varying throughout the allowable values of δ_{CP} . The CP-conserving values of $\delta_{CP} = 0, \pi$ have a lower(higher) oscillation maximum than the CP-violating values of $\delta_{CP} = -\pi/2 (\delta_{CP} = \pi/2)$. A sub-dominant

- shift in the energy of the oscillation peak is also present, which aids to aid in separating the two CP-conserving values of δ_{CP} .

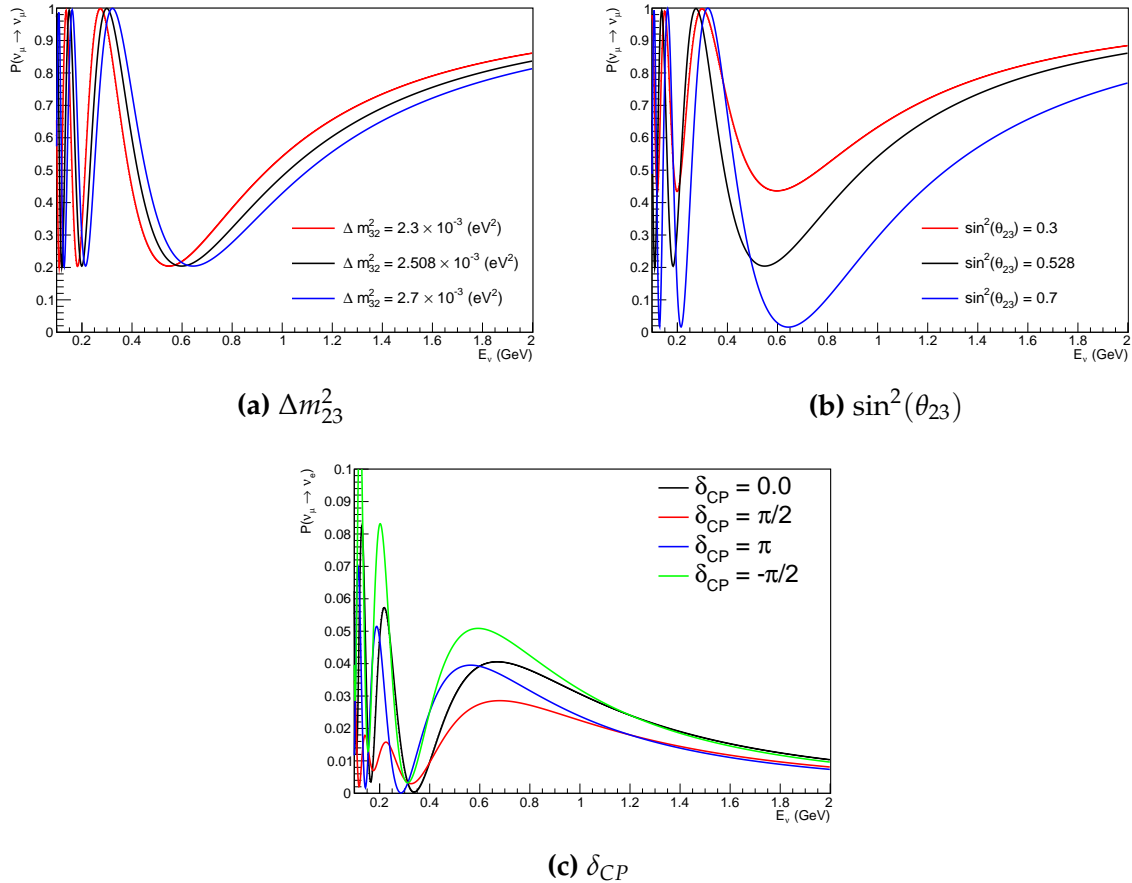


Figure 7.5: The oscillation probability for beam neutrino events given as a function of neutrino energy. All oscillation parameters assume the “Asimov A” set given in Table 2.2 unless otherwise stated. Each panel represents a change in one of the oscillation parameters whilst keeping the remaining parameters fixed.

- T2K’s sensitivity to $\sin^2(\theta_{23})$ and Δm_{23}^2 is observed as a shape-based variation of the muon-like samples, as illustrated in Figure 7.5. The value of Δm_{32}^2 laterally shifts the position of the oscillation dip (around $E_\nu \sim 0.6\text{GeV}$) in the $P(\nu_\mu \rightarrow \nu_\mu)$ oscillation probability. A variation of $\sin^2(\theta_{23})$ is predominantly observed as a vertical shift of the oscillation dip with second-order horizontal shifts being due to matter effects. The beam neutrinos have limited sensitivity to matter effects due to the relatively shorter baseline as well as the Earth’s mantle being a relatively low-density material

(as compared to the Earth's core). For some values of δ_{CP} , the degeneracy in the number of e-like events allows the mass hierarchy to be **resolved broken**. This leads to a δ_{CP} -dependent mass hierarchy sensitivity which can be seen in Figure 7.6.

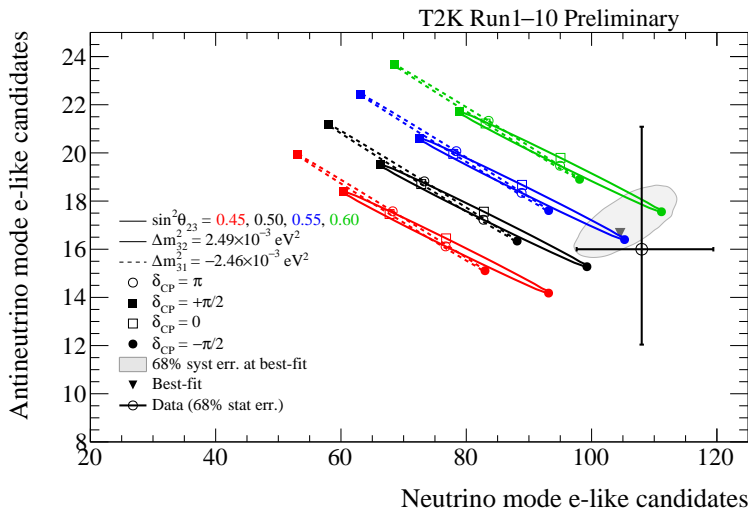


Figure 7.6: The number of electron-like events in the FHC and RHC operating mode of the beam, as a function of the oscillation probabilities. Both normal hierarchy (Solid)) and inverse hierarchy (Dashed) values of Δm_{23}^2 are given.

Whilst all oscillation channels should be included for completeness, the computational resources required to run a fit are limited and any reasonable approximations which reduce the number of oscillation probability calculations that need to be made should be applied. The $\nu_e \rightarrow \nu_{e,\mu,\tau}$ (and antineutrino equivalent) oscillations can be ignored for beam neutrinos as the $\nu_e/\bar{\nu}_e$ fluxes are approximately two orders of magnitude smaller than the corresponding $\nu_\mu/\bar{\nu}_\mu$ flux. Furthermore, as the peak neutrino energy of the beam is well below the threshold for charged current tau production ($E_\nu = 3.5\text{GeV}$ [51], only a small proportion of the neutrinos produced in the beam have the required energy. For the few neutrinos that have sufficient energy, the oscillation probability is very small due to the short baseline. Whilst these approximations have been made for the beam neutrinos, the atmospheric flux of ν_e is of the same order of magnitude as the ν_μ flux and the energy distribution of atmospheric neutrinos extends well above the tau production threshold.

2406 7.2. Treatment of Fast Oscillations

2407 As shown in Figure 7.7, atmospheric neutrino oscillations have a significantly more
2408 complex structure for upgoing neutrinos with energy below 1GeV. This is because the
2409 L/E dependence of the oscillation probability in this region induces rapid variations
2410 for small changes in L or E . As discussed in section 7.1, this is also the region in which
2411 atmospheric neutrinos have sensitivity to δ_{CP} . In practice, the direction of the neutrino
2412 is inferred from the direction of the final state particles traveling in the detector, which
2413 can be poor for low-energy neutrino interactions. This creates a distinct difference
2414 from the beam neutrinos where the position of the source is very precisely known.

2415 As a consequence of the unresolvable structure, ~~an average oscillation probability~~
2416 **ity an event rate consistent with the averaged oscillation probability** is observed in
2417 the subGeV upgoing region. This creates a computational problem: A significantly
2418 large amount of Monte Carlo statistics would be required to accurately predict the
2419 number of events if Monte Carlo averaging was the only technique used. This section
2420 describes the ‘sub-sampling’ approach developed for this analysis and compares it to
2421 the methodology used within the SK-only analysis.

2422 The official SK-only analysis uses the osc3++ oscillation parameter fitter [211]. To
2423 perform the fast oscillation averaging, it uses a ‘nearest-neighbour’ technique. For
2424 a given **Monte Carlo** neutrino event, the nearest twenty **Monte Carlo** neighbours in
2425 reconstructed lepton momentum and zenith angle are found and a distribution of their
2426 neutrino energies is built. The RMS, σ , of this distribution is then used to compute an
2427 average oscillation probability for the given neutrino Monte Carlo event.

2428 For the i^{th} event, the oscillation weight is calculated as

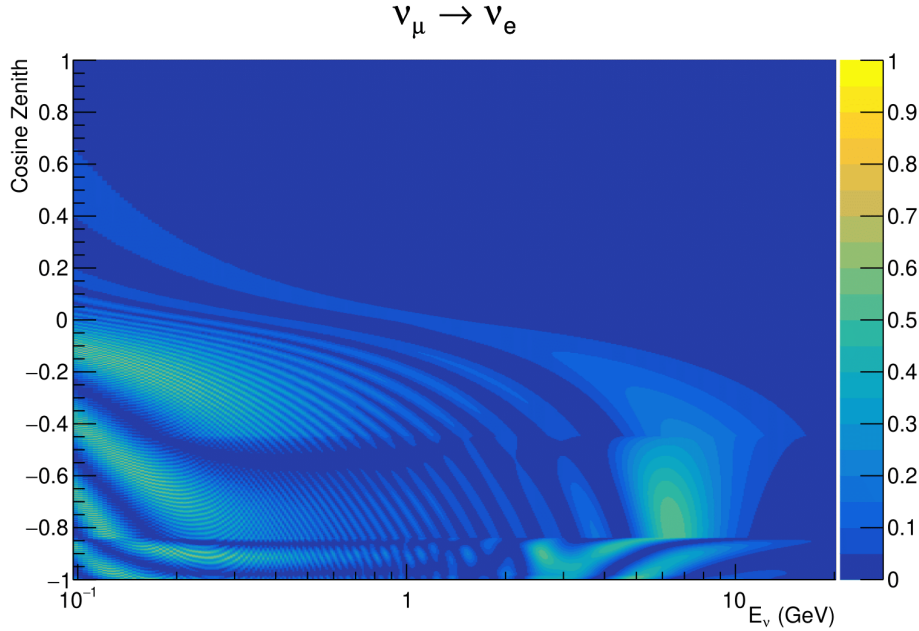


Figure 7.7.: The oscillation probability $P(\nu_\mu \rightarrow \nu_e)$, given as a function of neutrino energy and zenith angle, which highlights an example of the “fast” oscillations in the sub-GeV upgoing region.

$$W_i = \frac{1}{5}P(E_i, \bar{L}_i) + \frac{1}{5} \sum_{\beta=-1,-0.5,0.5,1} P(E_i + \beta\sigma_i, L_\beta), \quad (7.3)$$

where $P(E, L)$ is the oscillation probability calculation for neutrino energy E and path length L and the two path lengths, \bar{L}_i and L_β are discussed below. All of the oscillation probability calculations are performed with a fixed zenith angle such that the same density profile is used.

The uncertainty in the production height is controlled by using an “average” production height, \bar{L}_i , which represents the average path length computed using twenty production heights taken from the Honda flux model’s prediction [45]. For a given event, the production heights are sampled in steps of 5% of their cumulative distribution function. L_β values are similarly calculated but instead use different combinations of four production heights,

$$\begin{aligned}
 L_{-1.0} &= \frac{1}{4}L(45, 50, 55, 60), \\
 L_{-0.5} &= \frac{1}{4}L(35, 40, 65, 70), \\
 L_{+0.5} &= \frac{1}{4}L(25, 30, 75, 68), \\
 L_{+1.0} &= \frac{1}{4}L(15, 20, 85, 89).
 \end{aligned} \tag{7.4}$$

2439 This averaging technique works because of the inference between the zenith angle
 2440 and the reconstructed direction of final state particles in the detector. For low-energy
 2441 neutrinos, where the resolution of the true neutrino direction is poor, σ_i will be large,
 2442 resulting in significant averaging effects. Contrary to this, the inferred direction of
 2443 high-energy neutrinos will be much closer to the true value, meaning that σ_i will be
 2444 smaller, culminating in small averaging effects.

2445 **The below three paragraph has been re-worded**

2446 In practice, these calculations are performed prior to the fit as only oscillation
 2447 parameters at fixed points are considered. The MCMC technique used in this thesis
 2448 requires oscillation probabilities to be evaluated at arbitrary parameter values, not
 2449 known *a priori*. Calculating the five oscillation probabilities per event required by
 2450 the SK technique is computationally infeasible, so a different averaging technique is
 2451 used. However, the concept of the averaging technique can be taken from it.

2452 To perform a similar averaging as the SK analysis, a sub-sampling approach using
 2453 binned oscillograms has been devised. A coarsly binned oscillogram is defined in
 2454 $\cos(\theta_Z)$ and E_ν . For a given set of oscillation parameters, a single oscillation probability
 2455 will be assigned to each coarse bin. This value will then apply to all Monte Carlo
 2456 events which fall into that bin. To assign these oscillation probabilities, the probability
 2457 is calculated at $N \times N$ points on a grid within a particular bin. This ensemble of

2458 oscillation probabilities is averaged to define the coarse bin's oscillation probability,
2459 assuming a flat prior in E_ν and $\cos(\theta_Z)$. Figure 7.8 illustrates the $N = 2$ example where
2460 the assigned value to a coarse bin is the average of the four fine bins which fall in that
2461 coarse bin. Whilst the coarse bin edges do not have to be linear on either axis, the
2462 sub-division of the fine bins is linear over the range of a coarse bin.

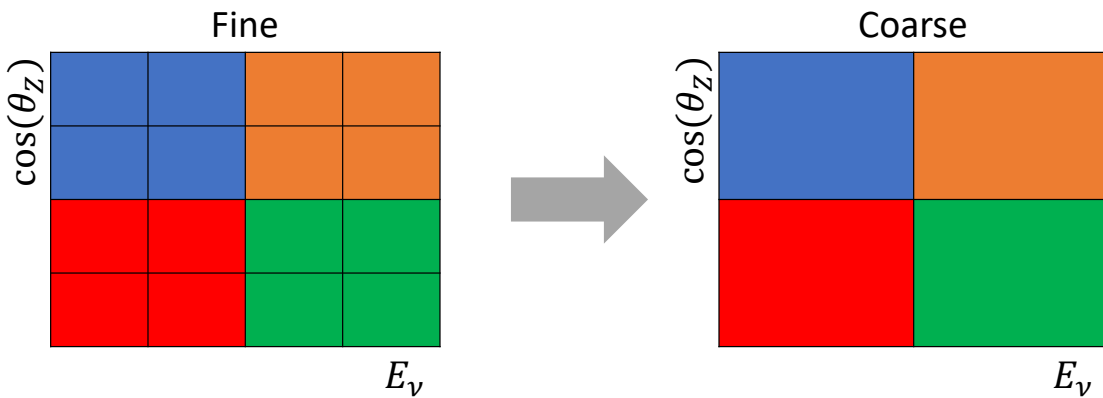


Figure 7.8.: Illustration of the averaging procedure for $N = 2$. The oscillation probabilities calculated on the finer left binning are averaged to obtain the oscillation probabilities in the coarser right binning. These averaged oscillation probabilities with the coarser binning are then applied to each event during the fit.

2463 The coarse binning is defined with 67×52 bins in true neutrino energy \times cosine
2464 zenith. It is picked to be identical to that provided in [213]. In general, the binning is
2465 logarithmically spaced in neutrino energy but has some hand-picked bin edges around
2466 the matter resonance to smoothly increased the bin density. This is to avoid smearing
2467 this region which can be well sampled by the Monte Carlo. The cosine zenith binning
2468 is approximately linearly spaced across the allowable range but the values of layer
2469 transitions are hit precisely: -0.8376 (core-mantle) and -0.4464 (mantle/transition
2470 zone). Bins are spread further apart for downgoing events as this is a region unaffected
2471 by the fast oscillation wavelengths and reduces the total number of calculations
2472 required to perform the calculation.

The choice of N is justified based on two studies. Firstly, the variation of event rates of each sample is studied as a function of N . For a given set of oscillation parameters thrown from the PDG prior constraints (detailed in Table 2.1), the oscillation probabilities are calculated using a given value of N . Each sample is re-weighted and the event rate is stored. The value of N is scanned from 1, which corresponds to no averaging, to 19, which corresponds to the largest computationally viable subdivision binning. The event rate of each sample at large N is expected to converge to a stationary value due to the fine binning fully sampling the small-scale structure. Figure 7.9 illustrates this behaviour for the SubGeV_elike_0dcy sample for 9 different throws of the oscillation parameters.

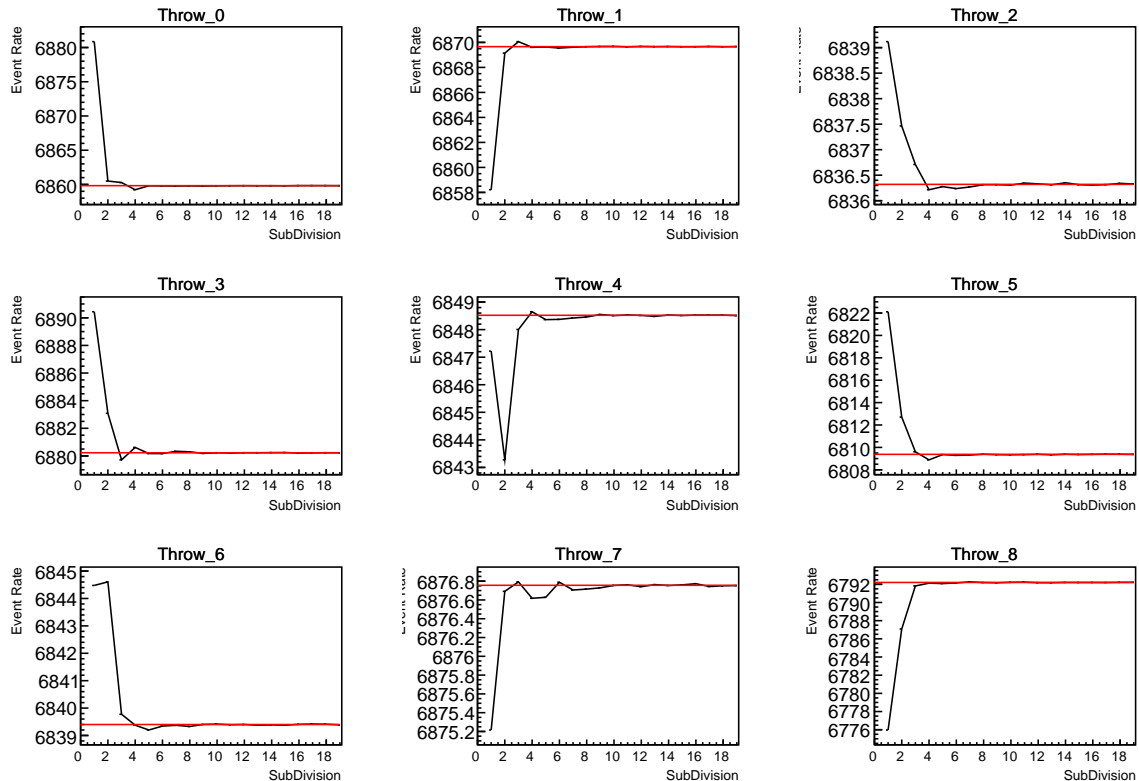


Figure 7.9.: Event rate of the SubGeV_elike_0dcy sample as a function of the number of subdivisions per coarse bin. Each subplot represents the event rate of the sample at a different oscillation parameter set thrown from the PDG priors detailed in Table 2.1. The red line in each subplot represents the mean of the event rate over the different values of sub-divisions for that particular oscillation parameter throw.

2484 Denoting the event rate for one sample for a given throw t at each N by λ_t^N , the
2485 average over all considered N values ($\bar{\lambda}_t = \frac{1}{24} \sum_{N=1}^{24} \lambda_t^N$) is computed. The variance in
2486 the event rate at each N is then calculated as

$$\text{Var}[\lambda^N] = \frac{1}{N_{\text{throws}}} \sum_{t=1}^{N_{\text{throws}}} (\lambda_t^N - \bar{\lambda}_t)^2 - \left[\frac{1}{N_{\text{throws}}} \sum_{t=1}^{N_{\text{throws}}} (\lambda_t^N - \bar{\lambda}_t) \right]^2. \quad (7.5)$$

2487 **The below paragraph, and associated figures, have been added**

2488 In practice the following procedure is undertaken. For a particular throw, the
2489 difference between the event rate at a particular choice of N and the mean of the
2490 distribution is calculated. This is illustrated in Figure 7.10. This value is then calculated
2491 for all the 2000 throws, generating a distribution of $\lambda_t^N - \bar{\lambda}_t$. This is repeated for each
2492 of the values of N considered within this study. The distributions of this value, for
2493 $N = \{1, 5\}$, are given in Figure 7.11. As expected, the distribution gets narrower and
2494 tends towards zero for the higher values of N .

2495 The aim of the study is to find the lowest value of N such that this variance is
2496 below 0.001. This utilises the width of the distributions given in Figure 7.11. This is
2497 the typical threshold used by T2K fitters to validate systematic implementation so has
2498 been set as the same criteria. The results of this study for each atmospheric sample
2499 used within this thesis are illustrated in Figure 7.12 for 2000 throws of the oscillation
2500 parameters. As can be seen, the variance is below the threshold at $N = 10$, and is
2501 driven primarily by the SubGeV_mulike_1dcy and SubGeV_elike_0dcy samples.

2502 The second study to determine the value of N is as follows. The likelihood for each
2503 sample is computed against an Asimov data set created with Asimov A oscillation
2504 parameters (Table 2.2). Following Equation 7.5, the variance of the log-likelihood over
2505 all considered N is computed. The results are shown in Figure 7.13.

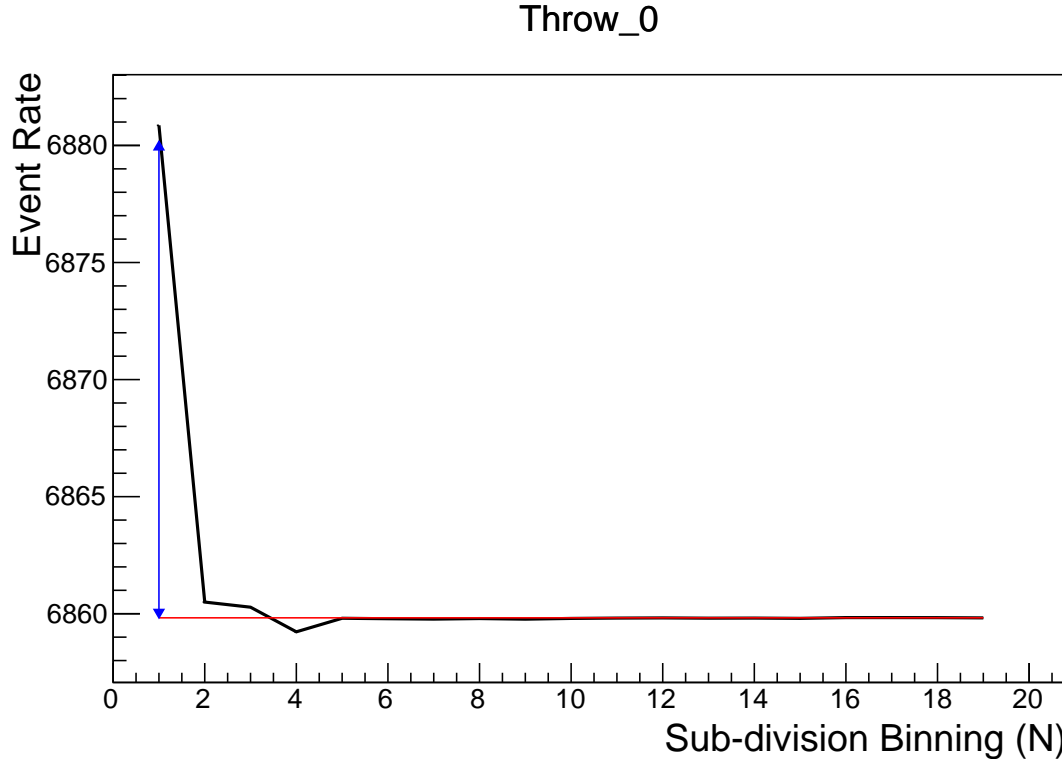


Figure 7.10.: Event rate of the SubGeV_elike_0dcy sample, for a particular oscillation parameter throw, as a function of the number of sub-divisions, N , per coarse bin. The difference between the mean event rate (red), $\bar{\lambda}$, and the event rate at $N = 1$, $\lambda^{N=1}$ is defined as $\lambda^N - \bar{\lambda}$ and illustrated by the blue arrow.

2506 A choice of $N = 10$ sub-divisions per coarse bin has a variance in both event rate
 2507 and log-likelihood residuals less than the required threshold of 0.001. The largest
 2508 value of the likelihood variance is of order 10^{-7} , corresponding to an error on the log-
 2509 likelihood of about 3×10^{-4} which is small enough to be negligible for the oscillation
 2510 analysis.

2511 Figure 7.14 illustrates the effect of the smearing using $N = 10$. The fast oscillations
 2512 in the sub-GeV upgoing region have been replaced with a normalisation effect whilst
 2513 the large matter resonance structure remains.

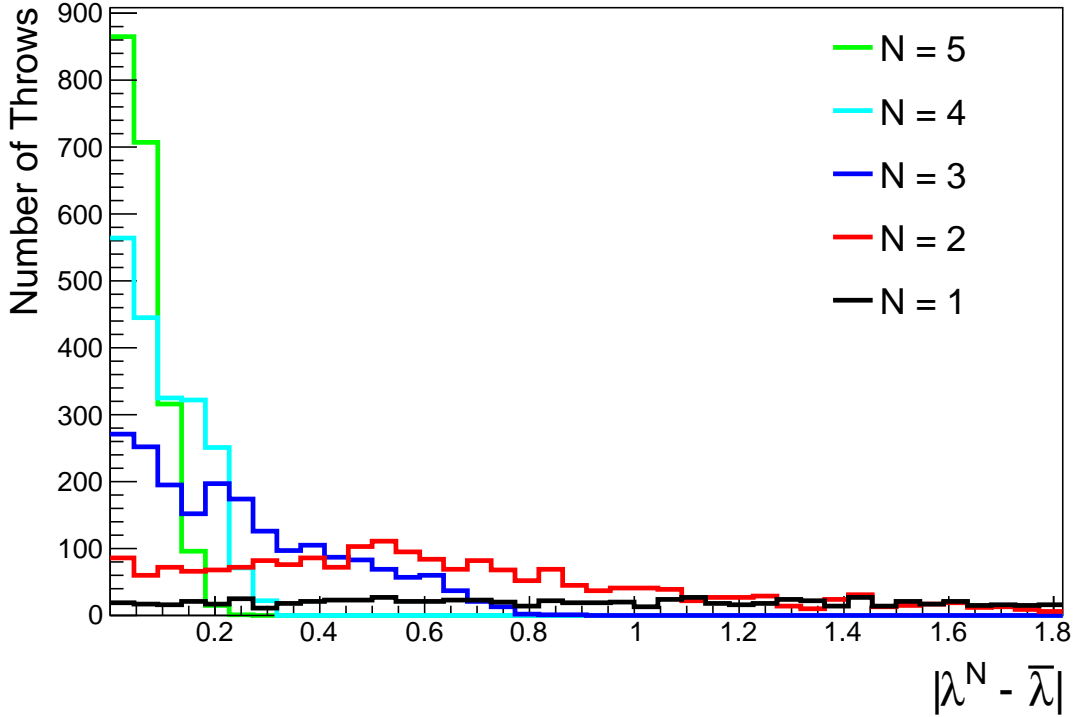


Figure 7.11.: The distribution of $\lambda^N - \bar{\lambda}$ for various values of N . As expected, the distribution gets narrower for larger values of N .

2514 7.3. Calculation Engine

2515 As previously discussed in section 7.2, the calculation of oscillation probabilities is
 2516 performed at run-time **due to utilising continuous oscillation parameters**. Conse-
 2517 quently, the time per calculation is crucial for fit performance. The initial fitting
 2518 framework used for this analysis was developed with ProbGPU [214]. This is a GPU-
 2519 only implementation of the prob3 engine [215]. It is primarily designed for neutrino
 2520 propagation in a beam experiment (single layer of constant density) with the atmo-
 2521 spheric propagation code not being used prior to the analysis in this thesis.

2522 Another engine, CUDAProb3 [216], has been **implemented within interfaced with**
 2523 the fitting framework used in this analysis. It has been specifically optimised for
 2524 atmospheric neutrino oscillation calculation so does not contain the code to replace

Oscillation Probability Calculation

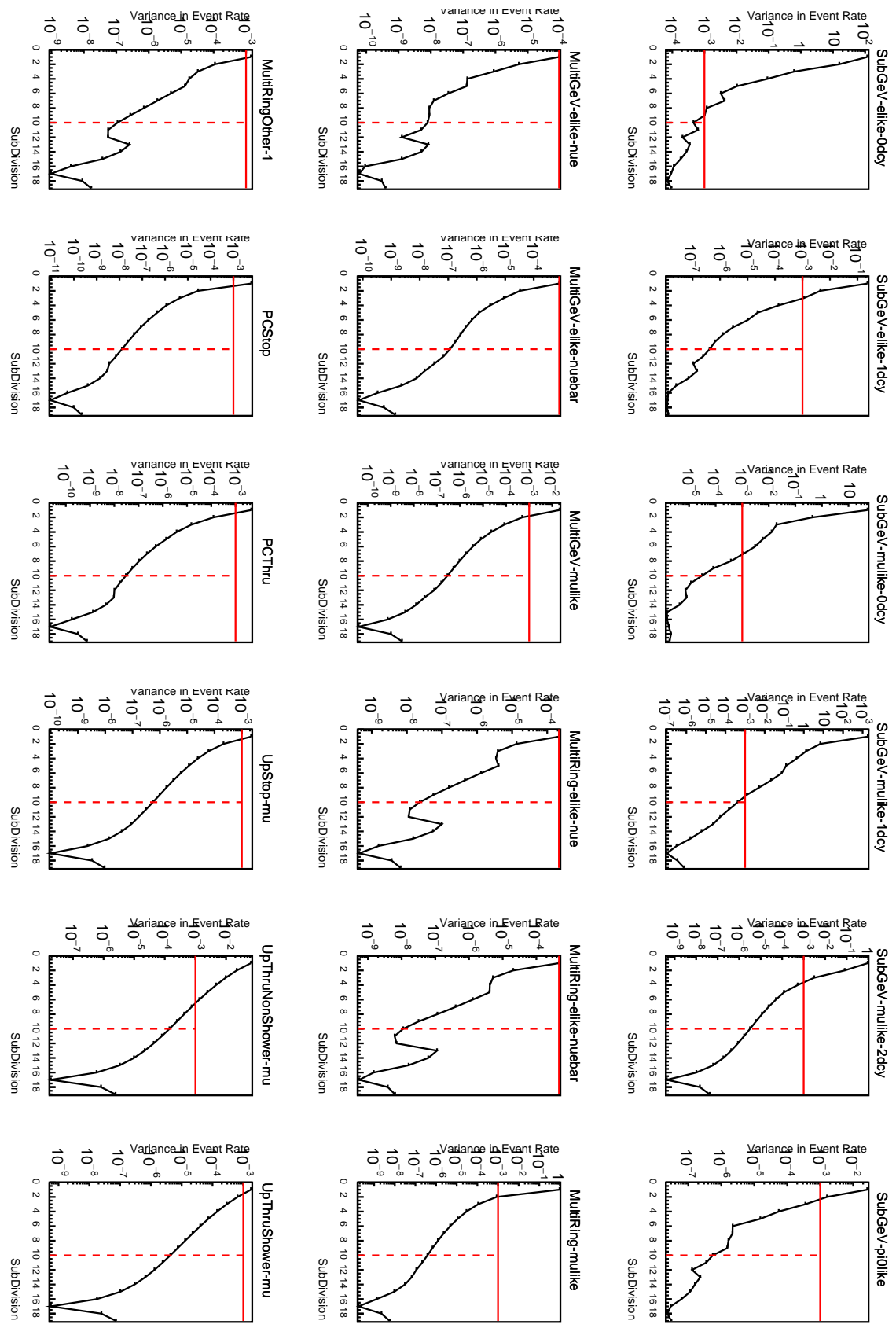


Figure 7.12: Variance of event rate for each atmospheric sample as a function of the number of sub-divisions per coarse bin. The solid red line indicates the 0.1% threshold and the dashed red line indicates the variance at a sub-division $N = 10$.

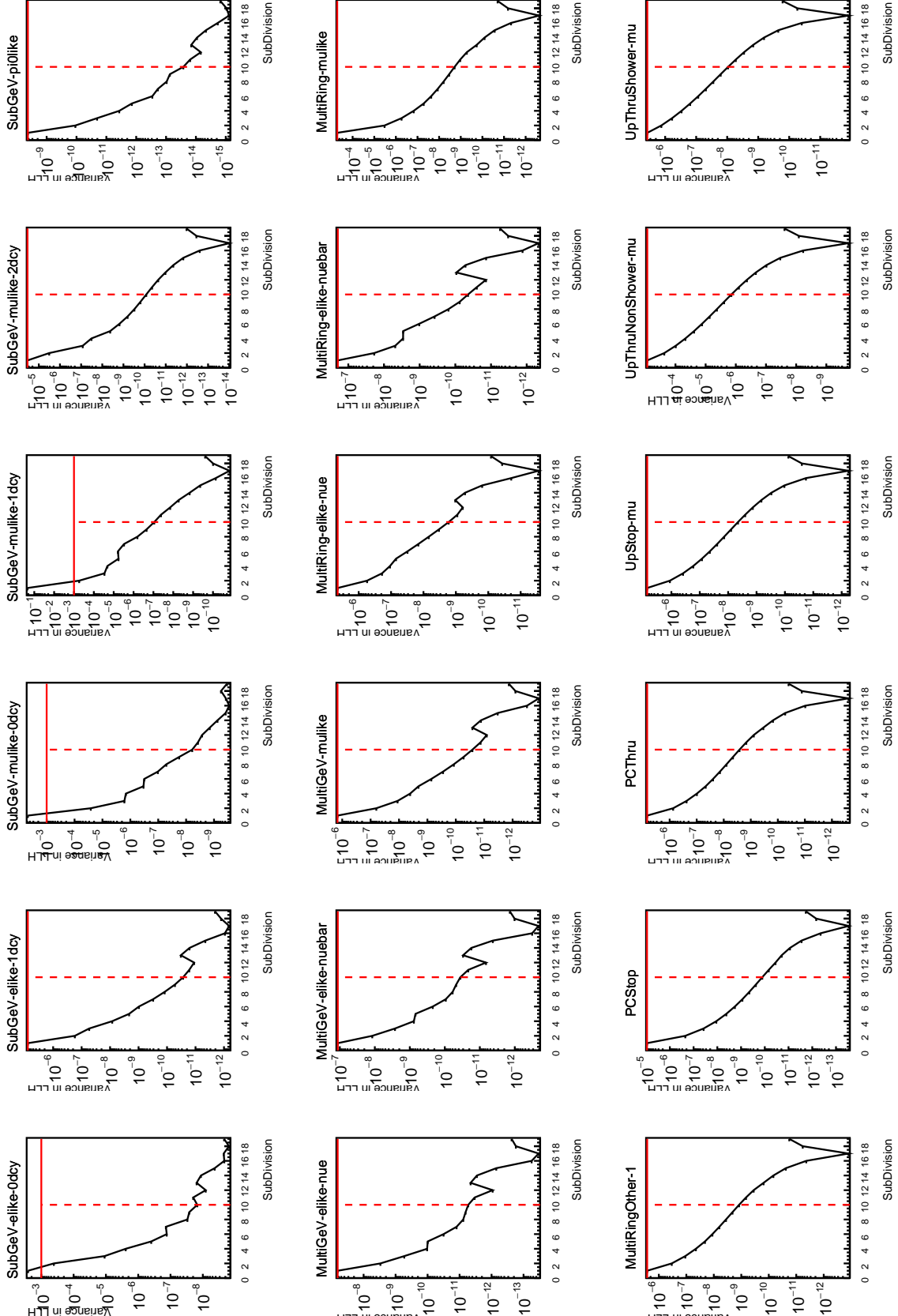


Figure 7.13: Variance of sample likelihood, when compared to 'Asimov data' set at Asimov A, for each atmospheric sample as a function of the number of sub-divisions per coarse bin. The solid red line indicates the 0.1% threshold and the dashed red line is a graphical indication of the variance at a sub-division $N = 10$.

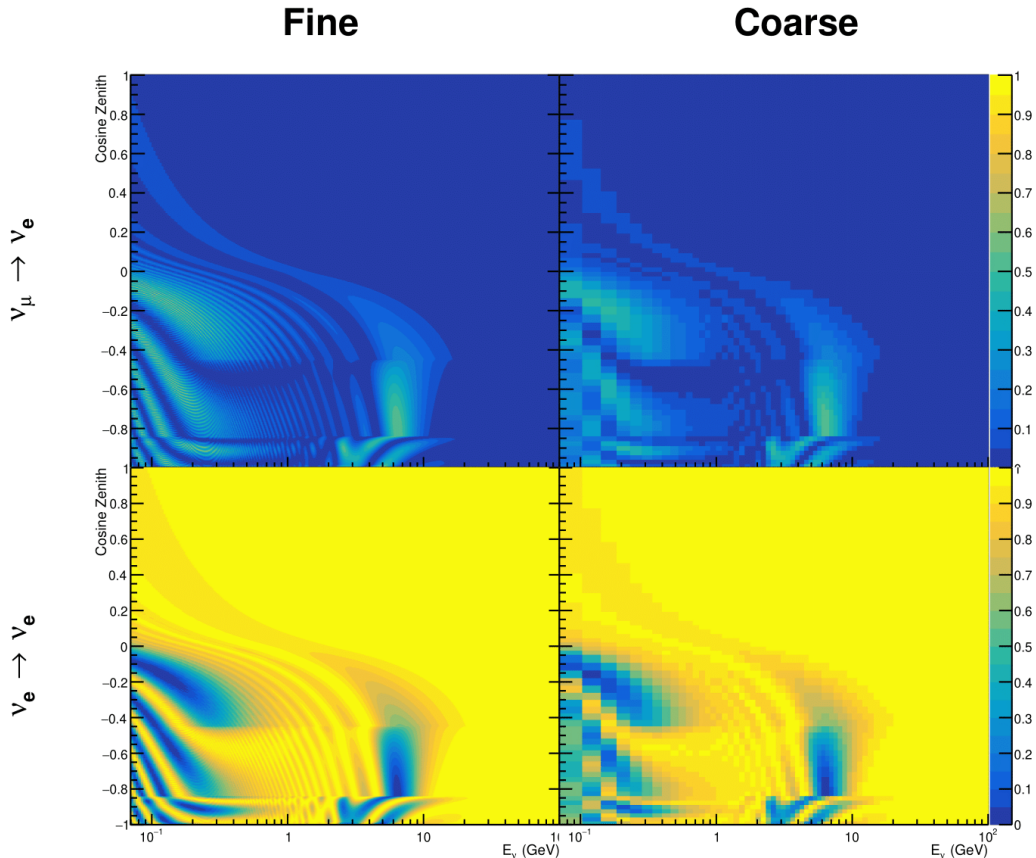


Figure 7.14.: The oscillation probability, $P(\nu_\mu \rightarrow \nu_e)$ (top row) and $P(\nu_e \rightarrow \nu_e)$ (bottom row), given as a function of neutrino energy and zenith angle. The left column gives the “fine” binning used to calculate the oscillation probabilities and the right column illustrates the “coarse” binning used to reweight the Monte Carlo events. The fine binning choice is given with $N = 10$, which was determined to be below the threshold from Figure 7.12 and Figure 7.13.

the beam oscillation calculation. The engine utilises object-orientated techniques as compared to the functional implementation of ProbGPU. This allows the energy and cosine zenith arrays to be kept on GPU memory, rather than having to load these arrays onto GPU memory for each calculation. **General memory interfacing is one of the slowest tasks which GPUs can do, so being able to eliminate this significantly reduces the time required for calculation. Reducing the memory transfer between CPU and GPU significantly reduces the time required for calculation.** This can be

2532 seen in Figure 7.15, where the GPU implementation of CUDAProb3 is approximately
2533 three times faster than the ProbGPU engine.

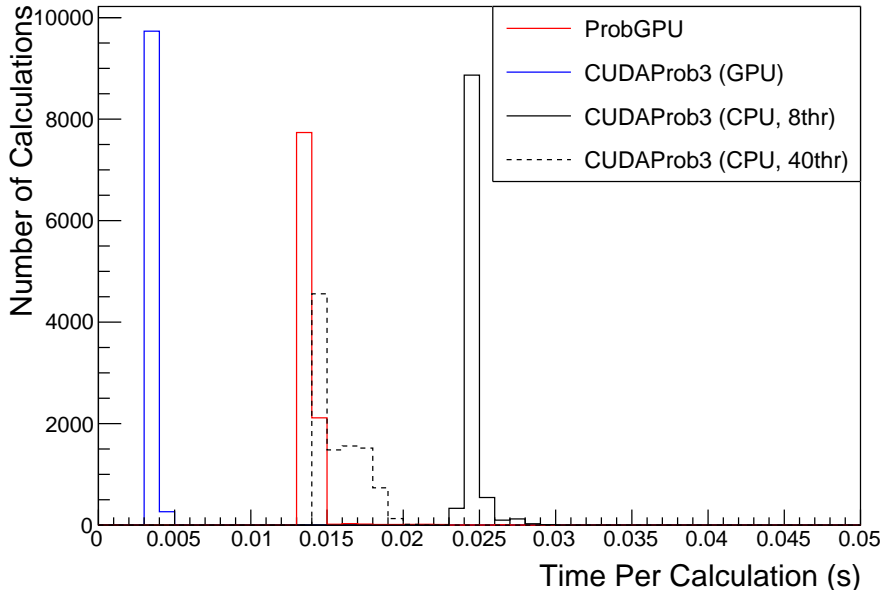


Figure 7.15.: The calculation time taken to both calculate the oscillation probabilities and fill the “coarse” oscilloscopes, following the technique given in section 7.2, for the CUDAProb3 and ProbGPU (Red) calculation engines. CUDAProb3 has both a GPU (Blue) and CPU (Black) implementation, where the CPU implementation is multithreaded. Therefore, 8-threads (solid) and 40-threads (dashed) configurations have been tested. Prob3, which is a CPU single-thread implementation has a mean step time of 1.142s.

2534 Another significant advantage of CUDAProb3 is that it contains a CPU multithreaded
2535 implementation which is not possible with the ProbGPU or prob3 engines. This elimi-
2536 nates the requirement for GPU resources when submitting jobs to batch systems. As
2537 illustrated in Figure 7.15, the calculation speed depends on the number of available
2538 threads. Using 8 threads (which is typical of the batch systems being used) is ap-
2539 proximately twice as slow as the ProbGPU engine implementation, but would allow
2540 the fitting framework to be run on many more resources. This fact is utilised for any
2541 SK-only fits but GPU resources are required for any fits which include beam samples
2542 due to the ProbGPU requirement. Based on the benefits shown by the implementation

2543 in this section, efforts are being placed into including linear propagation for beam
2544 neutrino propagation into the engine [217].

2545 **7.4. Matter Density Profile**

2546 For an experiment observing neutrinos propagating through the Earth, a model of
2547 the Earth's density profile is required. The model used within this analysis is based
2548 on the Preliminary Reference Earth Model (PREM) [212], as illustrated in Figure 7.1.
2549 Table 7.1 documents the density and radii of the layers used within the constant
2550 density approximaton used by the SK-only analysis [211]. The density measurements
2551 provided in the PREM model are provided in terms of mass density, whereas neutrino
2552 oscillations are sensitive to the electron number density. This value can be computed
2553 as the product of the chemical composition, or the Z/A value, and the mass density
2554 of each layer. Currently, the only way to measure the chemical composition value
2555 for layers close to the Earth's core is through neutrino oscillations. The chemical
2556 composition of the upper layers of the Earth's Mantle and the Transition zone is well
2557 known due to it being predominantly pyrolite which has a chemical composition value
2558 of 0.496 [218]. The chemical composition dial for the core layers is set to a value of
2559 0.468, as calculated in [219]. As this value is lesss well known, it is assigned a Gaussian
2560 error with a standard deviation equivalent to the difference in chemical composition in
2561 core and mantle layers. Figure 7.16 illustrates the effect of moving from the $Z/A = 0.5$
2562 method which is used in the official SK-only analysis to these more precise values.

2563 The beam oscillation probability in this thesis uses a baseline of 295km, density
2564 2.6g/cm^3 , and chemical composition 0.5 as is done by the official T2K-only analysis
2565 [220].

2566 **The below two paragraphs have been re-worded**

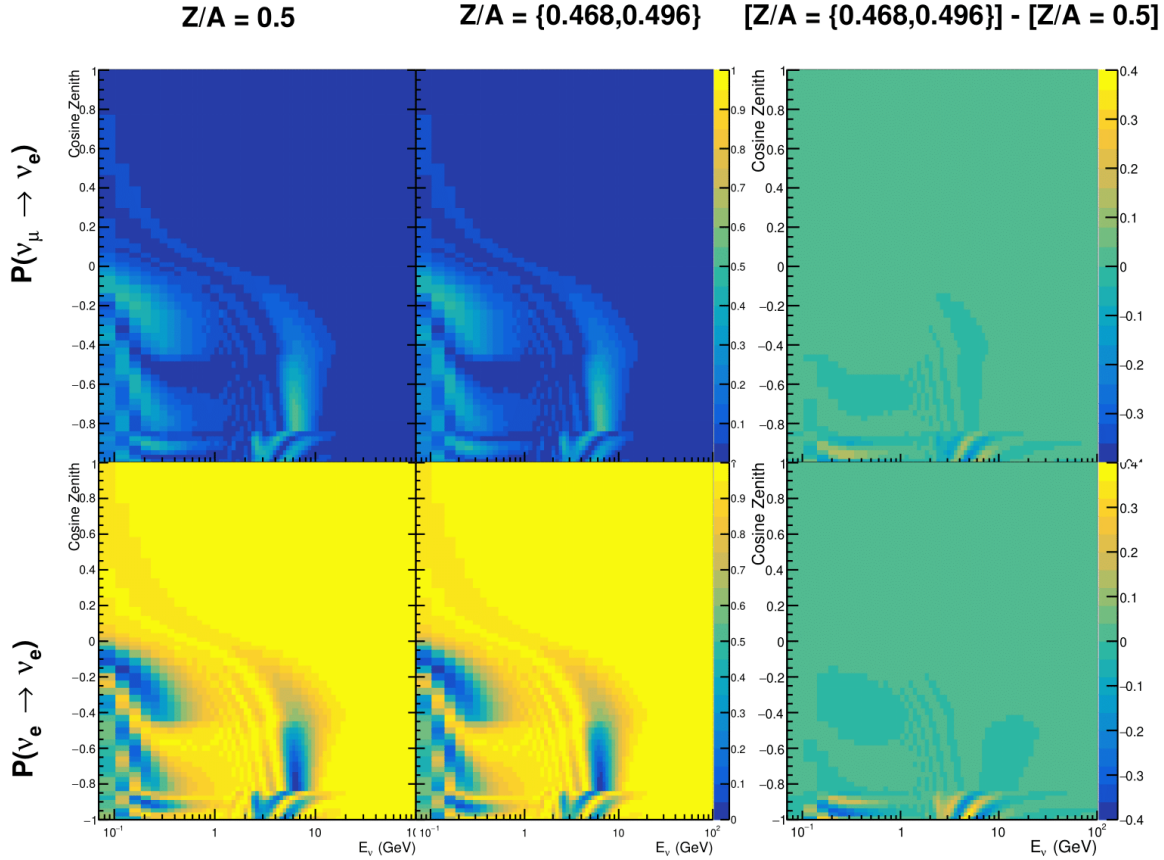


Figure 7.16.: The oscillation probability, $P(\nu_\mu \rightarrow \nu_e)$ (top row) and $P(\nu_e \rightarrow \nu_e)$ (bottom row), given as a function of neutrino energy and zenith angle. The left column gives probabilities where the constant $Z/A = 0.5$ approximation which is used in the official SK-only analysis. The middle column gives the probabilities where $Z/A = [0.468, 0.498]$ values are used, as given in Table 7.1. The right column illustrates the difference in oscillation probability between the two different techniques.

For a neutrino with given E_ν , $\cos(\theta_Z)$, the oscillation probability calculation engine must be passed a list of the matter regions that the neutrino traversed, with the path length and fixed density in each region. However, a neutrino passing through the earth experiences a range of radii, and thus a range of densities, in each region. In the SK-only analysis, the earth density model used is piecewise-constant, thereby ignoring this effect. For this thesis, the density values for the calculation engine are found by averaging the earth density along the neutrino's path,

$$\langle \rho \rangle_i = \frac{1}{t_{i+1} - t_i} \int_{t_i}^{t_{i+1}} \rho(t) dt \quad (7.6)$$

where t_i are the intersection points between each layer and t is the path length of the trajectory across the layer. This leads to an improved approximation. For this averaging, the simplification of the PREM model developed in [221] is used. The layers of the prem model are combined into four to reduce calculation time, with a quadratic fit to each section. This fit was not performed by the author of the thesis and is documented in [213]. The coefficients of the quadratic fit to each layer are given in Table 7.2 with the final distribution illustrated in Figure 7.17. The quadratic approximation is clearly much closer to the PREM model as compared to the constant density approximation.

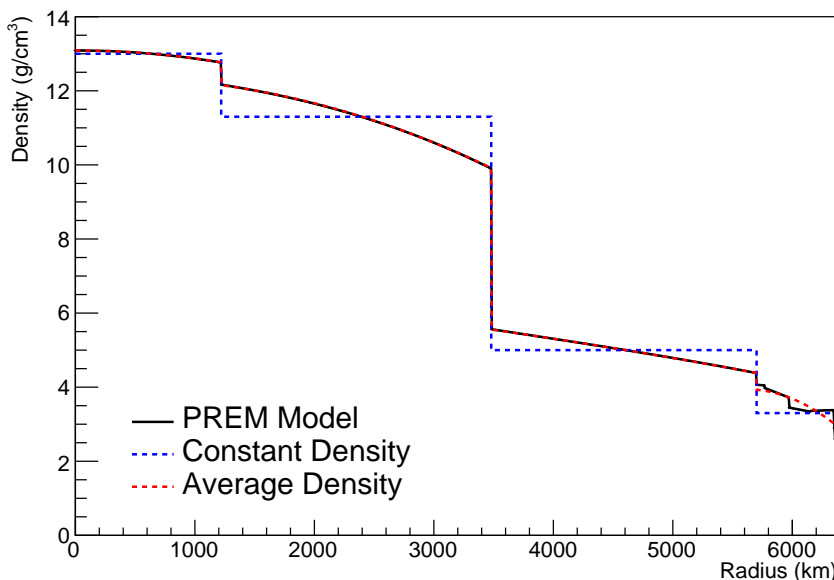


Figure 7.17.: The density of the Earth given as a function of the radius, as given by the PREM model (Black), the constant density four-layer approximation (Blue), as used in the official SK-only analysis, and the quadratic approximation of the PREM model (Red).

Layer	Outer Radius [km]	Density [g/cm ³]
Inner Core	1220	$13.09 - 8.84x^2$
Outer Core	3480	$12.31 + 1.09x - 10.02x^2$
Lower Mantle	5701	$6.78 - 1.56x - 1.25x^2$
Transition Zone	6371	$-50.42 + 123.33x - 69.95x^2$

Table 7.2.: The quadratic polynomial fits to the PREM model for four assumed layers of the PREM model. The fit to calculate the coefficients is given in [213], where $x = R/R_{Earth}$.

2583 The effect of using the quadratic density per $\cos(\theta_Z)$ model is highlighted in
 2584 Figure 7.18. The slight discontinuity in the oscillation probability around $\cos(\theta_Z) \sim -$
 2585 0.45 in the fixed density model, which is due to the transition to mantle layer boundary,
 2586 has been reduced. This is expected as the difference in the density across this boundary
 2587 is significantly smaller in the quadratic density model as compared to the constant
 2588 density model. Whilst the difference in density across the other layer transitions
 2589 is reduced, there is still a significant difference. This means the discontinuities in
 2590 the oscillation probabilities remain but are significantly reduced. However, as the
 2591 quadratic density approximation matches the PREM model well in this region, these
 2592 discontinuities are due to the Earth model rather than an artifact of the oscillation
 2593 calculation.

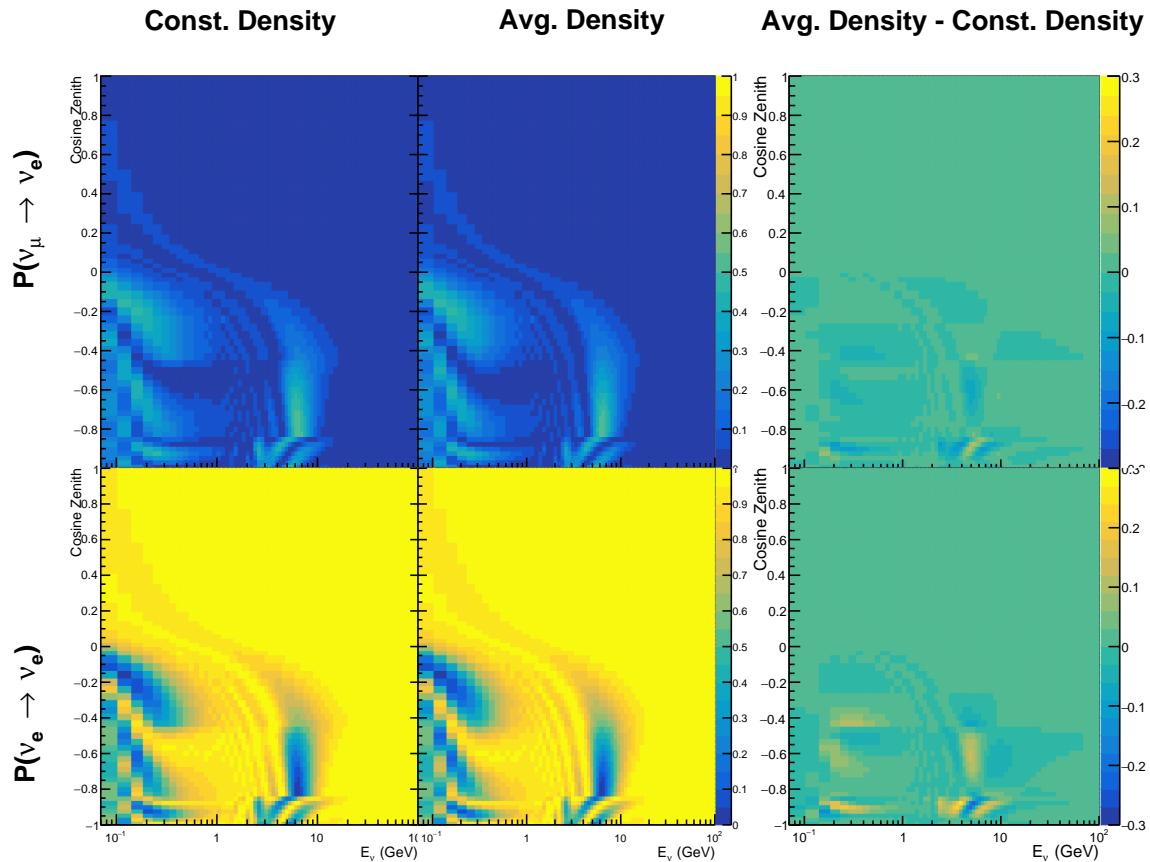


Figure 7.18.: The oscillation probability, $P(\nu_\mu \rightarrow \nu_e)$ (top row) and $P(\nu_e \rightarrow \nu_\mu)$ (bottom row), given as a function of neutrino energy and zenith angle. The left column gives probabilities where the four-layer constant density approximation is used. The middle column gives the probabilities where the density is integrated over the trajectory, using the quadratic PREM approximation, for each $\cos(\theta_Z)$ is used. The right column illustrates the difference in oscillation probability between the two different techniques.

²⁵⁹⁴ 7.5. Production Height Averaging

²⁵⁹⁵ As discussed in section 7.1, the height at which the cosmic ray flux interacts in the
²⁵⁹⁶ atmosphere is not known on an event-by-event basis. The production height can vary
²⁵⁹⁷ from the Earth’s surface to $\sim 50\text{km}$ above that. The SK-only analysis methodology
²⁵⁹⁸ (described in section 7.2) for including the uncertainty on the production height is
²⁵⁹⁹ to include variations from the Honda model when pre-calculating the oscillation
²⁶⁰⁰ probabilities prior to the fit. This technique is not possible for this analysis which
²⁶⁰¹ uses continuous oscillation parameters that can not be known prior to the fit. Conse-
²⁶⁰² quently, an analytical averaging technique was developed in [213]. The author of this
²⁶⁰³ thesis was not responsible for the derivation of the technique but has performed the
²⁶⁰⁴ implementation and validation of the technique for this analysis alone.

²⁶⁰⁵ Using the 20 production heights per Monte Carlo neutrino event, provided as 5%
²⁶⁰⁶ percentiles from the Honda flux model, a production height distribution $p_j(h|E_\nu, \cos \theta_Z)$
²⁶⁰⁷ is built for each neutrino flavour $j = \nu_e, \bar{\nu}_e, \nu_\mu, \bar{\nu}_\mu$. In practice, a histogram is filled with
²⁶⁰⁸ 20 evenly spaced bins in production height h between 0 and 50km. The neutrino energy
²⁶⁰⁹ and cosine zenith binning of the histogram is the same as that provided in section 7.2.
²⁶¹⁰ The average production height, $\bar{h} = \int dh \frac{1}{4} \sum_j p_j(h|E_\nu, \cos(\theta_Z))$, is calculated. The
²⁶¹¹ production height binning of this histogram is then translated into $\delta t(h) = t(\bar{h}) - t(h)$,
²⁶¹² where $t(h)$ is the distance travelled along the trajectory.

²⁶¹³ For the i^{th} traversed layer, the transition amplitude, $D_i(t_{i+1}, t_i)$, is computed. The
²⁶¹⁴ time-ordered product of these is then used as the overall transition amplitude via

$$A(t_{n+1}, t_0) = D_n(t_{n+1}, t_n) \dots D_1(t_2, t_1) D_0(t_1, t_0), \quad (7.7)$$

2615

where,

$$\begin{aligned} D_n(t_{n+1}, t_n) &= \exp[-iH_n(t_{n+1} - t_n)] \\ &= \sum_{k=1}^3 C_k \exp[ia_k(t_{n+1} - t_n)] \end{aligned} \quad (7.8)$$

2616

is expressed as a diagonalised time-dependent solution to the Schrodinger equation.

2617 The 0^{th} layer is the propagation through the atmosphere and is the only term that2618 depends on the production height. Using the substitution $t_0 = t(\bar{h}) - \delta t(h)$, it can be

2619 shown that

$$D_0(t_1, t_0) = D_0(t_1, \bar{h})D_0(\delta t). \quad (7.9)$$

2620

Thus Equation 7.7 becomes

$$\begin{aligned} A(t_{n+1}, t_0) &= D_n(t_{n+1}, t_n) \dots D_1(t_2, t_1) D_0(t_1, \bar{h}) D(\delta t) \\ &= A(t_{n+1}, \bar{h}) \sum_{k=1}^3 C_k \exp[ia_k \delta t], \\ &= \sum_{k=1}^3 B_k \exp[ia_k \delta t]. \end{aligned} \quad (7.10)$$

2621

The oscillation probability averaged over production height is then calculated as

$$\begin{aligned}
 \bar{P}(\nu_j \rightarrow \nu_i) &= \int d(\delta t) p_j(\delta t | E_\nu, \cos \theta_Z) P(\nu_j \rightarrow \nu_i) \\
 &= \int d(\delta t) p_j(\delta t | E_\nu, \cos \theta_Z) A(t_{n+1}, t_0) A^*(t_{n+1}, t_0) \\
 &= \sum_{km} (B_k)_{ij} (B_m)_{ij}^* \int d(\delta t) p_j(\delta t | E_\nu, \cos \theta_Z) \exp[i(a_k - a_m)\delta t]
 \end{aligned} \tag{7.11}$$

2622 In practice, implementation in CUDAProb3 [216] is relatively straightforward as
 2623 the majority of these terms are already calculated in the standard oscillation calculation.
 2624 Figure 7.19 illustrates the results of the production height averaging. As expected,
 2625 the main effect is observed in the low-energy downward-going and horizontal-going
 2626 events. Upward-going events have to travel the radius of the Earth, $R_E = 6371\text{km}$,
 2627 where the production height uncertainty is a small fraction of the total path length.

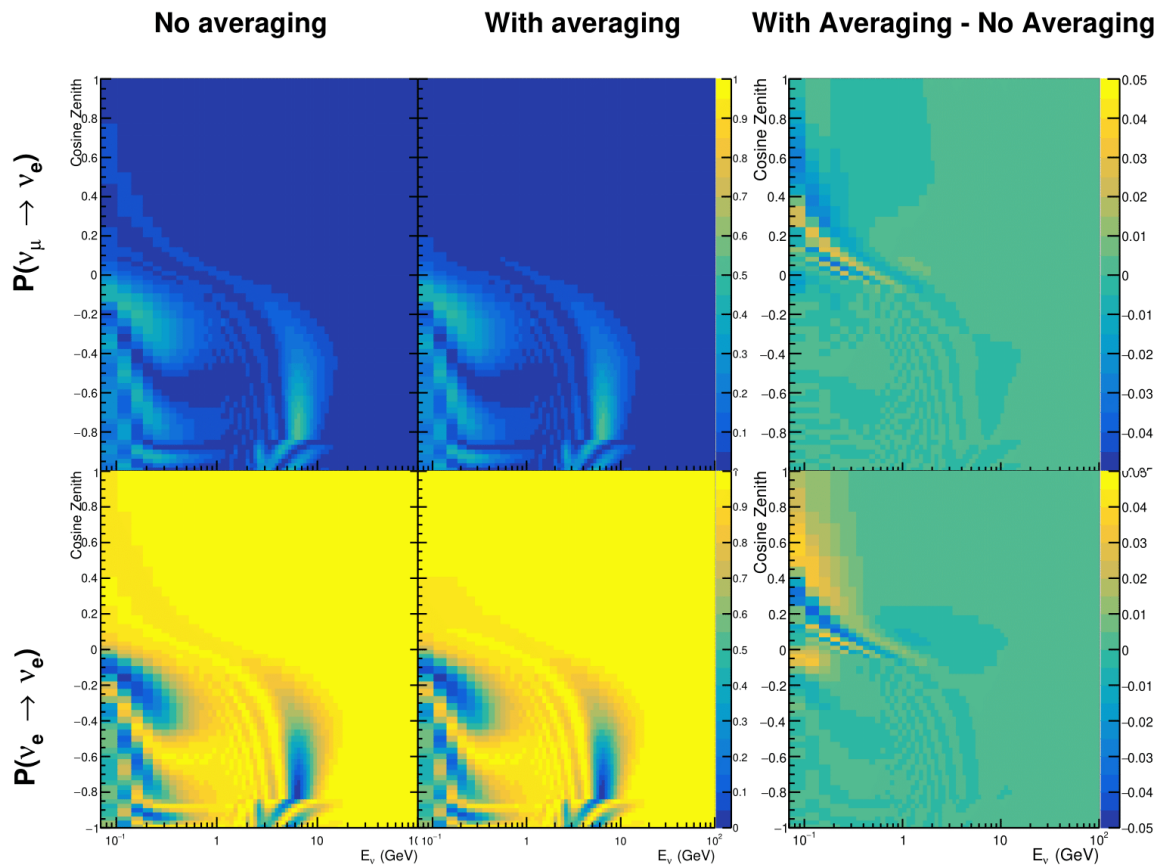


Figure 7.19.: The oscillation probability, $P(\nu_\mu \rightarrow \nu_e)$ (top row) and $P(\nu_e \rightarrow \nu_\mu)$ (bottom row), given as a function of neutrino energy and zenith angle. The left column gives probabilities where a fixed production height of 25km is used. The middle column gives the probabilities where the production height is analytically averaged. The right column illustrates the difference in oscillation probability between the two different techniques.

2628 **Chapter 8**

2629 **Oscillation Analysis**

2630 **8.1. Likelihood Calculation**

2631 This analysis performs a joint oscillation parameter fit of the ND280, and the SK
2632 atmospheric samples.

2633 Once the Monte Carlo predictions of each beam and atmospheric sample has been
2634 built, following from chapter 6, a likelihood needs to be constructed. This is done
2635 by comparing the Monte Carlo prediction to “data”. The data can consist of either
2636 an Asmiov Monte Carlo prediction, which is typically used for sensitivity studies,
2637 or real data. The Monte Carlo prediction is calculated at a particular point, $\vec{\theta}$, in the
2638 model parameter space, $N_i^{MC} = N_i^{MC}(\vec{\theta})$. Both the data and Monte Carlo spectra are
2639 binned, where the i^{th} bin content is represented by N_i^D and N_i^{MC} , respectively. The bin
2640 contents for the beam near detector, beam far detector and atmospheric samples are
2641 denoted with ND , FD and Atm , respectively. The binning index, i , runs over all the
2642 bins within the sample and all samples with that set. Taking the beam far detector
2643 samples as example, it would run over all the reconstructed neutrino energy bins in all
2644 samples (FHC1R μ , RHC1R μ , etc.). The likelihood calculation between data and Monte
2645 Carlo for a particular bin follows a Poisson distribution, where the data is treated as a
2646 fluctuation of the simulation.

2647 Following the T2K analysis presented in [80], the likelihood contribution from the
2648 near detector also includes a Monte Carlo statistical uncertainty term, derived from

2649 the Barlow and Beeston statistical treatment [222, 223]. In addition to treating the data
 2650 as a fluctuation of the Monte Carlo prediction, it includes a contribution from the
 2651 likelihood that the generated simulation is a statistical fluctuation of the actual true
 2652 simulation assuming infinite statistics. The technical implementation of this additional
 2653 likelihood term is documented in [195]. The term is defined as,

$$\frac{(\beta_i - 1)^2}{2\sigma_{\beta_i}^2}, \quad (8.1)$$

2654 where β_i represents a scaling parameter for each bin i , which is a value based on
 2655 the amount of Monte Carlo statistics in a bin [195]. $\sigma_{\beta_i} = \sqrt{\sum_i w_i^2 / N_i^{MC}}$, and $\sqrt{\sum_i w_i^2}$
 2656 represents the sum of the square of the weights of the Monte Carlo events which fall
 2657 into bin i .

2658 Additional contributions to the likelihood come from the variation of the systematic
 2659 model parameters. For those parameters with well-motivated uncertainty estimates,
 2660 a covariance matrix, V describes the prior knowledge of each parameter as well as
 2661 any correlations between the parameters. Due to the technical implementation, a
 2662 single covariance matrix describes each “block” of model parameters, e.g. beam flux
 2663 systematics. For simplicity, the covariance matrix associated with the k^{th} block is
 2664 denoted V^k . This substitution results in $\vec{\theta} = \sum_k^{N_b} \vec{\theta}^k$ and $V = \sum_k^{N_b} V^k$, for N_b number
 2665 of blocks describing: oscillation parameters, beam flux, atmospheric flux, neutrino
 2666 interaction, near detector, beam far detector and atmospheric far detector systematics
 2667 detailed in section 6.4. The number of parameters in the k^{th} block is defined as $n(k)$.

2668 The final likelihood term is defined as,

$$\begin{aligned}
& -\ln(\mathcal{L}) = & (8.2) \\
& \sum_i^{\text{NDbins}} N_i^{\text{ND},MC}(\vec{\theta}) - N_i^{\text{ND},D} + N_i^{\text{ND},D} \times \ln \left[N_i^{\text{ND},D} / N_i^{\text{ND},MC}(\vec{\theta}) \right] + \frac{(\beta_i - 1)^2}{2\sigma_{\beta_i}^2} \\
& + \sum_i^{\text{FDbins}} N_i^{\text{FD},MC}(\vec{\theta}) - N_i^{\text{FD},D} + N_i^{\text{FD},D} \times \ln \left[N_i^{\text{FD},D} / N_i^{\text{FD},MC}(\vec{\theta}) \right] \\
& + \sum_i^{\text{Atmbins}} N_i^{\text{Atm},MC}(\vec{\theta}) - N_i^{\text{Atm},D} + N_i^{\text{Atm},D} \times \ln \left[N_i^{\text{Atm},D} / N_i^{\text{Atm},MC}(\vec{\theta}) \right] \\
& + \frac{1}{2} \sum_k^{N_b} \sum_i^{n(k)} \sum_j^{n(k)} (\vec{\theta}^k)_i (V^k)_{ij}^{-1} (\vec{\theta}^k)_j.
\end{aligned}$$

2669 This is the value determined at each step of the MCMC to build the posterior
 2670 distribution, as discussed in chapter 4.

2671 8.1.1. Likelihood Scans

2672 Using the defintion of the likelihood presented in section 8.1, the response of each
 2673 sample to a variation particular parameter can be studied. Figure 8.1 presents the
 2674 variation of all the samples (beam and atmospheric) at SK. Each plot represents a
 2675 “scan”, where a particular parameter is scanned in some range. The “data” being
 2676 used within the definition of the likelihood equation is built using the Asimov A
 2677 oscillation parameter values defined in Table 2.2 alongside the pre-fit dial values as
 2678 discussed in subsection 6.4.3. Due to the correlations between oscillation parameters,
 2679 the value of $\chi^2 \sim 1$ does not equate to the typical 1σ sensitivity. However, it does give
 2680 an indication of which samples response the strongest to a variation in the oscillation
 2681 parameters. The point at which the likelihood tends to zero illustrates the value of the
 2682 parameter used to build the Asimov data prediction. The likelihood scans only include
 2683 the sample response and ignore the penalty contribution term from the variation of
 2684 the parameter.

2685 The response to Δm_{23}^2 is much larger in beam samples, specifically μ -like samples,
 2686 compared to atmospheric samples. This is to be expected as the beam neutrino
 2687 energy can be specifically tuned to match the maximal disappearance probability.
 2688 As discussed in section 7.1, the determination of the mass hierarchy is significantly
 2689 enhanced when using the atmospheric samples due to them transitioning through the
 2690 Earth’s core. So whilst the atmospheric samples do not add much information to the
 2691 constraint of $|\Delta m_{32}^2|$ beyond that of the beam analysis, they do enhance the ability to
 2692 determine the sign of the parameter.

2693 The sensitivity to $\sin^2(\theta_{23})$ is again dominated by the T2K experiment. However,
 2694 the difference in the response for atmospheric and beam samples is much smaller. Con-
 2695 sequently, one would expect that the joint fit would become more sensivity to $\sin^2(\theta_{23})$

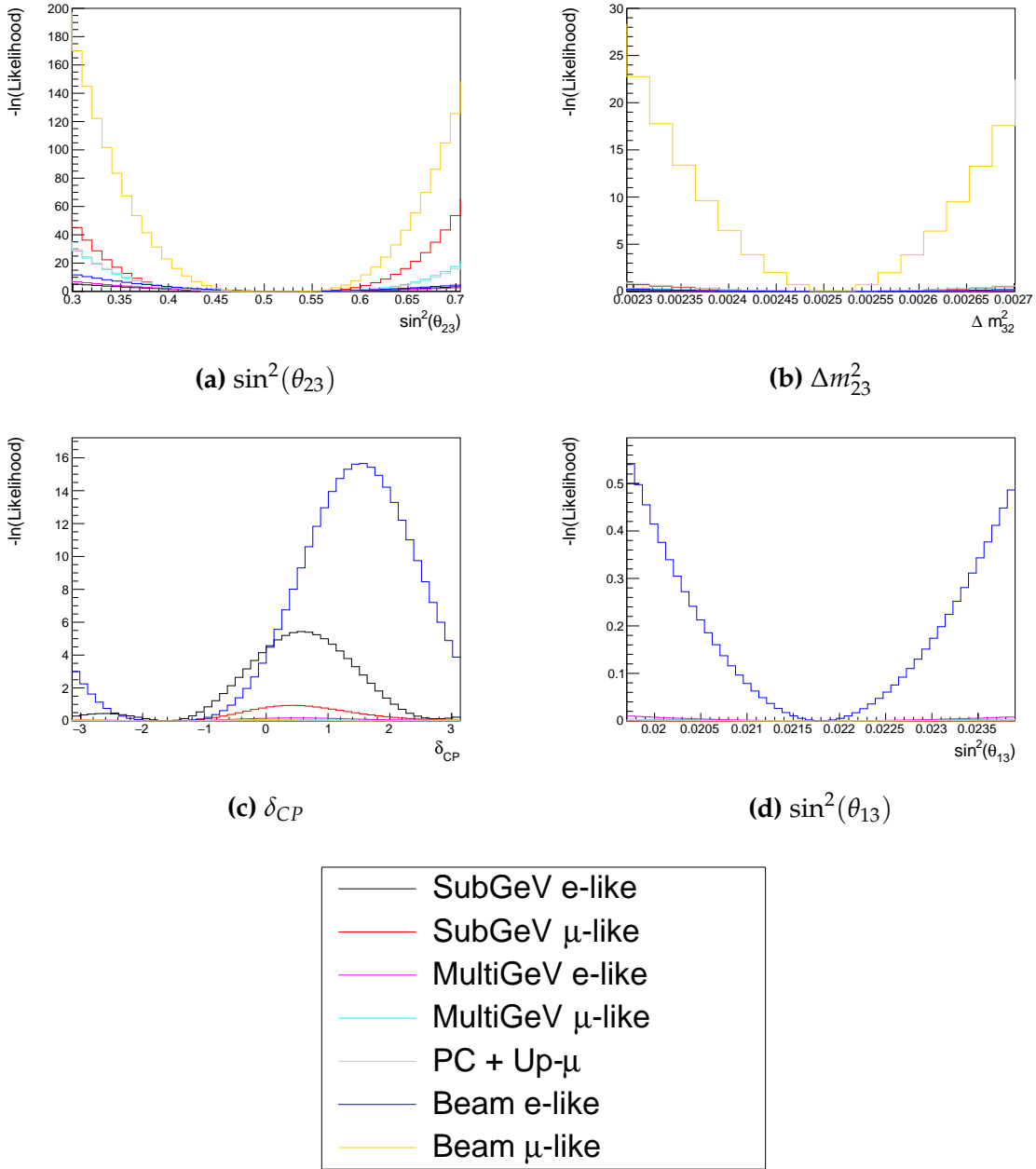


Figure 8.1.: The response of the likelihood, as defined in section 8.1, illustrating the response of the samples to the oscillation parameters. Δm_{12}^2 and $\sin^2(\theta_{12})$ are negated because these samples have no sensitivity to those parameters. The Asimov data set is built using the pre-fit dial values assuming Asimov A oscillation parameters defined in Table 2.2. DB: Need finer binning on delmsq23

than just T2K experiment alone. The summed response over all atmospheric samples becomes comparable to that of the muon-like beam samples. For this particular choice of Asimov point, the only samples which respond to the $\sin^2(\theta_{13})$ parameter are the

2699 electron-like beam samples. Consequently, no increase in sensitivity beyond that of
 2700 the T2K-only analysis is expected at that Asimov point. The Δm_{12}^2 and $\sin^2(\theta_{12})$ are
 2701 not considered as there is simply no sensitivity in any sample considered within this
 2702 analysis.

2703 As discussed, the correlations between oscillation parameters induce marginali-
 2704 sation effects within the response of the likelihood. That is to say, the response to
 2705 δ_{CP} is affected by the choice of $\sin^2(\theta_{13})$ or $\sin^2(\theta_{23})$. The two-dimensional scans of
 2706 the appearance ($\sin^2(\theta_{13}) - \delta_{CP}$) and disappearance ($\sin^2(\theta_{23}) - \Delta m_{23}^2$) parameters are
 2707 illustrated in Figure 8.2 and Figure 8.3, respectively.

2708 The appearance log-likelihood scans show the distinct difference in how the beam
 2709 and atmospheric samples respond. The beam samples have an approximately constant
 2710 width of the 2σ and 3σ contours, throughout all ranges of δ_{CP} . The atmospheric
 2711 samples response to δ_{CP} is very strongly correlated to the choice of $\sin^2(\theta_{13})$, with
 2712 the strongest constraints around $\delta_{CP} \sim 1$. Consequently, this difference allows some
 2713 of the degeneracy in a beam-only fit to be broken. Comparing the beam and joint
 2714 fit log-likelihood scans, the 2σ continuous contour in δ_{CP} for beam samples is broken
 2715 when the atmospheric samples are added. Furthermore, the width of the 3σ contours
 2716 also becomes dependent upon the value of δ_{CP} . Whilst these are encouraging results
 2717 for the joint fit, these are not sensitivity measurements as the nuisance parameters are
 2718 fixed.

2719 The disappearance log-likelihood scans in $\sin^2(\theta_{23}) - \Delta m_{23}^2$ space show the expected
 2720 result when considering the one-dimensional scans already discussed. The uncertainty
 2721 on the width of $|\Delta m_{32}^2|$ is mostly driven by the beam-only sensitivities. However, the
 2722 width of this contour in the inverted mass region ($\Delta m_{32}^2 < 0$) is significantly reduced
 2723 due to the ability of the atmospheric samples to select the correct mass hierarchy (these
 2724 log-likelihood scans use the Asimov A oscillation probabilities which assumes true

2725 normal hierarchy). The width of the uncertainty in $\sin^2(\theta_{23})$ is also reduce compared
2726 to a beam-only analysis, with a further decrease in the inverted hierarchy region due
2727 to mass hierarchy determination.

2728 In addition to the oscillation parameters, the response to the systematic model
2729 parameters can also be considered. Due to the correlated cross section model, the most
2730 informative DB: Finish this

2731 8.2. Monte Carlo Prediction

2732 Using the three sets of dial values defined in subsection 6.4.3, the predicted event rates
2733 for each sample are defined in Table 8.1. Both the oscillated event rates assuming
2734 Asimov A oscillation parameters (defined in Table 2.2) and the un-oscillated event
2735 rates are given.

2736 Generally, samples which target CCQE interaction modes observe a decrease in
2737 prediction when using the pre-fit dial values. This is in accordance with the Monte
2738 Carlo being produced assumed $M_A^{QE} = 1.21\text{GeV}$ whilst the pre-fit dial value should
2739 be $M_A^{QE} = 1.03\text{GeV}$, as suggested by [204]. Furthermore, the predicted event rates
2740 of samples which target CCRES interaction modes is significantly reduced when
2741 considering the post-ND fit. This follows the observations in subsection 6.4.3. The
2742 strength of the accelerator neutrino experiment can also be seen in the remarkable
2743 difference between the oscillated and unoscillated predictions in the FHC1Rmu and
2744 RHC1Rmu samples. There is a very obvious decrease in the expected event rate between
2745 the two predictions which is not as clearly observed in the atmospheric samples.
2746 This is due to the fact that the beam energy is tuned to the maximum disappearance
2747 probability, which is not the case for the naturally generated atmospheric neutrinos.

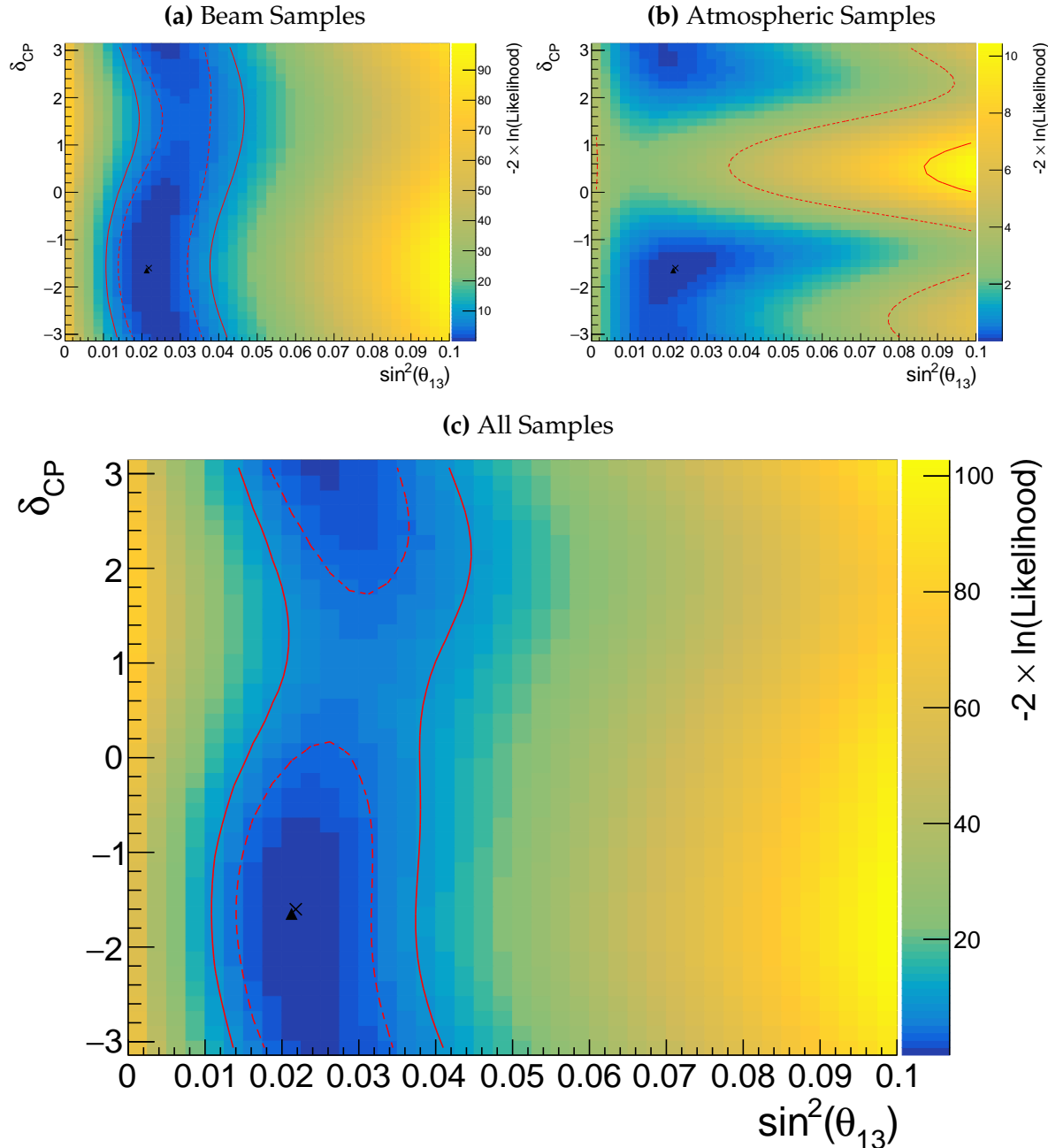


Figure 8.2.: Two-dimensional log-likelihood scan of the appearance ($\sin^2(\theta_{13})$ - δ_{CP}) parameters showing the response of the beam samples (top), atmospheric samples (middle) and the summed response (bottom). The Asimov A oscillation parameters, defined in Table 2.2, are assumed to be the true point (Black Cross). The position of the smallest log-likelihood is highlighted with the triangle. Prior uncertainty terms of the oscillation parameters are neglected. The two(three) sigma contour levels are illustrated with the dashed(solid) red line.

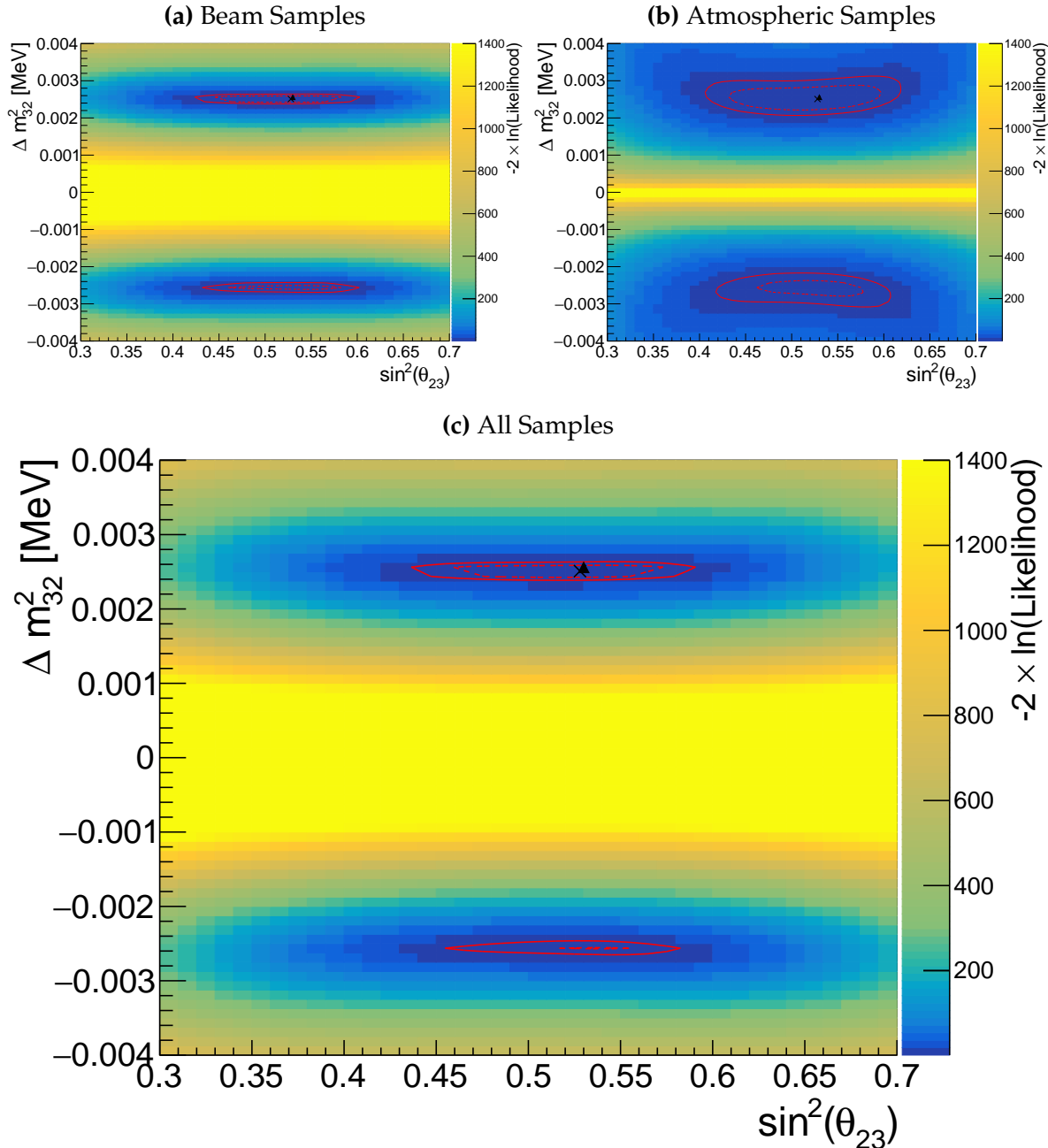


Figure 8.3.: Two-dimensional log-likelihood scan of the disappearance ($\sin^2(\theta_{23})$ - Δm_{32}^2) parameters showing the response of the beam samples (top), atmospheric samples (middle) and the summed response (bottom). The Asimov A oscillation parameters, defined in Table 2.2, are assumed to be the true point (Black Cross). The position of the smallest log-likelihood is highlighted with the triangle. Prior uncertainty terms of the oscillation parameters are neglected. The two(three) sigma contour levels are illustrated with the dashed(solid) red line.

Sample	Total Predicted Events					
	Generated		Pre-fit		Post-fit	
	Osc	UnOsc	Osc	UnOsc	Osc	UnOsc
SubGeV- <i>elike</i> -0d _c y	7121.0	7102.6	6556.8	6540.0	7035.2	7015.7
SubGeV- <i>elike</i> -1d _c y	704.8	725.5	693.8	712.8	565.7	586.0
SubGeV- <i>mulike</i> -0d _c y	1176.5	1737.2	1078.6	1588.1	1182.7	1757.1
SubGeV- <i>mulike</i> -1d _c y	5850.7	8978.1	5351.7	8205.1	5867.0	9009.9
SubGeV- <i>mulike</i> -2d _c y	446.9	655.2	441.6	647.7	345.9	505.6
SubGeV- <i>pi0like</i>	1438.8	1445.4	1454.9	1461.1	1131.1	1136.2
MultiGeV- <i>elike</i> - <i>nue</i>	201.4	195.6	201.1	195.3	202.6	196.7
MultiGeV- <i>elike</i> - <i>nuebar</i>	1141.5	1118.3	1060.7	1039.5	1118.5	1095.7
MultiGeV- <i>mulike</i>	1036.7	1435.8	963.1	1334.1	1015.2	1405.9
MultiRing- <i>elike</i> - <i>nue</i>	1025.1	982.2	1026.8	984.3	1029.8	986.4
MultiRing- <i>elike</i> - <i>nuebar</i>	1014.8	984.5	991.0	962.0	1008.9	978.5
MultiRing- <i>mulike</i>	2510.0	3474.4	2475.6	3425.8	2514.6	3480.4
MultiRingOther-1	1204.5	1279.1	1205.8	1280.3	1207.4	1281.0
PCStop	349.2	459.2	338.4	444.7	346.8	456.1
PCThrus	1692.8	2192.5	1661.5	2149.8	1689.2	2187.8
UpStop- <i>mu</i>	751.2	1295.0	739.7	1271.6	750.4	1293.0
UpThruNonShower- <i>mu</i>	2584.4	3031.6	2577.9	3019.4	2586.8	3034.0
UpThruShower- <i>mu</i>	473.0	488.6	473.2	488.7	473.8	489.4
FHC1R _{mu}	328.0	1409.2	301.1	1274.7	345.1	1568.0
RHC1R _{mu}	133.0	432.3	122.7	396.2	135.0	443.9
FHC1R _e	84.6	19.2	77.4	18.2	93.7	19.7
RHC1R _e	15.7	6.4	14.6	6.1	15.9	6.3
FHC1R _{e1de}	10.5	3.2	10.3	3.1	8.8	2.9

Table 8.1.: The Monte Carlo prediction of each sample observed at SK used within this analysis. Three model parameter tunes are considered, as defined in subsection 6.4.3. The oscillated predictions assumed Asimov A oscillation parameters provided in Table 2.2.

2749 **Appendix A**

2750 **Atmospheric Sample Spectra**

2751 This appendix documents the interaction mode breakdown of all the atmospheric
2752 samples used within the analysis. The generated tune of the model parameters and the
2753 Asimov A oscillation parameter set (defined in Table 2.2) are assumed. The livetime of
2754 SK-IV is taken to be 3244.4 days.

2755 **A.1. Binning**

2756 The lepton momentum and cosine zenith binning edges for the atmospheric samples
2757 used within this analysis are defined in Table A.1.

2758 **A.2. Fully Contained Sub-GeV Samples**

2759 The interaction mode breakdown of the fully contained Sub-GeV samples are shown
2760 in Figure A.1 and Figure A.2, for the samples with enriched CC0 π and CC1 π^\pm
2761 respectively.

2762 The CC0 π sample are dominated by CCQE events ($\sim 70\%$) with smaller contributions of 2p2h ($\sim 12\%$) and CC1 π ($\sim 10\%$) components. The energy peaks around 300 MeV, which is slightly below that of the T2K samples but still has significant contribution upto 1 GeV which overlaps the T2K sample energy range.

2766 The one-ring CC1 π samples, where the pion is tagged via its decay electron, are
2767 dominated by CC1 π events ($\sim 75\%$) with a small contribution of CCM π ($\sim 10\%$).
2768 The two-ring pion sample is mostly dominated by the NC1 π^0 via resonances, and
2769 has several equally-sized contributions from CCQE, NC1 π^\pm via resonances, and NC
2770 coherent pion production, where the π^0 likely comes from nucleon and π^\pm final state
2771 interactions in the nucleus.

Sample	$\cos(\theta_Z)$ Bins	Momentum Bin Edges ($\log_{10}(P)$ MeV)
SubGeV- <i>elike</i> -0dcy	10	2.0, 2.4, 2.6, 2.8, 3.0, 3.2
SubGeV- <i>elike</i> -1dcy	1	2.0, 2.4, 2.6, 2.8, 3.0, 3.2
SubGeV- <i>mulike</i> -0dcy	10	2.0, 2.4, 2.6, 2.8, 3.0, 3.2
SubGeV- <i>mulike</i> -1dcy	10	2.0, 2.4, 2.6, 2.8, 3.0, 3.2
SubGeV- <i>mulike</i> -2dcy	1	2.0, 2.4, 2.6, 2.8, 3.0, 3.2
SubGeV- <i>pi0like</i>	1	2.0, 2.2, 2.4, 2.6, 2.8, 3.2
MultiGeV- <i>elike</i> -nue	10	3.0, 3.4, 3.7, 4.0, 5.0
MultiGeV- <i>elike</i> -nuebar	10	3.0, 3.4, 3.7, 4.0, 5.0
MultiGeV- <i>mulike</i>	10	3.0, 3.4, 5.0
MultiRing- <i>elike</i> -nue	10	3.0, 3.4, 3.7, 5.0
MultiRing- <i>elike</i> -nuebar	10	3.0, 3.4, 3.7, 5.0
MultiRing- <i>mulike</i>	10	2.0, 3.124, 3.4, 3.7, 5.0
MultiRing- <i>Other1</i>	10	3.0, 3.4, 3.7, 4.0, 5.0
PC-Stop	10	2.0, 3.4, 5.0
PC-Through	10	2.0, 3.124, 3.4, 3.7, 5.0
Upmu-Stop	10	3.2, 3.4, 3.7, 8.0
Upmu-Through-Showering	10	2.0, 8.0
Upmu-Through-NonShowering	10	2.0, 8.0

Table A.1.: The reconstructed cosine zenith and lepton momentum binning assigned to the atmospheric samples. The “ $\cos(\theta_Z)$ Bins” column illustrates the number of bins uniformly distributed over the $-1.0 \leq \cos(\theta_Z) \leq 1.0$ region for fully and partially contained samples and $-1.0 \leq \cos(\theta_Z) \leq 0.0$ region for up- μ samples.

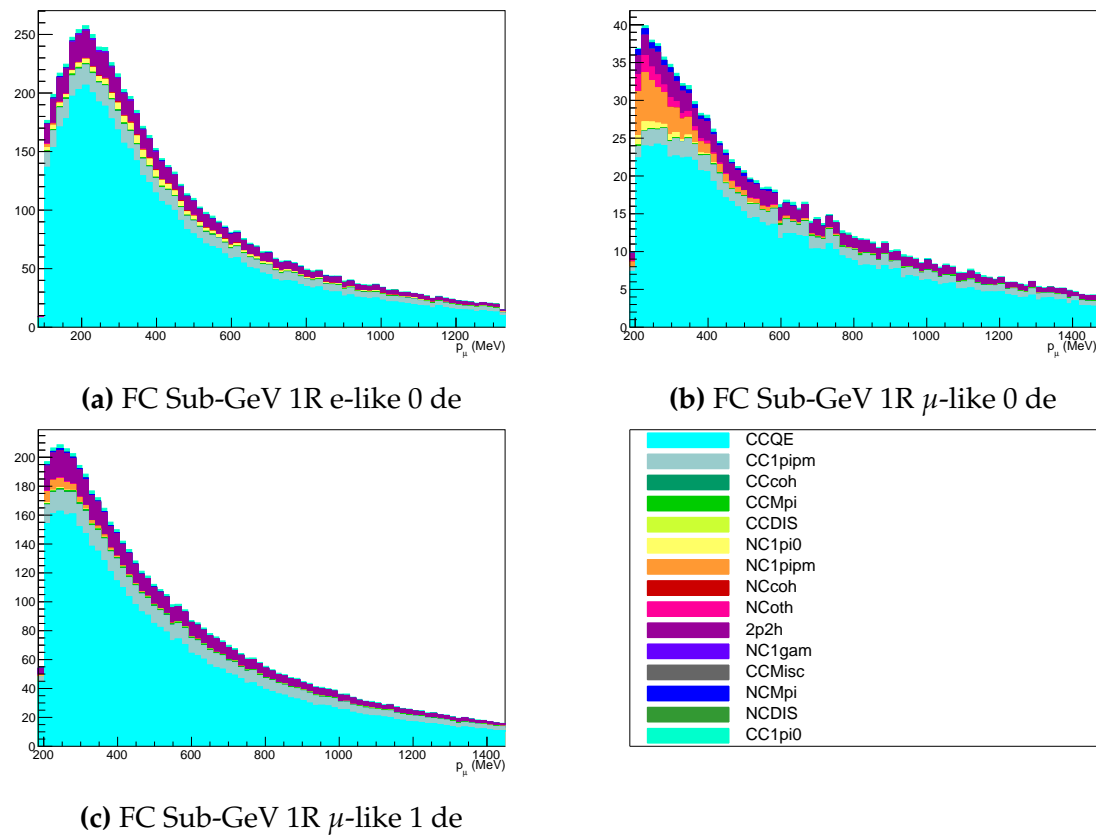


Figure A.1: Breakdown by interaction mode of the FC Sub-GeV atmospheric samples targeting CC 0π events.

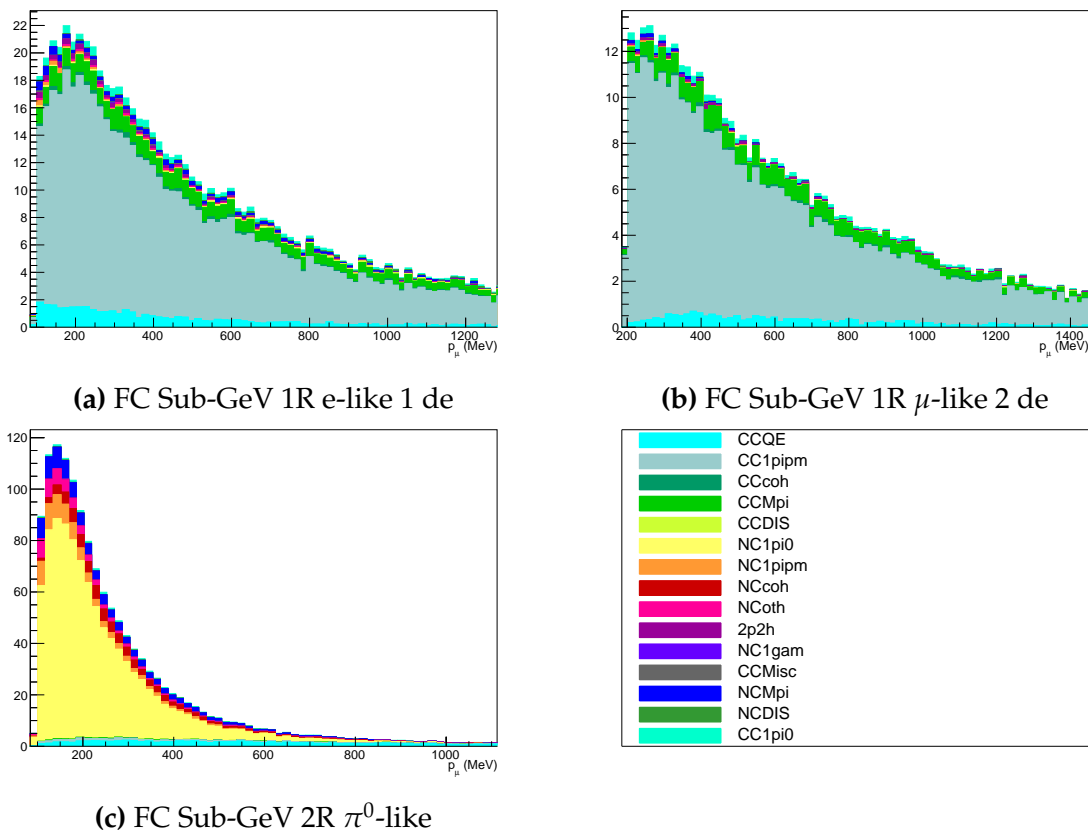


Figure A.2: Breakdown by interaction mode of the FC Sub-GeV atmospheric samples targeting single pion events.

²⁷⁷² A.3. Fully Contained Multi-GeV Samples

²⁷⁷³ The interaction mode breakdown of fully contained multi-GeV samples is highlighted
²⁷⁷⁴ in Figure A.3. Due to the event selection applied in SK which targets π^+ and π^-
²⁷⁷⁵ separation, the ν_e sample mainly consists of events with pions (single pion production
²⁷⁷⁶ or multi-pion/DIS interactions). The pion separation is explained in Section section 6.1.
²⁷⁷⁷ This reasoning also explains the significant CCQE contribution of the $\bar{\nu}_e$ sample. The
²⁷⁷⁸ muon-like sample is dominated by CCQE interactions with $\sim 10 - 15\%$ 2p2h and
²⁷⁷⁹ CC1 π contribution of events.

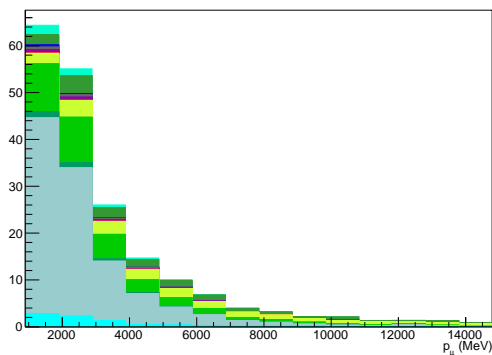
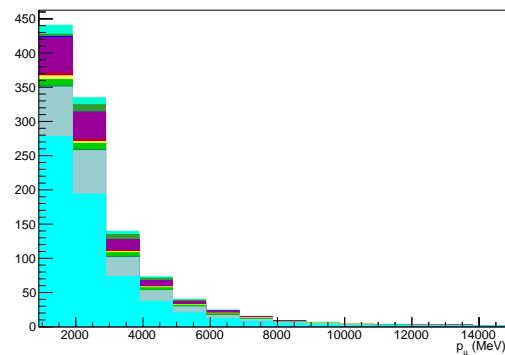
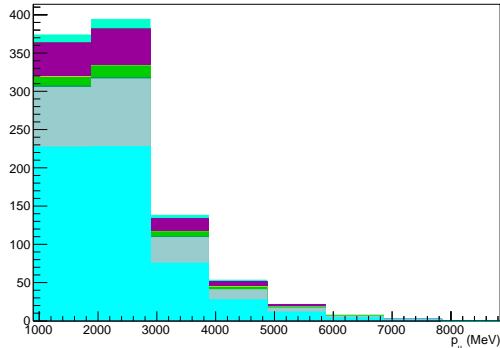
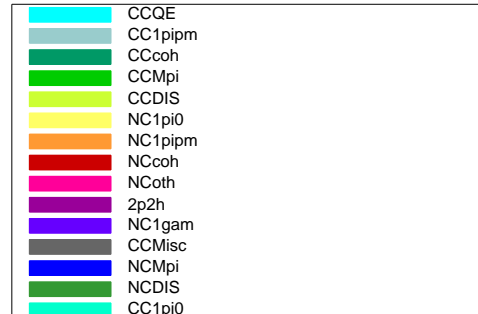
(a) FC Multi-GeV single ring ν_e -like(b) FC Multi-GeV single ring $\bar{\nu}_e$ -like(c) FC Multi-GeV single ring μ -like

Figure A.3: Breakdown by interaction mode of the FC Multi-GeV single ring atmospheric samples.

2780 A.4. Fully Contained Multi-Ring Samples

2781 The interaction mode breakdown of fully contained multi-ring events is shown in Figure A.4. These samples see more interaction modes contributing in general, and there
 2782 is a much larger contribution from multi-pion and DIS interaction modes, compared
 2783 to the other samples.

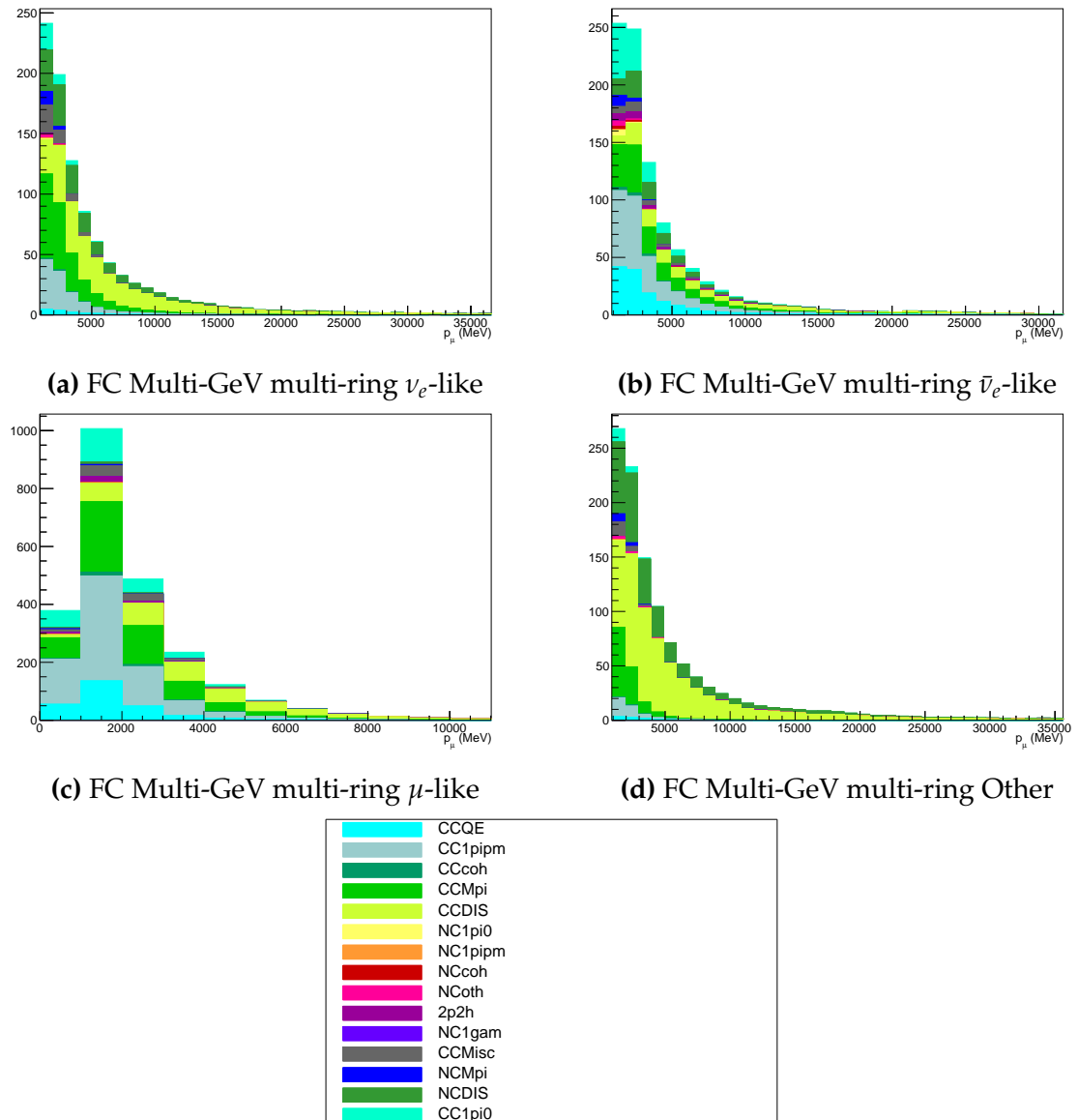


Figure A.4.: Breakdown by interaction mode of the FC Multi-GeV multi-ring atmospheric samples.

²⁷⁸⁵ A.5. Partially Contained Samples

²⁷⁸⁶ The breakdown for partially contained samples is highlighted in Figure A.5. As with
²⁷⁸⁷ the multi-ring samples, there is no dominating interaction mode. The neutrino energies
²⁷⁸⁸ of events in this sample extend into the tens of GeV and become dominated by DIS
²⁷⁸⁹ interaction modes in the high energy limit.

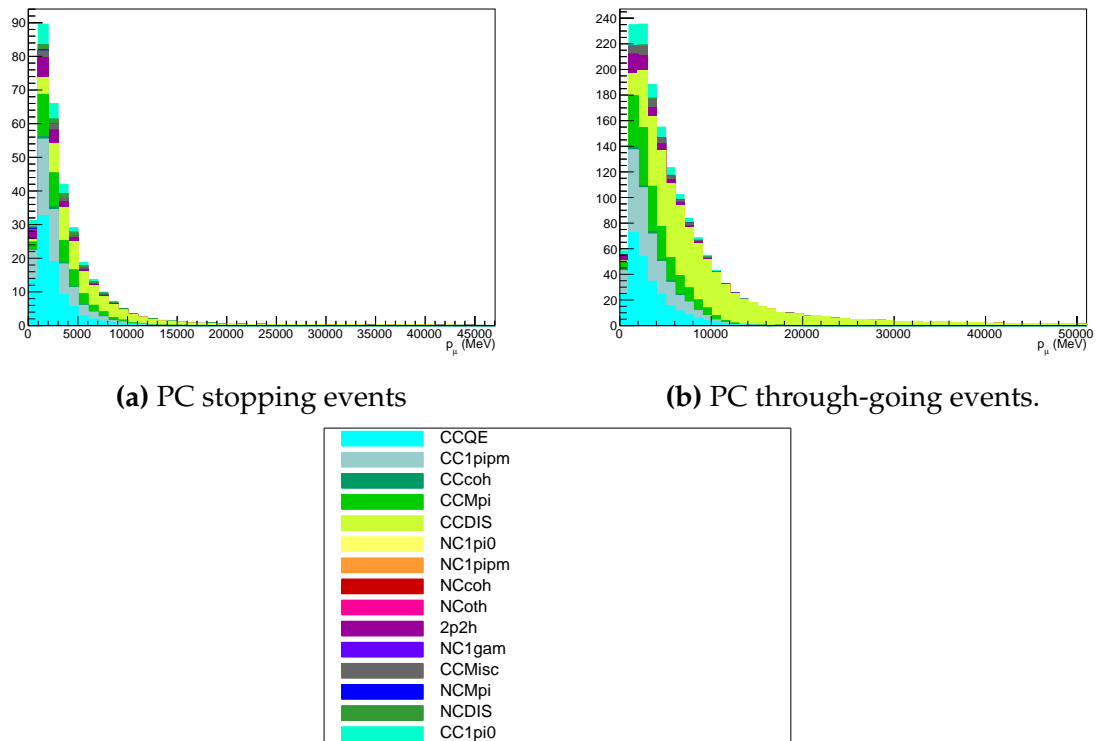
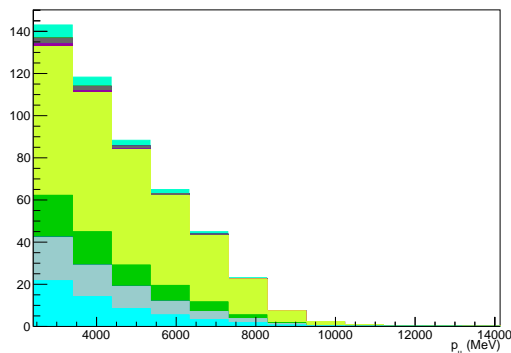
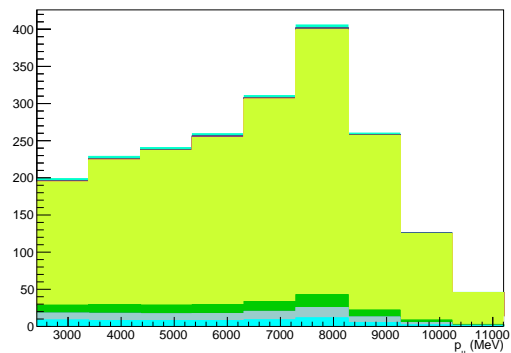
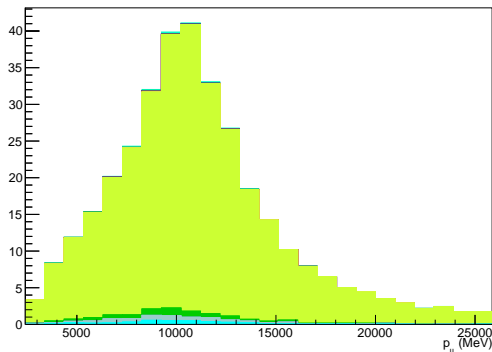
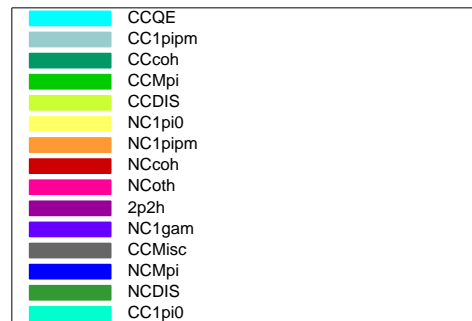


Figure A.5.: Breakdown by interaction mode of the PC atmospheric samples.

2790 A.6. Upward-Going Muon Samples

2791 The breakdown for upward-going muons is illustrated in Figure A.6. These samples
 2792 are significantly dominated by DIS interactions with energies extending up into the
 2793 hundreds of GeV.

(a) Up- μ stopping events(b) Up- μ through going non showering events(c) Up- μ through going showering events**Figure A.6.:** Breakdown by interaction mode of the atmospheric upward going muon samples.

₂₇₉₅ **Bibliography**

- ₂₇₉₆ [1] J. Chadwick, Verhandl. Dtsc. Phys. Ges. **16**, 383 (1914).
- ₂₇₉₇ [2] C. D. Ellis and W. A. Wooster, Proc. R. Soc. Lond. A Math. Phys. Sci. **117**, 109
₂₇₉₈ (1927).
- ₂₇₉₉ [3] W. Pauli, Phys. Today **31N9**, 27 (1978).
- ₂₈₀₀ [4] E. Fermi, Z. Phys. **88**, 161 (1934).
- ₂₈₀₁ [5] F. Reines and C. L. Cowan, Phys. Rev. **92**, 830 (1953).
- ₂₈₀₂ [6] C. L. Cowan, F. Reines, F. B. Harrison, H. W. Kruse, and A. D. McGuire, Science
₂₈₀₃ **124**, 103 (1956), <http://science.sciencemag.org/content/124/3212/103.full.pdf>.
- ₂₈₀₄ [7] G. Danby *et al.*, Phys. Rev. Lett. **9**, 36 (1962).
- ₂₈₀₅ [8] K. Kodama *et al.*, Physics Letters B **504**, 218 (2001).
- ₂₈₀₆ [9] LSND, A. Aguilar-Arevalo *et al.*, Phys. Rev. **D64**, 112007 (2001), hep-ex/0104049.
- ₂₈₀₇ [10] MiniBooNE Collaboration, A. A. Aguilar-Arevalo *et al.*, Phys. Rev. Lett. **110**,
₂₈₀₈ 161801 (2013).
- ₂₈₀₉ [11] Planck Collaboration *et al.*, aap **641** (2020).
- ₂₈₁₀ [12] The ALEPH Collaboration, The Delphi Collaboration, The L3 Collaboration, The
₂₈₁₁ SLD Collaboration, The LEP Electroweak Working Group, The SLD Electroweak
₂₈₁₂ and Heavy Flavour Groups, J. A. Bagger *et al.*, Physics Reports **427**, 257 (2006).
- ₂₈₁₃ [13] B. Pontecorvo, Sov. Phys. JETP **26**, 984 (1968), [Zh. Eksp. Teor. Fiz. 53, 1717 (1967)].
- ₂₈₁₄ [14] B. Pontecorvo, Sov. Phys. JETP **7**, 172 (1958), [Zh. Eksp. Teor. Fiz. 34, 247 (1957)].
- ₂₈₁₅ [15] M. Kobayashi and T. Maskawa, Progress of Theoretical Physics **49**, 652 (1973).
- ₂₈₁₆ [16] N. Cabibbo, Phys. Rev. Lett. **10**, 531 (1963).
- ₂₈₁₇ [17] A. M. and, Journal of Physics: Conference Series **587**, 012030 (2015).
- ₂₈₁₈ [18] A. Y. Smirnov, (2003).
- ₂₈₁₉ [19] S. Mikheyev and A. Smirnov, Soviet Journal of Nuclear Physics **42**, 913 (1985).

- [20] L. Wolfenstein, Phys. Rev. D **17**, 2369 (1978).
- [21] V. D. Barger, K. Whisnant, S. Pakvasa, and R. J. N. Phillips, Phys. Rev. D **22**, 2718 (1980).
- [22] The Super-Kamiokande Collaboration, Y. Ashie *et al.*, Phys. Rev. Lett. **93**, 101801 (2004).
- [23] SNO Collaboration, Q. R. Ahmad *et al.*, Phys. Rev. Lett. **89**, 011301 (2002).
- [24] 2015 Nobel prize in Physics as listed by Nobelprize.org, https://www.nobelprize.org/nobel_prizes/physics/laureates/2015/, Accessed: 22-06-2022.
- [25] J. A. Formaggio and G. P. Zeller, Rev. Mod. Phys. **84**, 1307 (2012), 1305.7513.
- [26] A. Bellerive, Int. J. Mod. Phys. A **19**, 1167 (2004).
- [27] R. Davis, D. S. Harmer, and K. C. Hoffman, Phys. Rev. Lett. **20**, 1205 (1968).
- [28] N. Vinyoles *et al.*, Astrophys. J. **835**, 202 (2017).
- [29] V. Gribov and B. Pontecorvo, Phys. Lett. B **28**, 493 (1969).
- [30] K. S. Hirata *et al.*, Phys. Rev. Lett. **63**, 16 (1989).
- [31] W. Hampel *et al.*, Phys. Lett. B **447**, 127 (1999).
- [32] SAGE Collaboration, J. N. Abdurashitov *et al.*, Phys. Rev. C **60**, 055801 (1999).
- [33] Q. R. Ahmad *et al.*, Phys. Rev. Lett. **89** (2002).
- [34] Borexino Collaboration, Nature **562**, 505 (2018).
- [35] B. Aharmim *et al.*, Astrophys. J. **653**, 1545 (2006).
- [36] M. Agostini *et al.*, (2020).
- [37] S. Andringa *et al.*, Adv. High Energy Phys. **2016**, 1 (2016).
- [38] J. F. Beacom *et al.*, Chin. phys. C **41**, 023002 (2017).
- [39] F. An *et al.*, J. Phys. G Nucl. Part. Phys. **43**, 030401 (2016).
- [40] J. Aalbers *et al.*, (2020), 2006.03114.
- [41] T. K. Gaisser and M. Honda, (2002).

- 2846 [42] G. D. Barr, T. K. Gaisser, P. Lipari, S. Robbins, and T. Stanev, Physical Review D
2847 **70** (2004).
- 2848 [43] M. Honda, T. Kajita, K. Kasahara, S. Midorikawa, and T. Sanuki, Physical Review
2849 D **75** (2007).
- 2850 [44] M. Honda, T. Kajita, K. Kasahara, and S. Midorikawa, Phys. Rev. D **70**, 043008
2851 (2004).
- 2852 [45] M. Honda, T. Kajita, K. Kasahara, and S. Midorikawa, Phys. Rev. D **83**, 123001
2853 (2011).
- 2854 [46] A. Fasso, A. Ferrari, P. R. Sala, and J. Ranft, (2001).
- 2855 [47] Y. Ashie *et al.*, Physical Review D **71** (2005).
- 2856 [48] F. Reines *et al.*, Phys. Rev. Lett. **15**, 429 (1965).
- 2857 [49] D. Casper *et al.*, Phys. Rev. Lett. **66**, 2561 (1991).
- 2858 [50] K. S. Hirata *et al.*, Phys. Lett. B **280**, 146 (1992).
- 2859 [51] Z. Li *et al.*, Physical Review D **98** (2018).
- 2860 [52] Kamiokande Collaboration *et al.*, (2017).
- 2861 [53] T2K Collaboration, Nature **580**, 339 (2020).
- 2862 [54] M. A. Acero *et al.*, Phys. Rev. Lett. **123**, 151803 (2019).
- 2863 [55] M. G. Aartsen *et al.*, Phys. Rev. Lett. **120** (2018).
- 2864 [56] P. Adamson *et al.*, Phys. Rev. Lett. **112** (2014).
- 2865 [57] M. S. Athar *et al.*, Progress in Particle and Nuclear Physics **124**, 103947 (2022).
- 2866 [58] G. Danby *et al.*, Phys. Rev. Lett. **9**, 36 (1962).
- 2867 [59] K. Abe *et al.*, Physical Review D **87** (2013).
- 2868 [60] MINOS Collaboration, D. G. Michael *et al.*, Phys. Rev. Lett. **97**, 191801 (2006).
- 2869 [61] G. Danby *et al.*, Phys. Rev. Lett. **9**, 36 (1962).
- 2870 [62] NOvA Collaboration, M. A. Acero *et al.*, Phys. Rev. Lett. **123**, 151803 (2019).
- 2871 [63] B. Abi, R. Acciarri, M. A. Acero, and G. e. a. Adamov, Eur. Phys. J. C Part. Fields

- 2872 **80** (2020).
- 2873 [64] Hyper-Kamiokande Proto-Collaboration *et al.*, Prog. Theor. Exp. Phys. **2015**,
2874 53C02 (2015).
- 2875 [65] C. Blanco, D. Hooper, and P. Machado, Physical Review D **101** (2020).
- 2876 [66] MicroBooNE Collaboration *et al.*, Search for an Excess of Electron Neutrino
2877 Interactions in MicroBooNE Using Multiple Final State Topologies, 2021.
- 2878 [67] KARMEN Collaboration, B. Armbruster *et al.*, Phys. Rev. D **65**, 112001 (2002).
- 2879 [68] S.-B. Kim, T. Lasserre, and Y. Wang, Adv. High Energy Phys. **2013**, 1 (2013).
- 2880 [69] M. Sajjad Athar *et al.*, Prog. Part. Nucl. Phys. **124**, 103947 (2022), 2111.07586.
- 2881 [70] K. Abe *et al.*, Nucl. Instrum. Methods Phys. Res. A **1027**, 166248 (2022).
- 2882 [71] F. P. An *et al.*, Phys. Rev. Lett. **108**, 171803 (2012).
- 2883 [72] RENO Collaboration, J. K. Ahn *et al.*, Phys. Rev. Lett. **108**, 191802 (2012).
- 2884 [73] Double Chooz Collaboration, Y. Abe *et al.*, Phys. Rev. Lett. **108**, 131801 (2012).
- 2885 [74] J. Collaboration *et al.*, TAO Conceptual Design Report: A Precision Measurement
2886 of the Reactor Antineutrino Spectrum with Sub-percent Energy Resolution, 2020,
2887 2005.08745.
- 2888 [75] for the RENO Collaboration, New results from RENO and the 5 MeV excess,
2889 AIP Publishing LLC, 2015.
- 2890 [76] Y. Abe *et al.*, Journal of High Energy Physics **2014** (2014).
- 2891 [77] Daya Bay Collaboration, D. Adey *et al.*, Phys. Rev. Lett. **123**, 111801 (2019).
- 2892 [78] M. P. Decowski, Nucl. Phys. B. **908**, 52 (2016).
- 2893 [79] The KamLAND Collaboration, A. Gando *et al.*, Phys. Rev. D **83**, 052002 (2011).
- 2894 [80] P. Dunne, Latest Neutrino oscillation results from T2K, 2020.
- 2895 [81] M. Tanabashi *et al.*, Phys. Rev. D. **98** (2018).
- 2896 [82] Particle Data Group, R. L. Workman and Others, PTEP **2022**, 083C01 (2022).
- 2897 [83] T2K Collaboration, K. Abe *et al.*, Phys. Rev. Lett. **112**, 181801 (2014).

- 2898 [84] Y. Fukuda *et al.*, Phys. Rev. Lett. **81**, 1562 (1998).
- 2899 [85] Linyan Wan, (2022).
- 2900 [86] K. Abe *et al.*, Nuclear Instruments and Methods in Physics Research Section
2901 A: Accelerators, Spectrometers, Detectors and Associated Equipment **737**, 253
2902 (2014).
- 2903 [87] S. Fukuda *et al.*, Nucl. Instrum. Methods Phys. Res. A **501**, 418 (2003).
- 2904 [88] Y. Itow *et al.*, (2001).
- 2905 [89] M. Jiang *et al.*, Prog. Theor. Exp. Phys. **2019** (2019).
- 2906 [90] S. Fukuda *et al.*, Nuclear Instruments and Methods in Physics Research Section
2907 A: Accelerators, Spectrometers, Detectors and Associated Equipment **501**, 418
2908 (2003), <http://www.sciencedirect.com/science/article/pii/S016890020300425X>.
- 2909 [91] Y. Nakano *et al.*, Nucl. Instrum. Methods Phys. Res. A **977**, 164297 (2020).
- 2910 [92] Hamamatsu, Hamamatsu Photonics Photomultiplier Tubes Handbook.
- 2911 [93] K. Abe *et al.*, Nucl. Instrum. Methods Phys. Res. A **1027**, 166248 (2022).
- 2912 [94] J. F. Beacom and M. R. Vagins, Phys. Rev. Lett. **93**, 171101 (2004).
- 2913 [95] L. Marti *et al.*, Nucl. Instrum. Methods Phys. Res. A **959**, 163549 (2020).
- 2914 [96] L. Marti *et al.*, (2019).
- 2915 [97] M. Vagins, Solar/DSNB Neutrino_SK-Gd, 2022.
- 2916 [98] J. Focht, PhD thesis, Massachusetts Institute of Technology, 2004.
- 2917 [99] T. Tanimori *et al.*, IEEE Transactions on Nuclear Science **36**, 497 (1989).
- 2918 [100] Super-Kamiokande Collaboration, J. Hosaka *et al.*, Phys. Rev. D **73**, 112001
2919 (2006).
- 2920 [101] H. Nishino *et al.*, Nucl. Instrum. Methods Phys. Res. A **610**, 710 (2009).
- 2921 [102] S. Yamada *et al.*, IEEE Transactions on Nuclear Science **57**, 428 (2010).
- 2922 [103] S. Yamada, Y. Hayato, Y. Obayashi, and M. Shiozawa, New online system
2923 without hardware trigger for the Super-Kamiokande experiment, in *2007 IEEE
2924 Nuclear Science Symposium Conference Record*, IEEE, 2007.

- 2925 [104] G. Carminati, Phys. Procedia **61**, 666 (2015).
- 2926 [105] P. A. Čerenkov, Phys. Rev. **52**, 378 (1937).
- 2927 [106] I. Frank and I. Tamm, Coherent visible radiation of fast electrons passing
2928 through matter, in *Selected Papers*, pp. 29–35, Springer Berlin Heidelberg, Berlin,
2929 Heidelberg, 1991.
- 2930 [107] The T2K Collaboration, KEK Proposal (2001),
2931 <http://neutrino.kek.jp/jhfnu/loi/loi.v2.030528.pdf>.
- 2932 [108] Y. Itow *et al.*, (2001), hep-ex/0106019.
- 2933 [109] The K2K Collaboration and S. H. Ahn, (2001), hep-ex/0103001.
- 2934 [110] The T2K Collaboration, KEK Proposal (2006), http://j-parc.jp/researcher/Hadron/en/pac_0606/pdf/p11-Nishikawa.pdf.
- 2936 [111] C. Bronner, Accelerator Neutrino I_Recent results from T2K, 2022.
- 2937 [112] T2K Collaboration, K. Abe *et al.*, Phys. Rev. Lett. **112**, 061802 (2014),
2938 <https://link.aps.org/doi/10.1103/PhysRevLett.112.061802>.
- 2939 [113] NINJA Collaboration, T. Fukuda *et al.*, Proposal for precise measurement of
2940 neutrino-water cross-section in NINJA physics run, Proposal for J-PARC and
2941 KEK, 2017.
- 2942 [114] T. Ovsiannikova *et al.*, Physics of Particles and Nuclei **48**, 1014 (2017),
2943 <https://doi.org/10.1134/S1063779617060478>.
- 2944 [115] M. Antonova *et al.*, Journal of Instrumentation **12**, C07028 (2017),
2945 <http://stacks.iop.org/1748-0221/12/i=07/a=C07028>.
- 2946 [116] The T2K Collaboration, K. Abe *et al.*, Phys. Rev. D **102**, 012007 (2020).
- 2947 [117] K. Abe *et al.*, Progress of Theoretical and Experimental Physics **2021** (2021).
- 2948 [118] The T2K Collaboration, K. Abe *et al.*, Nuclear Instruments
2949 and Methods in Physics Research Section A: Accelerators, Spectrometers,
2950 Detectors and Associated Equipment **659**, 106 (2011),
2951 <http://www.sciencedirect.com/science/article/pii/S0168900211011910>.
- 2952 [119] K. Matsuoka *et al.*, Nuclear Instruments and Methods in Physics Research Section
2953 A: Accelerators, Spectrometers, Detectors and Associated Equipment **624**, 591

- 2954 (2010), <http://www.sciencedirect.com/science/article/pii/S016890021002098X>.
- 2955 [120] K. Abe *et al.*, Phys. Rev. D. **103** (2021).
- 2956 [121] T. Vladisavljevic, *Predicting the T2K neutrino flux and measuring oscillation parameters* Springer theses, 1 ed. (Springer Nature, Cham, Switzerland, 2020).
- 2957
- 2958 [122] D. Beavis, A. Carroll, and I. Chiang, (1995).
- 2959 [123] P.-A. Amaudruz *et al.*, Nuclear Instruments and Methods in Physics Research
2960 Section A: Accelerators, Spectrometers, Detectors and Associated Equipment
2961 **696**, 1 (2012).
- 2962 [124] N. Abgrall *et al.*, Nuclear Instruments and Methods in Physics Research Section
2963 A: Accelerators, Spectrometers, Detectors and Associated Equipment **637**, 25
2964 (2011).
- 2965 [125] S. Assylbekov *et al.*, Nuclear Instruments and Methods in Physics Research
2966 Section A: Accelerators, Spectrometers, Detectors and Associated Equipment
2967 **686**, 48 (2012).
- 2968 [126] D. Allan *et al.*, Journal of Instrumentation **8**, P10019 (2013).
- 2969 [127] F. Vannucci, Advances in High Energy Physics **2014**, 1 (2014).
- 2970 [128] UA1 magnet sets off for a second new life, 2022.
- 2971 [129] S. Aoki *et al.*, Nuclear Instruments and Methods in Physics Research Section
2972 A: Accelerators, Spectrometers, Detectors and Associated Equipment **698**, 135
2973 (2013).
- 2974 [130] K. Suzuki *et al.*, Progress of Theoretical and Experimental Physics **2015**, 53C01
2975 (2015).
- 2976 [131] S. Brooks, A. Gelman, G. L. Jones, and X.-L. Meng, *Handbook of Markov Chain
2977 Monte Carlo* (CRC Press, 2011).
- 2978 [132] W. R. Gilks, S. Richardson, and D. J. Spiegelhalter, *Markov Chain Monte Carlo in
2979 Practice* (Chapman & Hall/CRC Interdisciplinary Statistics, 1995).
- 2980 [133] C. Wret, *Minimising systematic uncertainties in the T2K experiment using near-
2981 detector and external data*, PhD thesis, Imperial College London, 2018.
- 2982 [134] K. E. Duffy, *Measurement of the Neutrino Oscillation Parameters $\sin^2 \theta_{23}$, Δm_{32}^2 ,*

- 2983 $\sin^2 \theta_{13}$, and δ_{CP} in Neutrino and Antineutrino Oscillation at T2K, PhD thesis, Oriel
2984 College, University of Oxford, 2016.
- 2985 [135] T. Bayes, Rev. Phil. Trans. Roy. Soc. Lond. **53**, 370 (1764).
- 2986 [136] N. Metropolis, A. W. Rosenbluth, M. N. Rosenbluth, A. H. Teller, and E. Teller,
2987 Journal of Chemical Physics **21** (1970).
- 2988 [137] W. K. Hastings, Biometrika **57** (1970).
- 2989 [138] J. Dunkley, M. Bucher, P. G. Ferreira, K. Moodley, and C. Skordis, Mon. Not. R.
2990 Astron. Soc. **356**, 925 (2005).
- 2991 [139] Particle Data Group *et al.*, Prog. Theor. Exp. Phys. **2020** (2020).
- 2992 [140] H. Jeffreys, *The Theory of Probability* Oxford Classic Texts in the Physical Sciences
2993 (, 1939).
- 2994 [141] R. E. Kass and A. E. Raftery, J. Am. Stat. Assoc. **90**, 773 (1995).
- 2995 [142] T. Böhlen *et al.*, Nuclear Data Sheets **120**, 211 (2014),
2996 <http://www.sciencedirect.com/science/article/pii/S0090375214005018>.
- 2997 [143] R. Brun *et al.*, GEANT: Detector Description and Simulation Tool; Oct 1994 CERN
2998 Program Library (CERN, Geneva, 1993), <http://cds.cern.ch/record/1082634>,
2999 Long Writeup W5013.
- 3000 [144] T2K Collaboration, K. Abe *et al.*, Phys. Rev. D **87**, 012001 (2013).
- 3001 [145] C. Zeitnitz and T. Gabriel, Nuclear Instruments and Methods in Physics Research Section A: Accelerators, Spectrometers, Detectors and Associated Equipment **349**, 106 (1994),
3002 <http://www.sciencedirect.com/science/article/pii/0168900294906130>.
- 3003 [146] A. Fiorentini *et al.*, T2K Technical Note **217** (2017).
- 3004 [147] N. Abgrall *et al.*, Physical Review C **84** (2011).
- 3005 [148] N. Abgrall *et al.*, Physical Review C **85** (2012).
- 3006 [149] N. Abgrall *et al.*, Nuclear Instruments and Methods in Physics Research Section
3007 A: Accelerators, Spectrometers, Detectors and Associated Equipment **701**, 99
3008 (2013), <http://www.sciencedirect.com/science/article/pii/S016890021201234X>.

- 3011 [150] HARP Collaboration, M. Apollonio *et al.*, Phys. Rev. C **80**, 035208 (2009),
3012 <https://link.aps.org/doi/10.1103/PhysRevC.80.035208>.
- 3013 [151] B. Blau *et al.*, Nuclear Physics B - Proceedings Supplements **113**, 125 (2002).
- 3014 [152] S. Haino *et al.*, Physics Letters B **594**, 35 (2004).
- 3015 [153] NASA, U.S. Standard Atmosphere, 1976, 1976.
- 3016 [154] S. Roesler, R. Engel, and J. Ranft, The Monte Carlo Event Generator DPMJET-III,
3017 in *Advanced Monte Carlo for Radiation Physics, Particle Transport Simulation and*
3018 *Applications*, pp. 1033–1038, Springer Berlin Heidelberg, 2001.
- 3019 [155] K. Niita *et al.*, Radiation Measurements **41**, 1080 (2006).
- 3020 [156] T. Sanuki *et al.*, Physics Letters B **541**, 234 (2002).
- 3021 [157] P. Achard *et al.*, Physics Letters B **598**, 15 (2004).
- 3022 [158] K. Sato, Atmospheric Neutrino_Reviews on neutrino fluxes (low E atm nu),
3023 2022.
- 3024 [159] Y. Hayato and L. Pickering, The European Physical Journal Special Topics **230**,
3025 4469 (2021).
- 3026 [160] Y. Hayato, Acta Physica Polonica B **40** (2009).
- 3027 [161] C. L. Smith, Physics Reports **3**, 261 (1972),
3028 <http://www.sciencedirect.com/science/article/pii/0370157372900105>.
- 3029 [162] O. Benhar, A. Fabrocini, and S. Fantoni, Nuclear Physics A **497**, 423 (1989).
- 3030 [163] R. Bradford, A. Bodek, H. Budd, and J. Arrington, Nuclear
3031 Physics B - Proceedings Supplements **159**, 127 (2006),
3032 <http://www.sciencedirect.com/science/article/pii/S0920563206005184>,
3033 Proceedings of the 4th International Workshop on Neutrino-Nucleus Interac-
3034 tions in the Few-GeV Region.
- 3035 [164] A. A. Aguilar-Arevalo *et al.*, Physical Review D **81** (2010).
- 3036 [165] R. Gran, J. Nieves, F. Sanchez, and M. J. V. Vacas, Phys. Rev. D **88**, 113007 (2013),
3037 <https://link.aps.org/doi/10.1103/PhysRevD.88.113007>.
- 3038 [166] C. Berger and L. M. Sehgal, Phys. Rev. D **76**, 113004 (2007).

- 3039 [167] C. Berger and L. M. Sehgal, Phys. Rev. D **79**, 053003 (2009),
3040 <https://link.aps.org/doi/10.1103/PhysRevD.79.053003>.
- 3041 [168] T. Sjöstrand, Computer Physics Communications **82**, 74 (1994).
- 3042 [169] C. Bronner and M. Hartz, Tuning of the Charged Hadrons Multiplicities for Deep
3043 Inelastic Interactions in NEUT, in *Proceedings of the 10th International Workshop on*
3044 *Neutrino-Nucleus Interactions in Few-GeV Region (NuInt15)*, Journal of the Physical
3045 Society of Japan, 2016.
- 3046 [170] M. Glück, E. Reya, and A. Vogt, The European Physical Journal C **5**, 461 (1998).
- 3047 [171] A. Bodek and U.-k. Yang, Axial and Vector Structure Functions for Electron- and
3048 Neutrino- Nucleon Scattering Cross Sections at all Q^2 using Effective Leading
3049 order Parton Distribution Functions, 2010.
- 3050 [172] A. Bodek and U.-K. Yang, (2010).
- 3051 [173] S. Gollapinni, (2016).
- 3052 [174] E. S. P. Guerra *et al.*, Phys. Rev. D **99**, 052007 (2019).
- 3053 [175] GEANT4, S. Agostinelli *et al.*, Nucl. Instrum. Meth. **A506**, 250 (2003).
- 3054 [176] R. Brun, F. Bruyant, M. Maire, A. C. McPherson, and P. Zanarini, (1987).
- 3055 [177] K. Abe *et al.*, Physical Review Letters **121** (2018).
- 3056 [178] K. Abe *et al.*, Physical Review D **91** (2015).
- 3057 [179] R. Patterson *et al.*, Nuclear Instruments and Methods in Physics Research Section
3058 A: Accelerators, Spectrometers, Detectors and Associated Equipment **608**, 206
3059 (2009).
- 3060 [180] e. a. S. Berkman, T2K Technical Note **146** (2013).
- 3061 [181] e. a. A. Himmel, T2K Technical Note **219** (2015).
- 3062 [182] F. a. James, (1998), CERN Program Library Long Writeups.
- 3063 [183] X. Li and M. Wilking, T2K Technical Note **319** (2017).
- 3064 [184] S. Tobayama, *An Analysis of the Oscillation of Atmospheric Neutrinos*, PhD thesis,
3065 British Columbia U., 2016.

- 3066 [185] e. a. D. Barrow, T2K Technical Note **399** (2020).
- 3067 [186] A. Maghrabi, A. Aldosari, and M. Almutairi, Advances in Space Research **68**,
3068 2941 (2021).
- 3069 [187] Super-Kamiokande Collaboration, K. Abe *et al.*, Phys. Rev. D **97**, 072001 (2018),
3070 <https://link.aps.org/doi/10.1103/PhysRevD.97.072001>.
- 3071 [188] Particle Data Group, J. Beringer *et al.*, Phys. Rev. D **86**, 010001 (2012).
- 3072 [189] Y. N. and, Journal of Physics: Conference Series **888**, 012191 (2017).
- 3073 [190] M. Jiang, *Study of the neutrino mass hierarchy with the atmospheric neutrino data*
3074 *collected in Super-Kamiokande IV*, PhD thesis, Kyoto University, 2019.
- 3075 [191] S. N. K. Iyogi and Y. Obayashi., T2K Technical Note **027** (2011).
- 3076 [192] LeeKaPik, *Study of the neutrino mass hierarchy with the atmospheric neutrino data*
3077 *observed in Super-Kamiokande*, PhD thesis, Tokyo University, 2012.
- 3078 [193] The Super-Kamiokande Collaboration, R. Wendell *et al.*, Phys. Rev. D **81**, 092004
3079 (2010).
- 3080 [194] Super-Kamiokande Collaboration, J. Hosaka *et al.*, Phys. Rev. D **74**, 032002
3081 (2006).
- 3082 [195] L. M. et al, T2K Technical Note **395** (2020).
- 3083 [196] P. B. et al., T2K Technical Note **212** (2015).
- 3084 [197] W. Parker, *Constraining Systematic Uncertainties at T2K using Near Detector Data*,
3085 PhD thesis, Royal Holloway University of London, 2020.
- 3086 [198] V. B. et al., T2K Technical Note **246** (2015).
- 3087 [199] J. Misset, T2K Technical Note **318** (2017).
- 3088 [200] e. a. J. Chakrani, T2K Technical Note **414** (2022).
- 3089 [201] T2K Collaboration, M. Wascko, T2K Status, Results, and Plans, Neutrino 2018,
3090 2018.
- 3091 [202] e. a. Tomislav Vladisavljevic, T2K Technical Note **354** (2020).
- 3092 [203] G. Ambrosini *et al.*, Phys. Lett. B **420**, 225 (1998).

- 3093 [204] e. a. Edward Atkin, T2K Technical Note **344** (2019).
- 3094 [205] e. a. D. Barrow, T2K Technical Note **422** (2022).
- 3095 [206] e. a. D. Barrow, T2K Technical Note **426** (2022).
- 3096 [207] The MiniBooNE Collaboration, A. A. Aguilar-Arevalo *et al.*, Phys. Rev. D **81**,
3097 013005 (2010), <https://link.aps.org/doi/10.1103/PhysRevD.81.013005>.
- 3098 [208] P. de Perio and J. Imber, T2K Technical Note **186** (2014).
- 3099 [209] P. de Perio and J. Imber, T2K Technical Note **107** (2012).
- 3100 [210] C. V. Daniel Barrow, T2K-SK Detector Matrix Uncertainties - MaCh3 In-
3101 tegration, <https://git.t2k.org/t2k-sk/t2ksk-detcovmat/-/tree/feature/MaCh3Integration>, Accessed: 22-06-2022.
- 3103 [211] R. Wendell, *Three Flavor Oscillation Analysis of Atmospheric Neutrinos in Super-*
3104 *Kamiokande*, PhD thesis, University of North Carolina, 2008.
- 3105 [212] A. M. Dziewonski and D. L. Anderson, Phys. Earth Planet. Inter. **25**, 297 (1981).
- 3106 [213] e. a. D. Barrow, T2K Technical Note **425** (2022).
- 3107 [214] R. G. Calland, A. C. Kabeth, and D. Payne, **9**, P04016 (2014).
- 3108 [215] R. Wendell, <http://www.phy.duke.edu/raw22/public/Prob3++/>.
- 3109 [216] F. Kallenborn, C. Hundt, S. Böser, and B. Schmidt, Computer Physics Communi-
3110 cations **234**, 235 (2019).
- 3111 [217] L. Warsame, MaCh3 Analysis Progress.
- 3112 [218] S. Bourret, J. A. B. Coelho, and V. V. E. and, Journal of Physics: Conference Series
3113 **888**, 012114 (2017).
- 3114 [219] C. Rott, A. Taketa, and D. Bose, Scientific Reports **5** (2015).
- 3115 [220] K. Hagiwara, N. Okamura, and K. ichi Senda, Journal of High Energy Physics
3116 **2011** (2011).
- 3117 [221] D. Typinski, Earth Gravity, <http://www.typnet.net/Essays/EarthGravGraphics/EarthGrav.pdf>, Accessed: 24-06-2022.
- 3119 [222] R. Barlow and C. Beeston, Comput. Phys. Commun. **77**, 219 (1993).

- 3120 [223] J. S. Conway, Incorporating nuisance parameters in likelihoods for multisource
3121 spectra, 2011.